

**EARLY AGE DELAMINATION IN CONCRETE PAVEMENTS MADE WITH  
GRAVEL AGGREGATES**

A Dissertation

by

JUANYU LIU

Submitted to the Office of Graduate Studies of  
Texas A&M University  
in partial fulfillment of the requirements for the degree of

DOCTOR OF PHILOSOPHY

August 2006

Major Subject: Civil Engineering

**EARLY AGE DELAMINATION IN CONCRETE PAVEMENTS MADE WITH  
GRAVEL AGGREGATES**

A Dissertation

by

JUANYU LIU

Submitted to the Office of Graduate Studies of  
Texas A&M University  
in partial fulfillment of the requirements for the degree of

DOCTOR OF PHILOSOPHY

Approved by:

Chair of Committee,	Dan G. Zollinger
Committee Members,	Robert L. Lytton
	Dallas N. Little
	Alan B. Palazzolo
	Anal K. Mukhopadhyay
Head of Department,	David Rosowsky

August 2006

Major Subject: Civil Engineering

**ABSTRACT**

Early Age Delamination in Concrete Pavements Made with Gravel Aggregates.

(August 2006)

Juanyu Liu, B.E., Tongji University, P.R. China;

M.S., Texas A&M University

Chair of Advisory Committee: Dr. Dan G. Zollinger

Gravel aggregates had been used extensively in the Houston District of Texas Department of Transportation (TxDOT) for continuously reinforced concrete pavements construction for many years. However, some of these pavements have been subject to early age delamination and eventual spalling damage. Therefore, a series of studies funded by TxDOT since the early 1990's has been conducted to gain a better understanding of mechanisms, material properties, and construction practices, and to provide guidelines and recommendations for minimizing early-age delamination in concrete pavements made with gravel aggregates.

In this study, a test protocol to measure the bond strength between aggregates and cement mortar was established, and the effects of different material and construction parameters on the bond strength of concrete at early ages using a fractional factorial design were investigated. The significances of each factor to achieve better bonding performance were determined, and the optimum design combination was subsequently chosen and validated. Geometric parameters were proposed to characterize aggregate shape properties relative to bonding performance with the facilitation of the Aggregate Imaging System. A rating system based on utility theory was developed to evaluate the overall contribution of aggregate properties (i.e. physical, geometric, and chemical) to the concrete bonding capability and the feasibility of certain mixture design combinations. As for theoretical representation of the bond strength across the interfacial transition zone, a model of interfacial fracture energy between aggregate and mortar that represents the energy necessary to create a crack along the interface was formulated.

This model built the connection between concrete properties at the meso-level (represented by the interfacial fracture energy between aggregate and mortar) and the macro-level (represented by fracture toughness of concrete and significant influencing materials and construction factors). In addition, the moisture effects on stress development of concrete pavements at early ages using field data as inputs were numerically simulated, and a fracture mechanics-based approach was used to predict the occurrence of delamination. A delamination detection protocol for the field was developed to explore the feasibility and potential of utilizing Ground Penetration Radar technology in delamination detection. Research findings from laboratory investigation, field testing, theoretical modeling, and numerical analysis were further validated through field test sections, and the associated framework for delamination guidelines was established.

## ACKNOWLEDGEMENTS

Thanks to Dr. Dan G. Zollinger, chair of my committee. I am very appreciative of your invaluable guidance and inspiration, immense help and support, and constant trust and encouragement throughout my graduate studies. I am indebted to Dr. Robert L. Lytton for his invaluable guidance and advice, and the constant support and encouragement he offered me in the past six years. I would like to thank Dr. Dallas N. Little, Dr. Alan B. Palazzolo, and Dr. Anal K. Mukhopadhyay for their guidance, assistance and efforts during the dissertation phase.

My sincere appreciation goes to Dr. Amy Epps Martin, Dr. Chia-pei Chou, Dr. Jie Han, Dr. Baoshan Huang, Dr. Yunlong Zhang, Dr. Jose M. Roesset, and Dr. Giovanna Biscontin for their constant advice, care, encouragement, and support during my Ph.D study. I would like to express my sincere gratitude for all the support and assistance from our Rigid Pavements group including Ivan Avelar, Rakesh Busane, Dan Ye, Sehoon Jang, Youn Su Jung, Sang Ick Lee, Hassan Ghanem, and Chang-Seon Shon. I want to thank Dr. Fujie Zhou, Dr. Wenting Liu, Lee Gustavus, Tom Scullion, and Enad Mahmoud for their help during my study. I want to thank Pam Kopf, Cathy Bryan, Lupe Fattorini, and Teresa Boriski for their kind assistance.

Words can fail in expressing my love and gratitude to my family. There is always home and family to give me encouragement and comfort. Special thanks are given to Dr. Xiong Zhang for his continuous help, support, care, and patience during this study.

I want to give thanks to my friends who always provide me help, support and care. They are: Peggy Perrone, Dr. Hao Li, Dr. Ke Li, Dr. Peng Li, Dr. Xiaoxue Wang, Dr. Lubinda Walubita, Xiaojia Chen, Yi Lin, Grace Lo, Linhua Li, Yuanchang Xie, Reza Ashtiani, Veronica Castelo Branco, Kamilla Vasconcelos, Edward Ofori-Abebrese, and Edith Arambula. My life in United States is brighter because of them.

Last but not least, I want to thank TxDOT for funding this research study.

## TABLE OF CONTENTS

	Page
ABSTRACT .....	iii
ACKNOWLEDGEMENTS .....	v
TABLE OF CONTENTS .....	vi
LIST OF FIGURES .....	viii
LIST OF TABLES .....	xiii
<b>CHAPTER</b>	
<b>I INTRODUCTION .....</b>	<b>1</b>
General .....	1
Objective .....	2
Research Methodology .....	2
<b>II LITERATURE REVIEW .....</b>	<b>9</b>
General .....	9
Delamination Mechanism .....	9
Interfacial Bond between Aggregate and Mortar .....	11
<b>III LABORATORY INVESTIGATION .....</b>	<b>29</b>
General .....	29
Fracture Toughness to Represent Aggregate-Mortar Interfacial Bond .....	29
Measures to Improve Early Age Aggregate-Mortar Interfacial Bond .....	33
Taguchi Method .....	43
Experimental Design Analysis .....	47
<b>IV AGGREGATE PROPERTIES AND APPLICATION OF UTILITY THEORY .....</b>	<b>57</b>
General .....	57
Aggregate Surface Free Energy Measurement .....	57
Aggregate Shape and Texture Characteristics .....	66
Aggregate Physical Properties .....	81
Aggregate Chemical Properties .....	84
Utility Theory .....	86
<b>V INTERFACIAL FRACTURE ENERGY MODEL AND STRESS</b>	
<b>ANALYSIS APPROACH .....</b>	<b>93</b>

CHAPTER	Page
General .....	93
Interfacial Fracture Energy .....	93
Delamination Occurrence Prediction .....	111
VI FIELD TESTING.....	133
General .....	133
Ground Coupled GPR .....	133
GPR Testing .....	136
GPR Delamination Detection Protocol .....	149
Field Test Sections .....	154
VII CONCLUSIONS AND RECOMMENDATIONS .....	190
General .....	190
Conclusions .....	190
Recommendations .....	195
REFERENCES .....	197
APPENDIX A .....	215
APPENDIX B .....	231
VITA.....	250

## LIST OF FIGURES

FIGURE	Page
2.1 Spalling and delamination .....	10
2.2 Formation of horizontal delamination .....	10
2.3 Factors leading to porous aggregate-HCP interface .....	12
2.4 Various models of ITZ .....	14
2.5 Techniques used for measuring aggregate-cement bond strength .....	16
3.1 Geometry shapes of specimens. ....	32
3.2 Gradation curves for two aggregate types .....	34
3.3 Fracture toughness of concretes at different ages.....	35
3.4 Gradation curves for coarse aggregates .....	36
3.5 Compressive strength of concretes at different ages .....	37
3.6 Fracture toughness of concretes at different ages .....	37
3.7 Crushed gravel particles .....	38
3.8 Natural gravel particles .....	38
3.9 Fracture toughness comparison between concrete with and without dense graded aggregates .....	40
3.10 Effect of charging sequencing on 3-day concrete fracture toughness .....	41
3.11 ITZ of concrete with conventional charging sequencing .....	42
3.12 ITZ of concrete with modified charging sequencing .....	42
3.13 Compressive strength results .....	50
3.14 Fracture toughness results .....	51
3.15 1-day ITZ microstructure of test 3 mix .....	51
3.16 1-day ITZ microstructure of test 5 mix .....	52
3.17 1-day ITZ microstructure of test 6 mix .....	52



FIGURE	Page
3.18 Main effects plot of means .....	54
3.19 Main effects plot of S/N ratios .....	54
3.20 Fracture toughness of optimum combination.....	56
3.21 ITZ microstructure of optimum mix .....	56
4.1 USD setup .....	61
4.2 Aggregate shape components.....	67
4.3 AIMS set-up .....	70
4.4 Difference in gradient between particles.....	72
4.5 Illustration of the wavelet decomposition .....	74
4.6 Example of AIMS gradient angularity index curve .....	75
4.7 Example of AIMS texture index curve.....	76
4.8 Aggregate shape classification limits.....	78
4.9 Aggregate geometric properties summary .....	81
4.10 Aggregate gradation curves.....	82
4.11 ITZ comparisons of limestone and quartzite.....	86
4.12 Utility curve of 1-day $K_{IC}$ .....	91
5.1 Crack propagation and fracture energy for materials.....	96
5.2 Failure modes of coarse aggregates .....	97
5.3 RPCA of two aggregates .....	103
5.4 Fracture surface of concrete with VG .....	104
5.5 Effects of material factors on interfacial fracture energy .....	105
5.6 Schematic representation of crack blunting .....	106
5.7 Schematic representation of Equations 5.16 and 5.17 .....	108
5.8 Linear relation between $G_i$ and $G_c$ .....	111
5.9 Fracture limit curve .....	113

FIGURE	Page
5.10 Example of desorption-sorption isotherms of cement paste, established by powers .....	116
5.11 Geometry and mesh of modeling .....	123
5.12 Relative humidity trends from TMAC <sup>2</sup> .....	124
5.13 Development of elastic modulus of concrete .....	126
5.14 Diffusivity history at 8.02 cm below the surface of concrete .....	127
5.15 Mode I stress intensity factor history .....	128
5.16 Mode II stress intensity factor history .....	129
5.17 Sawcut effect comparison .....	131
5.18 Design methods comparison .....	132
6.1 Principle of GPR .....	134
6.2 Ground coupled GPR setup .....	136
6.3 The pavement section without sawcuts before the core was taken .....	137
6.4 The pavement section with sawcuts before the core was taken .....	138
6.5 Cored samples: (a) along the sawcut; (b) along the crack .....	138
6.6 GPR data from test area with the confirmed delamination .....	139
6.7 The coring sample with delamination: (a) top view of the coring hole; (b) fracture surface .....	140
6.8 Test section at IH10 without sawcut .....	141
6.9 Test section at SH 225 with sawcut .....	143
6.10 Core collected from location marked at Figure 6.9 .....	143
6.11 Test section at SH 225 without sawcut .....	144
6.12 Core collected from location marked at Figure 6.11 .....	144
6.13 Another test section at SH 225 without sawcut .....	145
6.14 Core collected from location marked at Figure 6.13 .....	145

FIGURE	Page
6.15 Crack #4 and concrete cores.....	147
6.16 GPR waveform of crack #4.....	147
6.17 Crack #9 and concrete cores.....	148
6.18 GPR waveform of crack #9.....	148
6.19 Example of GPR return waveform with subsurface problem .....	150
6.20 Typical GPR waveforms for bad and good locations.....	151
6.21 Comparison of intermittent negative peak values .....	153
6.22 Probability of peak differences.....	153
6.23 The schematic of test sections.....	157
6.24 Weather station setup.....	159
6.25 Ambient temperature and relative humidity cycles during field test operation.....	160
6.26 Solar radiation and wind speed cycles during field test operation .....	160
6.27 I-button and VWG setup .....	163
6.28 Temperature profile of test section 8.....	163
6.29 Maximum temperature for each test section .....	164
6.30 Main effects plot for maximum concrete temperature .....	164
6.31 CMS setup.....	165
6.32 Moisture profiles of test section 2.....	166
6.33 Evaporation rate of concrete at 24 hours.....	167
6.34 Free shrinkage with time for different sections.....	168
6.35 Maximum free shrinkage of concrete.....	169
6.36 Main effects plot for maximum free shrinkage .....	169
6.37 Gage strains with time for different sections.....	170
6.38 Maximum creep for different sections .....	171

FIGURE	Page
6.39 Main effects plot for maximum creep .....	171
6.40 Crack development with time .....	172
6.41 Crack spacing for concrete sections .....	173
6.42 4-day compressive strength of concrete for all test sections .....	174
6.43 Fracture toughness tests .....	175
6.44 Summary of fracture toughness for each section .....	176
6.45 Main effects plot for 1-day $K_{IC}$ .....	177
6.46 Main effects plot for 3-day $K_{IC}$ .....	178
6.47 GPR waveform at crack #48 of section 2.....	179
6.48 GPR waveform at crack #21 of section 4.....	179
6.49 Peak values comparison of GPR data from SH 288.....	180
6.50 Probability of $(V_2-V_1)$ for SH 288.....	181
6.51 Summary of probability of $(V_2-V_1)$ .....	181
6.52 Delamination prediction for section 3.....	183
6.53 Delamination prediction for section 2.....	183
6.54 Petrography analysis of section 2.....	184
6.55 Delamination prediction for section 4.....	185
6.56 Petrography analysis of section 4.....	185
6.57 Probability density function of stress difference.....	186
6.58 Assessment of probability of delamination occurrence .....	188
6.59 Flowchart structure of guideline.....	189

## LIST OF TABLES

TABLE	Page
3.1	Physical properties of different aggregates ..... 34
3.2	Physical properties of two gravel aggregates ..... 36
3.3	Mix proportion parameters for mixes with and without dense gradation ..... 39
3.4	An example of L8 (2**7) Taguchi design..... 45
3.5	The single-level Taguchi designs available..... 46
3.6	9 test runs according to orthogonal array ..... 49
3.7	Associated mix proportions for 9 test runs..... 49
3.8	Response table of experimental design with respect to means ..... 53
3.9	Response table of experimental design with respect to S/N ratios ..... 53
4.1	Surface energy components of water, n-hexane, and MPK @ 25 °C ..... 61
4.2	SE components for the aggregates ..... 66
4.3	Bond between water and aggregates ..... 66
4.4	Summary of methods for measuring aggregate characteristics..... 69
4.5	Features of analysis methods in AIMS..... 77
4.6	Aggregate sources and sizes..... 80
4.7	Physical properties of aggregates ..... 83
4.8	Rock components of aggregates..... 84
4.9	Overall evaluation for aggregates ..... 89
4.10	Summary of evaluations by rating systems..... 92
5.1	Experimental parameters for interfacial fracture energy investigation ..... 102
5.2	Comparison of interfacial fracture energies ..... 105
5.3	Regression analysis of interfacial fracture energy ..... 109
5.4	Material parameters in the example analysis ..... 126

TABLE		Page
6.1	Test variables for the field program .....	156
6.2	Concrete mix proportion (1 cubic yard) .....	157
6.3	Maximum probability of delamination occurrence .....	187

## CHAPTER I

### INTRODUCTION

#### GENERAL

Spalling is a very common distress type for all types of concrete pavements. It refers to the breakdown or dislodging of concrete segments along a joint or crack in a concrete slab within 0.6 m (2 ft) of a joint or crack (SHRP 1993), and does affect the quality of the pavement smoothness and ride quality, and has been very expensive to maintain and repair. Early age delamination, a very significant contributor of spall damage, is typically oriented parallel to and at a shallow depth below the surface of the pavement, developing often within days after paving (Zollinger et al. 2004). This failure plane, horizontally oriented near the pavement surface and in the vicinity of transverse cracks or joints, can eventually develop into spall damage by fatigue primarily due to repetitive traffic loads passing over the delaminated area.

Particularly in Texas, gravel aggregates have been extensively used in the Houston District for continuously reinforced concrete (CRC) pavements construction for many years, however, some of these pavements in many instances have been subject to debonding of gravel aggregate, early age delamination and eventual spalling damage.

There were several questions raised to minimize early age delamination in concrete pavements made with gravel aggregates. Can gravel aggregates continue to be used? How to evaluate aggregate performance? How to select feasible material design? Is it possible to detect the existing delamination in the field and predict the delamination occurrence? Accordingly, this study focuses on answering these questions, and providing guidelines and recommendations for using gravel aggregates in concrete paving.

---

This dissertation follows the style and format of the *Journal of Transportation Engineering* (ASCE).

## **OBJECTIVE**

The objective of this study is to develop a mechanistic understanding of the delamination process, and provide recommendations to minimize early age delamination for using gravel aggregates in concrete paving, which will address:

- Development of a test protocol to measure the bond strength between aggregates and cement mortar.
- Evaluation of the effectiveness of corrective measures and optimization of material design.
- Investigation of the effects of aggregate characteristics on the bonding performance of concrete.
- Development of early age delamination detection in the field.
- Approach development for predicting delamination occurrence.
- Modeling of aggregate-mortar interfacial fracture energy.

## **RESEARCH METHODOLOGY**

To meet the objective of this study, the following major tasks are conducted:

- Task 1: Literature review
- Task 2: Experimental design and laboratory testing
- Task 3: Aggregate properties characterization and application of utility theory
- Task 4: Approach for predicting the delamination occurrence and formulation of interfacial fracture energy model
- Task 5: Development of delamination detection protocol and test section validation
- Task 6: Guideline frame work development and recommendations to use gravel in CRC pavement construction



### **Task 1: Literature Review**

A comprehensive literature review was conducted to gather information on key subjects that pertain to this study such as research on interfacial transition zone (ITZ), current representations and measurements of interfacial bond between aggregates and mortar, the effects of concrete mixture proportions (i.e. various aggregate and non-aggregate factors), method of construction, and method of curing on bonding strength of concrete, previous efforts to improve bond strength and related information on the ITZ. A review of the bonding mechanism and details of a delamination and spalling modeling was reviewed; literature findings were summarized and documented. This task is presented in Chapter II.

### **Task 2: Experimental Design and Laboratory Testing**

Based on the previous study (Zollinger et al. 1993), fracture toughness of concrete is used to represent the bond between aggregate and mortar. A test method developed by Texas Transportation Institute (TTI) using a modified split tensile specimen based on size effect law (SEL) (Tang et al. 1999) is used to determine fracture toughness and process zone length.

Various possible corrective measures to improve the interfacial bonding between aggregate and mortar were conducted in the laboratory, to narrow down a list of possible corrective measures including application of different aggregate types, lowering water-cement ratio, improving curing, and application of ultra-fine fly ash among others.

A fractional factorial design (Taguchi method) based on “orthogonal array” (Taguchi et al. 1993) was used to evaluate the effects of various factors on the bonding strength. Test runs were made according to the fractional factorial design, where for each test run, compressive strength and fracture toughness at different ages were conducted.

Data analysis involved laboratory test data reduction and analysis relative to compressive strength, fracture toughness, and process zone length. According to the

Taguchi design, the test data was analyzed by statistical software such as MINITAB (Mathews 2004) to evaluate the significances of each factor to achieve better fracture toughness performance. The optimum combination was subsequently chosen and validated in further laboratory testing. Chapter III describes the work on this task.

### **Task 3: Aggregate Properties Characterization and Application of Utility Theory**

The aggregate properties investigated under this task include physical, geometric, and chemical properties. Physical properties investigated include aggregate gradation, oven-dry bulk specific gravity (BSG-od) and dry rodded unit weight (DRUW), and absorption capacity (AC). The aggregate shape and texture characteristics were analyzed using the Aggregate Imaging System (AIMS) available at TTI. Based on a statistical distribution of angularity and texture parameters, the concrete aggregates were evaluated at all size levels. The results were summarized and used to investigate the effects of the aggregates mechanical interlocking on the bonding mechanism.

The Universal Sorption Device (USD) was used to determine the surface energy of aggregates. This method utilizes a vacuum gravimetric static sorption technique that identifies gas adsorption characteristics of selected solvents with known surface free energy components to indirectly determine the surface energies of the aggregate (Cheng 2002). To investigate the effects of possible chemical interaction between aggregates and mortar, the mineralogy components of each aggregate type were classified.

Utility theory (Ledbetter et al. 1977) facilitates a way to compare dissimilar things based on their values and utilities, and can be used to synthesize and account for a variety of factors that play a role to varying degrees in engineering processes. A rating system based on utility theory was applied to evaluate the overall contribution of aggregate properties on concrete bonding. A combined value can be generated to represent the integral overall contribution of an aggregate for each aggregate type by assigning a user defined weighting factor to the rating of each individual aggregate property allowing for an overall rating to be combined from several single parameters.

The feasibility of selected combinations relative to the bonding mechanism can also be accomplished based on utility theory as that of the aggregate contribution, but with respect to mix design factors. Chapter IV provides the report of this task.

#### **Task 4: Approach for Predicting the Delamination Occurrence and Formulation of an Interfacial Fracture Energy Model**

The interfacial fracture energy between the aggregate and mortar can be described as the energy necessary to create a crack along this interface. Considering concrete as a three-phase composite material with the three phases being hardened cement paste, aggregate and interfacial zone between the hardened cement paste and aggregate, the interfacial fracture energy can be predicted based on the relation between fracture energy of concrete and fracture energies of its components.

Under this task, the relation between the interfacial fracture energy and related construction factors was investigated. The aggregate factors included maximum aggregate size, coarse aggregate factor, aggregate physical properties, aggregate shape characteristics (form, angularity, and texture), and chemical properties, and whether the overall performance of the aggregate can be represented by an overall rating of the contribution of aggregate to the bonding performance. Non-aggregate factors include water/cementitious ratio (w/cm), cement factor, ultra-fly ash content, and curing quality. The overall effects of all material, construction, and time factors on are closely related to the feasibility rating value of each design combination. Therefore, the final results build the connection between concrete properties at the meso-level (represented by the interfacial fracture energy between aggregate and mortar) and at the macro-level (represented by fracture toughness of concrete and significant influencing materials and construction factors).

Stress intensity and fracture toughness are key fracture mechanics parameters that can be used by materials engineers and designers in design analysis (Boresi et al. 1993; Irwin 1958; Irwin 1957; Hertzberg 1976). Within the scope of linear elastic

fracture mechanics, the stress field at the crack tip is determined by the stress intensity factors ( $K_I$ ). Therefore, by comparing  $K_I$  and critical stress intensity factor or fracture toughness ( $K_{IC}$ ) directly based on fracture criteria for unstable growth, one can then determine the crack stability of the material under given loading conditions. The  $K_{IC}$  value at early ages of concrete has been used to represent the nature of the interfacial bond between aggregate and mortar relative to the delamination. Therefore, it appears to be feasible to predict the occurrence of delamination by comparing the development of  $K_I$  and  $K_{IC}$ . In this manner, it can also be used for evaluating the effectiveness of pavement design methods to prevent delamination and spalling problems.

Till now, many methods have been adopted to compute  $K_I$ , such as finite element method, boundary element method, and finite difference method, etc. Among these, finite element method is the most popular tool. In this study, finite element software packages — Temperature and Moisture Analysis of Curing Concrete (TMAC<sup>2</sup>) (Jeong 2003) and ABAQUS (ABAQUS 2003) were applied to predict the development of  $K_I$ . Though temperature variation is also a factor in the delamination development, this study specifically focuses on early age concrete behavior associated with volumetric contraction due to moisture induced shrinkage. Therefore, a coupled hygro-mechanical stress analysis is numerically carried out using typical concrete pavement examples. The  $K_I$  at an early age is investigated by incorporating distribution and history of moisture relative to the material-related moisture transport property in the analysis. The correlation to the development of delamination was then evaluated by comparing the  $K_I$  against  $K_{IC}$  developed under lab investigation through examples with different design factors. The work in this task is included in Chapter V.

### **Task 5: Development of Delamination Detection Protocol and Test Section Validation**

As a non-destructive testing (NDT) technique, the ground penetrating radar (GPR) has been applied in pavements to determine the thickness of pavement layers and detect the

defects in the pavements (Saarenketo and Scullion 1994). In this study, ground coupled GPR from TTI was used to detect delaminations. Several highways paved with gravel aggregates in Houston district were selected for GPR testing. Visual observation and distress survey were also conducted. Concrete cores were taken from these sites to verify the nature of the delaminations.

The laboratory work and numerical analysis conducted in the previous tasks reveals important information on curing and climatic conditions, mixture design, aggregate combinations, time of placement, and method of early age crack control to provide sufficient guidance to establish test sections. Therefore, pavement test sections using gravel were established in November, 2005 to produce performance test data to validate measures, practices and techniques to minimize the development of delamination in CRC paving. Three continuous days from November 16<sup>th</sup> to 18<sup>th</sup> were spent for paving of total ten sections.

Field data has been collected through various techniques available to TTI, Texas Department of Transportation (TxDOT), University of Texas at El Paso (UTEP), and Center of Transportation Research (CTR). Weather data, concrete temperature and relative humidity profiles, and drying shrinkage development were monitored, and pavement surveys were conducted to monitor the crack pattern development over time in different test sections. Bonding strength was measured, and GPR technique was conducted on November 28<sup>th</sup> to track the delamination development. Correspondingly, results from stress analysis and GPR delamination detection protocol were further validated from visual observation of concrete cores taken on cracks. Chapter VI describes the detailed results about this task.

### **Task 6: Conclusions and Recommendations**

Upon completion of experimental data analysis, numerical simulation and modeling, and field testing and validation, the results were synthesized to draw conclusions and recommendations, as presented in Chapter VII. The conclusions include the significant

findings through the above tasks, and the recommendations include further investigation of material characteristics, validation and optimization of analysis approaches proposed in this study.

## **CHAPTER II**

### **LITERATURE REVIEW**

#### **GENERAL**

In this chapter, a comprehensive literature review was conducted to gather information on key subjects that pertain to this study such as current aggregate bond strength measurement techniques, the effects of concrete mixture proportions (i.e. various aggregate factors, w/cm, and application of mineral admixture etc), method of construction, and method of curing on the bonding performance of concrete pavements, and trials to improve bonding performance and information on the ITZ. The research status of bonding mechanism and development of delamination and spalling modeling was also reviewed, and the literature findings were summarized and documented.

#### **DELAMINATION MECHANISM**

As shown in Figure 2.1 (a) (Soares and Zollinger 1998), spalling refers to the breakdown or dislodging of concrete segments along a joint or crack in a concrete slab within 0.6 m (2 ft) of a joint or crack (SHRP 1993, Senadheera and Zollinger 1996) that can affect the structural slab integrity. A significant contributor to spalling is the existence of shallow, horizontal delaminations that is oriented parallel to and at a shallow depth below the surface of the pavement (Figure 2.1 (b)). As shown in Figure 2.2, water starts to evaporate from inside of concrete to the air once the concrete is paved. However, relative humidity distribution is not uniform, because the water at the surface or close to the surface is much easier to evaporate than that inside the concrete. The development of the moisture gradient is due to evaporation as a function of the ambient and curing conditions during and after placement of the concrete. If the loss of moisture is great enough in terms of evaporation and time, a failure plane, horizontally oriented near the

pavement surface and in the vicinity of transverse cracks or joints, can develop resulting in a weakening or lowering of the resistance of the pavement surface to spall damage.

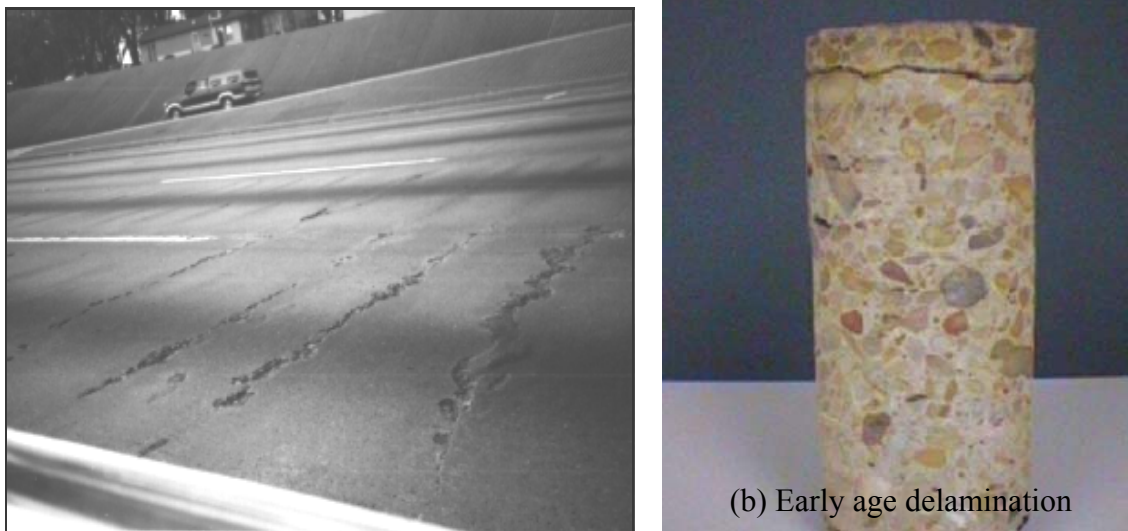


Figure 2.1 Spalling and delamination

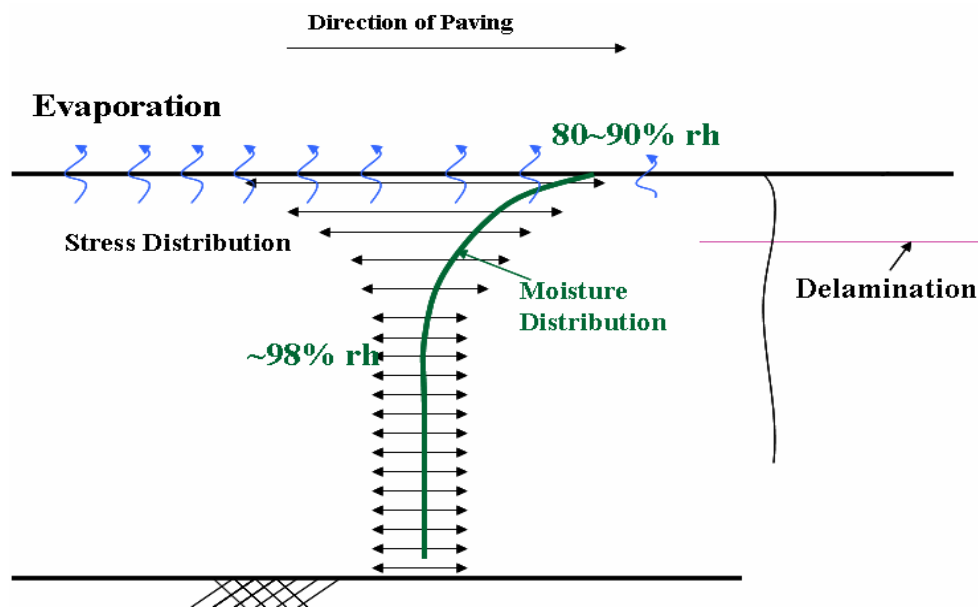


Figure 2.2 Formation of horizontal delamination

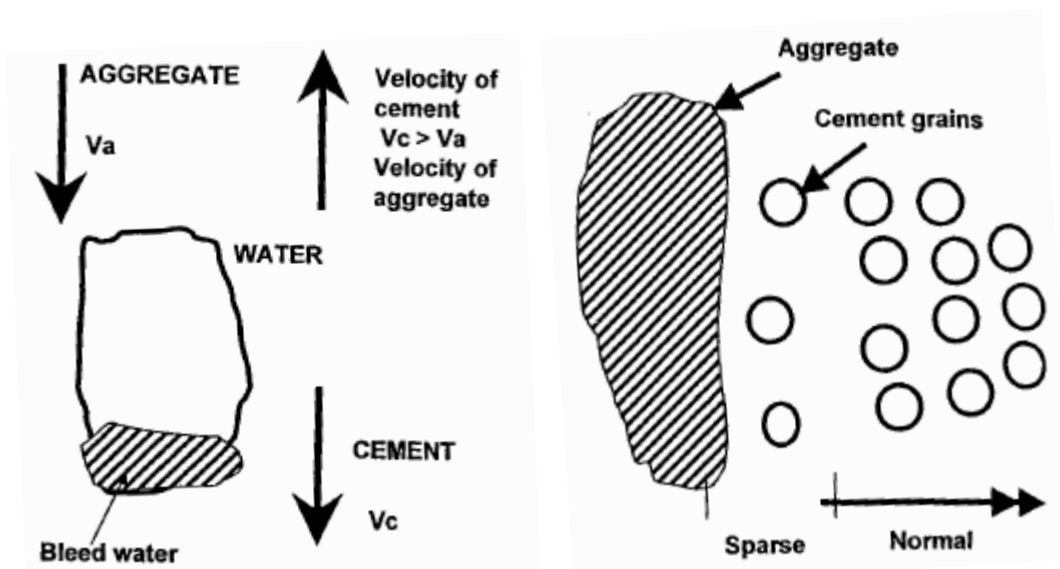


Early age delamination occurs when stresses caused by the moisture variation surpass the concrete shear strength. A design framework for delamination formation and subsequent spalling development was introduced by Soares and Zollinger (1998), where stresses due to moisture variation were considered within the scope of the formation of delamination fracture, and shear stress relative to delamination was determined from stress functions derived from median-thick plate theory in a fashion similar to that shown by Westergaard (1927) and Tang et al. (1993).

Conditions necessary for formation of delamination include low interfacial strength between the aggregate and mortar and sufficient evaporation of pore water from the hydrating concrete, resulting in differential drying shrinkage near the pavement surface (Wang and Zollinger 2000). In concrete mixtures made with certain coarse aggregate types, a greater tendency exists to cause early age delamination and eventual spalling. For that reason, experience relates spalling to certain aggregate types, their associated aggregate-mortar bond characteristics, and the tendency of concrete to allow water to evaporate during curing.

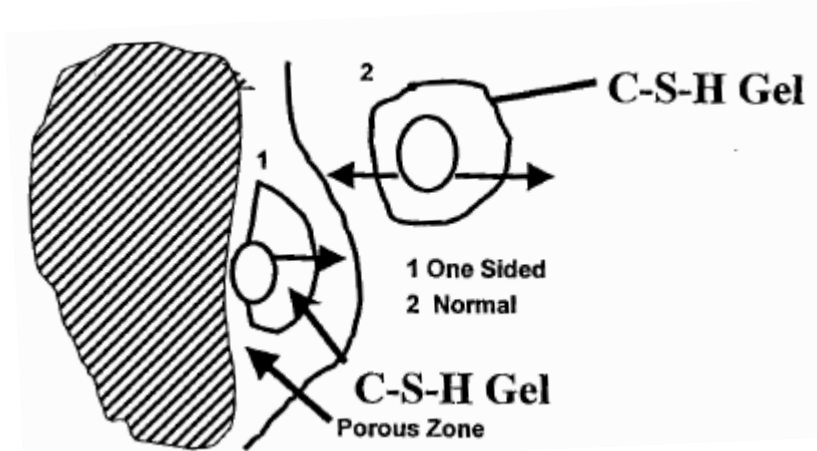
## **INTERFACIAL BOND BETWEEN AGGREGATE AND MORTAR**

The interfacial transition zone (ITZ) in concrete refers to the region surrounding a reinforcing phase as exists in concrete as "*aureole de transition*", derived originally from optical microscope observations made by Farran (Ollivier and Grandet 1980) many years ago. Scrivener and Pratt (1986) reported that "the relative movement of the sand and cement grains during mixing, and possibly settling of the aggregates before the cement paste sets, may lead to regions of low paste density around grains and to areas of localized bleeding at the aggregate-cement interface in which large Calcium hydroxide ( $\text{Ca}(\text{OH})_2$ ) crystals precipitate." The interface regions are, in general much different from the bulk cement paste in terms of morphology, composition, and density. At least in part due to bleeding referred to earlier, the interface region between aggregate and cement paste is more porous than bulk paste, leading to lower densities (Figure 2.3).



(a) Accumulation of Bleed Water

(b) Wall Effect

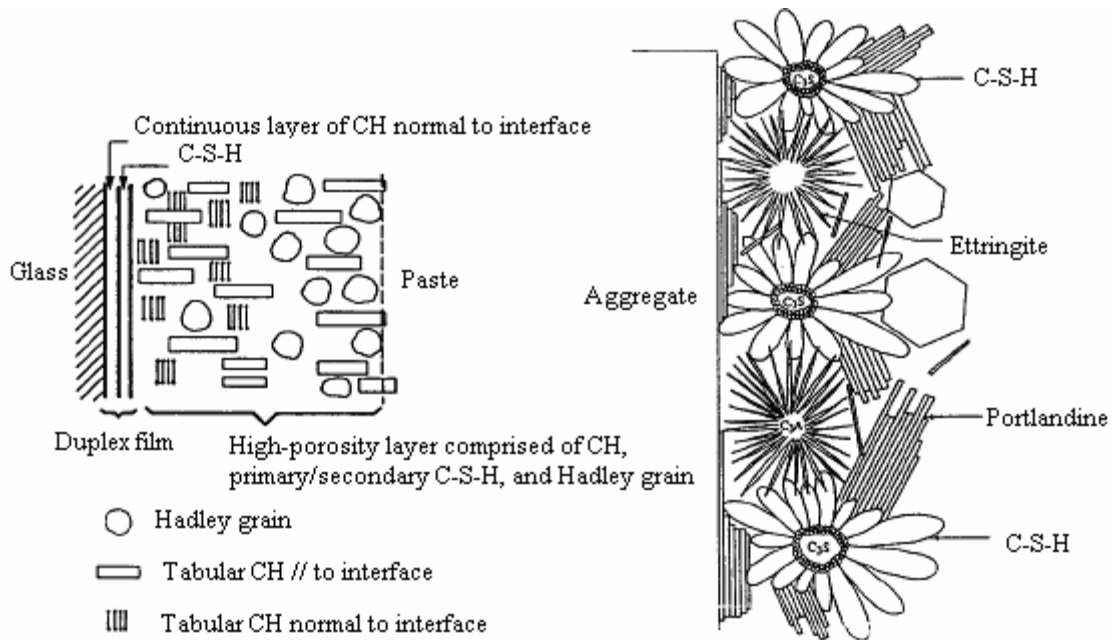


(c) One Sided Growth of C-S-H Gel

**Figure 2.3 Factors leading to porous aggregate-HCP interface (Subramanian 1999)**

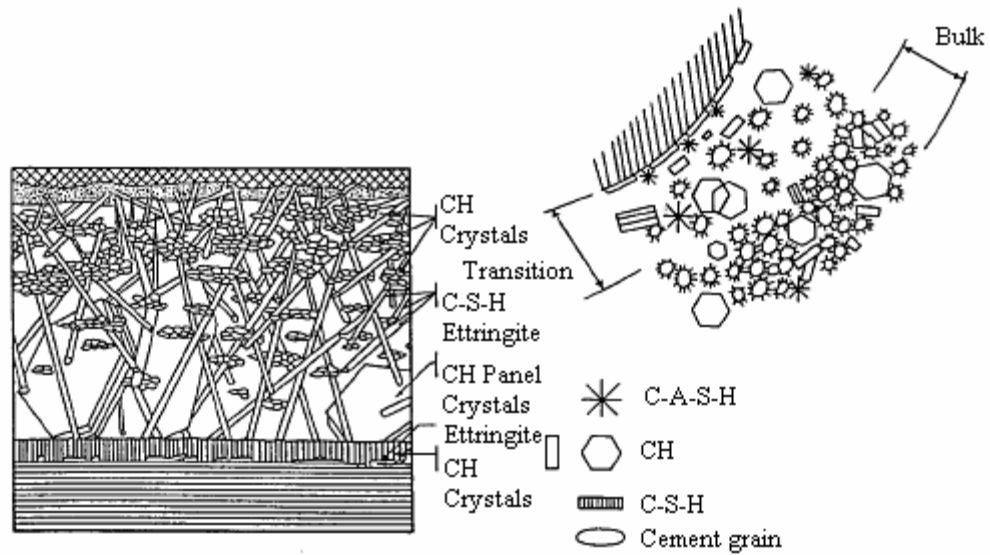
The major ITZ models in the literature come from Barnes (1980), Ollivier and Grandet (1980), Monteiro (1985), and Zimmelman (1985), as shown in Figure 2.4. These models differ primarily in the presence of a C-S-H film, preferential orientation of the  $\text{Ca(OH)}_2$  crystals at the interface (either horizontal or vertical), epitaxial development of  $\text{Ca(OH)}_2$  crystals within the transition zone, and the presence of ettringite in direct contact with the aggregate and in high concentration zone. The fracture path often runs along the cleavage planes of oriented  $\text{Ca(OH)}_2$  crystals. Mehta (1986) stated that “in mature pastes, the fracture surface generally contains unusually large areas of calcium hydroxide crystals.” Due to the large crystal size and, therefore, a small surface area, the inter-particle bonding forces between calcium hydroxide crystals or between calcium hydroxide crystals and other particles in the cement paste are weak.

Extensive studies have been done on the microstructure of cement paste/aggregate interfacial zone by using scanning electron microscopy (SEM), X-Ray Diffraction (XRD) and mercury intrusion porosimetry (MIP) techniques (Scrivener and Gartner 1988, Nehdi and Mindess 1997, Zhang et al. 1996, Winslow et al. 1994). Many studies (Scrivener and Pratt 1986, Monteiro et al. 1985, Scrivener and Gartner 1988, Larbi and Bijen 1990, Monteiro and Ostertag 1989) reported that the thickness of the interfacial region is approximately 40 to 50  $\mu\text{m}$ , with the major difference in characteristics from the bulk paste occurring within the first 20  $\mu\text{m}$  from the physical interface. The weakest part of the interface of this interfacial zone lies not right at the physical interface, but 5 to 10  $\mu\text{m}$  away from it within the paste fraction. Microscopic examination of polished concrete surfaces by Diamond et al. (1982) revealed that the mean spacing between the aggregate particles is only about 75 to 100  $\mu\text{m}$ . Even though the variability of this spacing is large, it suggests that with an interfacial zone thickness of approximately 50  $\mu\text{m}$ , most of the hydrated cement paste (HCP) lies within the interfacial zone and only a small volume of bulk HCP exists. This indicates that the representation of the actual concrete in the models is far from satisfactory.



a) The Barnes et al. Model as presented by Maso (1980)

b) The Ollivier-Grandet Model (1982)



c) The Zimbelman Model (1985)

d) The Monteiro Model (1986)

**Figure 2.4 Various models of ITZ**

## **Interfacial Bond Representation**

There are no standard test methods to measure or quantify strength of the interfacial zone. Some of the indirect methods of measuring bond are: (1) “push out” test, in which cement mortar is cast against a aggregate prism and the interface is tested in shear, (2) modified indirect tensile test, in which a predetermined notch is cast, the specimen is tested in the indirect mode and fracture face is analyzed, and (3) volumetric surface texture analysis (VST), through this test process the micro- and macro-texture of the fracture face can be analyzed and also the crack path can be determined. As shown in Figure 2.5, eleven of the techniques which have been used for measuring aggregate-mortar bond strength were summarized by Alexander et al. (1965), such as mid-point and one-third-point transverse tests, cantilever methods, conventional, centrifugal and indirect tensile tests, and axial compression tests on shear bond specimens.

Akçaoğlu et al.(2002) investigated the influence of surface, rigidity and size of aggregates and w/cm of the matrix on bond strength at the ITZ and the interrelationship between the bond and the matrix in the failure process of concrete under uniaxial compression, where they prepared cube mortar specimens inserted with a single spherical steel aggregate into the center of the specimens, and tensile strength and tensile strength loss after the application of 40%, 60%, and 80% of compressive strength were used to represent the interfacial bond strength. Rao and Prasad (2002) used two types of test specimens (fresh mortar cast against aggregate surface; and sandwich specimens) under double-edge notched compact tension, and the bond strength was calculated as the failure load divided by the actual failure surface of the interface.

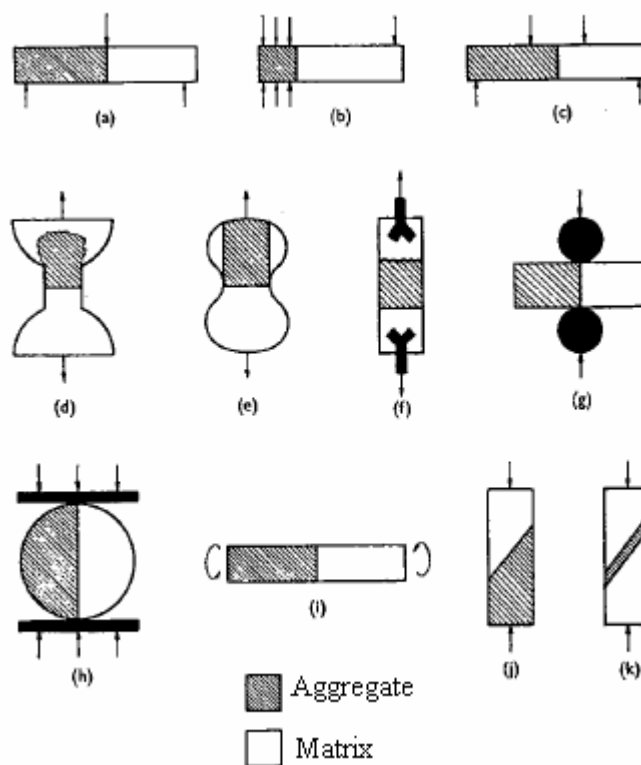


**Figure 2.5 Techniques used for measuring aggregate-cement bond strength**

No current strength theory has been applied directly to the interface between aggregate and cement paste due to the complexity of the microstructure. As a first approximation, Ping and Beaudoin (1992) built a relationship between interfacial bond strength and electrical conductivity of the transition zone, considering interfacial bond strength is directly proportional to the total area fraction of solid phases associated with fracture surface in the transition zone. The interfacial bond strength is linearly related to the electrical conductivity of the transition zone. Bond strength for the non-porous aggregate-portland cement paste system is proportional to the negative thickness ratio of the water layer and transition zone and inversely proportional to  $w/cm$  ratio.

The emerging technology with fractal analysis may pose as a considerable advance towards the development of new methods for aggregate-mortar bond, which will be better than techniques such as AASHTO T 177 Flexural Strength of Concrete

(Using Simple Beam with Center Point Loading) and AASHTO T 97 Flexural Strength of Concrete (Using Simple Beam with Third Point Loading), which have been used among others, to determine bond strength (Fowler et al. 1996).

### *Interfacial Microhardness*

As a nondestructive method, microhardness measurement is a measure of strength of metals and nonporous materials. The test method employs the Vicker's pyramid indenter placed in a conditioned box. Hardness is calculated by the following formula (Ramachandran 1995):

$$H_v (Kg\ mm^{-2}) = \frac{1854.4 \times P}{d^2} \quad (2.1)$$

where P = load (g), d = mean value of the indentation diagonals, and  $H_v$  = microhardness. Microhardness can be useful as a measure of strength development in cements and cement minerals hydrated for different lengths of time.

As a measure of specific surface energy, the hardness of materials has very close relation with mechanical properties of materials. Microhardness testing provides a tool for quantifying microstructural gradients across the ITZ. Microhardness measurements can contribute to characterization of the properties of the ITZ relative to the bulk cement paste matrix and also provide one means of estimating the width of the ITZ. Where the ITZ microstructure is weaker than the bulk region, a depression in the microhardness profile is expected within the zone of influence of the aggregate, the profile at the aggregate surface also being influenced by the strength of the paste–aggregate bond (Asbridge 2002).

The relation between the fracture behavior and microhardness makes it possible to predict the fracture parameters from microhardness measurements (Beaudoin 1982). Tamimi (1994) applied both minimum and maximum microhardness of cement paste–aggregate interface to represent the interfacial bond.

### *Fracture Parameters*

Through microstructural studies, Prokopski (1991) stated that it is the transition zone, and specifically, the aggregate-cement paste interface, where the greatest number of defects occur, and that the concrete failure process commences at the transition zone. Therefore, it is reasonable to utilize the methods of fracture mechanics to relate the fracture parameters to the structural defects (primary cracks). Fracture toughness (or critical stress intensity factor) was commonly used to represent the interfacial bond, because it can be used as a criterion to evaluate concrete quality (Prokopski and Langier 2000), and it can describe the sensitivity of coarse aggregate characteristics to the aggregate-mortar interfacial bond (Senadheera and Zollinger 1996).

A number of studies on the interface fracture mechanics of biomaterial systems have been made (Rice 1988; Hutchinson 1990). Fracture of a biomaterial interface can be expressed in terms of two parameters, an energy release rate,  $G$ , and a phase angle,  $\psi$ . Interface cracking occurs when  $G$  reaches a critical value, defined as the interface fracture energy,  $\Gamma_i$  (Büyüköztürk and Lee 1993). A micromechanical model (Mohamed and Hansen 1999) was developed based on the numerical simulation to investigate the crack-aggregate interaction in concrete materials, and the results showed that the tensile strength ratio, fracture energy ratio, and the moduli ratio between the aggregate and the matrix play the dominant role in determining the crack penetration condition.

Pye and Beaudoin (1992) proposed an energy approach to bond strength determination in cement systems, and they stated that interface fracture energy is a more appropriate descriptor of the quality of the cement paste-substrate bond due to the progressive failure of the bond. In the study conducted by Tan et al. (1995), Tschegg's wedge splitting test (Tschegg et al. 1995), already used for testing of concrete and asphalt, had been slightly modified for testing the fracture behavior of sandstone-matrix and limestone-matrix interfaces. Their results showed that the specific fracture energies of sandstone-mortar and limestone-mortar interfaces were much lower than for bulk mortar. Wong et al. (1999) investigated the mortar-aggregate interfaces from both the



three-point bending test of notched beams with mortar-aggregate interface above the notch and splitting tensile test on mortar-aggregate interface cubes. The parameters studied included: 1) interfacial flexural strength, 2) interfacial fracture energy, 3) interfacial fracture toughness; and 4) interfacial splitting tensile strength. The interfacial fracture toughness ( $K^{if}$ ) was determined based on the theory of interface fracture mechanics for bi-materials, which has the complex form of  $K^{if} = K_1^{if} + K_2^{if}$ , where the two components  $K_1^{if}$  and  $K_2^{if}$  denote the normal stress intensity and the shear stress intensity, respectively. The magnitude of the shear stress intensity is much smaller than that of the normal stress intensity, which indicates that the fracture of the interface between the cement mortars and the aggregates can be approximately considered as the Mode I fracture (tension mode of fracture), and thus the values of  $K_1^{if}$  are comparable with the toughness of mortar ( $K_{IC}^m$ ). The values of  $K_1^{if}$  were about one third of the values of  $K_{IC}^m$ , which is correlated with results of Saito and Kawamura's (1986). The interfacial fracture energy ( $G_F^{if}$ ) was only about 10% of the corresponding mortar fracture energy ( $G_F^m$ ). This is consistent with the results obtained by Mistui et al. (1994) from the aggregate push out test and by Tschegg et al. (1995) from the wedge splitting test. The ratio of  $G_F^{if}$  to  $G_F^m$  was much smaller than the ratio of  $K_1^{if}$  to  $K_{IC}^m$ , indicating the fact that fracture energy and fracture toughness reflect different aspects of the interfacial failure.

### **Factors Affecting Aggregate-Mortar Interfacial Bond**

Struble et al. (1980) categorized the nature of the cement-aggregate bond according to its morphological, chemical, and mechanical properties, and stated that the bond between cement paste and aggregate results from some combination of mechanical interlocking between cement hydration products and the aggregate surface, and a chemical bonding

resulting from a reaction between aggregate and cement paste. Therefore, the influencing factors of aggregate-mortar interfacial bond include both aggregate and non-aggregate factors, which will be summarized below.

### *Aggregate-related Factors*

The nature of the interfacial zone depends on the microstructure characteristics of the aggregate, in which any of the three mechanisms, physical interaction, physical-chemical interaction and mechanical interlock, may be dominant (Zhang and Gjørsvik 1990). The aggregate factors believed to be pertinent to the aggregate-mortar interfacial bonding include physical, geometric, and chemical properties, varied significantly with aggregate types (Senadheera and Zollinger 1996, Zimbelman 1985, Perry and Gillot 1977, Prokopsi and Halbiniak 2000).

The effects of aggregate type and size are important parameters in the formation of ITZ structure and subsequently in the failure process of concrete. Porous aggregates provide an excellent bond because the process of absorption increases and improves the contact area between the paste and the aggregate. The failure surfaces of the concrete made with larger size coarse aggregate show significant traces of pulling out of the aggregate from the matrix. Liu et al. (2006) summarized the reasons why larger aggregate size can have a detrimental effect on the interfacial bonding: 1) for a given volume of coarse aggregate, a larger maximum size reduces the specific surface area of aggregate; 2) an increased stress concentration and microcracks in the vicinity of the aggregate is expected with decreased surface area; 3) larger aggregate size results in the increases of the perimeter and thickness of interfacial layer between mortar and aggregate so that a larger flaw can be formed and the bond strength decreased; and 4) larger aggregate particles tend to accumulate more bleed water around it, which could lead to a higher local w/cm and subsequently, a higher porosity in the ITZ than the ITZ around the smaller aggregates. At the same w/cm and age, reducing the aggregate size from 2.36–4.75 mm range to 150–300  $\mu$ m range tends to reduce the porosity and

increase the content of unhydrated products in the region surrounding the aggregate (Elsharief et al. 2003). For low w/cm ratio composites, the effect of aggregate size on the weakness of ITZ and the failure process of concrete is of paramount importance (Akçaoğlu et al. 2002). With larger aggregates, low w/cm ratio matrices result in more critical ITZs with a more condensed microcrack cloud in a narrower region (higher tensile stress distribution) with increasing aggregate size which leads to lower bond strength. This indicates that the adverse effect of the rigid aggregate became more pronounced with increased matrix quality.

Indirect evidence of the bonding mechanisms due to mechanical interlocking aided by the aggregate surface texture has been established (Alexander et al. 1965, Hsu and Slate 1963) by comparing the bond strength of fractured rock surfaces with that of polished rock surfaces. Aggregate shape characteristics affect the proportioning of portland cement concrete mixtures, the rheological properties of the mixtures, aggregate-mortar bond, and the interlocking strength of the concrete join/crack (Al-Rousan 2004). Previous studies (Mindness et al. 2002, Kosmatka et al. 2002, Will 2000, Fowler et al. 1996) indicated that the bond strength between the cement paste and a given coarse aggregate generally increases as particles change from smooth and rounded to rough and angular. Rough, textured surfaces will improve the mechanical component of the bond by increasing the amount of surface area available for bonding with the paste for a given aggregate content. The surface roughness of the aggregate shows significant influence on the fracture toughness of the interface and the bond strength of the interface (Alexander 1993, Rao and Prasad 2002). Study conducted by Trende and Buyukozturk (1998) showed that for a given type of loading conditions the critical interface fracture energy release rate,  $G_i$ , increases with rougher aggregate surfaces for both Mode I and mixed mode tractions. The interlocking of angular particles results in a strong aggregate skeleton under applied loads, whereas round particles tend to slide by or roll over each other, resulting in an unsuitable and weaker structure. Using a high percentage of flat and elongated particles might cause problems when placing the concrete, which will result in voids and incomplete consolidation of the mix, and thus contribute to spalling.

In addition, it may cause a high internal stress concentration that leads to easier bond failure (Meininger 1998).

Alexandre et al. (1968) reported that bond strength varied widely according to the rock type and surface roughness of the aggregate, with the strengths varying by a factor of as much as two between different aggregates. Some researchers have used this as indirect evidence of chemical reaction between cement and rock types. Ozol (1978) pointed out that variation in bond strength could alternatively be explained by different roughness factors of different aggregates. However, regardless of whether the bond is primarily due to either mechanical interlocking or chemical reaction, the true surface area of the aggregate available for bonding is an important aspect of bonding. The true surface area entails the size, shape, and surface texture of aggregate particles.

Chemical bonds form as a result of chemical interaction between the hydrated cement compounds and the constituent minerals of the aggregate. Farran (1956) first concluded that the bond strength was due to a combination of chemical reactions between aggregate and cement paste, and epitaxial growth of  $\text{Ca(OH)}_2$  on the aggregate surface. Langton and Roy (1980) explored the difference in morphology of the transition zone present near reactive and non reactive aggregates. Suzuki and Mizumaki (1975, 1976) observed that the quantity and crystallinity of these products varied with different aggregates. Mehta and Monteiro (1988) concluded that the transition zone around limestone aggregate is strengthened while the transition zone around quartz aggregate does not show signs of strength increase. Senadheera and Zollinger (1996) also stated that carbonate aggregates produce higher bond strengths than silicate aggregates. They summarized that the surface chemical properties of common silicate minerals, such as quartz and feldspar, are different than those of the carbonate minerals because quartz, which is composed of silicon and oxygen atoms linked in tetrahedral coordination, yields a negatively charged surface through dissociation of hydrogen atoms. This results in a negative charge in the quartz surface and positive charges in the adjacent water medium. This structure is termed the double-layer structure at the quartz-water interface. This strong affinity to water results in a poor bond. However, the study conducted by Tasong

et al. (1998) showed that the limestone in particular produced a porous ITZ as a result of chemical interaction at an early age. The carbon dioxide gas given off as a result of a chemical interaction between the limestone and the hydrating cement paste is considered to be the main reason for this high porosity (Tasong et al. 1999), which accounts for the weaker bond between this rock and the cement paste at an early age.

### *Non-aggregate Factors*

Non-aggregate factors summarized here include w/cm, mineral and chemical admixtures, and processing methods.

#### Water-cementitious ratio (w/cm)

Numerous studies (Simeonov and Ahmad 1995, Zimbelman 1985, Simenow and Ahmad 1995) have indicated that the w/cm is a predominant influencing factor of aggregate-mortar interfacial bond. The structure of porosity of the transition zone, its thickness and properties, and the quality of the matrix are all closely related to w/cm. An increased porosity has been found to occur in the area of the aggregate-cement paste interface caused by the higher w/cm in this region with a simultaneous decrease in w/cm in the bulk of the matrix (Brant 1995), while reducing w/cm from 0.55 to 0.40 resulted in an ITZ with characteristics that were not distinguishable from those of the bulk paste as demonstrated by backscattered electron images (BSE) images (Elsharief 2003). Yuan and Gud (1998) reported that the local increase in w/cm in the area of the aggregate - cement paste interface is proportional to the amount of free unbound water, and any action increasing the contents of the solid phase reduces the effect of the transition zone on the strength properties of concrete. Simenow and Ahmad (1995) also pointed out that reduction in w/cm ratio makes this critical ITZ region narrower. However, according to Bentz et al.'s research (1992), w/cm has little effect on the transition zone thickness, while substantially influencing its porosity.

Prokopski and Langier (2000) conducted the fracture toughness investigations for concretes made from natural gravel aggregate, with various w/cms, without silica fume and with silica fume addition. The largest values of the critical stress intensity factor were showed by concretes with the lowest w/cm (both with and without silica fume addition). This was caused by considerably lower porosity of the aggregate-cement paste transition zone as observed in microstructural examinations, which had in this case a compact structure with a small number of structural defects. As the w/cm increased, an increase in the structural porosity of the aggregate-cement paste transition zone occurred, which caused a promoted propagation of cracks and resulted in lower values of stress intensity factor. For concretes with the lowest w/cm, the forces of adhesion of the aggregate to the cement paste were high (higher than the strength of gravel grains), which resulted in the propagation of cracks through the coarse aggregate grains and the formation of flat-surface fractures. In the case of concretes with a large w/cm, the aggregate-cement paste transition zone was highly porous and weak, which resulted in the development of a crack in this zone; the so-called overgrain fractures, highly irregular and rough. The microstructural examinations (Prokopski 1997) showed that the aggregate-cement paste transition zone in concrete from gravel aggregate with a small w/cm (concrete without silica fume addition) and both with a small w/cm and a silica fume addition was uniform and dense, with only a small number of structural discontinuities. A transgranular character of fracture was observed in this case, that its cracks going through the aggregate grains, which caused the formation of a flat fracture surface. The strength of the aggregate-cement paste interface was in this case higher than the strength of gravel grains, which resulted in highest values of fracture toughness.

#### Mineral and chemical admixtures

Extensive studies have also been done on use of mineral admixtures in concrete and their effects on the microstructure of ITZ (Goldman and Bentur 1992, Bentur and Cohen 1987, Charles-Gibergues 1982). Mineral admixtures influence the development of the

microstructure in the interfacial zone because of two main factors: (1) a densification of the packing of the particles if the size of the additions is much finer than the size of the cement grains; and (2) a modification of the hydration process.

Silica fume affects the pattern of crystallization and degree of orientation of  $\text{Ca(OH)}_2$  crystals at the aggregate surface, resulting in very thin interface during the first few days of hydration (Cheng-yi and Feldman 1985, Larbi and Bijen 1990, Toutanji et al. 1999, Wong et al. 1999). It has been identified to be able to strengthen the interfaces when used in concrete (Pope and Jennings 1992, Goldman and Bentur 1989, Rao and Prasad 2002). According to the results of their studies, addition of silica fume increased the interfacial bond strength and interfacial fracture energy by about 100%. The interfacial bond improvement effect of such materials is due to their small particle size and pozzolanic reactivity, leading to the elimination of water film on aggregate surfaces in noncoated aggregate–cement systems, denser microstructures and stronger interfacial bond.

Fly ash is another type of pozzolanic material widely being used as a cement replacement to produce high-performance concrete and high-volume fly ash concrete (Langley et al. 1989, Carette et al. 1993). Many researchers indicated that low-calcium fly ash (ASTM Class F) also improves the interfacial zone microstructures, although it is generally coarser and less reactive than silica fume. Mehta and Monteiro (1988) indicated that fly ash is effective in reducing the thickness of the interfacial zone and porosity in the interfacial zone after prolonged curing. Saito and Kawamura (1989) demonstrated that fly ash significantly reduced the degree of orientation of  $\text{Ca(OH)}_2$  crystals and suppressed the precipitation of  $\text{Ca(OH)}_2$  crystals and formation of ettringite in the interfacial zone. The research conducted by Bijen and Selst (1992) indicated that fly ash reduced not only the preferential orientation but also the quantity of  $\text{Ca(OH)}_2$ . Besides, Bentz and Garboczi (1991) predicted through computer simulation studies that replacing 20% of cement with fly ash with smaller particle size resulted in higher interfacial strength than that of the control portland cement paste. Wong et al. (1999) investigated the properties of fly ash-modified cement mortar-aggregate interface, and

the results showed that a 15% fly ash replacement increases the interfacial bond strength and interfacial fracture toughness at the ages of 28 and 90 days. Fly ash replacements at all the levels studied result in higher interfacial fracture energy at the age of 90 days due to the pozzolanic action of fly ash. Researchers also showed the interest in the effects of chemical admixtures on the contribution of ITZ (Xu et al. 2000).

### Processing methods

Buch and Early (1999) stated that the use of crushed aggregates, sand blasted aggregates and aggregates coated with calcium hydroxide can enhance the bond strength. There is a marginal improvement in the indirect tensile strength of sand blasted limestone concrete mixtures. The softer limestone is subjected to “roughening” under the sand blasting process and thereby improving the mortar-aggregate bond.

Sand Enveloped with Cement Concrete (SEC) was developed by Hayakawa and Itoh (1982). The procedure was basically the same as for mixing of conventional concrete, except that the water was divided into two portions and added into the mixer at two separate times. The amount of the first water addition was controlled to be 25% by weight of the cement to be used, including any surface moisture of the sand and gravel. The effectiveness of this two-stage mixing method in reducing the bleeding capacity and improving the interfacial bond was also evaluated by Tamimi (1994).

### **Methods of Improving Interfacial Bond**

According to the factors influencing aggregate-mortar interfacial bond described previously, ways to improve the interfacial bond are summarized below:

1) removing of excess water,

One can expect to get improved properties of the interface, simply by reducing the w/cm ratio, which is also confirmed by experimental results by Mitsui et al. (1993). When



w/cm ratio is reduced from 0.65 to 0.35, the push-out load (a measure of bond strength) was increased from 1200 N to 1600 N, and the porosity at a distance of 50  $\mu\text{m}$  was reduced from 24% to 18%. A further reduction in water content near the interface can be effected by using aggregates having slightly porous surfaces. The excess water is drawn into these pores and cement particles are also pulled towards surface, which is known as the filter effect (Bentz et al. 1987). Another suggestion is to reduce the surface tension of water through the use of a water reducing agent or surfactant, which will reduce the thickness of the water film on the aggregate.

Scholer (1967) suggested that the stress level for initiation of micro-level cracks in concrete is primarily a function of the mortar strength. Hence, one way to improve interfacial bond strength would be to improve the strength of the cement mortar (Buch and Early 1999). However, this needs to be compatible with the other functional needs of the resulting concrete mixture design. For example, if a higher cement content is used to increase mortar strength in concrete, the shrinkage strains in concrete may also increase, thereby reducing any benefit that may have been gained from increased mortar strength.

In addition, besides w/cm ratio, Ping and Beaudoin (1992) indicated that the thickness of the water layer on the aggregate surface at the beginning of the mixing is also a principal factor affecting bond strength at the interface between nonporous aggregate and portland cement paste. Therefore, another possible way is to decrease the water layer at the interface. From this view, SEC concrete (Hayakawa and Itoh 1982, Tamimi 1994) was developed as a concrete made by adding water at two separate times. Compared with the conventional concrete, the two stage concrete exhibits lower bleeding and increased values of both minimum and maximum micro-hardness of the cement paste-aggregate interface. This is attributed to lower w/cm ratio at the interface due to the "SEC" method, the resulting tighter packing of hydration products with more intergrowth and interlocking, subsequently, the densification of the interfacial zone.

2) improving the packing of small particles near aggregate face,

Average size of cement grain can be taken as say 30 to 40  $\mu\text{m}$ , if we add very small particles, say to 5  $\mu\text{m}$  diameter, the small particles will fill up the interstices and densify the interface and also improve the bond. Research conducted by Mitsui et al (1993) showed that normal concrete with  $w/cm = 0.35$  had a push-out load of 1600 N and a porosity of 18%. Addition of 10% micro silica ( $w/cm = 0.35$ ) dramatically improved the porosity characteristics to 3% and the push out load to 2600 N. Rao et al. (2002) also presented similar results that the bond strength of concrete increases due to the pozzolanic reaction of silica fume, which improves the physical interaction at the interface.

3) coating the aggregate faces with a reactive layer.

Zimbelmann (1987) suggested that the bond strength of the transition zone might be improved by inducing a chemical or physical reaction between the aggregate and the hydrated cement paste. By precoating the aggregate particles with a cement/silica fume slurry, the push-out load was increased from 2600 N to 4200 N and the porosity at the interface transition zone was practically eliminated (Mitsui et al. 1994). Guinea et al. (2002) investigated the effect of the bond between the matrix and the aggregates on the cracking mechanism and fracture parameters of concrete, where he applied surface treatments such as bitumen and paraffin coatings to weaken the bond, and an epoxy resin to increase it.

## **CHAPTER III**

### **LABORATORY INVESTIGATION**

#### **GENERAL**

As described in Chapter II, extensive research has been done to improve the interfacial bonding between aggregate and mortar. However, most of research has focused on later age of concrete (28 days or over). Since in our study, the interfacial bonding at early age is more critical than that at later ages, various possible corrective measures to improve the early age interfacial bonding were investigated in the laboratory, and the results were presented in this chapter. A fractional factorial design (Taguchi Method) based on an “orthogonal array”, which allows the user to analyze many factors with a few combinations (Mason et al. 1989), was used to evaluate the effects of various key factors on the bonding strength. The experimental design and associated laboratory testing are described. The analysis results of the Taguchi design by statistical software such as MINITAB are presented. The optimum combination is subsequently chosen and validated in the further laboratory tests.

#### **FRACTURE TOUGHNESS TO REPRESENT AGGREGATE-MORTAR INTERFACIAL BOND**

As described in Chapter II, fracture parameters have been used to represent aggregate-mortar interfacial bond. Investigation of the fracture toughness of concrete has been on the rise for decades, due to the recognition that structural behavior is controlled not only by compressive strength of concrete, but also by the independent material parameter related to fracture toughness. Previous research has indicated that  $K_{IC}$  at early ages of concrete can be used as criteria to evaluate concrete quality, and it can describe the sensitivity of coarse aggregate characteristics relative to the aggregate-mortar bond

(Zollinger et al. 1993). Therefore, in this study,  $K_{IC}$  was used to represent the interfacial bond between aggregate and mortar of a variety of coarse aggregates types and concrete mixtures, and was the target of the Taguchi Design in this study.

The size effect law (SEL) and its generalized theory summarizes the observed size effect on the nominal strength of concrete structures. It presents a fracture model of concrete in which  $K_{IC}$  and another associated fracture parameter, process zone length ( $c_f$ ), are objectives. It can be synthesized as (Tang et al. 1999):

$$\sigma_N = c_n \frac{K_{IC}}{\sqrt{g'(\alpha_0)c_f + g(\alpha_0)d}} \quad (3.1)$$

where,

$\sigma_N$  = nominal strength of specimen (or structure),

$c_n$  = arbitrarily defined constant, usually taken so as to make  $\sigma_N$  the maximum tensile stress in the specimen of the same type with no crack,

$d$  = specimen size,

$g(\alpha) = \pi c_n^2 \alpha F^2(\alpha)$ ,

$\alpha$  = geometry factor,

$F(\alpha)$  = geometry function, obtained with finite element analysis,

$g'(\alpha)$  = derivative of  $g(\alpha)$ , and

$\alpha_0$  = ratio of the initial crack length ( $2a_0$ ) to the specimen dimension  $d$ .

For specimens of a given geometry, Equation 3.1 can be converted to a linear regression:

$$Y = AX + C \quad (3.2)$$

where,

$$Y = \frac{c^2}{g'(\alpha_0)\sigma_N^2}$$

$$X = \frac{g(\alpha_0)}{g'(\alpha_0)} d$$

$$A = \frac{1}{K_{IC}^2}, \text{ and}$$

$$C = \frac{c_f}{K_{IC}^2}$$

It is obvious that after linear regression,  $K_{IC}$  can be calculated from the regression coefficients and values of  $g(\alpha_0)$  and  $g'(\alpha_0)$ .

The variable-notch, one-size, split-tensile test method (Tang et al. 1996) developed at TTI was based upon the above equations. This method allows for the use of specimens of the same size and shape but with different notch lengths, which provides for a great amount of convenience in specimen preparation. The various configurations illustrated in Figure 3.1 were utilized in order to enhance the accuracy of the test method relative to specimen geometry effects. For these split tensile specimens:

$$\sigma_N = \frac{P}{\pi b R} \quad (3.3)$$

where,

$b$  = length of the cylinder,

$R$  = radius of the cylinder =  $d/2$ , and

$P$  = the total compressive load.

Equation 3.3 also implies that  $c_n = 1/\pi$  in Equation 3.1. For the three different geometric shapes of the specimens in Figure 3.1, different  $F(\alpha)$  and associated  $g(\alpha)$  and  $g'(\alpha)$  were obtained based on finite element analysis (Tang et al. 1996). For the regular split cylinder (1 and 2 in Figure 3.1),

$$F(\alpha) = 0.964 - 0.026\alpha + 1.472\alpha^2 - 0.256\alpha^3 \quad (3.4)$$

and for the holed cylinder (3 in Figure 3.1),

$$F(\alpha) = 2.849 - 10.451\alpha + 22.938\alpha^2 - 14.940\alpha^3 \quad (3.5)$$

The cylindrical specimens are 6-in in diameter (i.e.,  $d$  in Equation 3.1), and 12-in in length (i.e.,  $b$  in Equation 3.3). The first specimen is notchless ( $2a_0 = 0$ ); the second specimen contains a small notch of  $2a_0 = 1$  in.; and the third specimen contains a 1-in diameter hole with a 1.5-in notch extending on each side of the hole, in such a way that  $2a_0$  is 4-in.

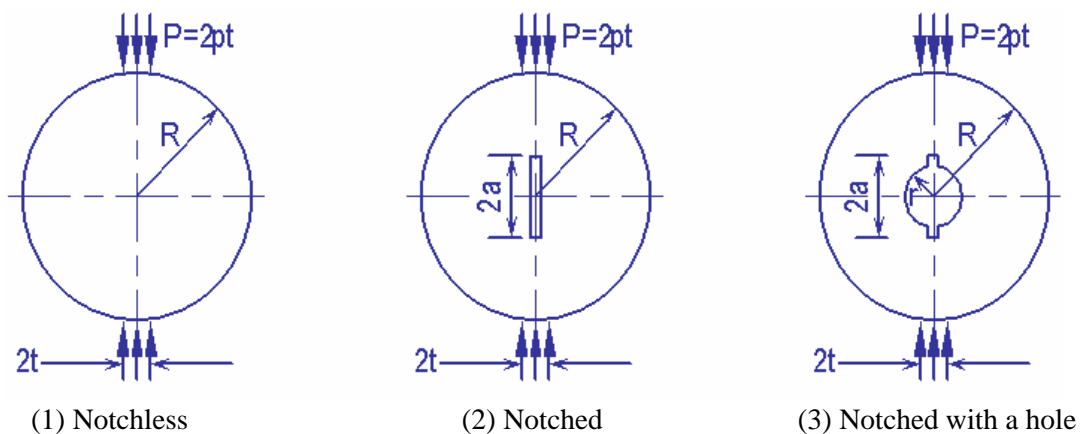


**Figure 3.1 Specimen geometries**

A spreadsheet was programmed to facilitate the above procedures. The only input necessary for the calculations is the maximum applied load for each of the three different specimens. By filling the measured maximum loads of specimens in the spreadsheet,  $K_{IC}$  is computed instantly.

## **MEASURES TO IMPROVE EARLY AGE AGGREGATE-MORTAR INTERFACIAL BOND**

Literature review in Chapter II indicated that aggregate-mortar interfacial bond can be improved by optimizing both materials and construction factors. In this section, based on the summary of measures of improving aggregate-mortar interfacial bond, and previous field practice, laboratory investigation of possible measures of improving aggregate-mortar interfacial bond were described to gain a better understanding of materials effects on bonding performance of concrete. Those improvements mainly aim to manipulate the ITZ through lowering w/cm ratio, modifying mixing cycles, using ultra-fine fly ash, and using dense-graded aggregates (or aggregate blending). The field practice about improvement on construction factors will be described in a later chapter.

### **Aggregate Types**

Previous experience suggests that coarse aggregate type has a significant influence on concrete performance (Senadheera and Zollinger 1996; Shelby and McCullough 1960). Two different aggregates were chosen to check the possibility of improvement of bonding performance by selecting specific aggregate type. One is natural gravel from Riverside campus, College Station, TX, and the other is limestone from Caldwell, TX. Table 3.1 and Figure 3.2 present physical properties and gradation of two aggregates, respectively. It can be seen that these two aggregates have same maximum aggregate size and specific gravity, and similar dry-rodded unit weight. However, limestone has higher absorption capacity than natural gravel. For the comparison study, normal indoors curing at room temperature was applied. Mix proportioning parameters included 6 sacks/cubic yard of cement factor, 0.75 of coarse aggregate factor, and 0.43 of water/cement ratio.

**Table 3.1 Physical properties of different aggregates**

Aggregate type	Gsb-od	%AC	DRUW (lb/ft <sup>3</sup> )
Natural gravel	2.58	0.70%	101.4
Limestone	2.58	1.87%	97.5

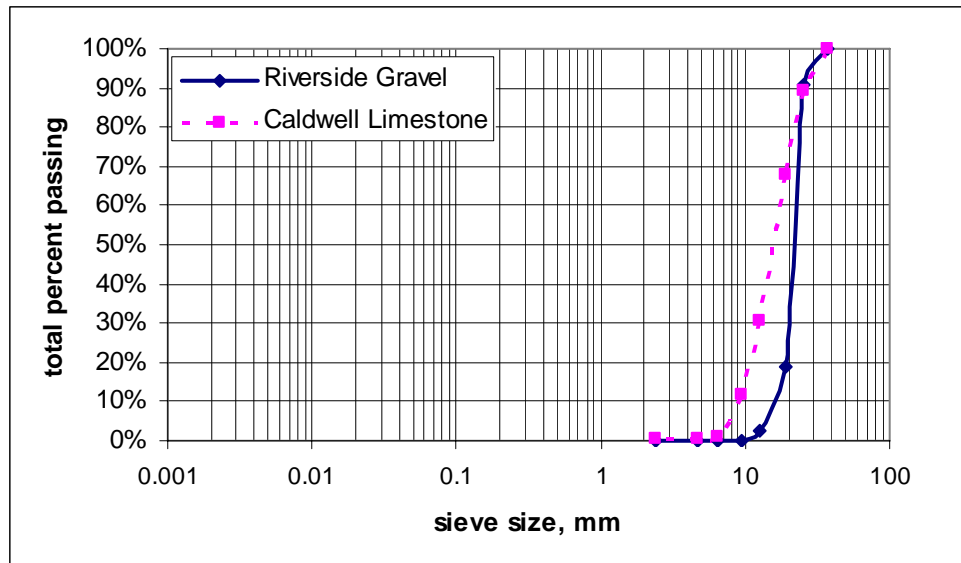
**Figure 3.2 Gradation curves for two aggregate types**

Figure 3.3 shows the fracture toughness results of concretes with different aggregates. For the two ages investigated, concrete with gravel aggregate showed lower fracture toughness values than that with limestone aggregate, which is in accordance with data that obtained through previous research work (Gutierriz de Velasco and McCullough 1981). It indicated that selecting the right aggregate type can benefit bonding performance of concrete. In the next chapter, a comprehensive investigation of aggregate properties will explain why different aggregate types can have different contribution to the concrete bonding capability.





**Figure 3.3 Fracture toughness of concretes at different ages**

### **Crushing Treatment of Aggregates**

To identify the effect of aggregate crushing in the bond strength of concrete, bond of concrete with crushed and natural siliceous river gravel were compared. Two gravels from Victoria, TX, were used; physical properties and gradation for each aggregate are shown in Table 3.2 and Figure 3.4, respectively. It is observed that the crushed gravel and the natural gravel have very similar size distribution. However, the latter has much higher absorption capacity than the former, whereas other properties are more or less similar. Mix proportioning parameters were same as previous section, which also included 6 sacks/cubic yard of cement factor, 0.75 of coarse aggregate factor, and 0.43 of w/cm.

According to the testing approach, lower fracture toughness values reflect lower bond strength. Based on the data up to 3 days for these two test runs (shown in Figures 3.5 and 3.6), concrete with natural gravel showed higher compressive strength and fracture toughness than that with crushed gravel, which means that crushing aggregates does not help to improve concrete bonding performance. Figures 3.7, 3.8, and 3.9 provide pictures of different aggregate particles, which show the difference in shape properties for different mineral components in aggregates. The crushed gravel particles

in Figure 3.7 shows smooth crushed faces but with high angularity. Those particles are mostly amorphous or crypto-crystalline silica particles, which predominate in the gravel. On the contrary, natural gravel particles in Figure 3.8 show surfaces with high roundness (low angularity) but with higher surface roughness than crushed gravel. This is correlated with lower early age fracture toughness in crushed gravel concrete than that of natural gravel. Further investigation and findings of the contribution of aggregate properties to bond strength of concrete will be described in Chapter IV.

**Table 3.2 Physical properties of two gravel aggregates**

Aggregate type	Gsb-od	%AC	DRUM (lb/ft <sup>3</sup> )	%Solid
Natural gravel	2.56	1.42	103.3	64.63
Crushed gravel	2.58	0.72	97	60.22

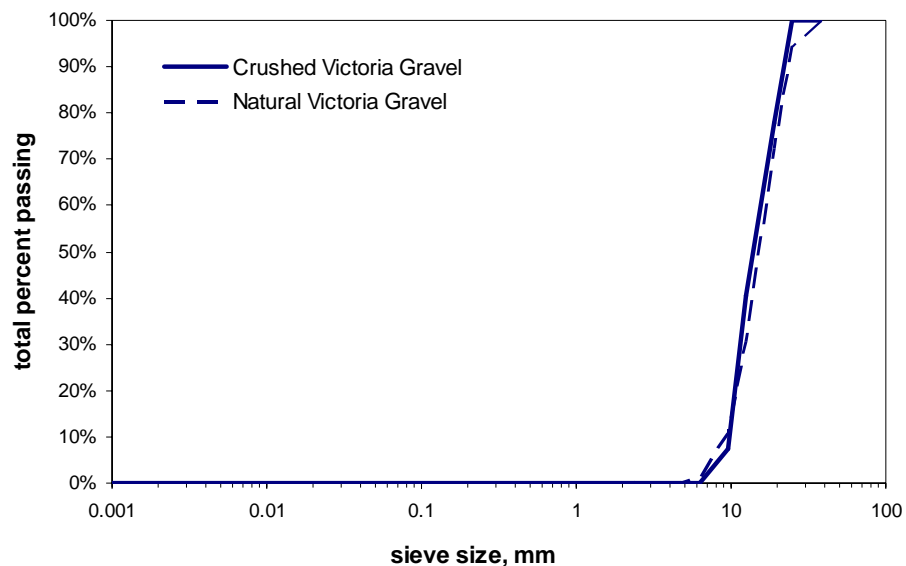


**Figure 3.4 Gradation curves for coarse aggregates**

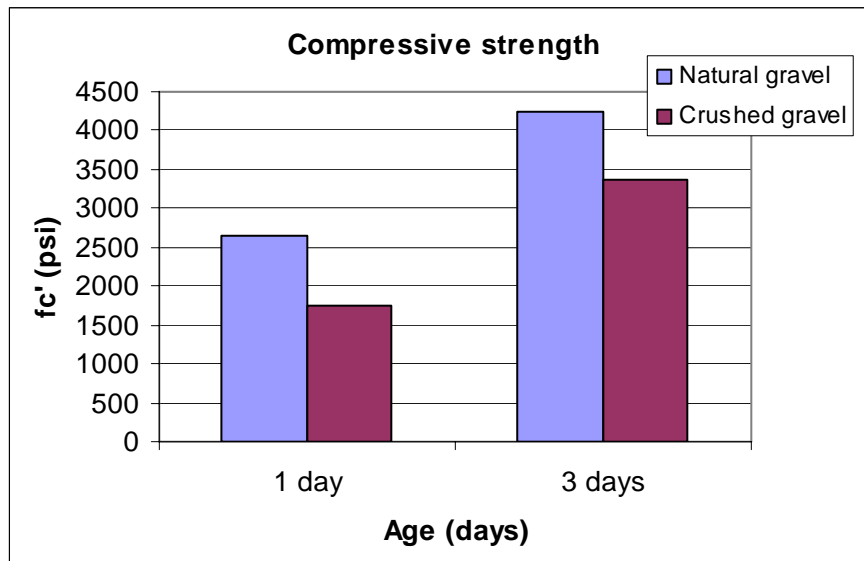


Figure 3.5 Compressive strength of concretes at different ages

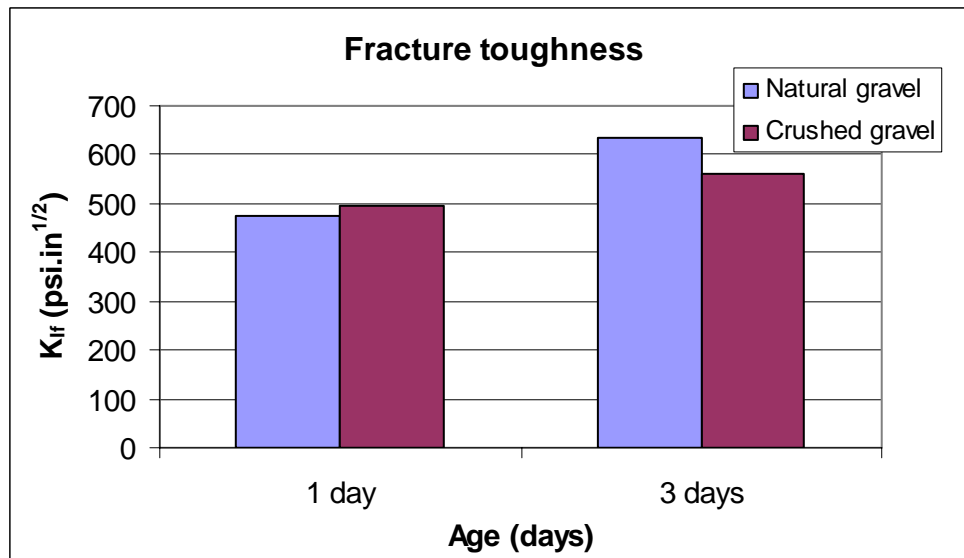


Figure 3.6 Fracture toughness of concretes at different ages



**Figure 3.7 Crushed gravel particles**



**Figure 3.8 Natural gravel particles**

### Dense Gradation of Aggregates

The bond strength comparison of concrete with dense graded and normal graded aggregates was also conducted in the laboratory. All aggregate sources were from Victoria, TX, and 25% of fly ash replacement (10% ultra-fine fly ash and 15% of Class F fly ash) by total cementitious materials were applied. The w/cm of concrete mixtures was 0.4, and specimens were cured in the moisture room before tested. Mix proportion parameters are summarized in Table 3.3, where the workability factor represents the fraction of total aggregate passing the 2.36-mm sieve and coarseness factor represents ratio between the weight fraction of particles retained on the 9.5-mm sieve to the weight of all particles retained on the 2.36-mm sieve (Shilstone 1990).

Figure 3.9 compares the fracture toughness values for concrete with and without dense graded aggregates. It is obvious that dense graded aggregates greatly improved the interfacial bonding performance of concrete at all early ages. It is because after dense gradation the aggregate in the concrete mixture becomes more compacted and denser, which greatly reduces the voids, subsequently the potential defects in the interface zone of concrete.

**Table 3.3 Mix proportion parameters for mixes with and without dense gradation**

Tests	Cement factor	Coarse agg. factor	Intermediate agg. factor	Workability factor	Coarseness factor
Normal	6	0.75	-	34.4	58.9
Dense	6	0.495	0.18	36	55.2

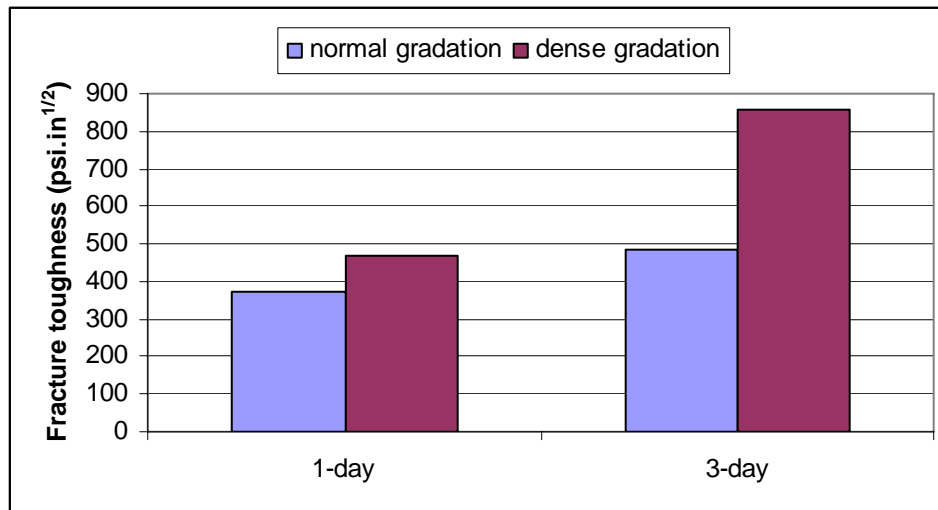


**Figure 3.9 Fracture toughness comparison between concrete with and without dense graded aggregates**

### **Charging Sequencing**

Using the same mix proportion of concrete mixture but using dense graded aggregates described above, two charging sequencings were compared to check the possible improvement of bonding performance. One is conventional charging sequencing based on ASTM C 192/C (ASTM 2000), and the other is named a modified charging sequencing, which includes the following steps:

- 1) Adding sand, total cementitious materials (cement and fly ash), and half of total water in the mixer, and mixing for 50 seconds,
- 2) Charging coarse and intermediate aggregates to the mixer, and mixing for another 30 seconds,
- 3) Adding rest of half water to the mixer, and mixing for another 50 seconds.

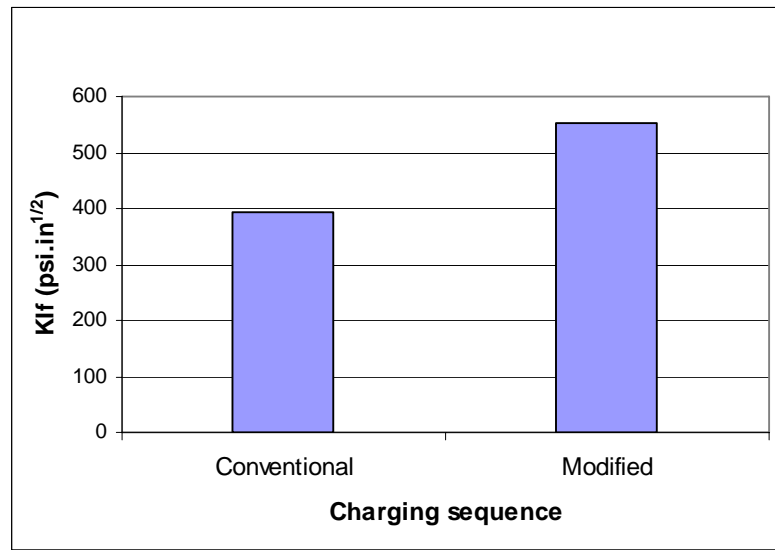


**Figure 3.10 Effect of charging sequencing on 3-day concrete fracture toughness**

3-day fracture toughness results for mixes with different charging sequencings were compared in Figure 3.10. Modified charging sequencing provided higher concrete fracture toughness. As described in Chapter II, an effective way to improve the interfacial bond is to decrease the water layer at the interface. From this view, compared with the concrete using the conventional charging sequence, the modified charging sequencing attributed to lower w/cm ratio at the interface due to the two-stage of adding water, the resulting tighter packing of hydration products with more intergrowth and interlocking, subsequently, the densification of the interfacial zone. In addition, during the casting process, fresh concrete with modified charging sequence showed better workability, placement and finishability. Figures 3.11 and 3.12 illustrate petrographic observation of ITZ for these two different concrete samples using a transmitted light optical microscope. It can be seen that coarse  $\text{Ca}(\text{OH})_2$  was well developed at the ITZ of concrete with conventional charging sequencing, while at the ITZ of concrete with

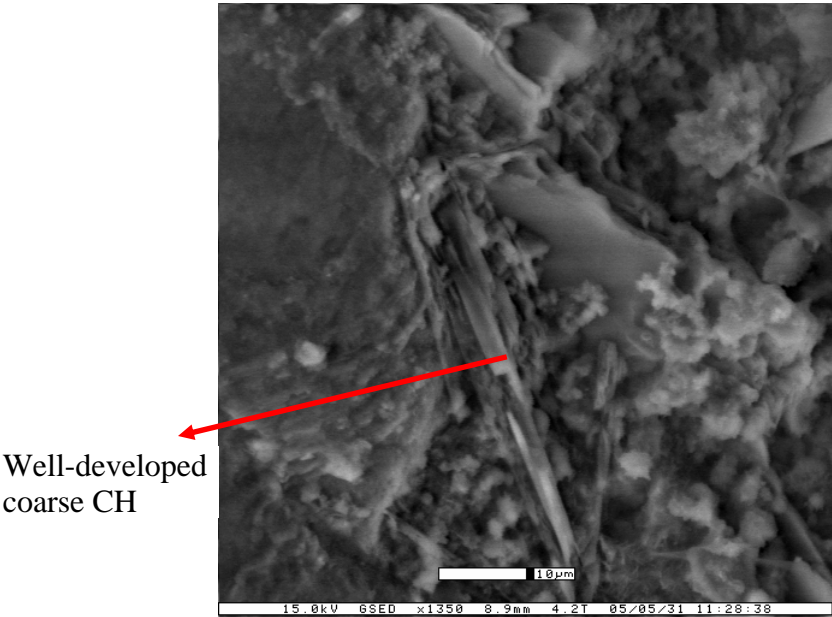


Figure 3.11 ITZ of concrete with conventional charging sequencing

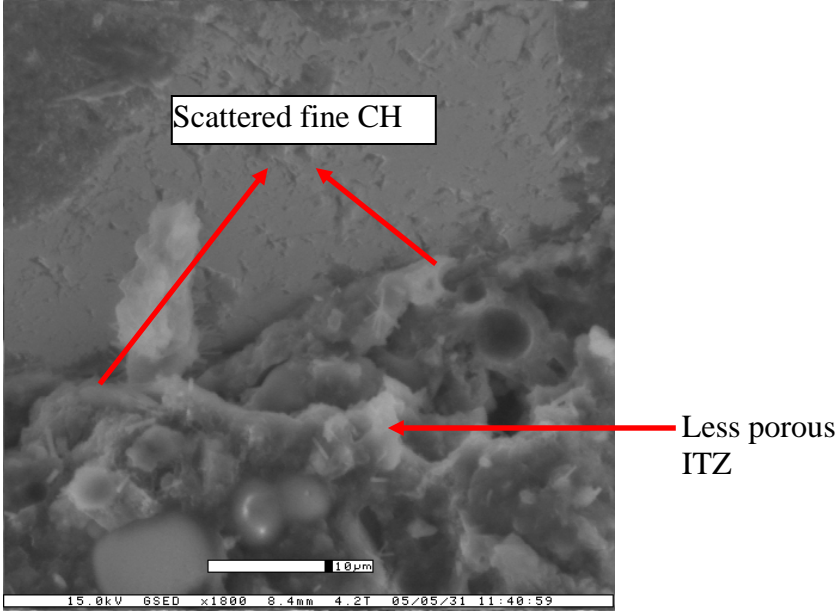


Figure 3.12 ITZ of concrete with modified charging sequencing



modified charging sequencing, only scattered fine CH occurred. Moreover, its ITZ was less porous, which indicated that modifying charging sequencing improved the ITZ structure, and then bonding performance of concrete. The results were also consistent with other researchers' work (Hayakawa, and Itoh 1982, Tamimi 1994).

## **TAGUCHI METHOD**

Dr. Genichi Taguchi is regarded as the foremost proponent of robust parameter design, which is an engineering method for product or process design that focuses on minimizing variation and/or sensitivity to noise. Taguchi's robust design methods are set apart from traditional quality control procedures and industrial experimentation in various respects. Of particular importance are: the concept of *quality loss functions*, the use of *signal-to-noise* (S/N) ratios, and the use of *orthogonal arrays*. Based on "Orthogonal Array", experiments can be designed to reduce "variance" for the experiment with "optimum settings" of control parameters. Thus, the integration of Design of Experiments with optimization of control parameters to obtain the BEST results is achieved in the Taguchi Method. Orthogonal arrays provide a set of well balanced (minimum) experiments and Dr. Taguchi's S/N ratios, which are log functions of desired output, serve as objective functions for optimization, help in data analysis and prediction of optimum results. When used properly, Taguchi designs provide a powerful and efficient method for designing products that operate consistently and optimally over a variety of conditions.

In robust parameter design, the primary goal is to find factor settings that minimize response variation, while adjusting (or keeping) the process on target. After factors affecting variation are determined, settings for controllable factors that will either reduce the variation, make the product insensitive to changes in uncontrollable (noise) factors, or both should be found. Engineering knowledge should guide the selection of factors and responses. Control factors and responses should also be scaled so that interactions are unlikely. When interactions among control factors are likely or not well

understood, a design that is capable of estimating those interactions should be chosen. Robust parameter design uses Taguchi designs (orthogonal arrays), which allows the user to analyze many factors with few runs. Taguchi designs are balanced, that is, no factor is weighted more or less in an experiment, thus allowing factors to be analyzed independently of each other.

Taguchi Method treats optimization problems in two categories: static problems and dynamic problems. Generally, a process to be optimized has several control factors which directly decide the target or desired value of the output. The optimization then involves determining the best control factor levels so that the output is at the target value. Such a problem is called as a "STATIC PROBLEM". There are 3 S/N ratios of common interest for optimization of Static Problems:

1) Smaller-the-better:

$$n = -10\text{Log}_{10}[\textit{mean of sum of squares of measured data}]$$

This is usually the chosen S/N ratio for all undesirable characteristics like “defects “etc. for which the ideal value is zero. Also, when an ideal value is finite and its maximum or minimum value is defined, then the difference between measured data and ideal value is expected to be as small as possible.

2) Larger-the-better:

$$n = -10\text{Log}_{10}[\textit{mean of sum of squares of reciprocal measured data}]$$

This case has been converted to SMALLER-THE-BETTER by taking the reciprocals of measured data and then taking the S/N ratio as in the smaller-the-better case.

3) Nominal-the-best:

$$n = 10\text{Log}_{10} \frac{\textit{square of mean}}{\textit{variance}}$$

This case arises when a specified value is MOST desired, meaning that neither a smaller nor a larger value is desirable.

## Creating Taguchi Design

Before a Taguchi design is chosen, all pre-experimental planning needs to be completed, including identifying the number of control factors that are of interest and the number of levels for each factor, and determining the number of runs you can perform and the impact of other considerations on your choice of design.

A Taguchi design, also known as an orthogonal array, is a fractional factorial matrix that ensures a balanced comparison of levels of any factor. In a Taguchi design analysis, each factor can be evaluated independently of all other factors. Each column in the orthogonal array represents a specific factor with two or more levels. Each row represents a run.

Table 3.4 displays the L8 ( $2^{7}$ ) Taguchi design (orthogonal array). L8 means 8 runs.  $2^{7}$  means 7 factors with 2 levels each. If the full factorial design were used, it would have  $2^{7} = 128$  runs. The L8 ( $2^{7}$ ) array requires only 8 runs — a fraction of the full factorial design. This array is orthogonal; factor levels are weighted equally across the entire design. The table columns represent the control factors, the table rows represent the runs (combination of factor levels), and each table cell represents the factor level for that run.

**Table 3.4 An example of L8 ( $2^{7}$ ) Taguchi design**

	<u>A</u>	<u>B</u>	<u>C</u>	<u>D</u>	<u>E</u>	<u>F</u>	<u>G</u>
1	1	1	1	1	1	1	1
2	1	1	1	2	2	2	2
3	1	2	2	1	1	2	2
4	1	2	2	2	2	1	1
5	2	1	2	1	2	1	2
6	2	1	2	2	1	2	1
7	2	2	1	1	2	2	1
8	2	2	1	2	1	1	2

In the above example, levels 1 and 2 occur 4 times in each factor in the array. If comparing the levels in factor A with the levels in factor B, it can be seen that B1 and B2 each occur 2 times in conjunction with A1 and 2 times in conjunction with A2. Each pair of factors is balanced in this manner, allowing factors to be evaluated independently.

**Table 3.5 The single-level Taguchi designs available**

Designs	Number of levels			
	2	3	4	5
L4 ( $2^3$ )	2-3			
L8 ( $2^7$ )	2-7			
L9 ( $3^4$ )		2-4		
L12 ( $2^{11}$ )	2-11			
L16 ( $2^{15}$ )	2-15			
L16 ( $4^5$ )			2-5	
L25 ( $5^6$ )				2-6
L27 ( $3^{13}$ )		2-13		
L32 ( $2^{31}$ )	2-31			

Table 3.5 summarizes the single-level Taguchi designs available. The number following the “L” indicates the number of runs in the design. For example, the L4 ( $2^3$ ) design has four runs. The numbers in the table indicate the minimum and maximum number of available factors for each design. For example, an L8 ( $2^7$ ) design can have from two to seven factors with two levels each; an L16 ( $4^5$ ) design can have from two to five factors with four levels each.

## **Application of Taguchi Method in Aggregate Study**

As mentioned in Chapter II, the bond of the aggregate-mortar interface at an early age is one of the most significant factors affecting the development of delamination, which itself is affected by both aggregate and non-aggregate factors. The aggregate factors believed to be pertinent to the aggregate-mortar interfacial bond include physical, chemical, and geometric properties varying significantly with aggregate type (e.g., Senadheera and Zollinger 1996; Alexander 1993; Rao and Prasad 2002; Monteiro and Mehta 1986; Tasong et al. 1998). The non-aggregate factors include w/cm, mineral admixtures, and curing methods, etc (e.g., Goldman and Bentur 1992; Bentur and Cohen 1987; Charles-Gibergues et al. 1982; Wu et al. 1999; Wainwright and Cabrera 1990; Zollinger et al. 1994). Therefore, a better understanding of those factors to the bonding performance of concrete is of great importance to successful paving construction practice for using aggregates to prevent delamination and spalling distresses.

Widely used as screening designs, fractional factorial experiments such as the Taguchi method allows the user to analyze many factors with a few runs (Mason et al. 1989). In addition, orthogonal arrays used in the Taguchi designs are balanced, that is, all factors are weighted equally in the experiment, thus allowing factors to be analyzed independently of each other (Mathews 2004). Therefore, it is desirable to apply the Taguchi method in this study when our purpose is to identify how important the effect of each key design factors plays on the aggregate-mortar interfacial bond, and which level can provide best performance.

## **EXPERIMENTAL DESIGN ANALYSIS**

The procedures of this experimental design in the study include the following steps:

- Determining the design or control factors for which we will try different levels,
- Selecting an appropriate orthogonal array for the experiment,

- Deciding how to measure the quality characteristic of interest,
- Conducting the experiment and identify the factors that most strongly affect the chosen target, and
- Predicting and verifying the optimum design combination.

Previous studies and experience indicated that aggregate type, w/cm, ultra-fine fly ash, and curing method have predominant effects on aggregate-mortar bond (Senadheera and Zollinger 1996; Alexander 1993; Rao and Prasad 2002; Monteiro and Mehta 1986; Tasong et al. 1998; Goldman and Bentur 1992; Bentur and Cohen 1987; Charles-Gibergues et al. 1982; Wu et al. 1999; Wainwright and Cabrera 1990; Zollinger et al. 1994). Therefore, aggregate type, w/cm, ultra-fine fly ash content, and curing method were chosen as the control factors in this study. For each factor, three different levels were utilized. Two gravels and one limestone (as a reference) aggregates were selected for the aggregate type factor, and VG, GG, and GL designated gravel from Victoria, Texas (TX); gravel from Garwood, TX; and limestone from Georgetown, TX, respectively. The ultra-fine (Micro<sup>3</sup>) fly ash was provided by Boral Industries Inc. Company, San Antonio, TX at three levels of 8%, 15%, and 20% replacement of cementitious materials, respectively. Typical Type I Portland cement was used, and the three levels for the w/cm ratio were 0.40, 0.42, and 0.45. The three levels for the curing methods included 1) wet mat curing (WMC) — sealing concrete specimens using plastic sheets after casting, 2) normal curing with curing compound (NCC) — spraying curing compound (1600-White series provided by W. R. Meadows, Inc.) on concrete after surface is dry, and 3) no curing (WOC) — keeping specimens in normal conditions without any treatment.

Assuming there is no interaction between each factor, an orthogonal array L<sub>9</sub> (3\*\*4) was selected for the experimental design, where the array L<sub>9</sub> requires only 9 runs out of 81 full factorial combinations of 4 factors with 3 levels each. This array is orthogonal in the fact that all factor levels are weighted equally across the entire design. Table 3.6 lists the 9 test runs according to the L<sub>9</sub> orthogonal array, and Table 3.7 lists associated mix proportions. For each test run, 6 cylindrical (6 by 12 in.) specimens (with

three different geometric shapes as shown in Figure 3.1) were cast for fracture toughness testing and 3 cylindrical (6 by 12 in) specimens for compressive strength testing.

**Table 3.6 9 test runs according to orthogonal array**

Tests	Aggregate type	Ultra-fine fly ash	w/cm	Curing
1	VG	8%	0.40	WMC
2	VG	15%	0.42	NCC
3	VG	20%	0.45	WOC
4	GG	8%	0.42	WOC
5	GG	15%	0.45	WMC
6	GG	20%	0.40	NCC
7	GL	8%	0.45	NCC
8	GL	15%	0.40	WOC
9	GL	20%	0.42	WMC

**Table 3.7 Associated mix proportions for 9 test runs**

Tests	Batch proportion weights (lbs/ft <sup>3</sup> )				
	Cement	CA*	Sand	Water	Fly ash
1	19.22	77.47	42.86	10.19	1.67
2	17.75	77.47	41.37	10.59	3.13
3	16.71	77.47	39.49	11.18	4.18
4	19.22	77.05	42.16	10.31	1.67
5	17.75	77.05	40.15	10.9	3.13
6	16.71	77.05	42.47	9.89	4.18
7	19.22	70.63	45.13	13.56	1.67
8	17.75	70.63	47.33	12.55	3.13
9	16.71	70.63	45.97	12.95	4.18

\* CA — coarse aggregates

For fracture toughness test, two types of steel inserts were inserted in the cylindrical molds when concrete was cast, and then pulled out by a slide hammer 3 or 4 hours after concrete was cast. The specimens were demolded 1 day after casting, and cured till the test date. During testing, two plywood strips was used for load bearing for

each test (ASTM C 496). The specimen was placed for the notch to be vertical to the platen of the testing machine, that is, in the direction of the compressive load. Maximum load for each specimen was then recorded after all of the specimens are broken. The measured maximum loads of specimens were filled in a programmed spreadsheet, and linear regression was performed to compute the  $K_{IC}$ .

Figures 3.13 and 3.14 illustrate compressive strength and fracture toughness results for the 9 test runs. Each test run showed different development with time. However, an increase in both compressive strength and  $K_{IC}$  with concrete age was observed. Figures 3.15, 3.16, and 3.17 illustrate examples of ITZ microstructure of concrete. It can be seen that for mixes of tests 3 and 5, there were  $\text{Ca}(\text{OH})_2$  along the aggregates. However, for mix of test 6, the amount of  $\text{Ca}(\text{OH})_2$  within the ITZ was reduced greatly, or practically there was no  $\text{Ca}(\text{OH})_2$  in the ITZ. Those observations matched the fracture toughness results very well, which indicated that the less  $\text{Ca}(\text{OH})_2$  within the ITZ and denser of ITZ structure, the stronger the interfacial bonding.

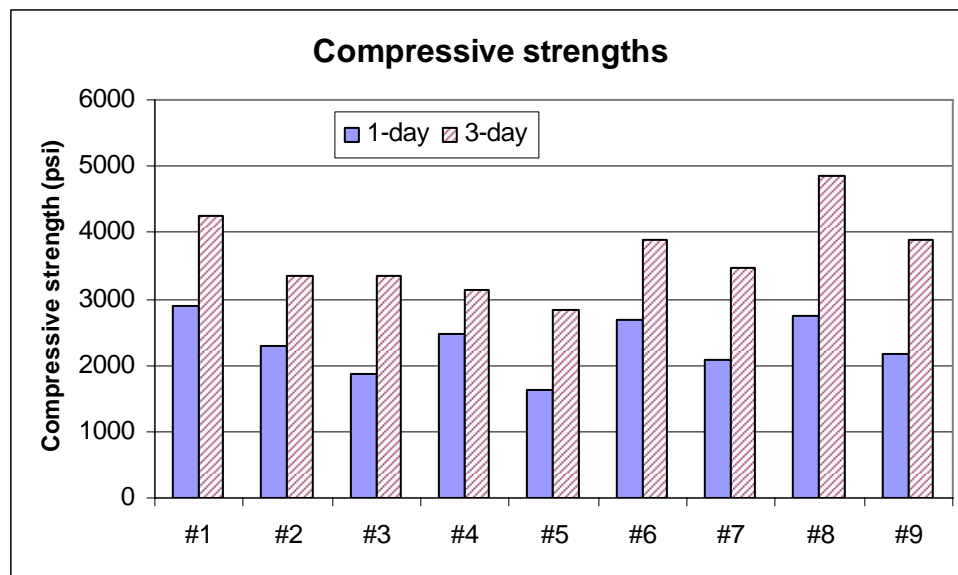


**Figure 3.13 Compressive strength results**



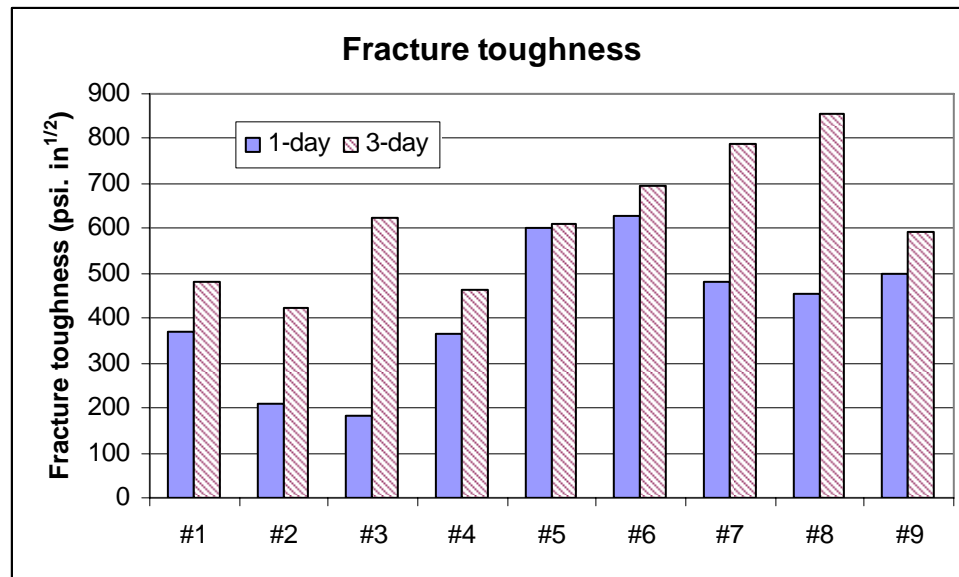


**Figure 3.14 Fracture toughness results**

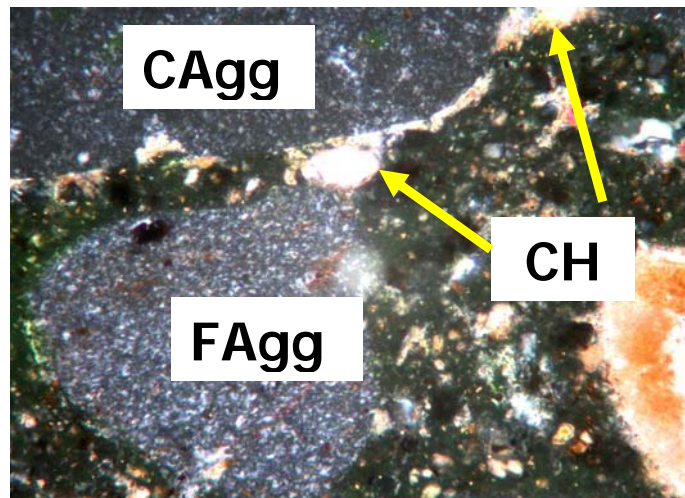


**Figure 3.15 1-day ITZ microstructure of test 3 mix**

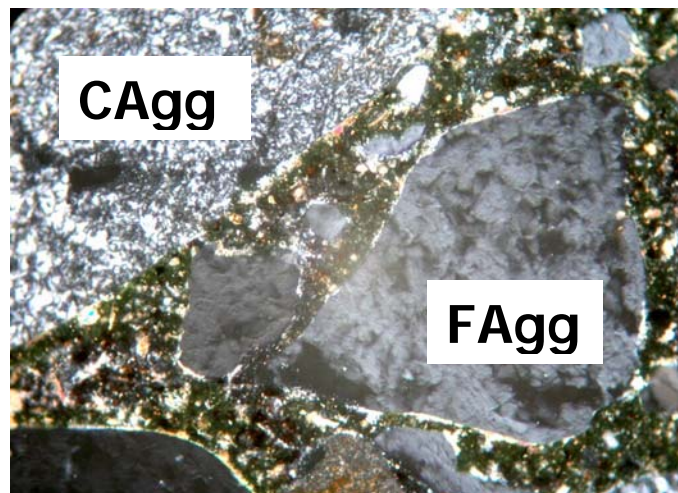


Figure 3.16 1-day ITZ microstructure of test 5 mix

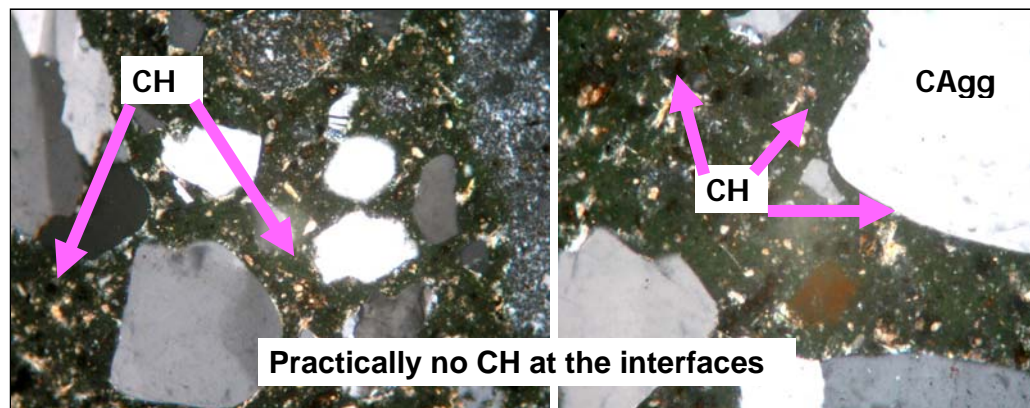


Figure 3.17 1-day ITZ microstructure of test 6 mix

Previous field experience has shown that a few days after paving is the most critical time for delaminations to form in concrete paving. On this basis, the 1-day  $K_{IC}$  value was selected as the output response in the experimental design. Both signal-to-noise ratios (S/N ratios, which provide a measure of robustness) and means (for static design) were used to evaluate the significances of factors. The option of *larger is better* was chosen for S/N ratio, because our goal is to maximize the value of  $K_{IC}$ .

The experimental design was analyzed by a statistical software named MINITAB (Mathews 2004) based on the  $K_{IC}$  values of all test runs. The MINITAB software is able to calculate response tables for both S/N ratios and means versus the control factors. These tables can then be used to determine whether the factors are significantly related to the  $K_{IC}$  performance and each factor's relative importance in the model. The response tables for means and S/N shown in Table 3.8 and 3.9 summarize the average of each response characteristic (i.e., means and S/N ratios) for each level of each factor from MINITAB software. The tables also include ranks of factors based on Delta statistics (Mathews 2004), which compares the relative magnitude of the effects of the respective factors. MINITAB assigns ranks based on Delta values; rank 1 to the highest Delta value, rank 2 to the second highest, and so on. The highest Delta value (or the rank) indicates the greatest impact of the factor on the target value of output. In terms of the Delta values, both response tables indicate the following decreasing rank order with respect to the relative importance of each factor to  $K_{IC}$ : aggregate type, curing method, w/cm, and ultra-fine fly ash content. Aggregate type was identified as the factor that most strongly affects the bond between aggregate and the mortar.

**Table 3.8 Response table of experimental design with respect to means**

Level	Aggregate type	Ultra-fine fly ash	w/cm	Curing method
1	253.238	406.637	483.753	489.749
2	530.763	420.425	357.871	439.160
3	478.422	435.361	420.799	333.515
Delta	277.525	28.724	125.882	156.234
Rank	1	4	3	2

**Table 3.9 Response table of experimental design with respect to S/N ratios**

Level	Aggregate type	Ultra-fine fly ash	w/cm	Curing method
1	47.629	52.112	53.487	53.634
2	54.257	51.687	50.538	51.995
3	53.590	51.677	51.451	49.848
Delta	6.628	0.4352	2.950	3.786
Rank	1	4	3	2

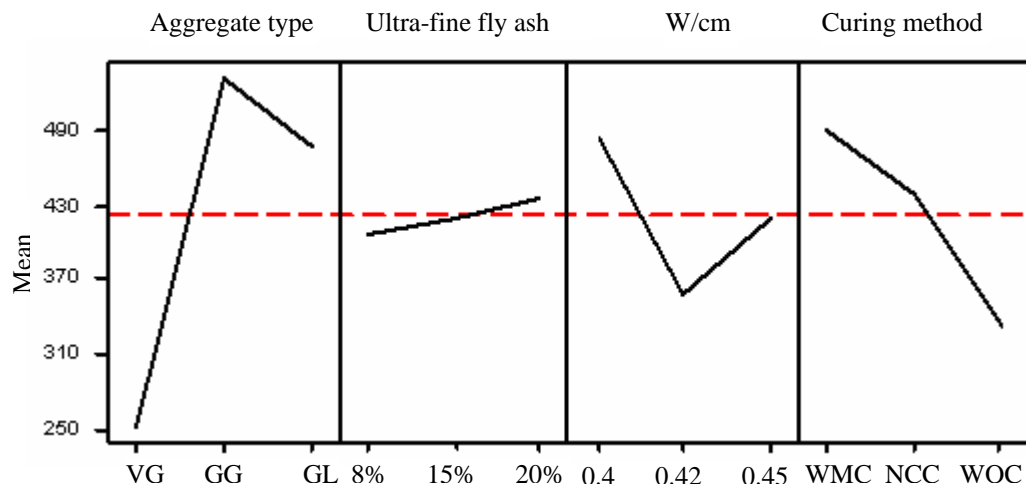


**Figure 3.18 Main effects plot of means**

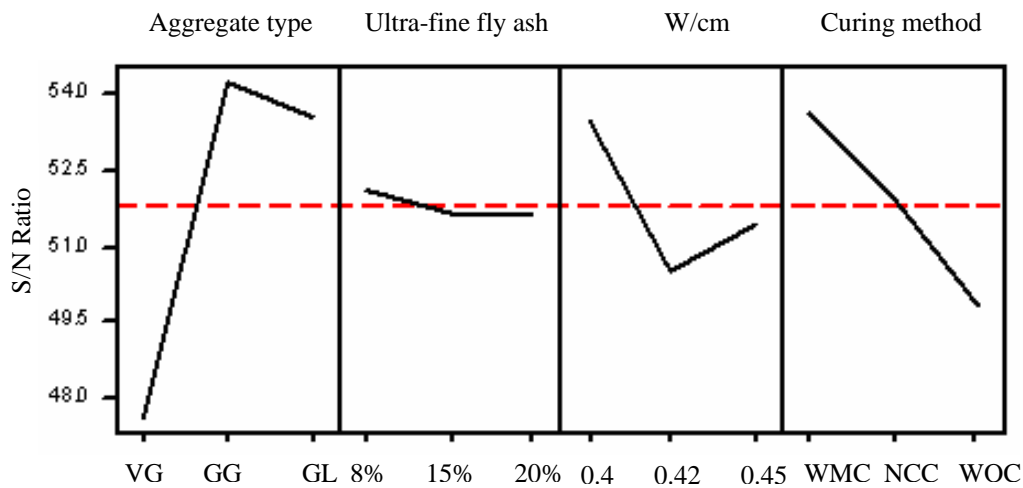


**Figure 3.19 Main effects plot of S/N ratios**

In addition, the level averages in the response tables can determine which level of each factor provides the best result. For each factor, higher level average indicates the better level of this factor in terms of the bonding performance. It can be also observed from the main effects plots (i.e., Figures 3.18 and 3.19), which display graphs of the averages in the response tables. A horizontal line is drawn at the grand mean of all

factors. The effect at each level can be identified from the difference between the means and the reference line. For example, for aggregate type factor, both main effects plots for means and S/N ratios indicate that level 2 provided the highest value, which means that GG provided the best performance. The result is different from findings of previous field practice, which normally showed the better performance of limestone.

For w/cm, the results show that level 1 (i.e., 0.4 of w/cm) was the best, and for curing method, level 1 (i.e., WMC) was the desired one. As for the ultra-fine fly ash factor, Figure 3.18 shows that level 3 (i.e., 20% of ultrafine fly ash) was the best, while Figure 3.19 shows level 1 (i.e., 8% of ultrafine fly ash). If looking at response tables for means and S/N ratios (Table 3.9 and 3.10), the factor of ultra-fine fly ash ranked the lowest, which means ultra-fine fly ash plays the least important role in the bonding performance of concrete at early age. In addition, three levels of ultra-fine fly ash have very close values of average for both means and S/N ratios, which also implied that this factor is not significantly related to the  $K_{IC}$ . Therefore, there will not be a significant difference on the bonding performance for varying content of ultra-fine fly ash. It may be because, at very early age of concrete, ultra-fine fly ash mainly plays a role as being a filler for densification of the packing of the particles instead of its pozzolanic reactivity.

Hence, considering all above reasons, the optimum design combination was chosen as: GG + 8% ultrafine fly ash + 0.4 of w/cm + WMC. The predicted results of S/N ratio and mean from the MINITAB software were 58.014, and 648.478, respectively, which were both higher than any value in the associated response tables (Table 3.8 and 3.9). Figure 3.20 illustrates the  $K_{IC}$  results of this optimum combination. The  $K_{IC}$  at 1-day reached up to  $722.34 \text{ psi}\cdot\text{in}^{1/2}$ , which was obviously higher than that of any test run. It can be seen from Figure 3.21 that there was no coarse  $\text{Ca}(\text{OH})_2$  but ultra-fine fly ash at the interfaces for the optimum mix, which indicated its dense ITZ structure and strong interfacial bonding. Therefore, the prediction of optimum design based on experimental design analysis was validated. Although different from findings of previous field practice, these results confirm that, with appropriate design, use of

gravel aggregate in concrete paving can still provide better and desirable bonding performance for concrete.

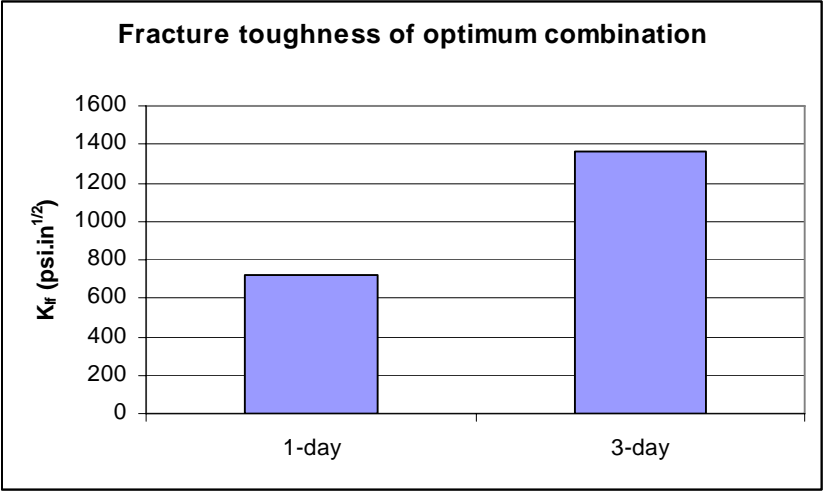


Figure 3.20 Fracture toughness of optimum combination

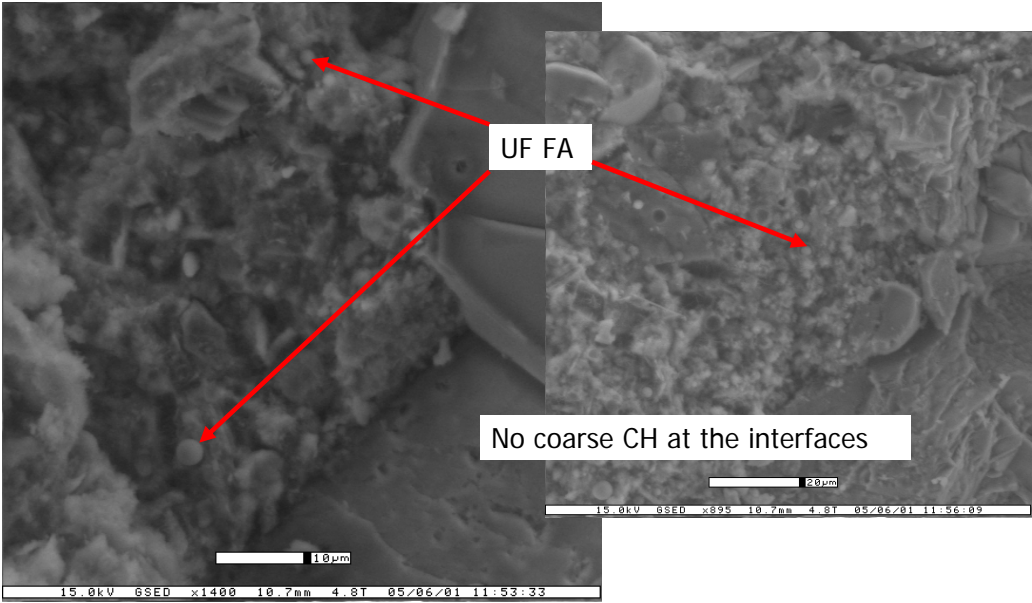


Figure 3.21 ITZ microstructure of optimum mix

## CHAPTER IV

### AGGREGATE PROPERTIES AND APPLICATION OF UTILITY THEORY

#### GENERAL

In Chapter III, among the four key construction design factors considered, aggregate type has the greatest effect on the bonding performance between aggregate and mortar. In addition, the GG's exhibition of best contribution on bonding performance among the three aggregates types considered in this study is different from previous research findings. Hence, in this chapter, a comprehensive investigation on aggregate characteristics including physical, geometric and chemical properties of aggregate types was conducted. A rating system using utility theory was developed to evaluate the overall contribution of aggregate properties to the bonding performance of concrete and the feasibility of design combinations.

#### AGGREGATE SURFACE FREE ENERGY MEASUREMENT

By definition, surface free energy of a solid is the energy needed to create or heal a unit surface area of material. The concept of surface energy can be explained from a molecular, mathematical and thermodynamics point (Cheng 2002). The surface free energy of aggregate is primarily composed of a nonpolar component — the Lifshitz van der Waals component; and an acid-base component — the Acid-Base component (Fowkes 1962; Good 1992). Equation 4.1 is used to describe the total surface free energy and its components:

$$\Gamma = \Gamma^{LW} + \Gamma^{AB} \quad (4.1)$$

where,

$\Gamma$  = surface free energy of aggregate,

$\Gamma^{LW}$  = Lifshitz–van der Waals component of the surface free energy, and

$\Gamma^{AB}$  = acid-base component of the surface free energy.

The Lifshitz-van der Waals force contains at least three components: London dispersion force, Debye induction force, and Keesom orientation force. The London dispersion force is the attraction between neighboring electronic shells. It is an induced dipole to induced dipole interaction. The Debye induction force is produced by a dipole inducing a dipole in a neighboring molecule. The Keesom orientation force is the interaction of two dipoles orienting themselves in relation to each other (Hefer 2004).

The acid-base interaction includes all interactions of electron donor (proton acceptor) - electron acceptor (proton donor) type bonds including hydrogen bonding. To quantitatively predict and treat the acid-base interaction, Good (1992) postulated a resolution of the acid-base term,  $\Gamma^{AB}$ , into a Lewis acidic surface parameter and a Lewis basic surface parameter. The relationship among the  $\Gamma^{AB}$  and its components is shown in Equation 4.2:

$$\Gamma^{AB} = 2\sqrt{\Gamma^+\Gamma^-} \quad (4.2)$$

where,

$\Gamma^+$  = Lewis acid component of surface interaction, and

$\Gamma^-$  = Lewis base component of surface interaction.

### **Surface Free Energy Measurement of Aggregate**

The measurement of the surface free energy of solids is not straightforward because it cannot be measured directly. There are several direct and indirect methods to measure surface energy of aggregate, including inverse gas chromatography (IGC) (Ahsan and Taylor 1999), atomic force microscopy (AFM) (Beach et al. 2002), microcalorimetry (Yildirim 2001), and universal sorption device (USD) (Cheng 2002).



Gas chromatography is a simple technique for the separation on the fact that each solute has a different interaction with the stationary phase, which results in different travel times for different solutes carried by an inert gas through a column with known characteristics. Therefore, the IGC at infinite dilution can be used to determine surface energy and its components by measuring the retention volumes of different probe gases through a column of small aggregate particles. These experiments are relatively fast and commercial devices are now available which makes the process fully automated. However, there is only one commercial instrument that supplies software for surface energy analysis.

The AFM is a direct method to measure the intrinsic surface forces that takes part in fundamental adhesion at an interface. It would be possible to obtain all the surface energy components by using cantilevers with chemically functionalized tips. The operation of this device requires some experience since carefully positioning of the tip near the surface is required. Practicality limitations associated with aggregate measurements result from the heterogeneity and topographical features on aggregate surfaces, not being compatible with the scale at which these instruments are designed to operate.

The microcalorimetry method is attractive in that the measurement of sorption heats is relatively simple, and could be used to obtain surface energies and its components. The conversion from enthalpy to free energies can be accomplished in two ways: 1) by measuring contact angles at different temperatures, or 2) by performing gas sorption experiments. However, a procedure which would require the measurement of contact angles of aggregates at different temperatures would be neither practical nor efficient.

The USD method is a vacuum gravimetric static sorption technique that identifies gas sorption characteristics of selected solvents to indirectly determine the surface energies of aggregate. Sorption methods are particularly suitable due to their ability to accommodate the peculiarity of sample size, irregular shape, mineralogy, and surface

texture associated with aggregates. Therefore, it was applied in this study for the surface energy measurements of aggregates.

The USD is comprised of a Rubotherm magnetic suspension balance system, a computer system (with Messpro software), a temperature control unit, a high quality vacuum unit, a vacuum regulator, pressure transducers, a solvent container, and a vacuum dissector. A schematic of the main components of the USD setup is illustrated in Figure 4.1.

The Rubotherm magnetic suspension balance has the ability to measure a sample mass of up to 200 g to an accuracy of  $10^{-5}$  g, which is sufficient for precise measurement of mass increase due to gas adsorbed onto aggregate surface. The whole USD system is fully automated with predetermined pressure set-points that automatically triggers when the captured balance readings reach equilibrium. Aggregate samples with the size between the No.4 and No.8 sieve size were thoroughly cleaned with distilled water and oven-dried for measurement.

During the USD test process, once the chamber is vacuumed, a solvent vapor is injected into the aggregate system. A highly sensitive magnetic suspension balance is used to measure the amount of solvent adsorbed on the surface of the aggregate. The vapor pressure at the aggregate surface is measured at the same time. The surface energy of the aggregate is calculated after measuring the adsorption of three different solvents (i.e. distilled water, *n*-Hexane, and Methyl Propyl Ketone (MPK)) with known specific surface free energy components, as listed in Table 4.1. Data (vapor pressure, adsorbed gas mass, and test time) are measured and captured electronically via the Messpro software.

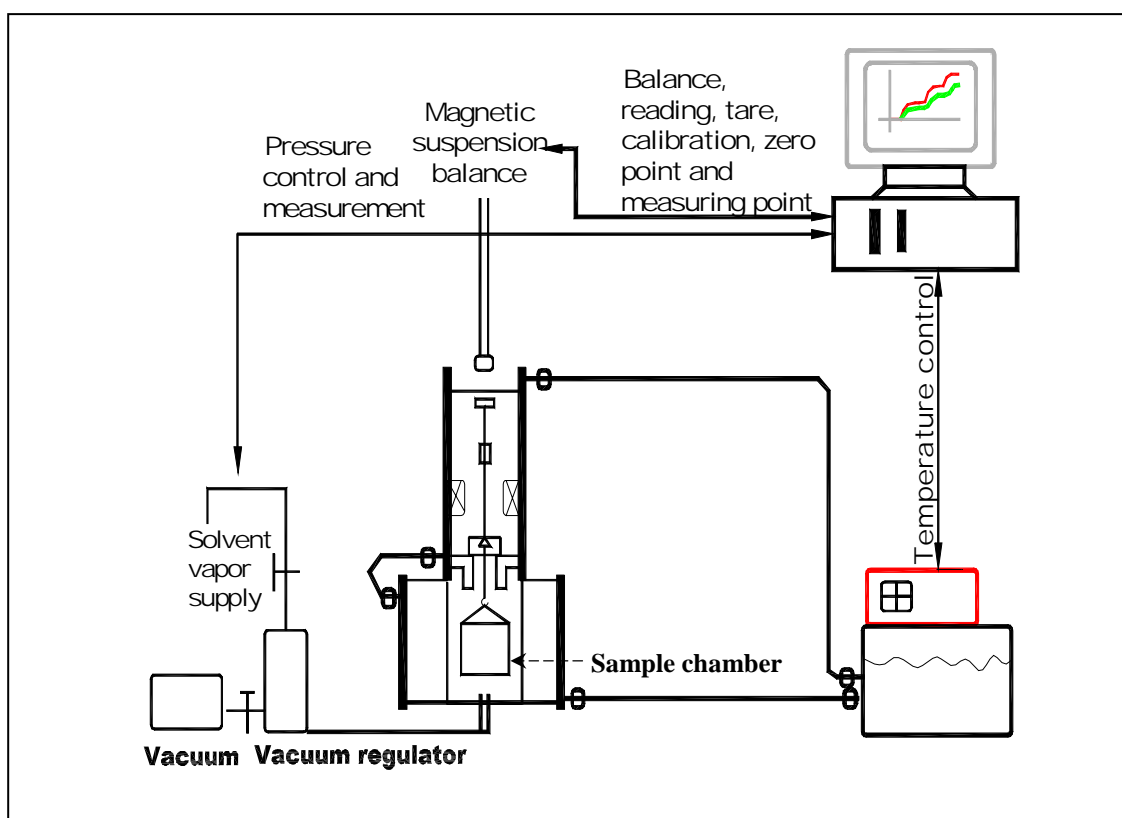


Figure 4.1 USD setup

Table 4.1 Surface energy components of water, n-hexane, and MPK @ 25 °C

Solvent	Surface Free Energy Components (ergs/cm <sup>2</sup> )				
	$\Gamma_{Li}$	$\Gamma_{Li}^{LW}$	$\Gamma_{Li}^{+}$	$\Gamma_{Li}^{-}$	$\Gamma_{Li}^{AB}$
Distilled water	72.60	21.60	25.50	25.50	51.00
n-hexane	18.40	18.40	0.00	19.60	0.00
MPK	24.70	24.70	0.00	0.00	0.00

Once the adsorbed solvent mass and vapor pressure on the aggregate surface have been measured and the adsorption data corrected for solvent vapor buoyancy using

the generalized Pitzer correlation model, the specific surface area of the aggregate is then calculated using the BET (Brunauer, Emmett, and Teller) model shown by Equation 4.3:

$$\frac{P}{n(P_0 - P)} = \left( \frac{c-1}{n_m c} \right) \frac{P}{P_0} + \frac{1}{n_m c} \quad (4.3)$$

where,

- $P$  = Vapor pressure (MPa),
- $P_0$  = Saturated vapor pressure (MPa),
- $N$  = Specific amount adsorbed on the surface of the absorbent (mg), and
- $n_0$  = Monolayer specific amount of vapor adsorbed on the surface of aggregate (mg).

For the type of isotherms associated with the pressure conditions in this USD test,  $n_m$  can be obtained from the slope and the intercept of the straight line that fits the plot of  $P/n(P-P_0)$  versus  $P/P_0$  best. The specific surface area (SSA) of the aggregate can then be calculated through the following equation:

$$SSA = \left( \frac{n_m N_o}{M} \right) \alpha \quad (4.4)$$

where,

$$\alpha = 1.091 \left( \frac{M}{N_o \rho} \right)^{2/3} \text{ for a hexagonal close-packing model (m}^2\text{),}$$

$$N_o = \text{Avogadro's number (} 6.02 \times 10^{23}\text{),}$$

$$M = \text{Molecular weight (g), and}$$

$$\rho = \text{Density of the adsorbed molecule in liquid at the adsorption conditions (g/cm}^3\text{).}$$

The result from the BET equation is used to calculate the spreading pressure at saturation vapor pressure ( $\pi_e$ ) for each solvent using Gibbs adsorption equation:

$$\pi_e = \frac{RT}{A} \int_0^{P_0} \frac{n}{P} dP \quad (4.5)$$

where,

- $\pi_e$  = Spreading pressure at saturation vapor pressure of the solvent (ergs/cm<sup>2</sup>),
- $R$  = Universal gas constant (83.14 cm<sup>3</sup> bar/mol.K), and
- $T$  = Absolute temperature (Kelvin,  $K$ ) ( $K = 273 + ^\circ\text{C}$ ).

The work of adhesion of a liquid on a solid ( $W_a$ ) can be expressed in terms of the surface energy of the liquid ( $\Gamma_l$ ) and  $\pi_e$  as shown in equations 4.6 and 4.7, where subscripts  $s$  and  $l$  represent solid (aggregate) and liquid (solvent), respectively:

$$W_a = \pi_e + 2\Gamma_l \quad (4.6)$$

$$\pi_e + 2\Gamma = 2\sqrt{\Gamma_s^{LW}\Gamma_l^{LW}} + 2\sqrt{\Gamma_s^+\Gamma_l^-} + 2\sqrt{\Gamma_s^-\Gamma_l^+} \quad (4.7)$$

Then, Equation 4.8 is used to calculate the  $\Gamma_s^{LW}$  of the surface for a non-polar solvent on the surface of the solid (aggregate).

$$\Gamma_s^{LW} = \frac{(\pi_e + 2\Gamma_l)^2}{4\Gamma_l^{LW}} \quad (4.8)$$

For a known mono-polar basic liquid vapor (subscript  $m$ ) and a known bipolar liquid vapor (subscript  $b$ ), the  $\Gamma_s^+$  and  $\Gamma_s^-$  values are calculated using equations 4.9 and 4.10 as follows.

$$\Gamma_s^+ = \frac{\left(\pi_e + 2\Gamma_{lm} - \sqrt{\Gamma_s^{LW}\Gamma_{lm}^{LW}}\right)^2}{4\Gamma_{lm}^-} \quad (4.9)$$

$$\Gamma_s^- = \frac{\left(\pi_e + 2\Gamma_{lb} - \sqrt{\Gamma_s^{LW}\Gamma_{lb}^{LW}} - 2\sqrt{\Gamma_s^+\Gamma_{lb}^-}\right)^2}{4\Gamma_{lb}^+} \quad (4.10)$$

Finally, the total surface energy of the aggregate ( $\Gamma_s$ ) is calculated as expressed by Equation 4.11.

$$\Gamma_s = \Gamma_s^{LW} + 2\sqrt{\Gamma_s^+\Gamma_s^-} \quad (4.11)$$

SE of two aggregates studied (i.e. VG and GL) were measured by USD method, and the results are listed in Table 4.2. The specific surface areas of the aggregate samples calculated using the adsorption isotherm of the three solvents are listed as well. The GL showed the higher acidic surface free energy, while the VG showed the higher basic components of surface free energy. The SSA of VG was considerably greater than that of GL, which means that it had a relatively rougher surface texture than the GL. It is also correlated to the results from investigation of aggregate geometric properties, which will be reported later. Though the VG had a little lower SE value than GL; however, its product of SE and SSA ( $195.70 \times 10^{-3}$  Joel/g) was much higher than that of GL ( $87.31 \times 10^{-3}$  Joel/g).

Further, the bond between the water and the aggregates were investigated, which is expressed by Equation 4.12.

$$\Delta G = \Delta G^{LW} + \Delta G^{AB} \quad (4.12)$$

Where,

$\Delta G$  = the total bond Gibbs free energy of the material surface per unit surface area,

$\Delta G^{LW}$  = the nonpolar, Lifshitz-van der Waals bond Gibbs free energy of the material surface, and

$\Delta G^{AB}$  = the polar, Acid-Base bond Gibbs free energy of the material surface.

The adhesive nonpolar bond component is determined by Equation 4.13.

$$\Delta G^{LW} = -\Gamma_{ij}^{LW} + \Gamma_i^{LW} + \Gamma_j^{LW} \quad (4.13)$$

And the adhesive polar bond component is of the same form and is determined by Equation 4.14.

$$\Delta G^{AB} = -\Gamma_{ij}^{AB} + \Gamma_i^{AB} + \Gamma_j^{AB} \quad (4.14)$$

The interactive term for the nonpolar LW adhesive surface energy component,  $\Gamma_{ij}^{LW}$  is given by Equation 4.15.

$$\Gamma_{ij}^{LW} = \left( \sqrt{\Gamma_i^{LW}} - \sqrt{\Gamma_j^{LW}} \right)^2 \quad (4.15)$$

And the interactive term for the polar AB adhesive surface bond energy component,  $\Gamma_{ij}^{AB}$  is given by Equation 4.16.

$$\Gamma_{ij}^{AB} = 2 \left( \sqrt{\Gamma_i^+} - \sqrt{\Gamma_j^+} \right) \left( \sqrt{\Gamma_i^-} - \sqrt{\Gamma_j^-} \right) \quad (4.16)$$

The results are summarized in Table 4.3. It shows that the total bond Gibbs free energy between water and VG was higher than that between water and GL. The total bond Gibbs free energy represents the ability of the solids to pull water. Immediately after pouring and before hardening, water filled pockets form under coarse aggregates. It is

expected that the VG has more preference to attract water than GL, which may have negative effect on concrete bonding performance.

**Table 4.2 SE components for the aggregates**

SE Component (ergs/cm <sup>2</sup> )	$\Gamma^+$	$\Gamma^-$	$\Gamma^{AB}$	$\Gamma^{LW}$	$\Gamma^{Total}$	SSA (m <sup>2</sup> /g)	$\Gamma^{Total} \times SSA$ (10 <sup>-3</sup> Joel/g)
VG	1.10	426.85	43.31	81.34	124.65	1.57	195.70
GL	1.62	362.71	48.51	79.89	128.4	0.68	87.31

**Table 4.3 Bond between water and aggregates**

i=water, j=agg	$\Gamma_{ij}^{AB}$	$\Gamma_{ij}^{LW}$	$\Delta G^{LW}$	$\Delta G^{AB}$	$\Delta G$ (ergs/cm <sup>2</sup> )
Water-VG	-124.91	19.11	83.83	219.22	303.06
Water-GL	-105.72	18.41	83.08	205.23	288.31

## AGGREGATE SHAPE AND TEXTURE CHARACTERISTICS

Researchers have distinguished between different aspects that constitute aggregate geometry. It has been found that the particle geometry can be fully expressed in terms of three independent properties: form, angularity (or roundness), and surface texture (Barett 1980). A schematic diagram that illustrates the difference between these properties is shown in Figure 4.2. Shape or form, the first order property, reflects variations in the proportions of a particle. Angularity, the second order property, reflects variations at the corners, that is, variations superimposed on shape. Surface texture is used to describe the surface irregularity at a scale that is too small to affect the overall shape (Al-Rousan 2004).



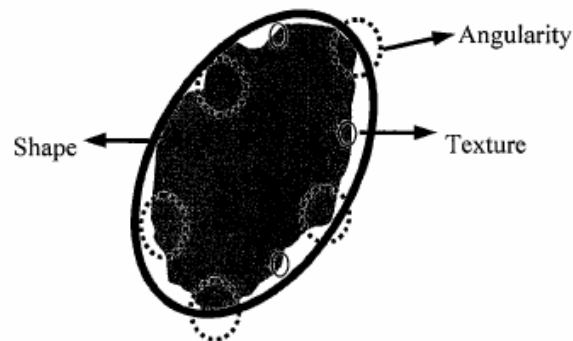


**Figure 4.2 Aggregate shape components (Masad 2001)**

Aggregate shape characteristics affect the proportioning of portland cement concrete mixtures, the rheological properties of the mixtures, aggregate-mortar bond, and the interlocking strength of the concrete joint/crack (Al-Rousan 2004). Previous studies (Mindness et al. 2002; Kosmatka et al. 2002; Will 2000) indicate that the bond strength between the cement paste and a given coarse aggregate generally increases as particles change from smooth and rounded to rough and angular. Rough, textured surfaces will improve the mechanical component of the bond by increasing the amount of surface area available for bonding with the paste for a given aggregate content. The interlocking of angular particles results in a strong aggregate skeleton under applied loads, whereas round particles tend to slide by or roll over each other, resulting in an unsuitable and weaker structure. Using a high percentage of flat and elongated particles might cause problems when placing the concrete, which will result in voids and incomplete consolidation of the mix, and thus contribute to local distress. Therefore, three components — texture, angularity, and content of flat/elongated aggregates have different (positive or negative) effects on bonding performance of concrete materials, which can be used to represent the effects of geometric properties of aggregates.

Table 4.4 (Al-Rousan et al. 2004) summarizes direct and indirect test methods that have been used by highway state agencies and research projects for measuring some

aspects of aggregate shape properties. Direct methods are defined as those wherein particle characteristics are measured, described qualitatively and possibly quantified through direct measurement of individual particles. In indirect methods, particle characteristics are lumped together as geometric irregularities and determined based on measurements of bulk properties.

The comparative analysis and intensive evaluation conducted by Al-Rousan et al. (2004) highlighted the advantages of AIMS in measuring aggregate shape properties:

- Able to capture images and analyzing the shape of a wide range of aggregate sizes and types,
- Measures all three aggregate shape properties (form, angularity, and texture) for all aggregate types and for different aggregate sizes,
- Capable of performing two and three dimensional analysis as needed,
- Captures images of aggregates at specified resolutions in order to minimize the influence of particle size on shape results,
- Uses image analysis techniques that are based on sound scientific concept,
- Rapid, computer automated, accurate, practical and user friendly, and
- Able to work in central and field laboratories.

Figure 4.3 shows the entire AIMS set-up, and it was utilized to facilitate this study.

**Table 4.4 Summary of methods for measuring aggregate characteristics (Al-Rousan et al. 2004)**

Test	References for the test method	Direct (D) or Indirect (I) method	Field (F) or Central (C) laboratory application
Uncompacted void content of CA	AASHTO* TP56, NCHRP Report 405, Ahlrich (1996)	I	F, C
Index for particle shape and texture	ASTM D3398	I	F, C
Angle of internal friction from direct shear test	Chowdhury et al. (2001)	I	C
Percentage of fractured particles in CA	ASTM D5821	D	F, C
Flat and elongated CA	ASTM D4791	D	F, C
Multiple ratio shape analysis	David Jahn (Martin Marietta, Inc.)	D	F, C
VDG-40 videograder	Emaco, Ltd. (Canada), Weingart and Prowell (1999)	D	F, C
Computer particle analyzer	Mr. Reckart (W. S. Tyler Mentor Inc.), Tyler (2001)	D	C
Micromeritics optisizer PSDA	Mr. M. Strickland (Micromeritics optisizer)	D	C
Video Imaging System (VIS)	John B. Long Company	D	C
Buffalo wire works PSSDA	Dr. Penumadu, University of Tennessee	D	C
Camsizer	Jenoptik Laser Optik System and Research Technology	D	C
WipShape	Marez and Zhou (2001)	D	C
University of Illinois Aggregate Image Analyzer (UIAIA)	Tutumluer et al. (2000), Rao (2001)	D	C
Aggregate Imaging System (AIMS)	Masad (2003)	D	C
Laser-Based Aggregate Analysis System	Kim et al. (2001)	D	C

\* AASHTO = American Association of State Highway and Transportation Officials



**Figure 4.3 AIMS set-up**

### **Parameters Representing Aggregate Shape**

In AIMS analysis system a number of indices have been proposed to characterize particle form, angularity, and texture. Among the form parameters, sphericity is expressed in terms of three dimensions:

$$Sphericity = \sqrt[3]{\frac{d_s * d_i}{d_l^2}} \quad (4.17)$$

where,

$d_l$  = longest dimension of the particle,

$d_i$  = intermediate dimension of the particle, and

$d_s$  = shortest dimension of the particle.

The form index, describing form in two-dimensions, uses incremental changes in the particle radius. The length of a line that connects the center of the particle to the

boundary of the particle is termed radius. The form index is expressed by the following equation:

$$Form\ Index = \sum_{\theta=0}^{\theta=360-\Delta\theta} \frac{|R_{\theta+\Delta\theta} - R_{\theta}|}{R_{\theta}} \quad (4.18)$$

where,

$\theta$  = the directional angle, and

R = the radius in different directions.

If a particle was a perfect circle, the form index would be zero. Although the form index is based on two-dimensional measurements, it can easily be extended to analyze the three-dimensional images of aggregates. Another way of presenting form of a particle is by using Flat and Elongated Ratio (FER), which is:

$$FER = \frac{d_l}{d_s} \quad (4.19)$$

The analysis methods of angularity have used mainly black and white images of 2-dimensional projections of aggregates, with the assumption that the angularity elements in 2-dimensions are a good measure of the 3-dimensional angularity. For the gradient method, the angle of orientation values of the edge-points ( $\theta$ ), and the magnitude of the difference in these values ( $\Delta\theta$ ) for adjacent points on the edge are calculated to describe how sharp or how rounded the corner is, as illustrated in Figure 4.4. The angularity values for all boundary points are calculated and their sum accumulated around the edge to finally form a measure of angularity, which is noted, the gradient index (GI) (Chandan et al. 2004):

$$GI = \sum_{i=1}^{N-3} |\theta_i - \theta_{i+3}| \quad (4.20)$$

where,

$i$  = the  $i$ th point on the edge of the particle, and

$N$  = the total number of points on the edge of the particle.

Masad et al. (2001) proposed the angularity index, which is described by the following equations:

$$\text{Angularity Index} = \sum_{\theta=0}^{\theta=360-\Delta\theta} \frac{|R_{P\theta} - R_{EE\theta}|}{R_{EE\theta}} \quad (4.21)$$

where,

$R_{P\theta}$  = the radius of the particle at a directional angle,  $\theta$ , and

$R_{EE\theta}$  = the radius of an equivalent ellipse at the same  $\theta$ .

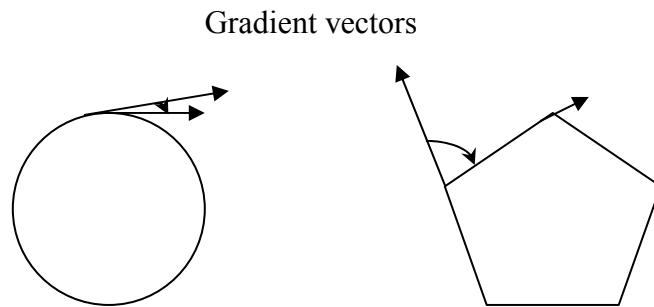


**Figure 4.4 Difference in gradient between particles**

The index relies on the difference between the radius of a particle in a certain direction and a radius of an equivalent ellipse taken in the same direction as a measure of angularity. Both gradient and radius angularity results are presented in AIMS.

Wavelet analysis method is used in AIMS for texture characterization. The wavelet transform works by mapping an image onto a low-resolution image and a series of detail images, as shown in Figure 4.5. The original image is shown in Figure 4.5a. It is decomposed into a low-resolution image (Image 1 in Figure 4.5b) by iteratively blurring the original image. The remaining images contain information on the fine intensity variation (high frequency) that is lost in Image 1. Image 1 can be further decomposed similarly to the first iteration, which gives a multi-resolution decomposition and facilitates quantification of texture at different scales. Image 2 contains the information lost in the y-direction, Image 3 has the information lost in the x-direction, and Image 4 contains the information lost in both x- and y-direction. Texture index is taken at a given level as the arithmetic mean of the squared values of the detail coefficients at that level:

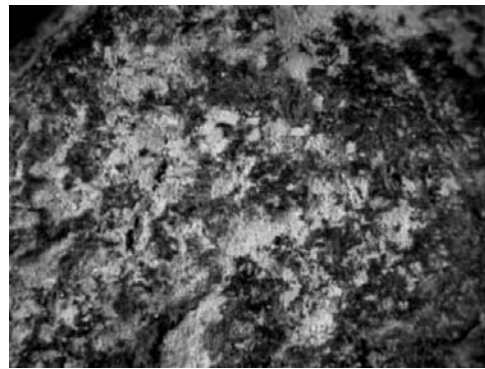
$$\text{Texture Index}_n = \frac{1}{3N} \sum_{i=1}^3 \sum_{j=1}^N (D_{i,j}(x,y))^2 \quad (4.22)$$

where,

N = the level of decomposition,

i = 1, 2, or 3, for the three detailed images of texture, and

j = the wavelet coefficient index.



(a) Original image

Image 1

Image 2

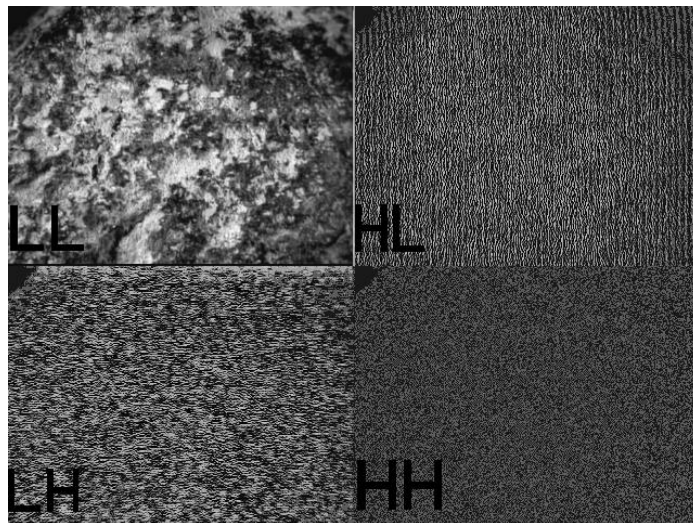


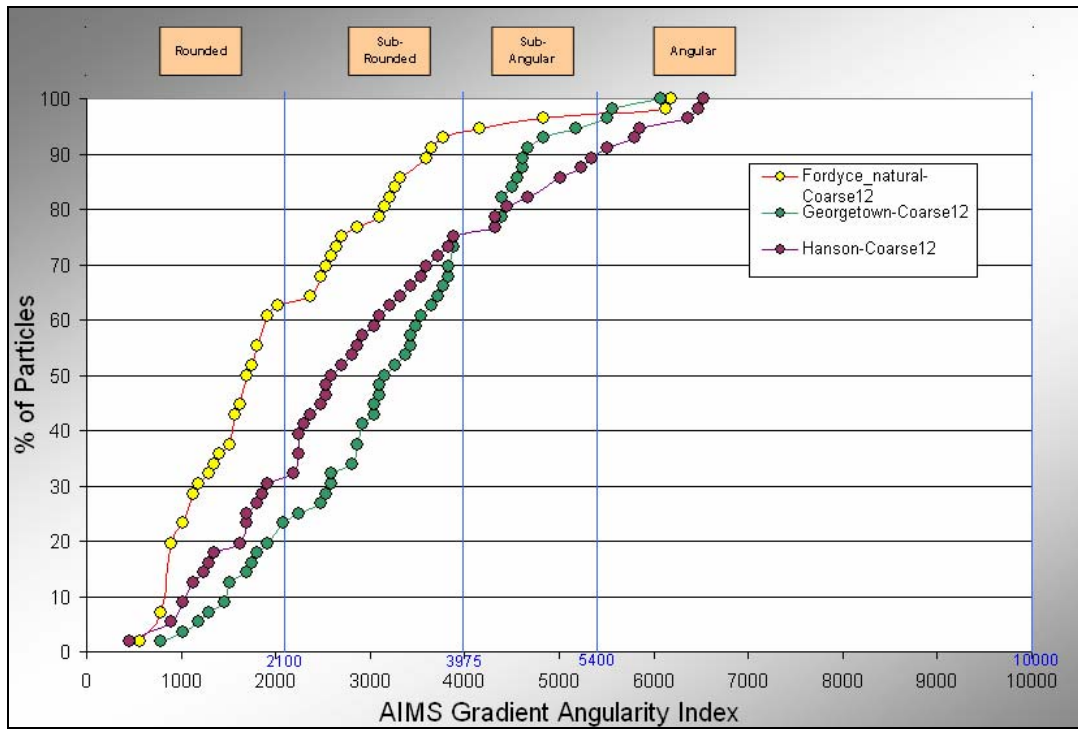
Image 3

Image 4

(b)

**Figure 4.5 Illustration of the wavelet decomposition (Chandan 2004)**





**Figure 4.6 Example of AIMS gradient angularity index curve**

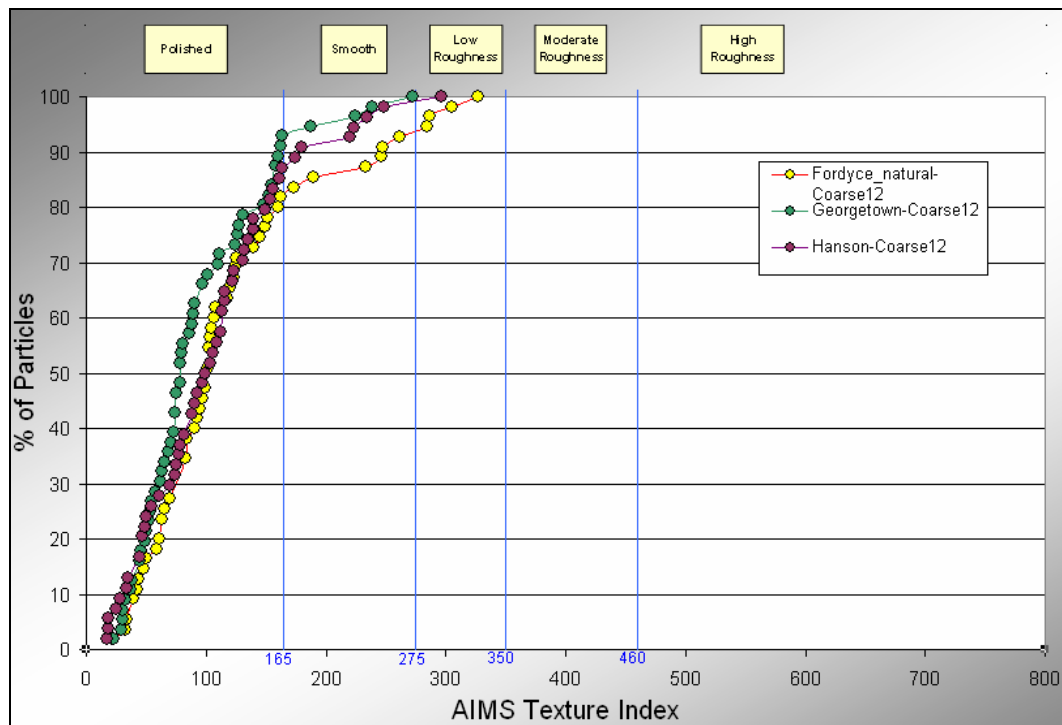


**Figure 4.7 Example of AIMS texture index curve**

The output of the analysis software can be an Excel file with summary reports and graph illustrations for all size combined or individual sizes. It also shows the results in terms of a cumulative distribution curve and some statistics such as standard deviation, mean, and values of first, second, and third quartiles. Figures 4.6 and 4.7 show the examples of output from analysis software.

Table 4.5 summarized the features of each shape parameter used in the AIMS. Texture index and gradient angularity index were picked up for this study. The sphericity value gives a very good indication on the proportions of a particle dimensions. However, one cannot determine whether an aggregate has flat, elongated or flat and elongated particles using the sphericity alone. Therefore, percentage of flat/elongated aggregates was used, which can be obtained from AIMS analysis summary report.

The blue lines in Figures 4.6 and 4.7 show the aggregate shape classification limits, as also summarized in Figure 4.8. For example, if texture index of aggregate is

below 165, it is defined as polished texture. If the value is higher than 460, it is defined high roughness.

For each size level of each aggregate type, AIMS analysis software provides the results in terms of cumulative distribution functions and statistical parameters such as average texture index ( $TI_k$ ), angularity index ( $GI_k$ ), and percentage of flat/elongated aggregates ( $\%E_k$ ) based on 56 particles for each individual size level. To consider the

**Table 4.5 Features of analysis methods in AIMS**

<b>Method</b>	<b>Description</b>	<b>Features</b>
Texture index using wavelet	Used by AIMS analysis software (AIMSTXTR)	<ul style="list-style-type: none"> <li>• Capable of separating aggregates with different texture characteristics</li> <li>• Most unique among the texture parameter</li> </ul>
Gradient angularity index	Used by AIMS analysis software (AIMSGRAD)	<ul style="list-style-type: none"> <li>• Capable of separating aggregates with different angularity characteristics</li> <li>• Capable of separating angularity from form</li> <li>• Most unique among angularity parameters</li> </ul>
Radius angularity index	Used by AIMS analysis software (AIMSRAD)	<ul style="list-style-type: none"> <li>• Captures angularity but it is not capable of separating two dimensional form from angularity</li> </ul>
2-D form index	Used by AIMS analysis software (AIMSFORM)	<ul style="list-style-type: none"> <li>• Captures two dimensional form but it is not capable of separating form from angularity</li> </ul>
Sphericity	Used by AIMS analysis software (AIMSSPH)	<ul style="list-style-type: none"> <li>• Capable of separating aggregates with different form characteristics</li> <li>• Captures unique characteristics of aggregates</li> <li>• Most unique among the form parameters</li> </ul>

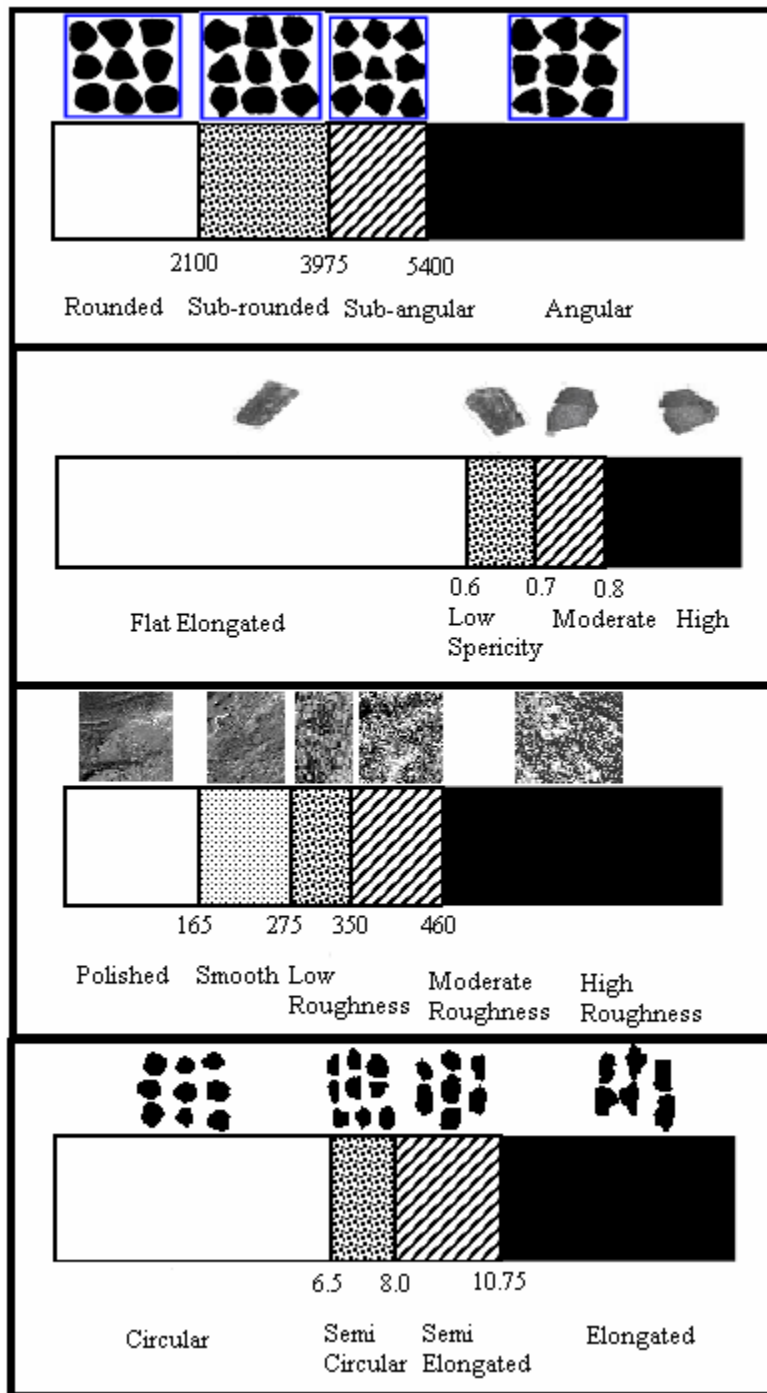


Figure 4.8 Aggregate shape classification limits (Al-Rousan 2004)

overall contribution of aggregates at all size levels in concrete, overall shape and texture parameters were proposed based on these original statistical parameters from AIMS, which can be expressed as:

$$STI = \frac{\sum \%A_k \cdot TI_k}{460} \quad (4.23)$$

where,

STI = overall standardized texture index,

$\%A_k$  = percentage of aggregates on the size k sieve, and

460 = threshold value for high roughness particle in AIMS.

$$SGI = \frac{\sum \%A_k \cdot GI_k}{5400} \quad (4.24)$$

where,

SGI = overall standardized gradient angularity, and

5400 = threshold value for angular particle in AIMS.

and,

$$OS = \sum \%A_k \cdot \%E_k \quad (4.25)$$

where,

OS = overall percentage of flat/elongated aggregates.

After standardized by the threshold value, STI ranges from 0 to 1. The higher the value of STI, the rougher the aggregate surface. SGI ranges from 0 to 1 as well. The closer to 1, the more angular the aggregate is. In terms of OS, a higher value indicates more flat/elongated aggregates in the concrete. Therefore, these three parameters can represent various effects (positive or negative) of aggregate shape on concrete bonding performance.

Before measurements, aggregates were cleaned, dried, and sieved to four size levels: passing 1 in but retaining on  $\frac{3}{4}$  in sieves; passing  $\frac{3}{4}$  in but retaining on  $\frac{1}{2}$  in sieves; passing  $\frac{1}{2}$  in but retaining on  $\frac{3}{8}$  in sieves; and passing  $\frac{3}{8}$  in but retaining on #4 sieves. Table 4.6 shows sources and sizes of aggregates tested.

**Table 4.6 Aggregate sources and sizes**

Aggregate	Source	Aggregate description	Aggregate sizes			
			25.4-19.0 mm (1-3/4")	19.0-12.5 mm (3/4"-1/2")	12.5-9.5 mm (1/2"-3/8")	9.5-4.75 mm (3/8"-#4)
GG	Garwood, TX	Uncrushed river gravel	X	X	X	X
VG	Victoria, TX	Uncrushed river gravel	X	X	X	X
GL	Georgetown, TX	Limestone	X	X	X	X

A summary of these aggregate shape parameter results is illustrated in Figure 4.9. It can be seen that different aggregates showed different behaviors in terms of these three independent components. The decreasing rank orders of bonding performance as measured are GG, GL, and VG with respect to angularity; VG, GG, and GL with respect to texture; and VG, GG, and GL with respect to percentage of flat/elongated particles. GG is the most angular aggregate, and VG has the roughest aggregate surface and also highest amount of flat/elongated particles.

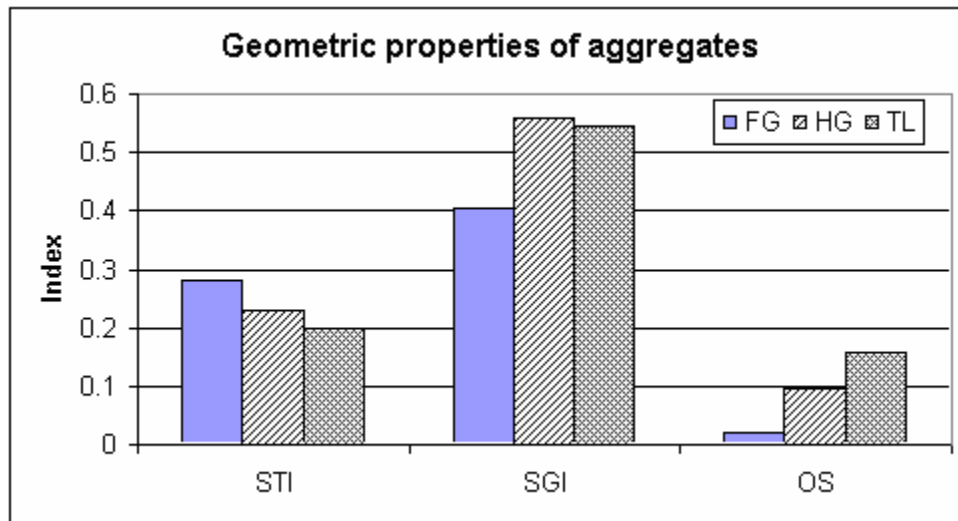


**Figure 4.9 Aggregate geometric properties summary**

## **AGGREGATE PHYSICAL PROPERTIES**

Gradation (also called particle-size distribution or grain-size distribution) refers to the proportions – by mass or weight – of aggregate particles distributed in special particle-size ranges (Somayaji 2001). It affects the workability of concrete which may, in turn, affect the segregation of constituents, bleeding, water-cement requirements, handling, placing, and finishing characteristics. These factors may then affect strength, volume change, durability, and the economy of concrete.

The gradations for three aggregates studied are illustrated in Figure 4.10. Not only maximum size but also the fineness modulus can be calculated from the gradation curves of aggregates. It is useful as an indicator of the average size of an aggregate. A lower fineness modulus of aggregate indicates a larger percentage of finer materials; similarly, a higher number means fewer finer particles or plenty of coarser particles. The fineness modulus cannot be used as a single description of the grading of an aggregate, but it is valuable for measuring slight variations in the aggregate gradation. It gives an indication of the probable behavior of a concrete mix made with aggregate having a certain grading, and the use of the fineness modulus in assessment of aggregates and in

mix proportioning has had many advocates (Neville 1995; Popovics 1966). Therefore, both of these two parameters were used to investigate size effect of aggregates studied, where the results are summarized in Table 4.7.

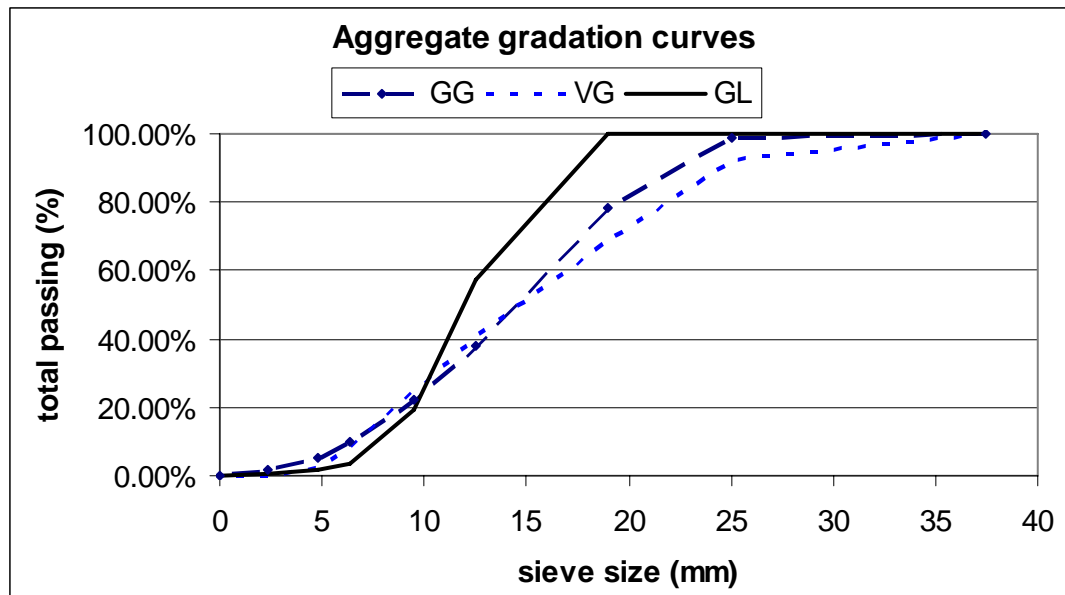


**Figure 4.10** Aggregate gradation curves

It is obvious that there was a finer grading associated with GL aggregate than the gravel aggregates. The two gravel aggregates had the same maximum aggregate size; however, the VG aggregate had higher contents of particles at larger size levels than GG, which can also be found from their fineness modulus data. Larger aggregate size can have a detrimental effect on the bonding due to the following reasons: 1) for a given volume of coarse aggregate, a larger maximum size reduces the specific surface area of aggregate; 2) an increased stress concentration and microcracks in the vicinity of the aggregate is expected with decreased surface area; 3) larger aggregate size results in the increases of the perimeter and thickness of interfacial layer between mortar and aggregate so that a larger flaw can be formed and the bond strength decreased (Akcaoglu



et al. 2002); and 4) larger aggregate particles tend to accumulate more bleed water around it, which could lead to a higher local w/cm and subsequently, a higher bulk porosity and the size and porosity in the interfacial transition zone (ITZ) than the ITZ around the smaller aggregates (Elsharief et al. 2003; Basheer et al. 1999). Therefore, in terms of aggregate size effect, the decreasing rank order of bonding performance as evaluated is GL, GG, and VG.

Other physical properties are also summarized in Table 4.7. It can be seen from Table 4.7 that all three aggregate types, especially the two types of gravel, had very close values of bulk specific gravity in the oven-dry condition (BSG-od) and dry rodded unit weight (DRUW). AC represents the maximum amount of water the aggregate can absorb. As for the AC, the two gravels had very close values. However, GL had much higher AC than the gravel aggregates, which means that the GL aggregate is much more porous and absorbent. Though abnormally high absorption capacities indicate high – porosity aggregates, which may have potential durability problems, this property is beneficial to the bond performance at early ages, because the process of absorption increases and improves the contact area between the mortar and the aggregate. Therefore, in terms of AC, the bonding performance rank can be predicted as GL, VG, and GG in a decreasing order.

**Table 4.7 Physical properties of aggregates**

Aggregate type	GL	VG	GG
Max. size (in)	3/4	1	1
Fineness Modulus	6.78	7.04	6.92
BSG-od	2.50	2.56	2.56
DRUW (lbs/ft <sup>3</sup> )	94.17	103.3	102.74
AC (%)	4.79	1.42	1.05

## AGGREGATE CHEMICAL PROPERTIES

Struble et al. (1980) stated that one of the sources of the aggregate-mortar interfacial bond is a chemical bond resulting from a reaction between the aggregate and the cement paste. Therefore, in this study an attempt was made to provide evidence elucidating the role played by aggregates in influencing ionic chemical interactions at the interface.

The total bond Gibbs free energy between water and aggregates could be a good parameter to represent the chemical characteristics of aggregate relative to the concrete bonding performance, since it represents the preference of aggregate to pull water. However, it didn't make it due to the equipment problem. In an alternative way, the mineralogy analysis of aggregates was conducted by visual observation and optical microscope analysis, as shown in the rock components table (Table 4.8). It was found that these two gravels are actually mixtures of several rock components. GG is a combination of chert (i.e. microcrystalline quartz), quartzite, and acid volcanic, while VG is composed of chert, quartzite, limestone and acid volcanic. It can be seen that VG and GG have almost similar chert content. However, GG has a much higher content of quartzite than VG. GG has no limestone in it, but VG contains about 21.09% of limestone. Different compositions of rock components for these aggregates lead to different chemical activities and subsequently, the aggregate-mortar bond.

**Table 4.8 Rock components of aggregates**

Aggregate type	GL	VG	GG	
Rock components (%)	Chert	/	67.26	68.38
	Quartzite	/	8.03	24.21
	Limestone	100	21.09	/
	Volcanic	/	3.42	6.25

The study on ITZs of different rock types at varied curing ages conducted by Tasong et al. (1999) provided reasonable interpretations of the results obtained in this

study. Figure 4.11 compares the ITZs of limestone and quartzite at an early age by SEM analysis. It shows that very high porosity formed in the limestone ITZ (shown in Figure 4.11 (a)), while it was not found in the quartzite ITZ. Instead, the cement paste side at quartzite ITZ did not show any microstructural differences compared with its bulk paste (shown in Figure 4.11 (b)). Different from previous findings by other researchers (Monteiro and Mehta 1986), carbon dioxide gas given off as a result of a chemical interaction between the limestone and the hydrating cement paste is considered to be the main reason for this high porosity (Tasong et al. 1999), which accounts for the weaker bond between this rock and the cement paste at an early age.

The study on  $\text{Ca(OH)}_2$  orientation index at ITZ for different rock types proved similar conclusions as well, which represents the degree of preferred orientation of  $\text{Ca(OH)}_2$  crystals with their c-axes normal to the aggregate surface (Grandet and Ollivier 1980). Higher values of  $\text{Ca(OH)}_2$  orientation index represents more  $\text{Ca(OH)}_2$  crystals orientated with their c-axes perpendicular to the ITZ, which weaken the ITZ structure and associated bonding between aggregate and mortar. The  $\text{Ca(OH)}_2$  orientation index at the limestone ITZ was higher than that of the bulk paste at all ages studied, while that at the quartzite ITZ was more or less the same as that of the bulk cement paste at all ages studied. In addition, for all ages studied, quartzite ITZ provided lower  $\text{Ca(OH)}_2$  orientation index than limestone, which indicates the poorer ITZ of the former than the latter. The low  $\text{Ca(OH)}_2$  orientation index at the quartzite ITZ could be due to a pozzolanic reaction between  $\text{Si}^{4+}$ , leached out of the rock, and the  $\text{Ca(OH)}_2$  or the hydroxyl ion to produce calcium silicate (CSH), which is known to enhance the density of the ITZ and subsequently increase the bond strength.

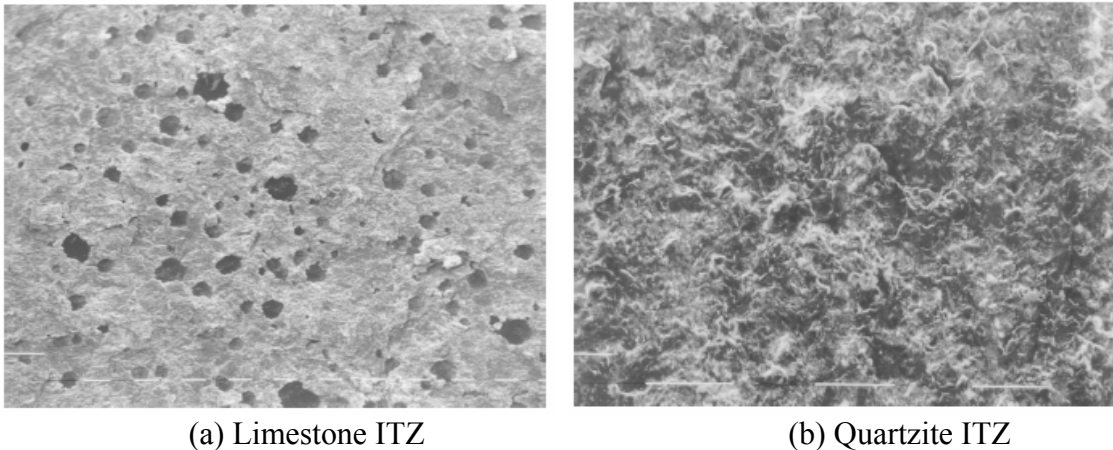


**Figure 4.11 ITZ comparisons of limestone and quartzite (Tasong et al. 1999)**

Though detailed information of mineralogy analysis by XRD technique is recommended for further study, it is not surprising that due to the higher content of quartzite and no limestone in GG, GG was expected to provide the more beneficial chemical reaction than the other two aggregate types. The very porous nature of the ITZ associated with the reaction of limestone with the cement paste at an early age resulted in a negative effect on the bonding strength. Therefore, the decreasing rank order of bonding strength as evaluated in terms of aggregate chemical properties is GG, VG, and GL.

### **UTILITY THEORY**

To put it in its simplest form, utility theory is a way to compare dissimilar things (apples and oranges) based on the following concepts (Ledbetter et al. 1977):

Value – the worth attached to an object or a service, and

Utility – capability of a practice or measure to satisfy a particular need or provide a desirable result

It can be used to synthesize and account for a variety of factors that play a role to varying degrees in a decision or evaluation processes. A basic premise in utility theory is

that decisions are arrived at using a rational basis, i.e., there is a set of transitive preferences for the outcome of the courses of action available, and the best of the alternatives will be chosen on the basis of maximizing some parameter. Furthermore, these preferences can be rated in terms of their relative power (utility) to satisfy the decision maker's desires.

MacCrimmon has classified the various methods of formally modeling a multiple objective decision making process into: a) weighting methods, b) sequential elimination methods, c) mathematical programming methods, and d) spatial proximity methods. Among MacCrimmon's classification scheme, weighting methods are the most appropriate models relative to choosing a particular method. The weighting methods are further subdivided into a) trade-offs, b) simple additive weighting, c) hierarchical additive weighting, and d) quasi-additive weighting. Hierarchical additive weighting was selected in this case because of its relative simplicity.

A utility curve is a mapping from one scale of measurement to a second. The first scale represents a result variable that can be quantified, and the second scale is the level of value (satisfaction, utility) that is generated. Use of a utility curve provides a means to characterize the decision variable. It allows one to determine the utility of any decision variables once a particular value of that variable is known.

In accordance with the hierarchical additive weighting method of decision analysis, the individual utilities for each decision criterion must be weighted and added together to give an overall utility for each design method. Weighted expected values are added directly according to the following relation:

$$E(u) = \sum_{i=1}^n w_i E_i(u) \quad (4.26)$$

where,

$E_i(u)$  = the average rating of the  $i$ th attribute component,

$w_i$  = the weight of the  $i$ th attribute component,

$E(u)$  = the overall expected rating of utility, and  
 $n$  = the number of attribute components.

### **Overall Evaluation of Aggregate Contribution**

Based on the investigation of the aggregate physical, geometric, and chemical properties described in the previous chapter, it can be seen that any property alone could not be used to completely evaluate bond strength. This is because the aggregate-mortar interfacial bond for a given cement paste was found not to be a simple function of any one of aggregate properties, but a function of all three properties aggregated together. In addition, different relative importance existed in the different aggregate properties and different components within the property, which then affected the overall contribution of that particular property (i.e., physical, geometric, and chemical) to the interfacial bond of the concrete.

As previously introduced, utility theory facilitates a way to compare dissimilar things based on their values and utilities. Therefore, a rating system based on utility theory was applied to evaluate the overall contribution of aggregate properties on concrete bonding performance. A combined value can be generated to represent the integral overall contribution of the aggregate properties for each aggregate type by assigning a pre-determined weighting factor to the rating of each individual aggregate property allowing for all rating values to be combined into a single parameter in Equation 4.26.

Table 4.9 lists a summary of overall evaluation for aggregates investigated, where the rating system is on a scale of 0 (poor) to 10 (best). Higher overall expected rating value indicates better overall aggregate contribution to the bonding performance, which is identified based on the combination of physical, geometric, and chemical properties with suggested weighting values of 4, 3, and 3, respectively. These weighting values were assigned on the basis that physical properties (with a value of 4) are the most basic properties relating to concrete mix and construction design. Geometric and

chemical properties (with a value of 3 each) were assumed to have equal contribution and then were assigned equal weighting values.

Within each property, there are sub-attribute components with individual weighting values. Within the scope of this study, the aggregate contribution in terms of physical property was evaluated with respect to 1) aggregate size effect, and 2) AC; while 1) angularity, 2) texture, and 3) percentage of flat/elongated particles were considered in the evaluation of the aggregate contribution in terms of geometric properties. As shown in Table 4.9, different rating values were assigned to each aggregate type based on the analysis of bonding performance in each attribute component in the previous chapter. Higher rating values represented better performance of components for different aggregate types. Equation 4.26 was applied twice to 1) get overall rating values for physical and geometric property considering their sub-attributes, and then 2) to obtain the combined rating values representing overall aggregate contribution in terms of all three properties. The overall ratings considering all attributes and their sub-attributes were 6.1, 4.5, and 5.0 for GG, GL, and VG, respectively, which indicated that GG provided best overall contribution, GL was the second, and VG was the poorest. This result also matched the experimental design analysis very well.

**Table 4.9 Overall evaluation for aggregates**

	Weight	Attribute	Weight	Rating		
				GG	VG	GL
Physical properties	4	size effect	5	5	3	8
		AC	5	4	4	8
Geometric properties	3	angularity	3.5	8	3	6
		texture	3.5	6	8	3
		%flat particles	3	5	8	3
Chemical properties	3	/	/	8	4	2
Overall rating				6.1	4.5	5.0

Therefore, it is possible to draw a conclusion that with appropriate combination of properties, any coarse aggregate type can provide positive effects on the bonding performance between the aggregate and the mortar. In addition, for a given aggregate type, based on the overall evaluation of the aggregate contribution, aggregate blending is also a possible means to optimize the physical properties of aggregates, and then the aggregate contribution to bond strength of concrete. Based on the composite contribution of the individual aggregate properties to the bonding strength of concrete as depicted by utility theory, this approach allows for the selection of the best aggregate type in concrete paving construction.

### **Feasibility Evaluation of Design Combinations**

The previous Taguchi design analysis indicated the relative importance of the design factors relative to the bond strength, and different effects of levels for each factor. Therefore, utility theory can be also used to evaluate the feasibility of mixture design combinations relative to the bonding performance. The basic idea behind the use of utility theory is that if there is a set of prerequisite preferences associated with the end result of a given design combination, then the best combination can be chosen on the basis of maximizing the rating.

It can be accomplished in a similar manner as that of the aggregate evaluation, but with respect to 1) aggregate contribution, 2) w/cm, 3) curing method and 4) ultra-fine fly ash content. A combined value can be generated to represent the integral overall performance of a design combination by assigning a user defined weighting factor to the rating of each individual component allowing for all rating values to be combined into a single parameter using Equation 4.26. Figure 4.12 shows the correlation between the rating values and bonding performance in the utility curve, where the rating system is on a scale of 0 (poor) to 10 (best). It indicates that the higher rating values, the better the bonding performance and the more feasible the design combinations.



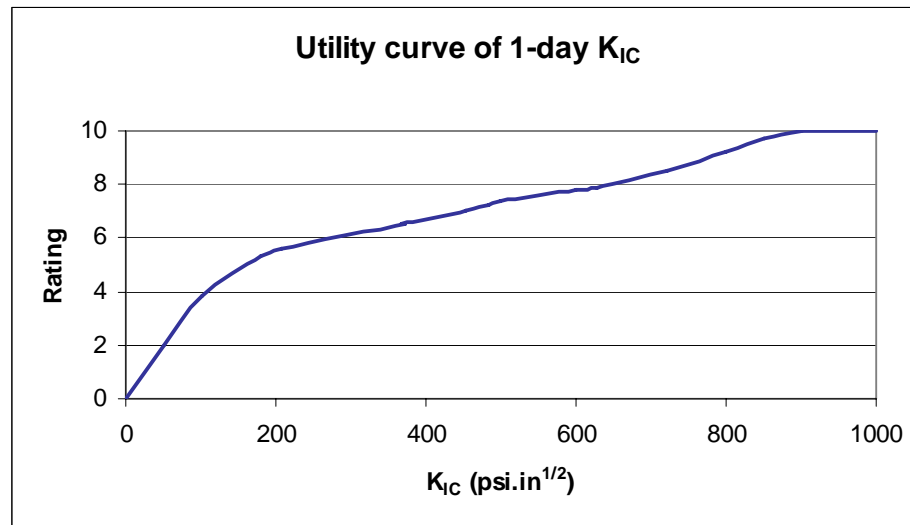


**Figure 4.12 Utility curve of 1-day  $K_{IC}$**

Table 4.10 provides an example of this approach by comparison of test run 1 (i.e., VG + WMC + 0.4 of w/cm + 8% of ultra-fine fly ash), test run 3 (i.e., VG + WOC + 0.45 of w/cm + 20% of ultra-fine fly ash), and the optimum design (i.e., GG + WMC + 0.4 of w/cm + 8% of ultra-fine fly ash). As shown in Table 4.10, different weights and ratings were assigned to the design factors due to the different relative importance of each factor to  $K_{IC}$  and different levels of each factor (Table 3.10 and 3.11). Higher weights represented greater importance given to the factors relative to  $K_{IC}$ , and corresponding to the higher levels in Table 3.10 and 3.11, higher ratings represented better performance relative to bond strength. Optimum design combination provided highest overall rating value, which was also correlated with the previous result from experimental design. The overall rating values of test run 1 (i.e., 6.6) was higher than that of test run 3 (i.e., 5.6). Therefore, the design of test run 1 is more feasible (Figure 4.12), which is consistent with the  $K_{IC}$  results of these two designs (Figure 3.15). In addition, these two designs used the same aggregate type. However they provided different bonding performance due to different selections of other factors. Therefore, for a given gravel aggregate type, it is possible to improve the bonding performance of concrete by selecting optimum levels of other design factors.

**Table 4.10 Summary of evaluations by rating systems**

	Weight	Rating		
		Test 1	Test 3	Optimum
Aggregate type	4	4.5	4.5	8.0
Curing method	3	8.0	5.4	8.0
W/cm	2	8.0	6.9	8.0
Ultra-fine fly ash content	1	7.5	8.0	7.5
Overall rating		6.6	5.6	8.0

The application of utility theory to the evaluation of overall contribution of aggregate properties to the bonding performance of concrete, and feasibility of design combinations enable the selection of the best aggregate type, and aggregate blend to optimize the design combinations for concrete paving construction to relieve delamination and further spalling distresses.

## **CHAPTER V**

### **INTERFACIAL FRACTURE ENERGY MODEL AND STRESS ANALYSIS APPROACH**

#### **GENERAL**

To further investigate the strength characteristics of the interface between aggregate and mortar, in this chapter, a model of interfacial fracture energy between aggregate and mortar was formulated based on the relation between fracture energy of concrete and fracture energies of its components. The relation between the interfacial fracture energy, material, and construction factors was investigated. The final results built the connection between concrete properties at the meso-level (represented by the interfacial fracture energy between aggregate and mortar) and at the macro-level (represented by fracture toughness of concrete and significant influencing materials and construction factors).

An approach to predict the delamination occurrence by numerical simulation and laboratory investigation was also proposed. It's based on comparing  $K_I$  (stress intensity factors) and  $K_{IC}$  (critical stress intensity factor or fracture toughness) directly in terms of fracture criteria for unstable growth. One can then determine the crack stability of the material under given loading conditions. It can also be used for evaluating the effectiveness of pavement design methods to prevent delamination and spalling distress.

#### **INTERFACIAL FRACTURE ENERGY**

The specific fracture energy is one of the important material properties of concrete. It is defined as the area under the load-deflection curve per unit fractured surface area, and is used to characterize the process of fracture (Pettersson 1980). Fracture energy and fracture toughness reflect different aspects of the interfacial failure. As stated by Pye and Beaudoin (1992), interface fracture energy is a more appropriate descriptor of the quality

of the cement paste-substrate bond due to the progressive failure of the bond. However, the testing of interfacial fracture properties is not as easy as other property testing to perform. Work was conducted to formulate an interfacial fracture energy model to investigate the characteristics of fracture process at the aggregate-matrix interface and build the relation between it and the macro fracture property of concrete.

The energy approach states that crack extension (i.e. fracture) occurs when the energy available for crack growth is sufficient to overcome the resistance of the material. According to the First Law of Thermodynamics, when a system goes from a nonequilibrium state to equilibrium, there will be a net decrease in energy. Griffith (1920) applied this idea to the formation of a crack, and his model is based on a global energy balance: for fracture to occur, the energy stored in the structure must be sufficient to overcome the surface energy of the material (Anderson 1995). For a plate subjected to a constant stress,  $\sigma$ , which contains a crack  $2a$  long under plane stress condition, the fracture stress can be presented as:

$$\sigma_f = \left( \frac{2E\gamma_s}{\pi a} \right)^{1/2} \quad (5.1)$$

where,

$E$  = modulus of elasticity,

$\gamma_s$  = surface energy of the material, and

$a$  = half-crack length.

Equation 5.1 is valid only for ideally brittle solids such as ceramics and glass. In such a material, a crack can be formed merely by breaking atomic bonds;  $\gamma_s$  reflects the total energy of broken bonds per unit area. However, when a crack propagates through a metal, dislocation motion occurs in the vicinity of the crack tip, resulting in additional energy dissipation. Irwin (1948) and Orowan (1948) independently modified the Griffith expression to account for materials that are capable of plastic flow, as given by:

$$\sigma_f = \left( \frac{2E(\gamma_s + \gamma_p)}{\pi a} \right)^{1/2} \quad (5.2)$$

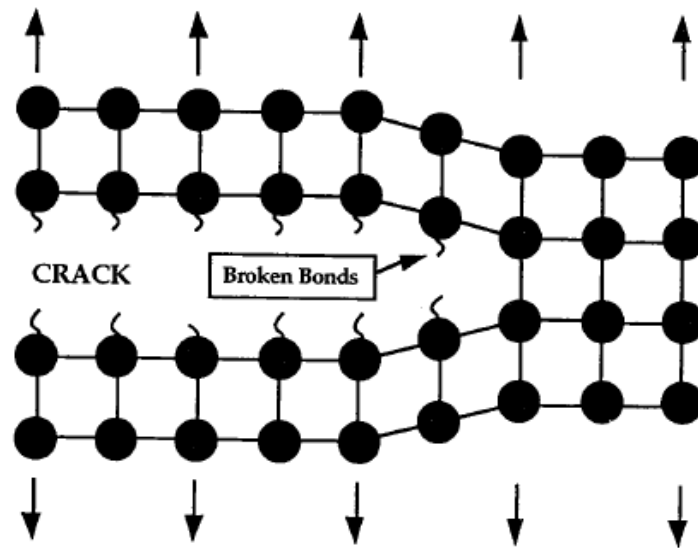
where  $\gamma_p$  is the plastic work per unit area of surface created, and is typically much larger than  $\gamma_s$ .

Therefore, the Griffith model can be generalized to account for any type of energy dissipation:

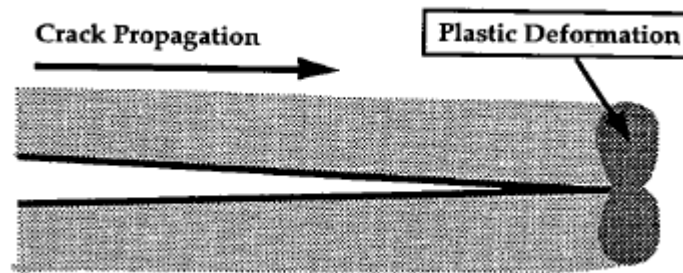
$$\sigma_f = \left( \frac{2Ew_f}{\pi a} \right)^{1/2} \quad (5.3)$$

Where  $w_f$  is the surface fracture energy, which may include the surface energy, plastic work, or other type of energy dissipation associated with a propagating crack. It can consider various materials properties such as plastic, viscoelastic, or viscoplastic properties, and also phenomena such as crack meandering and branching during crack propagation. Figure 5.1 illustrates various types of material behavior and the corresponding fracture energy.

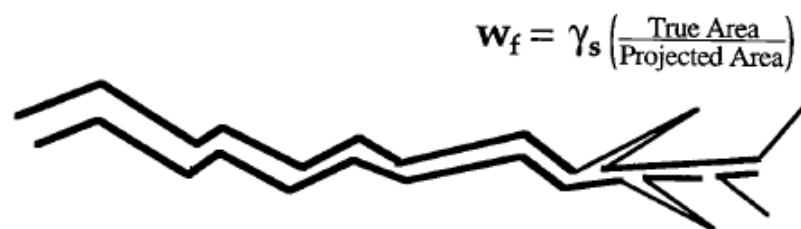
Therefore, considering concrete as a quasi-brittle composite, interfacial fracture energy is more suitable than interfacial surface energy to represent the energy necessary to create a crack along the interface between aggregate and mortar. The results showed later will also indicate this.



(a) Ideally brittle material ( $w_f = \gamma_s$ )



(b) Quasi-brittle elastic-plastic material ( $w_f = \gamma_s + \gamma_p$ )



(c) Brittle material with crack meandering and branching

**Figure 5.1 Crack propagation and fracture energy for materials (Anderson 1995)**

### Formulation of Interfacial Fracture Energy Model

Interfaces which represent discontinuities are intrinsic to the concrete composites, and their structural performance is generally influenced by these interfaces (Mindess 1988). The concrete may be considered as a kind of three-phase composite material with the three phases being hardened cement paste, aggregate and interfacial zone between the hardened cement paste and aggregate. Normally, when concrete fails, there are two modes of failure of the coarse aggregate as shown in Figure 5.2: (a) the crack deflects around the aggregates, i.e., debonding of the coarse aggregate, or (b) the crack penetrates through the aggregates, i.e., rupture of the coarse aggregate. The nature and path of crack propagation illustrated in Figure 5.2. Depending on the strength of the interface relative to the aggregate and to the matrix, a crack will propagate either in mode (a) or (b), producing a different crack roughness. The type of propagation influences the energy consumption and the interlock effects, and has a direct effect on concrete toughness.

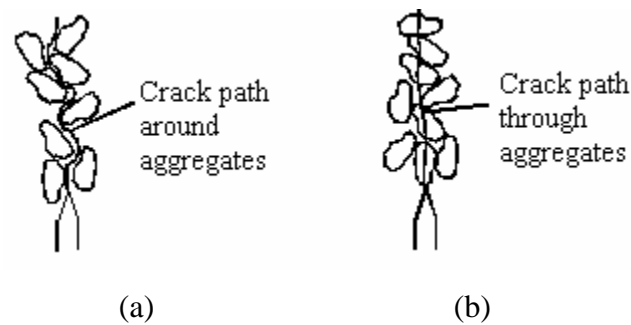


**Figure 5.2 Failure modes of coarse aggregates**

Therefore, interfacial fracture energy between aggregate and mortar which represents the energy necessary to create a crack along the interface can be predicted based on the following equation:

$$G_c \cdot A_{lig} = G_m \cdot A_m + G_a \cdot A_{r-a} + G_i \cdot A_{d-a} \quad (5.4)$$

where,

$G_c$ ,  $G_m$ ,  $G_a$ , and  $G_i$  = fracture energy of concrete, mortar, coarse aggregate and interface,

$A_{lig}$  = ligament area =  $A_m + A_a = A_m + A_{r-a} + A_{d-a}$ ,

$A_m$  = the cracking surface passing through mortar,

$A_{r-a}$  = the cracking surface passing through coarse aggregates, or the surface area of ruptured coarse aggregates, and

$A_{d-a}$  = the cracking surface area of interface, or the surface area of debonding coarse aggregates.

A parameter to represent the failure mode of aggregates along the fracture surface, rupture probability of coarse aggregate (RPCA), was defined as the ratio of the area of ruptured coarse aggregates ( $A_{r-a}$ ) to the total projected area of coarse aggregates ( $A_a$ ) (Wu et al.1999):

$$RPCA = \frac{A_{r-a}}{A_a} = \frac{A_{r-a}}{A_{r-a} + A_{d-a}} \quad (5.5)$$

The higher the RPCA, the more ruptured coarse aggregates and the stronger the interface between aggregate and mortar.

Therefore, Equation 5.4 can be described as:

$$\begin{aligned} G_c &= G_m \cdot \frac{A_m}{A_{lig}} + G_a \cdot \frac{A_{r-a}}{A_{lig}} + G_i \cdot \frac{A_{d-a}}{A_{lig}} \\ &= G_m \cdot \left(1 - \frac{A_a}{A_{lig}}\right) + G_a \cdot \frac{A_{r-a}}{A_a} \cdot \frac{A_a}{A_{lig}} + G_i \cdot \frac{A_{d-a}}{A_a} \cdot \frac{A_a}{A_{lig}} \\ &= G_m \cdot \left(1 - \frac{A_a}{A_{lig}}\right) + G_a \cdot RPCA \cdot \frac{A_a}{A_{lig}} + G_i \cdot (1 - RPCA) \cdot \frac{A_a}{A_{lig}} \end{aligned} \quad (5.6)$$

Stereology is a geometrical statistical tool for an objective quantitative analysis that enables an unbiased estimation of the three dimensional (3D) structural parameters,



such as volume and specific surface area, from observations of lower dimensions (Underwood 1968). Certain important relationships exist connecting the stereological parameters for two dimensional (2D) measurement and the ones for 3D structure. As for structural analysis of material structure, a relevant 2D parameter reflecting the composition aspect is the area fraction of phase of interest ( $A_A$ ), which can be accurately determined from a full section of the structure.  $A_A$  is an unbiased estimator of  $V_V$  for the phase of interest (Hu 2004). Therefore, based on stereological theory, the area ratio in the above equation can be converted to volume ratio as follows.

$$V_V = \frac{V_a}{V_c} = A_A = \frac{A_a}{A_{lig}} \quad (5.7)$$

where,

$V_V$  = volume fraction (volume of feature per unit test volume),

$V_a$  = volume of coarse aggregates, and

$V_c$  = volume of concrete.

Then, Equation 5.6 can be further presented as:

$$G_c = G_m \cdot (1 - V_V) + G_a \cdot RPCA \cdot V_V + G_i \cdot V_V (1 - RPCA) \quad (5.8)$$

The interfacial fracture energy can be defined as:

$$G_i = \frac{G_c - G_m \cdot (1 - V_V) - G_a \cdot RPCA \cdot V_V}{2V_V \cdot (1 - RPCA)} \quad (5.9)$$

Equation 5.9 indicates that the interfacial fracture energy between aggregate and mortar can be back-calculated based on the relation with fracture energy of concrete and mortar.

Digital image analysis (DIA) technique (Wu et al. 1999) can be applied to calculate the length and area of ruptured coarse aggregates, and all coarse aggregates on

the fracture surfaces to calculate the RPCA value based on Equation 5.5. Previous research (Wu et al. 1999, Wu et al. 2002) has indicated that the RPCA can be regarded as an intrinsic parameter that characterizes the strength of concrete determined by both the properties of matrix and aggregate. It depends on the interfacial bond strength and also the aggregate characteristics including the intrinsic strength, size, shape, and also the reactivity of the coarse aggregates. There is a very good correlation between  $K_{IC}$  and RPCA (Wu et al. 2002):

$$K_{IC} = (0.182 + 1.32RPCA) \quad (r = 0.881) \quad (5.10)$$

where,  $K_{IC}$  here is in the unit of  $\text{MPa}\cdot\text{m}^{1/2}$ . After rewriting Equation 5.10, the following equation can be used to predict the RPCA in this study:

$$RPCA = \left( \frac{K_{IC}}{910.0461} - 0.182 \right) / 1.32 \quad (5.11)$$

where,  $K_{IC}$  in Equation 5.11 is in the unit of  $\text{psi}\cdot\text{in}^{1/2}$ .

Fracture energy is defined as the amount of energy required to create a crack of one unit of area. Sometimes it is also called the critical strain energy release rate or toughness (Pettersson 1980). The critical stress intensity factor (or fracture toughness) is a measure of the magnitude of the stress concentration which exists in front of the crack tip when the crack starts to propagate. The relation between fracture energy and fracture toughness can be expressed as (Knott 1973):

$$K_C = \sqrt{G_C E} \quad (5.12)$$

where,  $E$  is the Young's modulus, and sub C in  $K_C$  and  $G_C$  here represents 'critical'. Therefore,  $G_c$  and  $G_m$  in Equation 5.9 can be back-calculated once their Young's moduli and fracture toughness values are known. As described in previous chapters, variable-

notch one-size split-tensile test is applied to calculate the fracture toughness values of concrete and mortar. Young's modulus  $E$  can be calculated indirectly from the compressive strength using the ACI Building Code formula (ACI 1996):

$$E = 57,000(f_c')^{1/2} \quad (5.13)$$

where,  $f_c'$  is the compressive strength in units of psi. As for  $G_a$  values in the model, they are not equivalent to two times the surface free energies of the aggregates ( $2\gamma_i$ ) due to the same reason pointed out in the previous section regarding the interfacial surface energy and fracture energy. Instead, those values are referenced to a database of fracture mechanics parameters for rocks (Atkinson 1987, Lin 1998).

In addition, the relation between volume of coarse aggregates in the concrete,  $V_a$ , and yield of concrete,  $V_c$ , can be described as:

$$V_a = \frac{W_a}{BSG \cdot \gamma_w} = \frac{CAF \cdot V_c \cdot DRUW}{BSG \cdot \gamma_w} \quad (5.14)$$

where,

$W_a$  = coarse aggregate amount in mass,

$BSG$  = bulk specific gravity of coarse aggregate,

$CAF$  = coarse aggregate factor,

$DRUW$  = dry-rodded unit weight of coarse aggregate, and

$\gamma_w$  = unit weight of water = 62.4 lb/in<sup>2</sup>.

Therefore, the following equation

$$V_V = \frac{V_a}{V_c} = \frac{CAF \cdot DRUW}{BSG \cdot \gamma_w} \quad (5.15)$$

relates  $V_V$  to the physical properties of coarse aggregates.

Overall, Equations 5.9, 5.11, 5.12, 5.13, and 5.15 are proposed as a formulation of aggregate-mortar interfacial surface energy inherently, incorporating aggregate failure modes and concrete, mortar and coarse aggregate properties.

## Results and Analysis

Various experimental factors (as shown in Table 5.1) were considered to investigate the development of fracture energy on the mortar-aggregate interface at early ages.

**Table 5.1 Experimental parameters for interfacial fracture energy investigation**

Experimental parameters	Levels	
Time	3	1-day, 3-day, 7-day
Aggregate type	2	VG, GL
W/cm	3	0.4, 0.42, 0.45
Cement factor	2	5.5, 6
% ultra-fine fly ash replacement	4	0, 8%, 15%, 20%
Curing method	3	WMC, NCC, WOC

### *Comparison between VG and GL*

Figure 5.3 shows RPCA development of concretes made with both aggregates, keeping other design parameters constant (i.e.  $w/cm = 0.40$ ,  $CF = 6$ , and WOC). The results were also correlated with analysis of fracture surface area of specimens by Senadheera and Zollinger (1995). With time, the RPCA increases, which indicates that the mortar-aggregate bond becomes stronger, causing more aggregates to rupture. Research conducted by Guinea et al. (2002) also showed similar results. In addition, due to different fracture energies of these two aggregates, there is a large difference in

aggregate failure modes. VG is “harder” with a fracture energy of 35 N/m, while GL is “softer” with a fracture energy of 15 N/m. Therefore, especially at very early ages, most of VG aggregates debond (as shown in Figure 5.3), while most of GL aggregates rupture. As a result, when the load is applied, these two different concretes present different crack paths and associated different energies released.

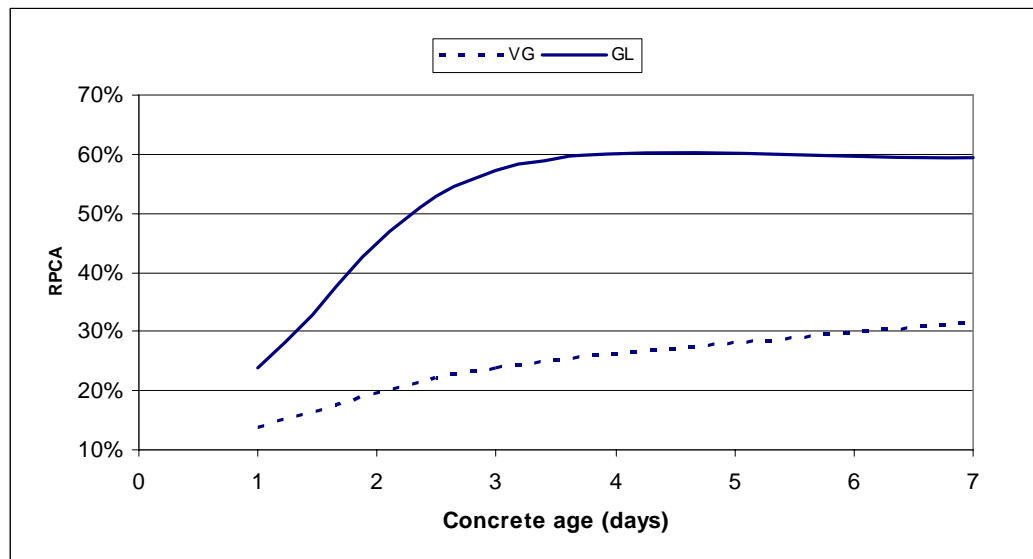


**Figure 5.3 RPCA of two aggregates**



**Figure 5.4 Fracture surface of concrete with VG**

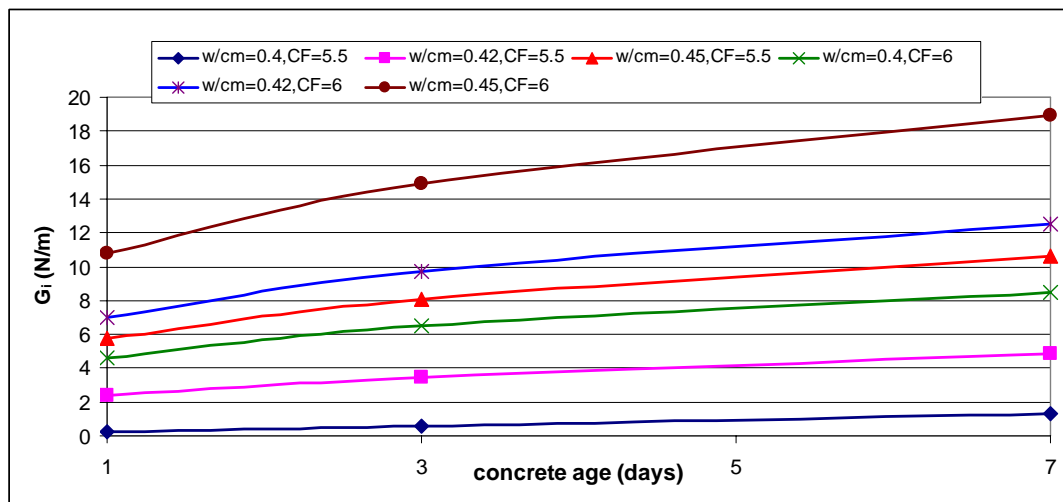
Table 5.2 compared the interfacial fracture energies of concretes made with two different aggregates, calculated based on Equations 5.9, 5.11, 5.12, 5.13, and 5.15. Other design parameters were kept constant (i.e.  $w/cm = 0.42$ ,  $CF = 6$ , and  $WMC$ ). It can be seen that at each age, the interfacial fracture energy of concrete made with GL was much higher than that made with VG, which indicated that much higher energy is required (or needed) to create a new unit surface area of interface for concrete made with GL than concrete made with VG. In addition, once a crack initiates, it propagates along path which requires the lowest energy consumed. Therefore, VG prefers failure mode a (i.e. the crack deflects around the aggregates), and GL prefers failure mode b (i.e. the crack penetrates through the aggregates) as shown in Figure 5.2.

**Table 5.2 Comparison of interfacial fracture energies**

Concrete age (days)	$G_{i\_VG}$ (N/m)	$G_{i\_GL}$ (N/m)
1	6.98	37.28
3	9.70	37.42
7	12.51	48

### *Effects of Cementitious Factors*

Figure 5.5 illustrates the development of interfacial fracture energy of different concretes made with VG but with different w/cms and cement factors. For all concretes, interfacial fracture energy of concrete increases with the time. In addition, at all age of concrete made with same aggregate, interfacial fracture energy increases with w/cm and cement factor.

**Figure 5.5 Effects of material factors on interfacial fracture energy**

From the point of view of the concrete failure process, aggregates affect crack propagation through two ways: 1) by creating and initiating cracks; and 2) by arresting the propagation of cracks. For normal concrete, aggregates are stronger than the matrix. If a crack starts to spread under a given load from a pore in the matrix or from an interface there is a chance that it may be blunted by an aggregate and then will be stopped, as schematically shown in Figure 5.6.

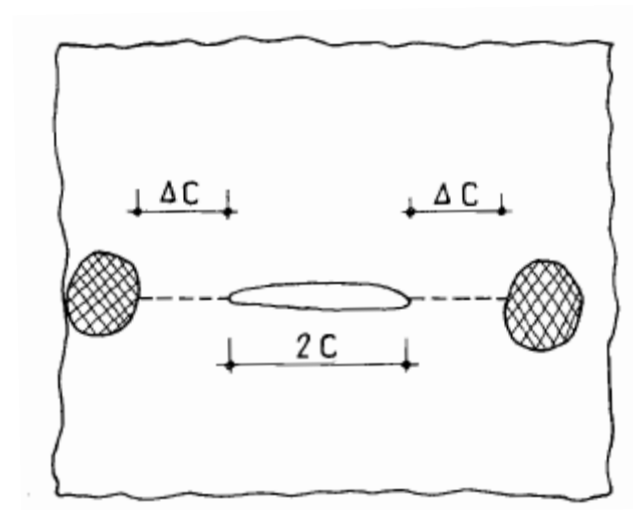


**Figure 5.6 Schematic representation of crack blunting (Wittmann 1983)**

$2c_m$  is assumed to be the length of the initial crack in the matrix. Once the stress level reaches  $\sigma_m$ , the crack will spread in an unstable way according to:

$$\sigma_m = \sqrt{\frac{2E\gamma_m}{\pi c_m}} \quad (5.16)$$



$\gamma_m$  denotes the fracture surface energy of the matrix, and  $2\gamma_m$  denotes the fracture energy of the matrix. Assuming the crack meets an aggregate when it has grown by  $\Delta C$ , at the crack tip the condition for further crack growth has now changed:

$$\sigma_A = \sqrt{\frac{2E\gamma_A}{\pi(c_m + \Delta C)}} \quad (5.17)$$

In Equation 5.17,  $\gamma_A$  stands for the fracture surface energy of the aggregate. In normal concrete,  $\gamma_A$  is higher than  $\gamma_m$  and therefore the resulting curve is shifted towards the right as shown in Figure 5.7. In this case, the crack runs from point  $P_1$  and is arrested at point  $P_2$ . From point  $P_2$  to point  $P_3$ , if the load is increased to  $\sigma_A$ , the crack will propagate through the aggregate. Normally the energy required for the crack to circumvent the aggregate is less than that for the crack to penetrate the aggregate. Therefore, in most of cases, before the load is reached to  $\sigma_A$ , the crack will already have propagated around the aggregate. Therefore, according to this crack arresting mechanism, this type of crack path absorbs more energy (or increases interfacial fracture energy) than that of penetrating the aggregate by increasing the tortuosity of the crack path which 1) increases the length of crack extension, and 2) deflects the direction of crack propagation.

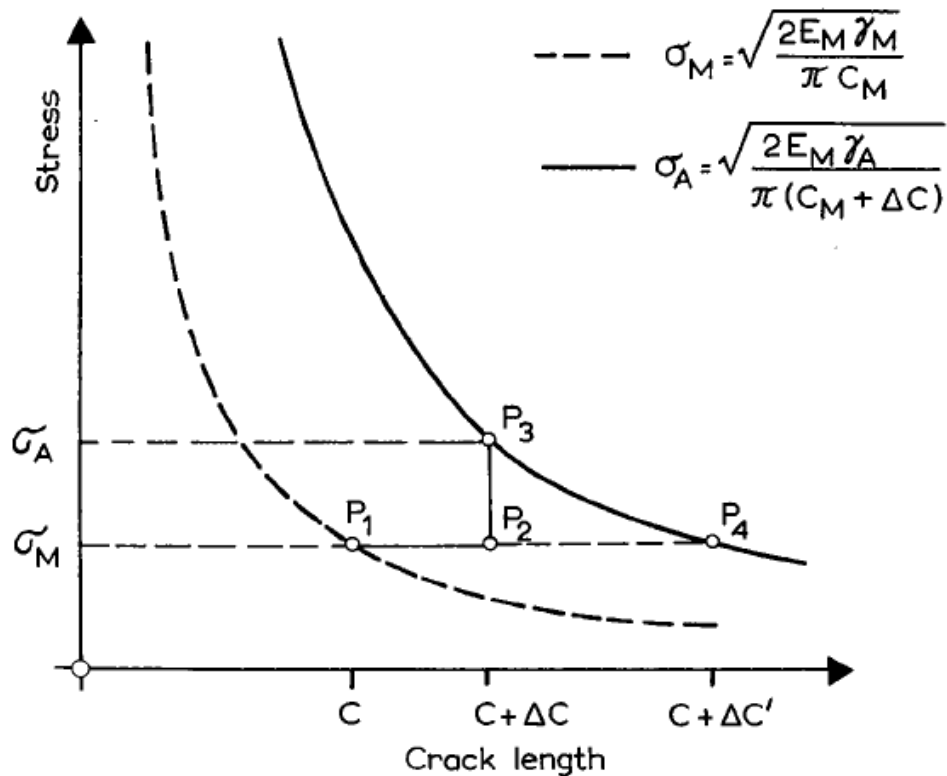


**Figure 5.7 Schematic representation of Equations 5.16 and 5.17 (Wittmann 1983)**

Immediately after pouring and before hardening, sedimentation (bleeding) takes place. This process causes water filled pockets under coarse aggregates, which are most likely the initiation of horizontal cracks (Wittmann 1983). As shown in Figure 5.5, for concrete made with same aggregate type and same cement factor, the increase of  $w/cm$  results in an increase of the water content in concrete. Therefore, concrete with higher  $w/cm$  has more water accumulated under the aggregates than that with lower  $w/cm$ , which results in more cracks and defects along the interface and more energy consumed, leading to higher ductility. In a similar manner, for concrete made with same aggregate type and same  $w/cm$ , an increase of the cement factor also results in an increase of water content in concrete. Therefore, concrete with a higher cement factor has more cracks and

defects along the interface and higher interfacial fracture energy than that with lower cement factor.

*Fracture Energy of Interface, Concrete and Matrix*

The relationship among fracture energy of interface, concrete, and mortar were also investigated for concretes made with different types of aggregates, as summarized in Table 5.3. It can be seen that the interfacial fracture energy can be linearly related to both concrete and mortar fracture energy for concretes made with different aggregates.

**Table 5.3 Regression analysis of interfacial fracture energy**

Concrete made with “harder” aggregates (such as VG): $G_i = 1.9445G_c - 1.5871G_m - 0.505$ ( $R^2 = 0.98$ )			
Predictor	Coefficient	t Stat	P-value
Constant	-0.505	-0.879	0.393
$G_c$	1.9445	30.688	$5.95 \times 10^{-15}$
$G_m$	-1.5871	-21.352	$1.22 \times 10^{-12}$
Concrete made with “softer” aggregates (such as GL): $G_i = 5.3151G_c - 0.8343G_m - 44.74$ ( $R^2 = 0.99$ )			
Predictor	Coefficient	t Stat	P-value
Constant	-44.74	-8.271	$1.69 \times 10^{-4}$
$G_c$	5.3151	23.888	$3.53 \times 10^{-7}$
$G_m$	-0.8343	-1.101	0.313

Both equations in Table 5.3 show high t values and low P values for the coefficients of  $G_c$  and  $G_m$ , indicating the high significance of regression relations.  $G_i$  increases with the increase of  $G_c$  and the decrease of  $G_m$ . Previous research including three-point bending test of notched mortar-aggregate interface beam by Wong et al. (1999), aggregate push out test by Mitsui et al. (1994), and the wedge splitting test by

Tschegg et al. (1995) showed that the interfacial fracture energy was only about 10% of the corresponding mortar fracture energy. However, the results in this study showed that the ratio of interfacial fracture energy to mortar fracture energy ranged from 0.04 to 11.17. This is because that concretes investigated in the previous research are at their later ages (from 28-day to 90-day), at which concretes are fully developed; while early ages of concretes (from 1-day to 7-day) were focuses of this study. Typically at an early age of concrete, the strengths of concrete and cement mortar are not fully developed, and the fracture energies of interface, mortar and concrete are much lower than those at late ages. In addition, the development of these parameters with the time was different, and also varied with different material combinations. The fracture resistance of the interface is lower than that of the bulk paste due to micro-cracks in the ITZ initiating and propagating around the aggregates.

Figure 5.8 shows a linear relation between  $G_i$  and  $G_c$ . In Chapter IV, a utility curve was developed to relate the fracture toughness of concrete to the overall effects of material, construction, and time factors on bonding performance. Therefore, based on the relation as presented in Figure 5.8, the interfacial fracture energy can be predicted once a design combination is known. Though further validation is needed, the approach described in this section builds the connection between concrete properties at the meso-level (represented by the interfacial fracture energy between aggregate and mortar) and at the macro-level (represented by fracture toughness of concrete and significant influencing materials and construction factors).

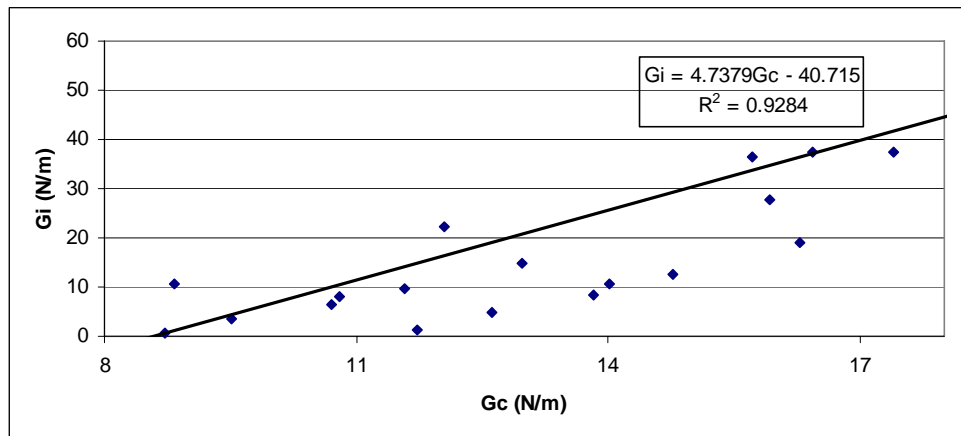


**Figure 5.8 Linear relation between  $G_i$  and  $G_c$**

## **DELAMINATION OCCURRENCE PREDICTION**

During the first three days after paving the moisture gradients near the surface of the pavement slab can actually generate stresses large enough to create delaminations in the concrete. It is possible to predict early age delamination in the concrete. In this study, a fracture mechanics based approach is illustrated facilitated by numerical analysis to predict the time when delamination would occur. As described in previous chapters, one necessary condition for delamination to develop is the sufficient evaporation of pore water from the hydrating concrete resulting in differential drying shrinkage near the pavement surface. As a consequence of its dominating effect, the nature of the moisture profile in hardening concrete particularly near the evaporative surface was also considered in this prediction protocol.

### **Criterion for Delamination Occurrence**

Stress intensity and fracture toughness are key fracture mechanics parameters that can be used by materials engineers and designers in design analysis (Boresi et al. 1993; Irwin 1957; Hertzberg 1976). By comparing  $K$  (stress intensity factors) and  $K_C$  (critical stress

intensity factor or fracture toughness) directly, one can then determine the crack stability based on fracture criteria for unstable growth of the material under given loading conditions. In the previous chapters, fracture toughness was used to represent the nature of the interfacial bond between the aggregate and mortar relative to delamination. Therefore, it appears to be feasible to predict the occurrence of delamination by comparing the development of  $K$  and  $K_C$ .

An early experimental study on the measurement of the fracture toughness of mortar-aggregate interfaces in concrete was performed by Hillemeier and Hilsdorf (1977). They reported test results for cases involving mode I loading conditions. However, the crack along the aggregate-matrix interfaces may have been caused either by tensile or by shear stresses or by combinations of tensile and shear stresses (Taylor and Broms 1964). Büyüköztürk and Lee (1993) stated that cracking of mortar-aggregate interfaces involves mixed mode fracture effects due to the difference in the properties between mortar and aggregate, as well as due to loading conditions, which means that the stress field in the vicinity of the crack front is defined not only by the stress intensity factor  $K_I$ , but also by  $K_{II}$  (Richard et al. 2005). In this case, plane mixed mode conditions are characterized by the superposition of the fracture modes I and II. As can be seen in Figure 5.9, the beginning of unstable crack growth can be described by a fracture limit curve. If the loading condition on a crack in a structure corresponds to the point P, no unstable crack growth is to be expected. If in contrast to this, the load level increases in such a way, which, for example point C of the fracture limit curve is reached, immediate unstable crack growth will occur.

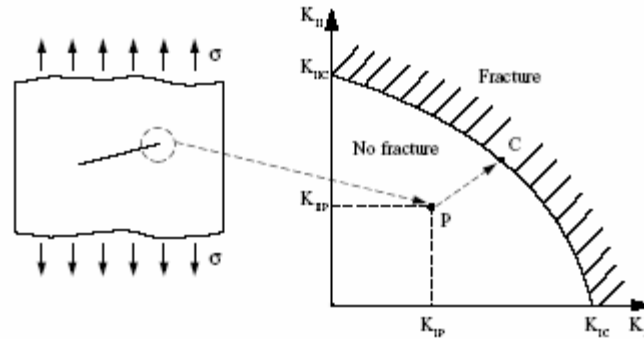


**Figure 5.9 Fracture limit curve (Richard et al. 2005)**

However, different researchers have different opinions about this. Previous research (Tan et al. 1995) showed that for the same interfaces the specific fracture energy in shear (mode II) is an order of magnitude higher than in tension (mode I). Since interfacial cracking precedes bulk cracking, initiation of interfacial cracks in mode I is the critical step for failure. The mode II fracture energy is found to be far larger than the mode I fracture energy (Bažant and Pfeiffer 1987), and the critical stress intensity factor  $K_{IC}$  is about a fifth of  $K_{IIC}$ , which means that  $G_{IIF}$  is about 25 times as large as  $G_{IF}$  (Ozbolt et al. 1999). In addition, the predicted values of mode II stress intensity factor ( $K_{II}$ ) were much smaller than those of mode I stress intensity factor ( $K_I$ ), which will be shown later. Therefore, in our study, the crack initiation in mode I was thought as the predominant type. Then the criterion for predicting early age delamination occurrence is that delamination occurs when  $K > K_{IC}$ .

Till now, many methods have been adopted to compute  $K$ , such as finite element method, boundary element method, and finite difference method, etc. Among these, finite element method is the most popular one. In this study, finite element software packages — Temperature and Moisture Analysis of Curing Concrete (TMAC<sup>2</sup>) (Jeong 2003) and ABAQUS (2003) were applied to predict the development of  $K$ .

## Concrete Moisture Diffusivity Profiles

The nature of the moisture profile in hardening concrete particularly near the evaporative surface and the associated drying shrinkage are subjects of great interest relative to their effects on the formation of early aged delamination at cracks and joints in concrete pavements. Moisture flow and diffusion in concrete have been a significant topic in the research of concrete pavement materials (Bazant and Najjar 1972; Parrott 1988; Parrott 1991; Xin et al. 1995; Buch and Zollinger 1993).

In freshly placed concrete, moisture movements are typically characterized by high rates of diffusion followed by gradually lower rates 10 to 12 hours after placement. This drying characteristic is inherently related to a material property referred to as the moisture diffusivity ( $D$ ) which has been generally accepted to be dependent upon the pore water content within the cement paste. It has been observed that moisture diffusivity may change significantly with variations in the moisture content or the relative humidity (from 100 to 70 percent) of the concrete (Pihlajavaara 1964; Kasi and Pihlajavaara 1969; Bazant 1970; Bazant and Najjar 1972). At constant water content ( $w$ ), moisture diffusivity changes little with time in mature concrete in contrast with the dramatic changes fresh concrete undergoes during the first 24 hours after placement. In this regard, diffusivity in early-aged concrete is not only a function of humidity but also of concrete age and porosity. The moisture diffusivity is important in modeling moisture flow in hardening concrete.

The rate of moisture flow through concrete can be expressed by the velocity of flow ( $J$ ) representing the mass of evaporable water passing through a unit area perpendicular to the direction of flow per unit time. The velocity of flow by Darcy's law is derived from energy gradients (Bazant and Najjar 1972):

$$J = -C \cdot \text{grad } \mu \quad (5.18)$$



where,  $\mu$  is Gibb's free energy (GFE) per unit mass of evaporable water and the coefficient  $C$  characterizes the permeability of porous concrete. Equation 5.18 is restricted to small energy gradients and laminar flow conditions. Assuming water vapor behaves as an ideal gas, Gibb's free energy is (Bazant and Najjar 1972):

$$\mu = \left( \frac{RT}{MV_w} \right) \cdot \ln H + \mu_{sat}(T) \quad (5.19)$$

where,

$R$  = universal gas constant (8.3143 J/mol<sup>o</sup>K),

$T$  = absolute temperature (°K),

$M$  = molecular weight of water (18.015 g/mol),

$V_w$  = specific volume of water (1 cm<sup>3</sup>/g),

$H$  = humidity of concrete  $\left( = \frac{RH}{100} \right)$ , and

$RH$  = relative humidity of concrete (%)

Equation 5.18 can be rewritten in terms of temperature (T) and humidity (H) of concrete as (Bazant and Najjar 1972):

$$J = -c \cdot grad H \quad (5.20)$$

where the coefficient  $c$  is permeability as a function of temperature and humidity of concrete as below:

$$c = \left( \frac{RT}{MV_w} \right) \times \left( \frac{C}{H} \right) \quad (5.21)$$

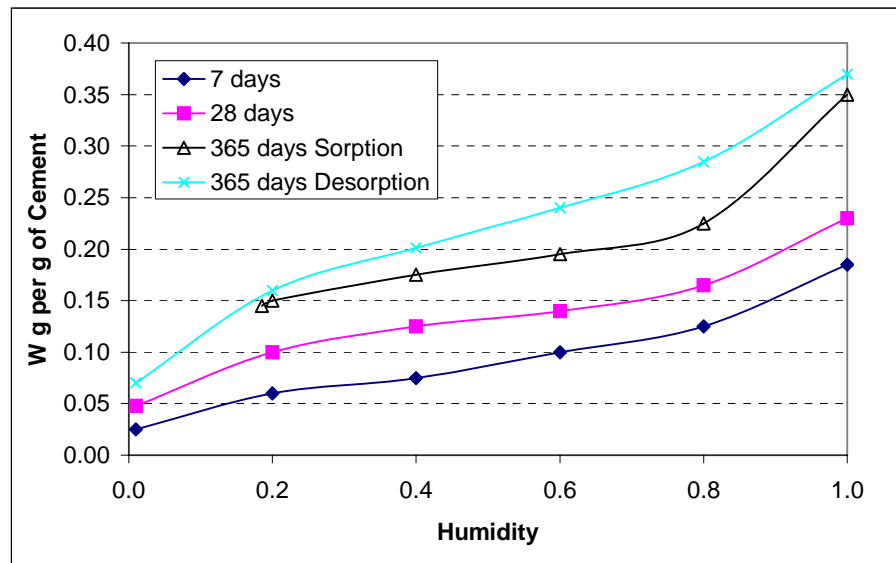


**Figure 5.10 Example of desorption-sorption isotherms of cement paste, established by powers (Bazant 1970)**

The relationship between humidity and water content within concrete at a constant temperature and the degree of hydration is described by desorption or sorption isotherms as illustrated in Figure 5.10 (Bazant and Najjar 1972). It should be noted that the isotherm for sorption is different from the isotherm for desorption. This characteristic may be due to the various states of equilibrium of the pore water. An investigation by Parrott (1988) implied the significance of porosity with respect to the position of the desorption or sorption isotherm within concrete. The results indicated that a greater amount of moisture loss in drying concrete would occur in regions nearest to exposed drying surfaces which may be also regions of greater porosity. Therefore, it can be explained that there is a greater volume of coarse pores at positions nearer to an exposed concrete surface and consequently the relationship between weight loss and relative humidity of concrete will vary with distance from the exposed surface. In this respect, the performance and behavior of a concrete pavement may be affected by the porosity of the surface. It should also be noted that the resulting desorption isotherm at any time during hydration of hardening slab concrete must be interpreted not only as a

function of the degree of hydration, but also as a function of porosity. At a given porosity, the desorption isotherm may be expressed in the differential form as (Bazant and Najjar 1972):

$$dH = kdw \quad (5.22)$$

$$k = \left( \frac{\partial H}{\partial w} \right)_w \quad (5.23)$$

where the parameter  $k$  represents the slope of the moisture isotherm where the mass of water ( $w$ ) is described as a function of humidity ( $H$ ). Moisture movements in an unsaturated porous medium is effected by temperature profiles of the medium (Huang 1979; Suh et al. 1988; Somasundaram et al. 1989). Thus, the calculation of humidity in hydrating concrete requires additional terms under variable temperature conditions as (Bazant and Najjar 1972):

$$dH = kdw + KdT + dH_s \quad (5.24)$$

where,

$K$  = hygrothermic coefficient ( $= \left( \frac{\partial H}{\partial T} \right)_w$ ), and

$dH_s$  = change in humidity ( $H$ ) due to hydration at a constant water content ( $w$ ) and time ( $t$ ).

The hygrothermic coefficient represents the change in humidity due to one degree of change in temperature at a constant water content and a given level of hydration. It should be noted that the pore water content ( $w$ ) includes both the evaporable or capillary water ( $w_c$ ) and the non-evaporable water ( $w_n$ ) per unit volume of materials.

The rate of moisture flow in unit volume of concrete is determined from:

$$\frac{\partial w}{\partial t} = -\text{div}J \quad (5.25)$$

Substituting Equation 5.20 into Equation 5.25 and subsequently substituting Equation 5.25 into Equation 5.24 leads to:

$$\frac{\partial H}{\partial t} = k \cdot \text{div}(c \cdot \text{grad}H) + \frac{\partial H_s}{\partial t} + K \frac{\partial T}{\partial t} \quad (5.26)$$

which is the diffusion equation for the drying concrete under variable temperature conditions. Equation 5.26 is further developed to be Equation 5.27.

$$\frac{\partial H}{\partial t} = kc \frac{\partial^2 H}{\partial x^2} + k \frac{\partial c}{\partial x} \frac{\partial H}{\partial x} + \frac{\partial H_s}{\partial t} + K \frac{\partial T}{\partial t} \quad (5.27)$$

Permeability ( $c$ ) is also a function of the porosity and indirectly a function of position  $x$ . Because permeability change with position  $x$  is assumed to be very small, the second term in the equation 5.27 is considered to be negligible and is consequently dropped from the diffusion equation as:

$$\frac{\partial H}{\partial t} = D \frac{\partial^2 H}{\partial x^2} + \frac{\partial H_s}{\partial t} + K \frac{\partial T}{\partial t} \quad (5.28)$$

where  $D (= k \cdot c)$  is moisture diffusivity ( $L^2/t$ ).

### **Governing Differential Equations**

Drying shrinkage occurs as a result of evaporation of pore water to the surrounding environment; however it is probably the least widely recognized cause of volume change

in concrete paving. Stress occurs when the shrinkage is restrained. Though temperature variation is also a factor in the delamination development, this study specifically focused on early-age concrete behavior associated with volumetric contraction due to moisture induced shrinkage. Delamination is caused by differential drying shrinkage induced stress. The drying process is mainly related to the moisture variation in concrete. Whether delamination occurs or not is mainly related to this stress level in concrete. Therefore, in this study, early-age concrete subjected to moisture induced shrinkage was modeled as an isotropic, time-dependent material subjected to coupled hygro-mechanical loading conditions.

For two-dimensional problems we consider three strain components, namely,

$$\varepsilon_x = \frac{\partial u}{\partial x} \quad (5.29)$$

$$\varepsilon_y = \frac{\partial v}{\partial y} \quad (5.30)$$

$$\gamma_x = \frac{\partial v}{\partial x} + \frac{\partial u}{\partial y} \quad (5.31)$$

The relations between the components of stress and the components of strain are presented as:

$$\varepsilon_x = \frac{1}{E_1} (\sigma_x - \nu_1 \sigma_y) + (1 + \nu_1) \alpha H \quad (5.32)$$

$$\varepsilon_y = \frac{1}{E_1} (\sigma_y - \nu_1 \sigma_x) + (1 + \nu_1) \alpha H \quad (5.33)$$

$$\gamma_{xy} = \frac{2(1+\nu_1)}{E_1} \tau_{xy} \quad (5.34)$$

Compared with original Hooke's law, there is one more term at the right side of Equation 5.32 and 5.33, which is the strain component due to the moisture variation.

The differential equations of equilibrium for two-dimensional problems are (Timoshenko and Goodier 1970):

$$\frac{\partial \sigma_x}{\partial x} + \frac{\partial \tau_{xy}}{\partial y} + X = 0 \quad (5.35)$$

$$\frac{\partial \sigma_y}{\partial y} + \frac{\partial \tau_{xy}}{\partial x} + Y = 0 \quad (5.36)$$

Converting Equation 5.32, 5.33, and 5.34 to equations represented by displacement components, then substituting them into Equations 5.29, 5.30, and 5.31, and subsequently substituting into Equation 5.35 and 5.36, the equilibrium equations are finally developed as:

$$\frac{\partial}{\partial x} \left( \frac{E}{(1+\nu)(1-2\nu)} \left( (1-\nu) \frac{\partial u}{\partial x} + \nu \frac{\partial v}{\partial y} \right) \right) + \frac{\partial}{\partial y} \left( \frac{E}{2(1+\nu)} \left( \frac{\partial u}{\partial y} + \frac{\partial v}{\partial x} \right) \right) + \frac{\alpha E}{(1-2\nu)} \frac{\partial H}{\partial x} + X = 0 \quad (5.37)$$

$$\frac{\partial}{\partial x} \left( \frac{E}{2(1+\nu)} \left( \frac{\partial u}{\partial y} + \frac{\partial v}{\partial x} \right) \right) + \frac{\partial}{\partial y} \left( \frac{E}{(1+\nu)(1-2\nu)} \left( \nu \frac{\partial u}{\partial x} + (1-\nu) \frac{\partial v}{\partial y} \right) \right) + \frac{\alpha E}{(1-2\nu)} \frac{\partial H}{\partial y} + Y = 0 \quad (5.38)$$

where,

- E = elastic modulus of concrete,
- $\nu$  = Poisson's ratio of concrete,
- $\alpha$  = coefficient of shrinkage, and

$H$  = relative humidity of concrete.

For two-dimensional analysis, Equation 5.28 is converted to

$$\frac{\partial H}{\partial t} = D \left( \frac{\partial^2 H}{\partial x^2} + \frac{\partial^2 H}{\partial y^2} \right) + \frac{\partial H_s}{\partial t} + K \frac{\partial T}{\partial t} \quad (5.39)$$

If the dry bulb temperature,  $T$ , used in Equation 5.39 is assigned a constant temperature value (though it is not a realistic assumption), the third item in the right side of the equation will become zero, simplifying Equation 5.39 to:

$$\frac{\partial H}{\partial t} = D \left( \frac{\partial^2 H}{\partial x^2} + \frac{\partial^2 H}{\partial y^2} \right) + \frac{\partial H_s}{\partial t} \quad (5.40)$$

If the humidity change due to self-desiccation is assumed to be insignificantly small, Equation 5.40 reduces to:

$$\frac{\partial H}{\partial t} = D \left( \frac{\partial^2 H}{\partial x^2} + \frac{\partial^2 H}{\partial y^2} \right) \quad (5.41)$$

Equation 5.37, 5.38 and 5.41 are governing equations used in this analysis. The third term on the left side of Equations 5.37 and 5.38 indicate that the relative humidity of the concrete influences the force equilibrium of the concrete by strains due to shrinkage or swelling. The proportionality between drying shrinkage and the decrease of pore humidity is dictated by the coefficient of shrinkage, which is analogous to the coefficient of thermal expansion, and it is equivalent of the ultimate shrinkage (Lim 2002).

It has been noted that there are some similarities between the coupled thermal stress problem and the coupled hygro-mechanical stress analysis warranted by dimension analysis and comparison, though time dependency is not addressed (Zhang 2004). For example, the relative humidity is corresponding to the temperature and the moisture diffusivity is corresponding to the thermal conductivity. Heat transfer and the

coupled thermal stress have been studied in the mechanical engineering for decades. Some methods for conducting this type of analysis are already well-established and a lot of commercial software packages, for examples, ABAQUS, and ANSYS have provided options to solve the differential equations numerically. Therefore, the program specifically for the coupled thermal stress approach in ABAQUS was used for the coupled hygro-mechanical stress analysis. Considering the time-dependency of E, H, and D in the above equations, subroutines were developed to facilitate the input and updating of those parameters.

### **Numerical Study**

Although the definition of the term early-age is somewhat arbitrary, the analysis of drying and stress development was conducted up to about 7 days (604800 seconds). Figure 5.11 shows the typical geometry and finite element mesh of the pavement section studied, and the mechanical boundary conditions are also shown. The concrete slab was 0.3-meter (12-in) thick. Due to the symmetry of the pavement structure, a 1-meter (3.3-ft) of length was chosen. The finite element analyses were made with the ABAQUS program using rectangular mesh of 4-node quadrilateral elements. Full bond between concrete slab and foundation was modeled by fixing displacements in all directions. Only vertical displacements were allowed for the left and right side of the structure, since the section was considered as a part of the whole pavement. For some cases, the concrete slab was also notched to simulate the sawcut effects, with a notch width of 4 mm.

The ABAQUS program offers the contour integral method for the evaluation of stress intensity factors, which means that in a finite element model each evaluation can be thought of as the virtual motion of a block of material surrounding the crack tip. Each such block is defined by contours: each contour is a ring of elements completely surrounding the crack tip or crack front from one crack face to the opposite crack face. The beginning of unstable crack growth as well as the crack growth direction can be



determined by the use of one of fracture criteria (Erdogan and Sih 1963; Sih 1974; Bilby and Cardew 1975). Here, the criterion of energy release rates by Nuismer (1975) was chosen for calculating the direction of cracking initiation.

At the time of concrete placement, a concrete mixture is assumed to be completely wet. Therefore, the initial boundary condition was as follows:

$$H = 1.0 \text{ at } t = 0 \quad (5.42)$$

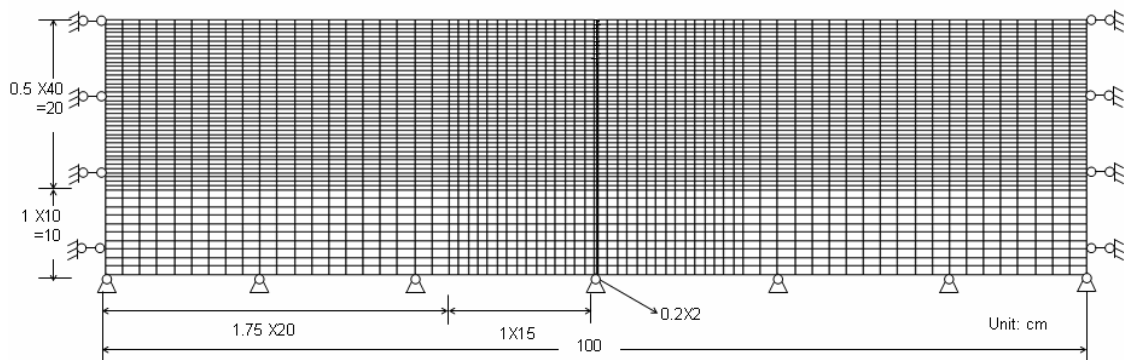


**Figure 5.11 Geometry and mesh of modeling**

The stress intensity factor at an early age was investigated by incorporating distribution and history of moisture relative to the material-related moisture transport property in the analysis. Since the moisture differences between ambient conditions and those inside the concrete cause moisture to migrate from the concrete to the surrounding atmosphere. Hence, the boundary conditions were the humidity histories at the surface and bottom of the concrete slab.

TMAC<sup>2</sup> program, a finite element program developed by TTI, produces the temperature and moisture profiles and accounts for the interaction between them at any points in a hydrating concrete slab as a function of time and ambient boundary conditions (Jeong 2003). The input data include climatic parameters, mix design,

materials properties, parameters for hydration, and construction parameters. The finite element mesh of TMAC<sup>2</sup> has total 120 rectangular elements (5 columns × 24 rows) with 539 nodal points (9 nodal points per each element). This program was used to predict the humidity histories, with the assumption that the humidity at concrete surface has been assumed to be the same as the humidity of ambient condition during the analysis period. Figure 5.12 shows an example of relative humidity trends at the bottom and the surface of the slab estimated from TMAC<sup>2</sup> program.

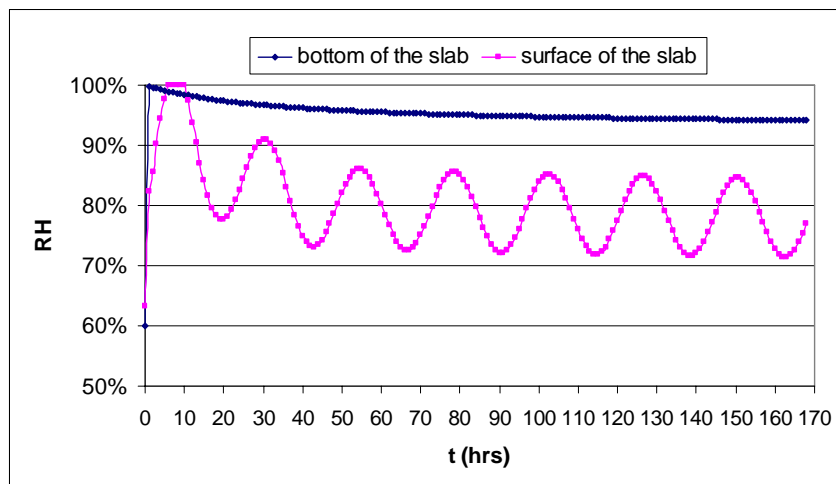


**Figure 5.12 Relative humidity trends from TMAC<sup>2</sup>**

A typical Poisson's ratio of 0.15 was used for the concrete. The history of elastic modulus of concrete was converted from that of compressive strength based on their relationship from the ACI building code formula (Equation 5.13) (ACI 1996), where compressive strength data were obtained from laboratory testing. The coefficient of shrinkage, equivalent of the ultimate shrinkage, was determined by the BP model (Bazant and Panula 1978):

$$\alpha = \varepsilon_{ult-shr} = 1330 - 970y \quad (5.43)$$

where,

$$y = (390z^{-4} + 1)^{-1}$$

$$z = 0.381\sqrt{f'_{cyl28}} \left[ 1.25\sqrt{\frac{a}{cm}} + 0.5\left(\frac{g}{s}\right)^2 \right] \sqrt[3]{\frac{1 + \frac{s}{cm}}{\frac{w}{cm}}} - 12$$

$\frac{a}{cm}$  = total aggregate/cementitious ratio,

$\frac{g}{s}$  = coarse Aggregate/fine aggregate,

$\frac{s}{cm}$  = fine aggregate/cementitious ratio,

$\frac{w}{cm}$  = water/cementitious ratio, and

$f'_{cyl28}$  = 28-day compressive strength of concrete (ksi).

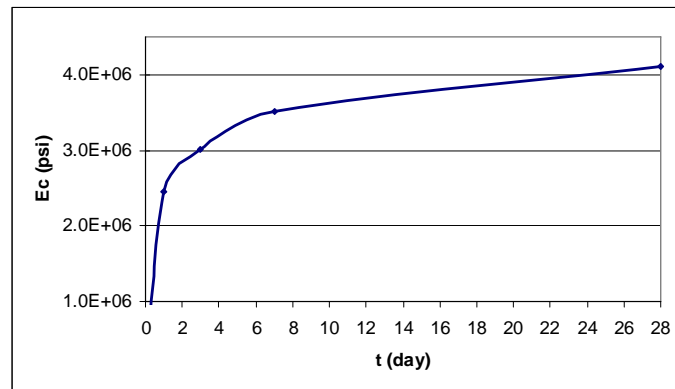
Three Subroutines (i.e., USDFLD, UMAT and UMTHT) were developed to facilitate the numerical analysis. Because all material properties used in the analysis were time dependent, USDFLD was used to obtain stress, strain and relative humidity from previous calculation step. UMAT was used to update the stiffness matrix of the FEM simulation and UMTHT was used to update the corresponding moisture diffusivity matrix during the simulation.

### **Example of Stress Intensity Factor Development**

An example of typical concrete with material characteristics shown in Table 5.4 was selected for analysis purposes. The development of the concrete elastic modulus is illustrated in Figure 5.13.

**Table 5.4 Material parameters in the example analysis**

Parameters	w/cm	Cement factor	a/cm	g/s	s/cm	$f'_{cyl28}$ (ksi)	$\alpha$ (micro-strain)
	0.45	5.5	6.336	4.351	1.985	5.207	424.5

**Figure 5.13 Development of elastic modulus of concrete**

The distribution and history of moisture diffusivity was back-calculated from TMAC<sup>2</sup> program by transforming the governing equations of moisture diffusion to calibrate predicted humidity. Details can be referred from the previous section and also the reference (Jeong 2003). It can be seen from Equation 5.43 that  $D$  is the function of both curing time and concrete dimensions. Figure 5.14 shows an example of the prediction of the diffusivity history at 8.02 cm below the concrete surface.

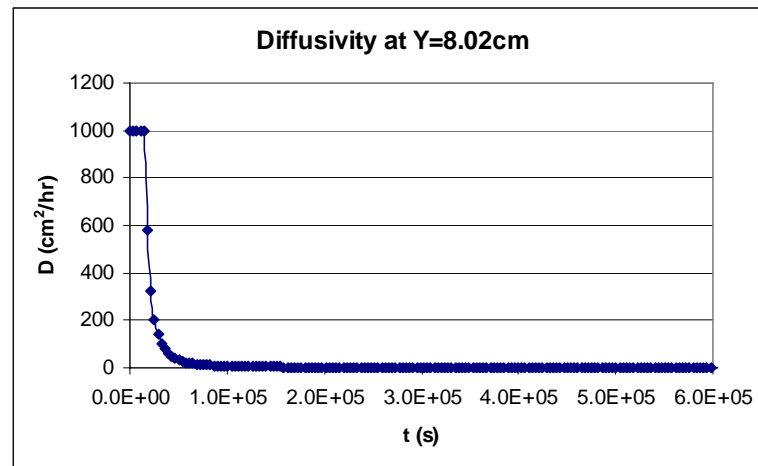


**Figure 5.14 Diffusivity history at 8.02 cm below the surface of concrete**

The evaluation of the stress intensity factor  $K_I$ , where the relative displacement of mating crack surfaces normal to the fracture plane, is shown in Figure 5.15. From Figure 5.15, it can be seen that instead of increasing with the time monotonically, the development of  $K_I$  with the time showed a cycling pattern with the cyclic change of relative humidity profiles, similar to the stress analysis. There were seven sets of peak-and-trough values within the analysis period, which indicates that everyday there were maximum and minimum stress values consistent with the relative humidity profiles. In addition, with time, the maximum and minimum stress values increased with a gradually lower rate.

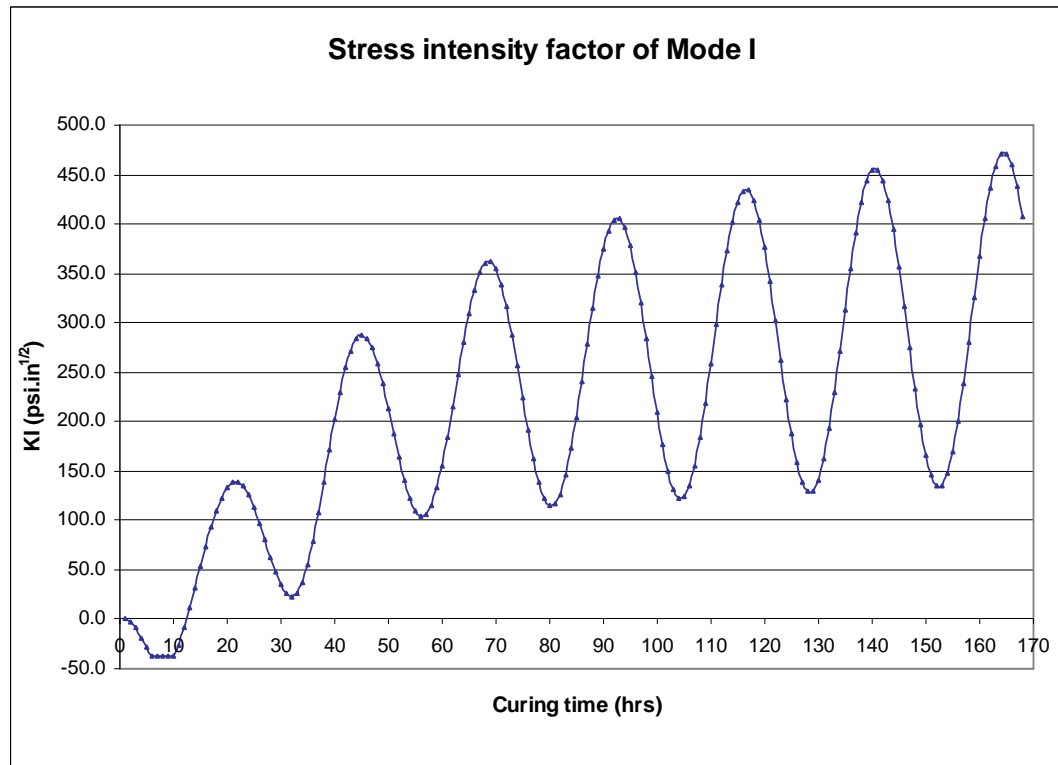


**Figure 5.15 Mode I stress intensity factor history**

As mentioned before, the development of  $K_{II}$  was also conducted. The values of  $K_{II}$  associated with the  $K_I$  values in Figure 5.15, which correspond to in-plane shear, were shown in Figure 5.16. Similarly, the development of  $K_{II}$  followed cyclic patterns as well, though toward the direction of negative values, where the negative symbol indicated the direction of the crack propagation. The values of  $K_{II}$  were much lower than those of  $K_I$ . This is the reason that we neglected mode II crack in our analysis.

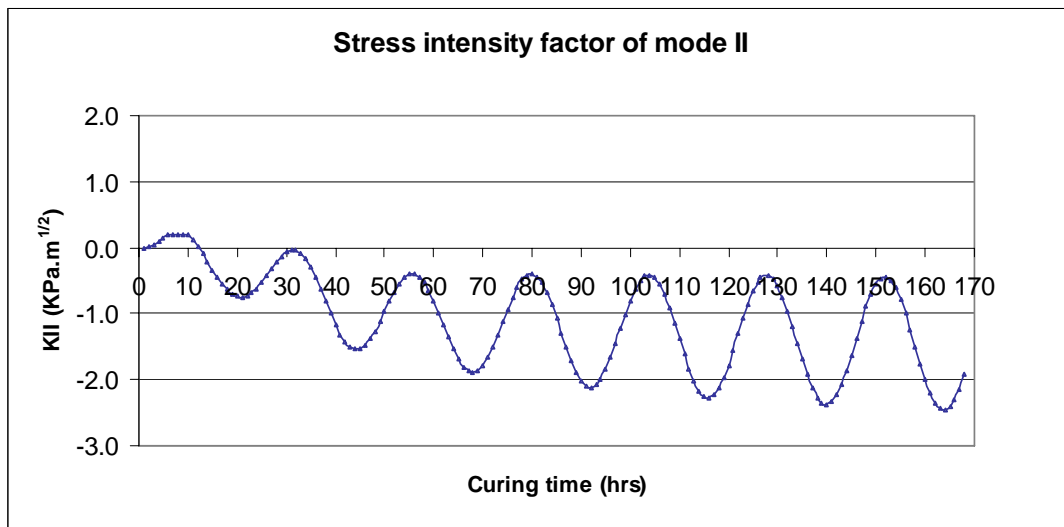


**Figure 5.16 Mode II stress intensity factor history**

### **Prediction of Delamination Occurrence**

The occurrence of delamination can be determined by comparing  $K_I$  against the fracture toughness  $K_{IC}$  developed under laboratory investigation. Two examples were utilized to show the ability of this method to select and evaluate the effectiveness of pavement design methods to prevent delamination and spalling in concrete paving.

#### *Crack Induction*

The sawcutting technique has been used widely to form controlled cracking and relieve the stress level at the surface of concrete pavements (Tang et al. 1994), and it is considered as one of remedial measures of delamination in concrete pavements. For the simulation of sawcutting, both horizontal and vertical directions were considered as the direction of crack initiation for  $K_I$  prediction. However, the results showed that for a vertical existed sawcut, the predicted  $K_I$  values with vertical crack initiation were much higher than those with horizontal crack initiation. Therefore,  $K_I$  values with vertical crack initiation were used for comparison. Figure 5.17 compares the effect of sawcut

depth on the  $K_I$  development of concrete pavement made with VG, 0.45 of w/cm, and without any curing treatment. The  $a/h$  represented the relative sawcut depth, where  $a$  was the sawcut depth, and  $h$  was the thickness of the concrete slab. The notch depths were 0, 1, 2, 3, 4, and 6 in, respectively, corresponding to the relative sawcut depths of 0, 1/12, 1/6, 1/4, 1/3, and 1/2.

From Figure 5.17, it can be seen that without sawcut most of  $K_I$  values were lower than  $K_{IC}$ , which means that the probability of delamination to occur at the sawcut front is very low. Instead it could occur at any other locations. With the increase of the sawcut depth, the local stress at the sawcut tip increased significantly, which greatly increased the probability of occurring of delamination at the sawcut front, while reducing the stress at other locations. Among different relative sawcut depth, relative depth of 1/4 provided the highest  $K_I$  values through the period studied. In addition, almost all values of  $K_I$  exceeded the corresponding  $K_{IC}$ , which indicated that delamination would occur at the sawcut location through the early age of concrete instead of other locations in the pavement. Continually increasing relative notch depth (i.e. 1/3 and 1/2) resulted in a decreased  $K_I$  profile. It may be because of lower moisture gradient and associated strain energy. Therefore, within the scope of this study, cutting the pavement 1/4 of whole slab thickness provided the best performance in terms of relieving delaminations in concrete pavements.



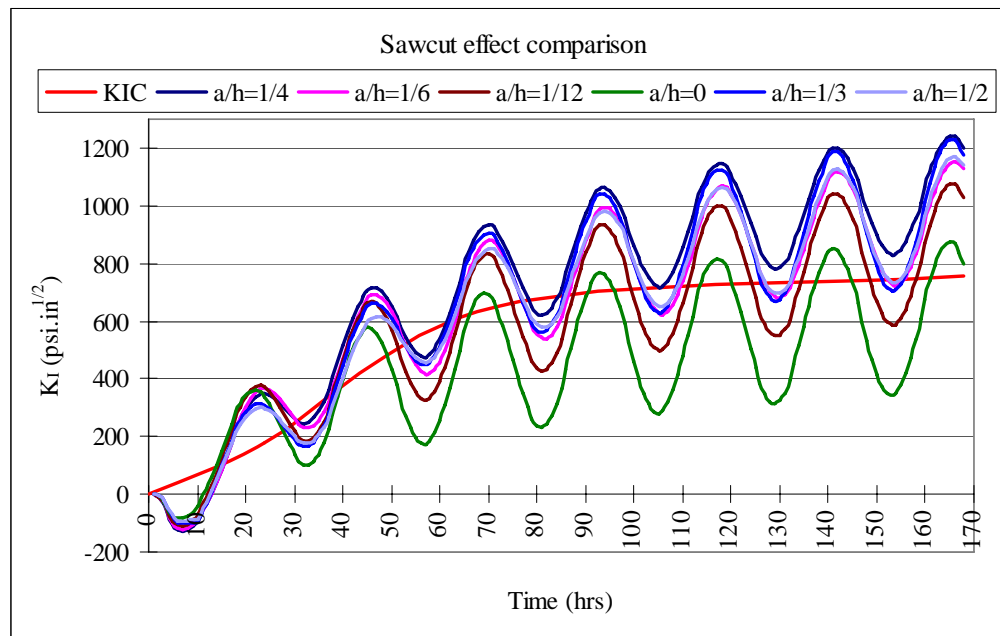


**Figure 5.17 Sawcut effect comparison**

### *Optimization of Design Factors*

As described in Chapter III and IV, current research on using gravel aggregates in concrete paving suggested a way to optimize the combination of construction and material design factors for improving delamination resistance. These factors include aggregate type, w/cm, replacement with ultra-fine fly ash, and curing method. Figure 5.18 shows the results from two different design combinations. One is a) GG + 0.4 of w/cm + 8% of ultra-fine fly ash + WMC, which is the optimum design combination from analysis of the laboratory data; and the other is b) VG + 0.45 of w/cm + 20% ultra-fine fly ash + WOC, which provided a low  $K_{IC}$  based on laboratory results. From Figure 5.18, it can be seen that for combination b, the earliest delamination occurs within 15 hours after concrete was paved when the  $K_I$  development exceeds  $K_{IC}$ . However, for combination a, the stress level in the pavement is reduced, and over the analysis period,  $K_I$  did not surpass  $K_{IC}$ . Therefore, no delamination occurs, which signifies the

effectiveness of this method. The result was also confirmed from field tests on SH 290, where similar materials design was used at one of test sections and there was no delamination from concrete cores taken at that section.

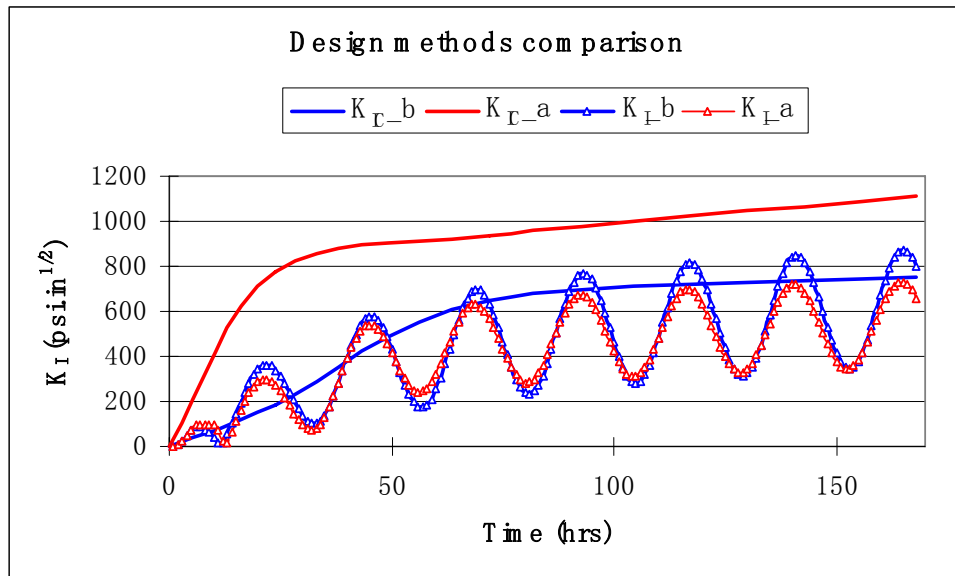


Figure 5.18 Design methods comparison

## **CHAPTER VI**

### **FIELD TESTING**

#### **GENERAL**

Evaluation of the delamination in concrete pavements under different curing conditions and mixture combinations is also an important part in this study. One way is retrieving cores from selected areas for visual confirmation of delamination, but a more efficient way is the application of NDT method which would be capable of collecting a large amount of data in a relatively short period of time and extend the findings from the visual observations to a broader area of pavement. In this chapter, the application of ground coupled GPR to detect delamination occurrence was described. A delamination detection protocol was developed, and validated by visual observation and concrete coring test.

Pavement test sections using gravel aggregates were established to validate measures and practices from laboratory investigation, field testing, and numerical analysis. The results were also presented in this chapter.

#### **GROUND COUPLED GPR**

The GPR technique can provide continuous and nondestructive measurement compared to some traditional highway detection methods (Maser 2000, Liu et al. 2004). The unique ability of GPR to rapidly evaluate subsurface conditions has been identified through various applications, including 1) subgrade investigations, 2) bedrock evaluation, 3) locating sinkholes, 4) detecting frost damage, 5) identifying defects such as stripping or voids, 6) pavement moisture-content measurement, 7) monitoring crack growth within the pavement structure, 8) detecting subsurface problems in hot mix surfacings and asphalt stabilized bases, 9) measuring the thickness of recently

constructed concrete pavements, and 10) assisting with the pavement evaluations as the first step in the pavement rehabilitation process (Saarenketo and Scullion 1994, Maser 2000, Scullion et al. 1995).

GPR is a pulse-echo method. GPR systems typically have three components (Saarenketo and Scullion 1994): 1) a pulse generator which generates a single pulse of a given frequency and power, 2) an antenna which transmits the pulse into the medium, and 3) a sampler or a recorder which captures and stores the reflected signals from the medium. Figure 6.1 illustrates the principle of GPR technique. The GPR transmits short pulses of electromagnetic energy into the pavement structure. These pulses are then reflected and refracted at each layer interface, and the reflected energy is collected and displayed as a waveform with amplitudes and arrival times of reflections. It is the travel time and strength of these echoes that are used in determining certain pavement characteristics.

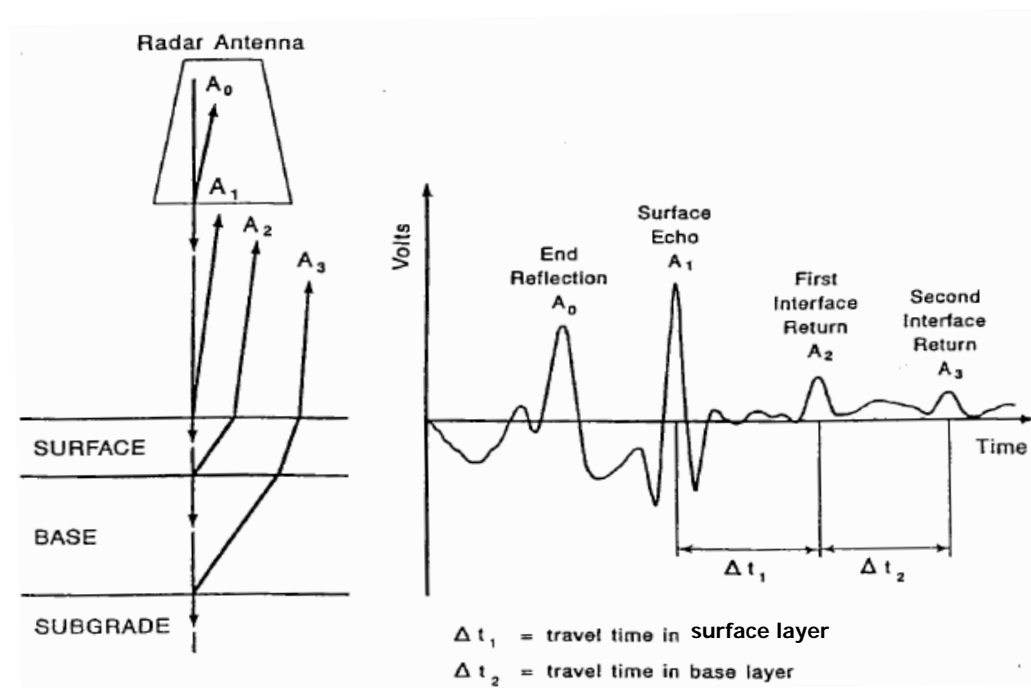


Figure 6.1 Principle of GPR (Scullion et al. 1992)

Although GPR data analysis in the past was performed visually and only by experienced personnel, today GPR data processing is fully automated allowing for processing of large quantities of data with a minimum effort. Signal process systems such as DACQ (Scullion et al. 1992), COLORMAP (Scullion et al. 1995) were developed for facilitating the interpretation of GPR data. The former one is an automated peak tracking system in which the user identified significant peaks within the GPR trace and the software automatically traced these peaks throughout the entire file. The latter one is a Windows based system for rapidly reviewing and interpreting GPR data. Another Windows based software named GPRView has similar functions as COLORMAP (Liu et al. 2004).

There are two types of GPR systems in common use: air-launched system and ground-coupled system. Figure 6.2 shows the setup of ground coupled GPR system. Compared with air-launched system, the clear advantage of ground coupled antennae is their depth of penetration and better vertical resolution. High frequency ground coupled GPR has been found to work well with concrete pavements for applications such as detecting mid-depth delamiantions, and locating steel or identifying possible sub slab defects such as voids (Scullion et al. 1997). Some specific comments on the applicability of GPR for characterizing in-place concrete pavements were summarized in study conducted by Zollinger et al. (2004): 1) layer thickness measurements in concrete slabs are different from those in HMA pavements; 2) voids under JCP slabs filled with water can be detected by visual review of the graphical output and/or using site calibrated interpretation algorithms, and 3) the hand-held contact type GPR equipment has been used successfully to determine dowel alignment to an accuracy of  $\pm 3$  mm ( $\pm 0.12$  in) in the vertical and the lateral planes.



**Figure 6.2 Ground coupled GPR setup**

## **GPR TESTING**

In this study, ground coupled GPR was applied to several highways made with gravel aggregates within Houston district, Texas to monitor the process of delaminations. These tests included 1) test at SH 6 (intersection between FM 529 and SH 6) on February 6, 2004; 2) test on IH 10 (near Baytown) and SH 225 on February 27, 2004; and 3) test on US 290 (near Hempstead) on September 23, 2004. Cores were also taken either adjacent to or on the transverse cracks from these sites to confirm the nature of the delaminations. Detailed data information is included in Appendix A.

### **GPR Test on SH 6 on February 6, 2004**

11 cracks within 3 test sections built in previous research were picked up for GPR monitoring. For each crack, GPR data was collected at different distances to the shoulder

by pulling ground coupled antenna from upstream side of crack to the downstream side. For each location, the length which the antenna passed was 6 feet. Visual survey was also conducted for those selected sections, and another impact echo technology was applied by research members from UTEP to monitor the progress of the delaminations. Cores were taken both along the transverse cracks and transverse saw-cuts for visual confirmation of delaminations.



**Figure 6.3 The pavement section without sawcuts before the core was taken (the arrow shows the location where the core was taken)**



**Figure 6.4 The pavement section with sawcuts before the core was taken (the arrow shows the location where the core was taken)**



(a)



(b)

**Figure 6.5 Cored samples: (a) along the sawcut; (b) along the crack**



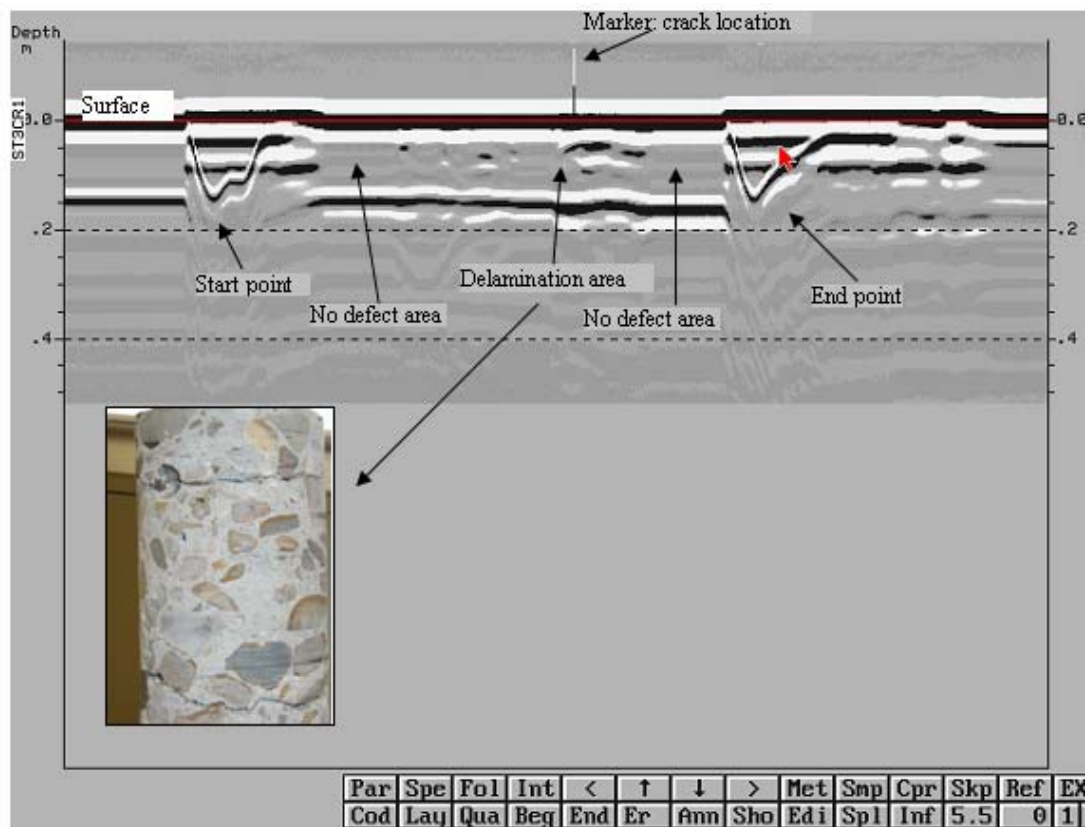


**Figure 6.6 GPR data from test area with the confirmed delamination**

Figures 6.3 and 6.4 show the pavement sections with and without sawcuts before cores were taken. It is obvious that in the section without sawcuts there were random transverse cracks, while in the section with sawcuts, transverse cracks occurred just along the sawcuts. It is because sawcuts initiate the cracks and defects and cause stress concentration at the tips, which relieve stresses and control cracks at other locations. In addition, there was no indication of delamination in the core taken beside the transverse sawcut, while significant delamination along the transverse crack without sawcuts, which can be also seen from Figure 6.5. The delamination for the section without sawcut was also confirmed from GPR data showed in Figure 6.6. As shown in Figure 6.6, during the testing, the marker was made at the location of the crack, where the core was taken. In the ‘no defect area’, there were no strong reflections. In this area the concrete is

judged to be solid. In the ‘delamination area’ which was at the right of the crack marker, there were obvious disturbance of GPR signals, which indicated the occurrence of delamination.



**Figure 6.7 The coring sample with delamination: (a) top view of the coring hole; (b) fracture surface**

The full-depth core with confirmed delamination (shown in Figure 6.5 (b)) was split into three parts due to significant delamination. Figure 6.7 shows the detailed observations from concrete core specimens. Both (a) and (b) showed that the interfacial zone is weaker than the coarse aggregate, cracks prefer to propagate along the interfacial zone, while the coarse aggregates debond, and then deflect and bridge cracks.

#### **GPR Test at IH 10 and SH 225 on February 27, 2004**

8 cracks within 5 test sections were picked up for GPR monitoring. For each crack, GPR data was collected at 7 different locations (i.e. 1, 2, 3, 4, 5, 6, and 7 feet to the shoulder)

by pulling ground coupled antenna from upstream side of crack to the downstream side with constant interval of 6 feet. Visual survey was also conducted for those selected sections, and another impact echo technology was applied at the same locations by research members from UTEP to monitor the progress of the delaminations. Cores were taken besides transverse cracks / sawcut from different pavement sections along IH10 and SH-225 to confirm delamination where spalling is not manifested on surface but delamination suspected inside.

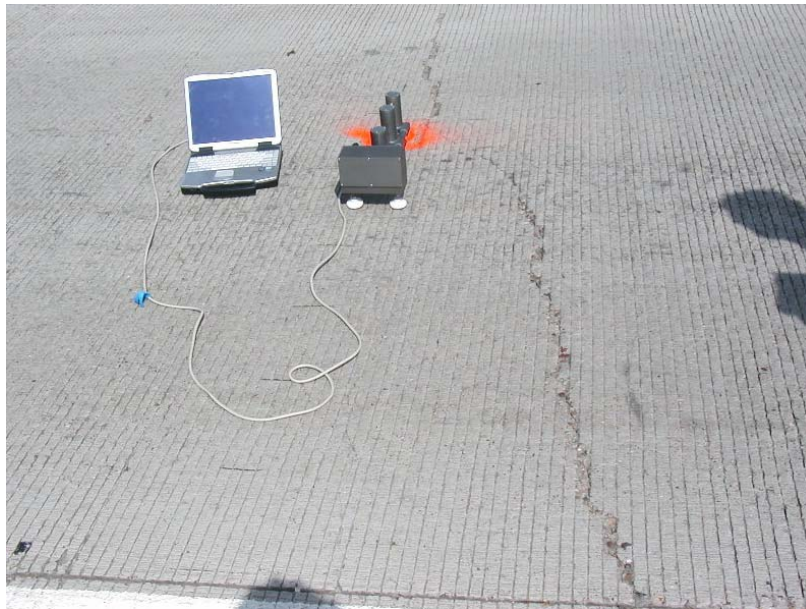


**Figure 6.8 Test section at IH10 without sawcut**

Figures 6.8 to 6.14 show selected test sections where GPR data was collected and concrete cores were retrieved (red circles besides the cracks represent the core locations). Generally spalling distress is very prominent at IH10 as shown in Figure 6.8. One core was taken besides one fine transverse crack where spalling was not observed. The idea was to check the presence of delamination (in any) inside. This core sample from I-10 did not show any delamination, which indicated delamination may not take

place under fine transverse cracks. However, observation on more number of cores besides fine transverse cracks or application of GPR / impact echo to detect delamination (if any) in more number of locations is necessary in order to prove it.

The concrete pavement test section at SH 225 was paved on November 11, 1991, and was opened for traffic on December 12, 1991. Till the date when GPR test was conducted, the test section is already 13 years old. The layout of experimental sections within the SH 225 test section is indicated in previous research (Senadheera and Zollinger 1996), and section 2, 3 (without early age sawcut) and 9 (with early age sawcut) were picked up for our GPR tests. As for SH 225, spalling distress is not prominent although cracking is prominent. We have collected several cores to check the presence of delamination (if any) inside. Delamination was observed at 4-5 inch below in pavement sections without sawcut at SH 225 (shown in Figures 6.11 and 6.13). On the other hand, de-lamination was not observed in core taken (besides one prominent crack) from pavement section with sawcut (Figure 6.10). The observations were consistent with those obtained by Senadheera and Zollinger (1996) 14 years ago. They summarized that there were delaminations present near random transverse cracks and there was no indication of delamination in cores taken at the transverse sawcuts. Early age sawcutting helps in releasing some of the strain energy generated due to shrinkage and temperature change in the pavement, and it is very effective to minimize delaminations at shallow depths, which was also verified from stress analysis described in Chapter V.



**Figure 6.9** Test section at SH 225 with sawcut

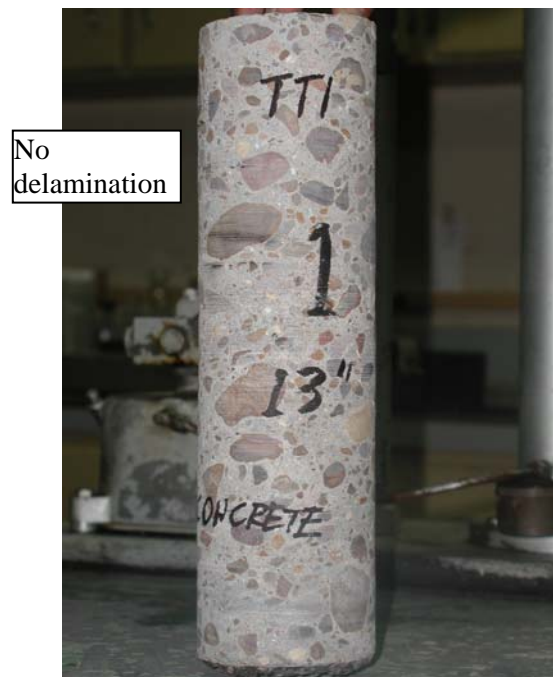


**Figure 6.10** Core collected from location marked at Figure 6.9

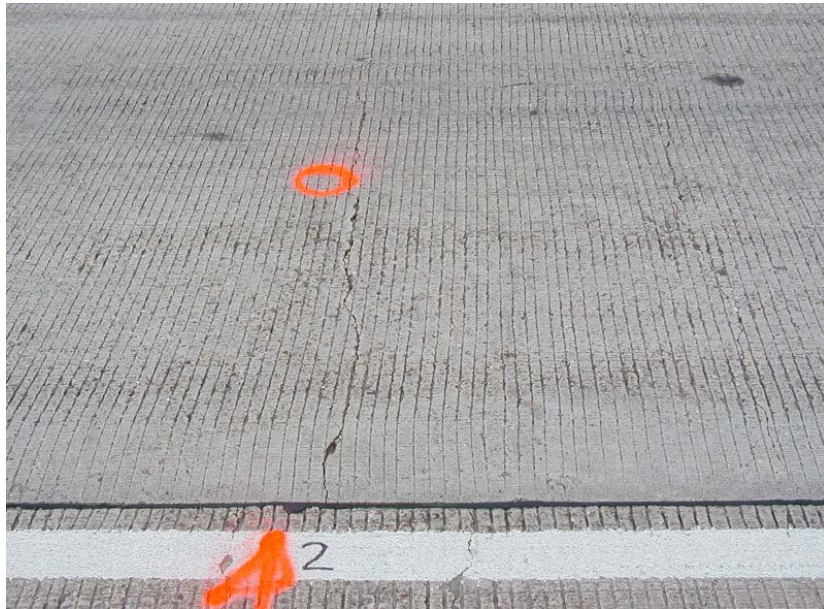


**Figure 6.11 Test section at SH 225 without sawcut**

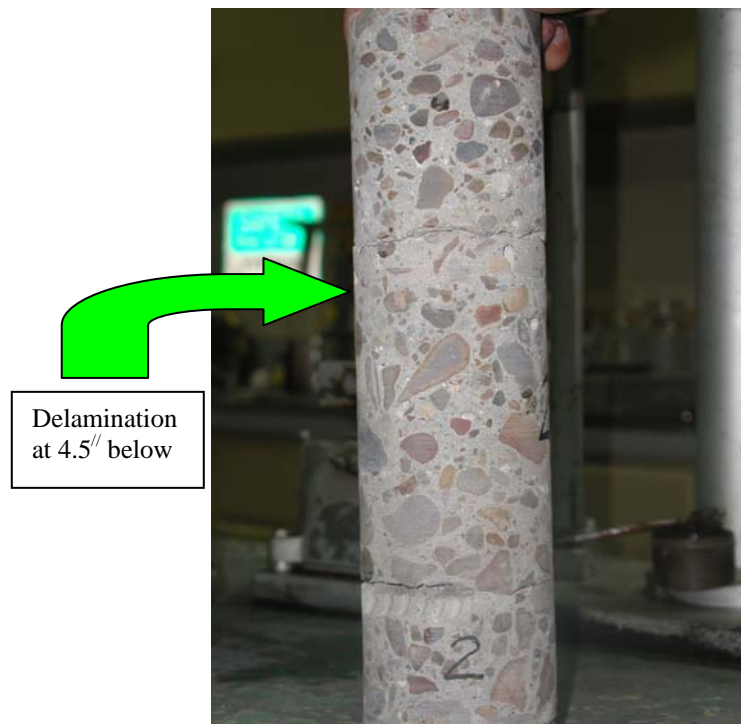


**Figure 6.12 Core collected from location marked at Figure 6.11**



**Figure 6.13** Another test section at SH 225 without sawcut

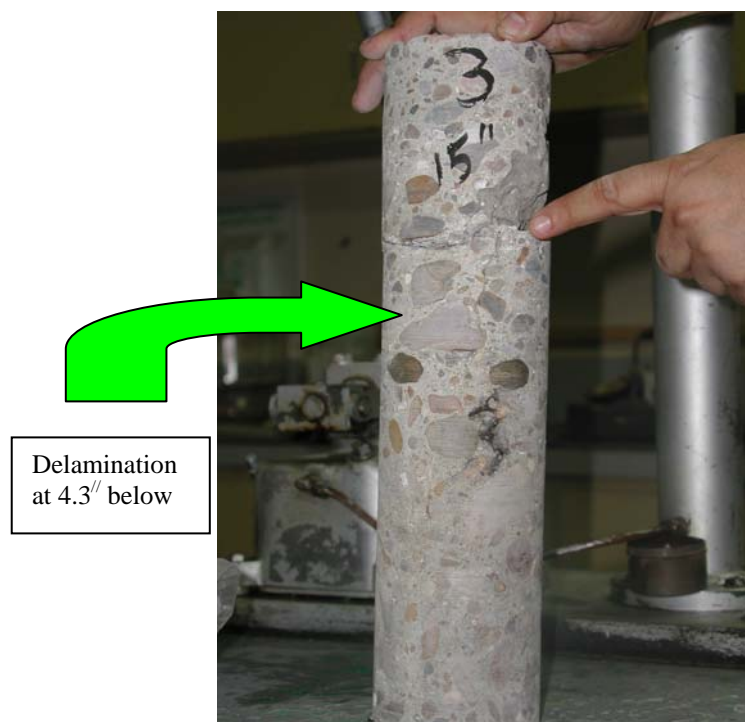


**Figure 6.14** Core collected from location marked at Figure 6.13

### **GPR Test at US 290, Hempstead on September 23, 2004**

This test section was constructed in August 1992. Till the date when GPR test was conducted, the test section is already 12 years old. The layout of experimental sections within the US 290 test section is presented in previous research (Senadheera and Zollinger 1996), and 12 cracks within section 1, 2, 3, and 4 were picked up for GPR monitoring. For each crack, GPR data was collected at seven different locations (i.e. 2, 5, 7, 8, and 10 feet to the shoulder) by pulling ground coupled antenna from upstream side of crack to the downstream side at constant interval of 6 feet. Visual survey was also conducted for those selected sections, and another impact echo technology was applied by research members from UTEP to monitor the progress of the delamination. 15 cores were taken both along the transverse cracks and transverse sawcuts for visual confirmation of delamination.

Figures 6.15 to 6.18 show the conditions of two of investigated cracks. One is crack #4 at station 2 (shown in Figure 6.15(a)), where concrete was paved during day time with siliceous gravel, CRCP 89 steel standard, transverse sawcut and polyethylene film curing. With transverse sawcuts, slight cracking or spalling existed. From GPR waveform (shown in Figure 6.16), it can be seen that disturbance of GPR signals only occurred around the cracking. Concrete cores (shown in Figure 6.15 (b)) were taken at different locations along the crack; however, no delamination was detected. The other is crack #9 at station 3 (shown in Figure 6.17 (a)), where concrete was paved during day time with limestone, CRCP 89 steel standard, and two coats of standard TxDOT curing compound curing. Without transverse saw cuts, the pavement was severely spalled. From GPR waveform (shown in Figure 6.18), it can be seen that disturbance of GPR signals was almost everywhere. However, there was no delamination occurred from concrete cores retrieved (shown in Figure 6.17 (b)). In fact, there was no any delamination detected from all 15 cores taken from locations adjacent to selected cracks. However, an extensive coring test conducted in June 1993 from all test sections (Senadheera and Zollinger 1996) showed that there were delaminations detected. It also





(a)

(b)

**Figure 6.15 Crack #4 and concrete cores**

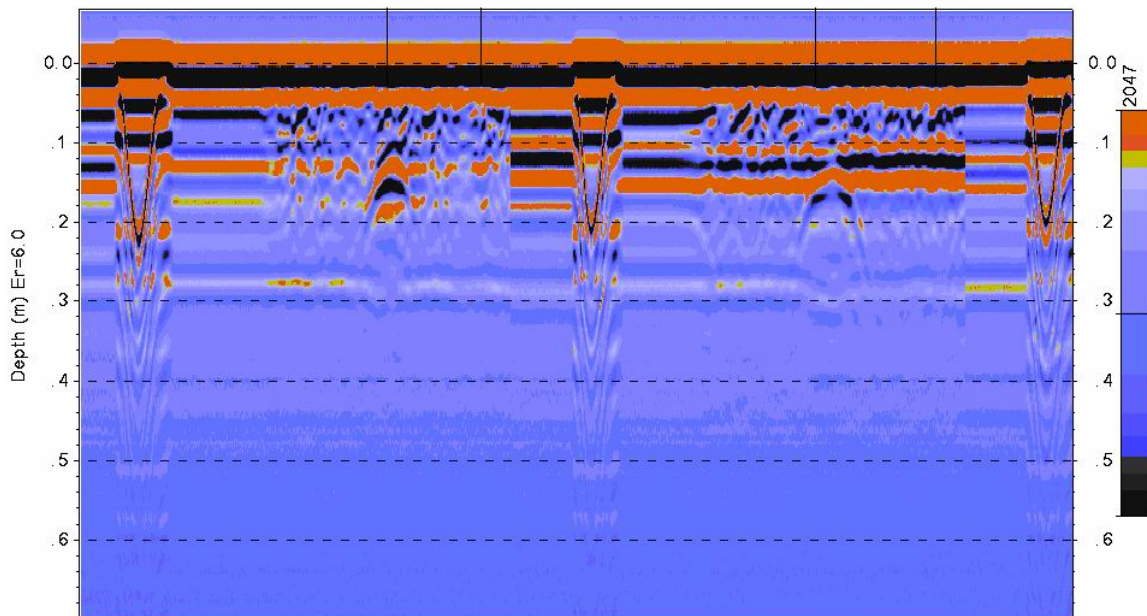


**Figure 6.16 GPR waveform of crack #4**

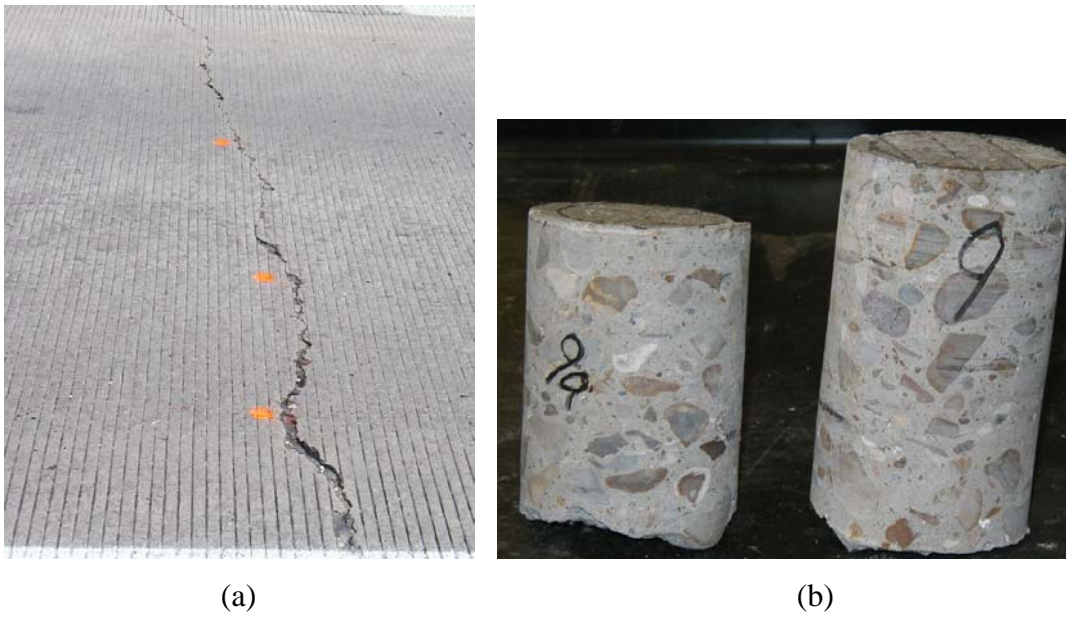


Figure 6.17 Crack #9 and concrete cores

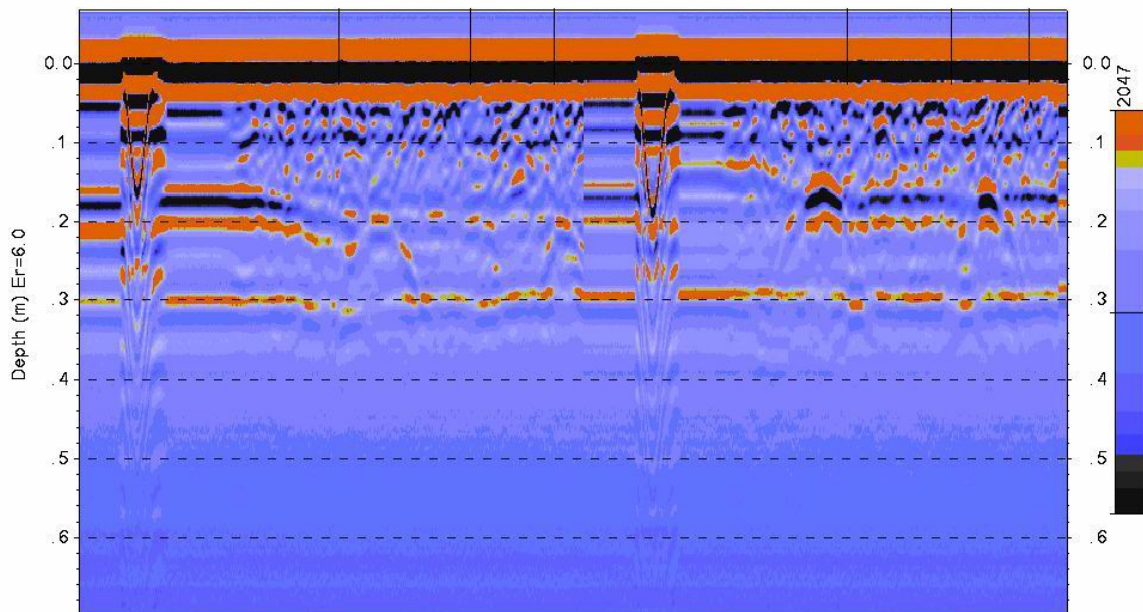


Figure 6.18 GPR waveform of crack #9

implies coring test cannot be a detecting method but a validating method for other NDTs. The analysis from GPR delamination detection protocol, which will describe in the next section, also indicates the possibility of delamination existing in US 290, though it was not present from selected cores.

## **GPR DELAMINATION DETECTION PROTOCOL**

The data interpretation for GPR in asphalt pavement applications has been very successfully. However, when GPR was applied to early age delamination detection in concrete pavements, there were difficulties we faced. Firstly, there was no metal plate file available for ground coupled GPR technique, which is a mandatory file for calculating layer thicknesses for air launched GPR system. Secondly, concrete is very similar in dielectric properties to the granular base. Thirdly, early age delamination below the surface is rather shallow. Because the GPR pulse energy travels down through the material and echoes are created at boundaries of dissimilar materials, and it is the travel time and strength of these echoes that are used in determining certain pavement characteristics, in our case, it may cause the boundary not significant to be detected by the echoes, and the GPR waveform very difficult to be interpreted. This is also the reason why through the GPR tests conducted on several highways, in some cases early age delamination can be determined directly from GPR waveforms, and then confirmed from concrete cores retrieved later. However, in some cases it is very difficult to determine the possibility of delamination occurrence based on visual review of the graphical output only.

Therefore, it is very necessary to improve the analysis quality and facilitate data interpretation for GPR technique. In this section, an analysis approach of GPR data was proposed to improve quality of data interpretation and accuracy of delamination detection. It includes the following several steps: 1) initial evaluation, 2) comparison of negative intermittent peaks, and 3) establishment of threshold voltage difference.

The GPR return waveform from a pavement with a homogeneous surface layer and in generally “good” condition is shown in Figure 6.1. Peaks  $A_1$ ,  $A_2$ , and  $A_3$  are reflections from the top of the surface, base and subgrade, respectively. The surface layer is classified as “homogeneous and uniform” because there are no significant peaks between  $A_1$  and  $A_2$ . However, in Figure 6.19, a negative peak C occurs between major peaks A and B, which signifies a layer of lower dielectric properties. In Texas, when there are intermittent negative peaks in the surfacing layer, they are usually related to the presence of a low density layer within the surface layer due to significant defects or deterioration (Scullion et al. 1995). On this basis, the subsurface condition can be initially evaluated.

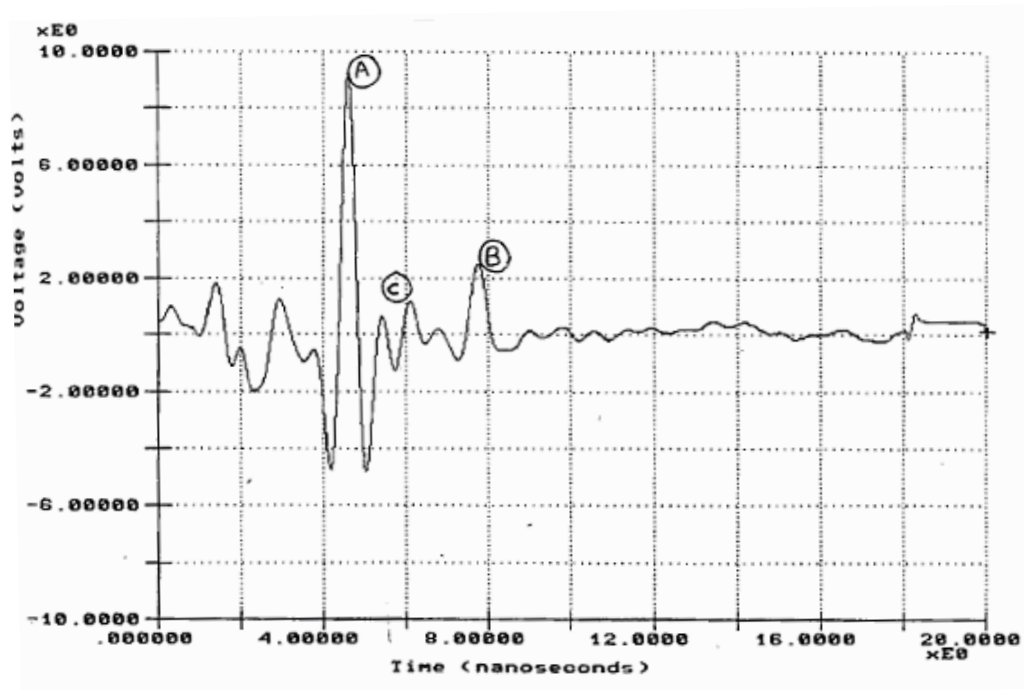


**Figure 6.19 Example of GPR return waveform with subsurface problem (Scullion et al. 1995)**

Though the metal plate file is not available for our study, it is still possible to develop site calibrated interpretation algorithm based on the GPR signals. Before GPR test, a simple NDT method, also referred to as the “sounding method” was applied to determine the good and bad locations, by dropping a heavy steel bar on the pavement and listening to the sound emanating from the pavement. If the pavement is homogeneous solid concrete (good locations), the sound emanating from the pavement is a high-pitched “ringing” sound. If there is a delaminated concrete segment, the sound is a low frequency “rattling” sound. Based on this method, in our study, normally the locations with “bad” condition were those adjacent to a transverse crack (either or both sides of the transverse cracks), while the locations with “good” condition were those away from the crack. It is also correlated to the observations by Senadheera and Zollinger (1996). Using the GPR waveform of locations with “good” conditions at the same pavement section as a reference or site calibration, we can know how “bad” those locations with “bad” conditions are (or the severity level of the subsurface). On this basis, a data retrieving program was developed to obtain data for GPR waveforms (i.e., voltage versus travel time curves) at any trace point, which made quantitative comparison possible between locations with “good” and “bad” conditions.

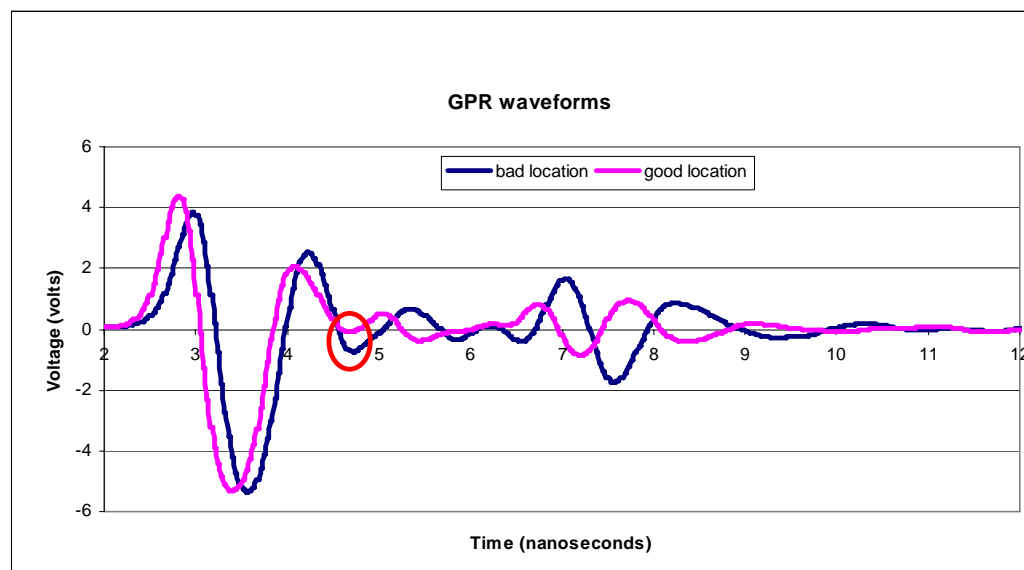


**Figure 6.20 Typical GPR waveforms for bad and good locations**

Figure 6.20 compares typical GPR waveforms for “good” and “bad” locations. The red circle indicates the major difference between these two waveforms. Compared with the waveform of good location, there is a very significant intermittent negative peak for the one of bad location.

In order to find the correlation between those intermittent negative peaks in the GPR waveforms and the early age delamination in concrete slab, for each location of each crack where the GPR was conducted, all GPR data were reduced. Detailed information of 164 sets of data is listed in Table A-1 of Appendix A. Using the intermittent negative peak value of locations with “good” conditions ( $V_1$ ) as a reference, the difference between negative peak voltage values of “good” and “bad” locations ( $V_2 - V_1$ ) can be used to evaluate the delamination situation. Figure 6.21 illustrates the summary of peak values comparison of GPR data from SH 6 and US 290, where  $V_2$  represents the intermittent negative peak value of location with “bad” condition. After calibrated by  $V_1$ , it is certain that there is no delamination detected from GPR if the value of  $(V_2 - V_1)$  is great than zero. Figure 6.22 illustrates the probability of  $(V_2 - V_1)$  less than a certain value for GPR data from SH 6 and US 290. The curve for US 290 shifted to the right, compared with that for SH 6, which indicated that the concrete slab condition of US 290 is better than that of SH 6. This finding is also correlated to the results from observations of concrete cores retrieved from these roads.

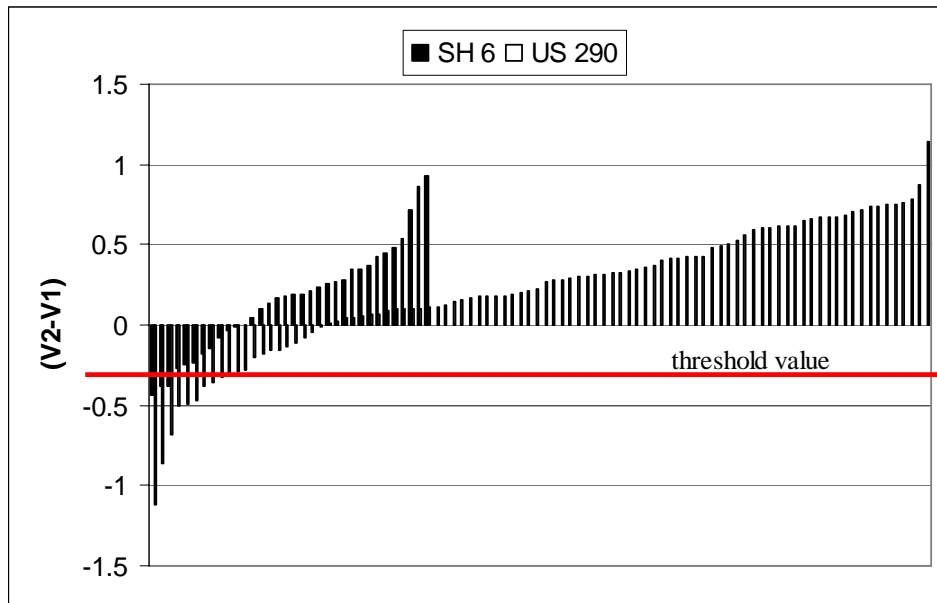


Figure 6.21 Comparison of intermittent negative peak values

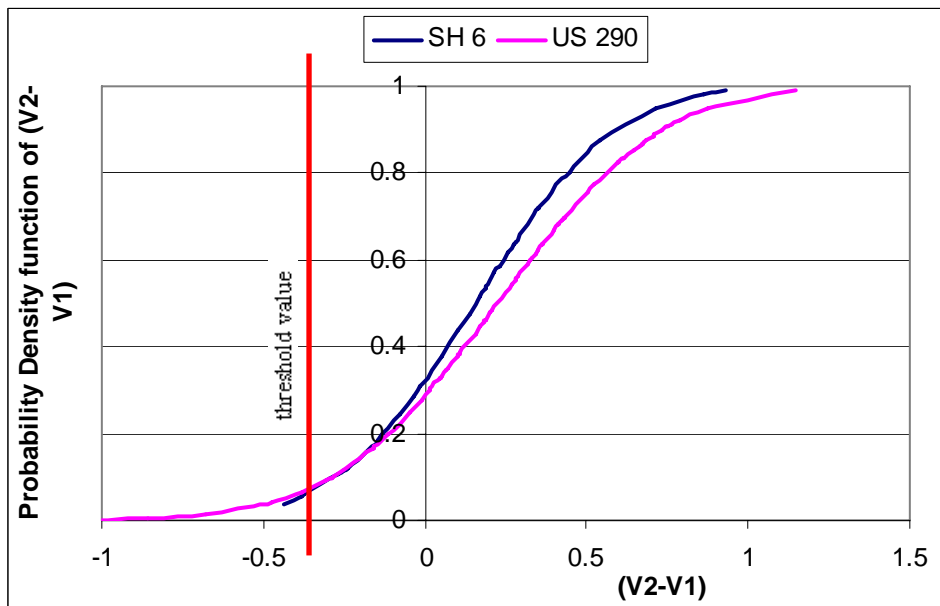


Figure 6.22 Probability of peak differences

In addition, by correlating the GPR results with associated concrete cores taken at the same locations, it is found that if the value of  $(V_2 - V_1)$  is not low than a certain negative value, early age delamination will not occur. This value is the threshold value which can identify the delamination occurrence for concrete pavements from ground coupled GPR data. Within the scope of this study, -0.3 was determined as the threshold value.

Therefore, this approach makes easily and quantitatively interpreting the ground coupled GPR data possible, which greatly explores the application of GPR to the concrete pavements research. The approach was also preliminarily validated through winter test sections built at SH 288, which will be described later.

## **FIELD TEST SECTIONS**

The laboratory work revealed important information on curing and climatic conditions, mixture design, aggregate combinations, time of placement, and method of crack control to provide sufficient guidance to establish test sections and formulate a framework of the guideline for using gravel aggregates in concrete paving. To this end, gravel test sections using Fordyce materials were established in November, 2005 on SH 288 to produce performance test data to validate measures and trends relative to the practices and techniques to minimize the development of spall related delamination in CRC paving. Three continuous days from November 16<sup>th</sup> to 18<sup>th</sup> were dedicated to paving a total of ten sections. Field data was collected through various types of instrumentation and monitoring by personnel from TTI, TxDOT, UTEP, and CTR over a period of days since paving. Weather data, concrete temperature and relative humidity profiles, and drying shrinkage development were monitored, and pavement surveys were conducted to monitor the crack pattern development over time in each test section. Bonding strength in the field was measured and ground coupled GPR was conducted on November 28<sup>th</sup> and December 19<sup>th</sup> to track the delamination development. The stress analysis to predict



delamination occurrence and GPR field delamination detection protocol were further validated through visual observation of concrete cores on associated cracks retrieved.

### **Field Testing Program**

10 test sections were located on SH 288 approximate 3 miles south of Beltway 8. The field test section design was finalized through several discussion and meetings. The design has ultimately narrowed down to 3 factors, i.e., fly ash content, curing method, and batching sequence with a total of 10 test sections, as summarized in Table 6.1. These combinations were a result of 2 different fly ash replacements, 3 curing methods, and 2 charging sequences. 2 different fly ash contents were: 1) a combination of 10% of ultra-fine fly ash and 15% of Class F fly ash, and 2) 25% of Class F fly ash. The curing methods consisted of high reflective resin-based curing (HRC) compound, normal (conventional) resin-based (NC) curing compound, and wet mat curing. For 2 curing compounds, 2 times of application (10 minutes and 30 minutes after paving) were carried out. The HRC was applied by hand spray. A modified charging sequence was formulated to minimize the available water at the aggregate-paste interface which consisted of 1) mixing 75 ~ 80% of the water with the fine aggregate and the cementitious materials for 50 seconds, then 2) adding the coarse aggregates and mixing for 30 seconds, and 3) adding the rest of water and mixing for 50 seconds; the normal charging sequence consisted of the traditional mixing of the materials together at the same time.

**Table 6.1 Test variables for the field program**

Test Section	FA replacement (%)	Curing	Charging sequence
1	(10+15) *	HRC	Normal
2	(10+15)	HRC	Modified
3	(10+15)	NC	Normal
4	(10+15)	NC	Modified
5	25 **	HRC	Normal
6	25	Wet Mat	Modified
7	25	NC	Normal
8	25	NC	Modified
9	(10+15)	Wet Mat	Normal
10	25	Wet Mat	Normal

\* 10% ultrafine fly ash and 15% Class F fly ash

\*\* 25% Class F fly ash

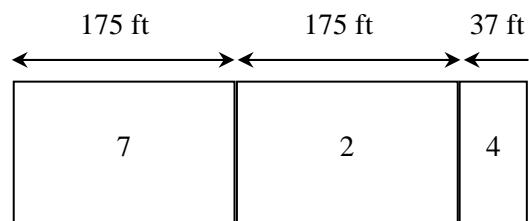
*HRC = High Reflective Curing Compound, and NC = Normal Curing Compound.*

The concrete mixtures for test sections were designed with dense graded aggregates supplied by the Fordyce Company, Victoria, Texas. Prior to paving the test sections, dense graded mix was developed in the laboratory at TTI, and trail batched mixtures successfully met the required strength and workability levels. The design of w/cm was 0.4, using a cement factor of 6 and a Type I/II cement. Table 6.2 shows the mix proportions of concrete on 1 cubic yard batch basis.

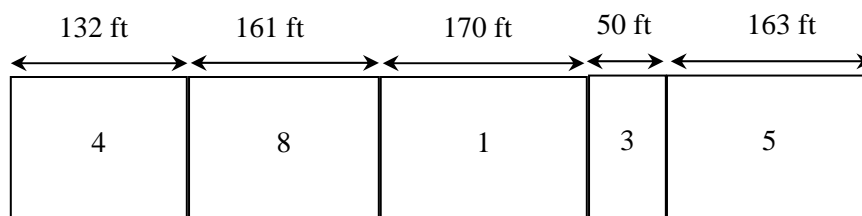
**Table 6.2 Concrete mix proportion (1 cubic yard)**

Mixture Component	Weight
Cement (lbs)	423
Total fly ash (lbs)	141
Coarse aggregate (1 1/2in, OD, lbs)	1370
Intermediate aggregate (3/8in, OD, lbs)	498
Fine aggregate (Sand, OD, lbs)	1215
Net water (lbs)	225
Air-entraining Admixture (oz)	2
Water reducer (oz)	23

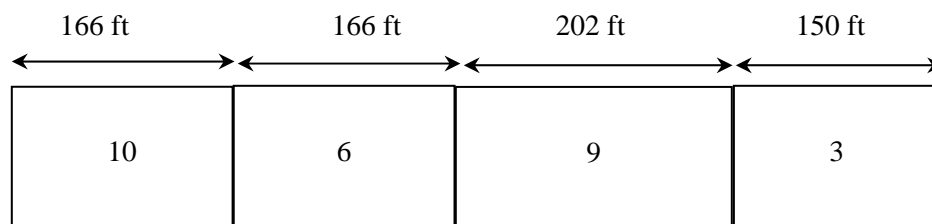
First day paving (11/16/2005)



Second day paving (11/17/2005)



Third day paving (11/18/2005)

**Figure 6.23 The schematic of test sections**

As previously noted, a total of 10 test sections were constructed over a three-day period. The planned construction length for each test section was 175ft. However, the actual lengths of 10 sections varied, as shown in Figure 6.23.

### **Field Test Data and Analysis**

The field test data and analysis presented here include 1) weather data, concrete temperature and relative humidity profiles, and drying shrinkage development, 2) pavement condition such as the crack pattern development over time in each test section, 3) field bond strength of concrete and 4) GPR data. The data information in first 3 items was further used as inputs for stress analysis to predict associated delamination occurrence, and GPR data was analyzed by the field delamination detection protocol. The results were further validated by associated concrete coring tests.

#### *Weather Data*

The development of delaminations, and spalling distresses in CRCP at an early age is significantly affected by climatic factors. Therefore, a weather station (shown in Figure 6.24) was used to collect weather data in the field which recorded ambient relative humidity, ambient temperature, solar radiation, wind direction, wind speed, and rainfall. This data was collected at hourly intervals on a continuous basis.



**Figure 6.24 Weather station setup**

Figures 6.25 and 6.26 record the trends of relative humidity, temperature, solar radiation and wind speed with time over the placement period and beyond (from 11/16/2005 to 11/21/2005). As shown in Figure 6.25, relative humidity shows the inverse relation with the temperature, i.e. the higher temperature associates with the lower relative humidity, and vice versa. Over the first several days after construction, ambient temperatures ranged from a low 40 °F in the morning hours to a high 65 °F in the afternoon. The relative humidity ranged from a low around 20% in the afternoon to a high almost 100% in the morning. As shown in Figure 6.26, 0.65 kW/m<sup>2</sup> of maximum solar radiation and 0.62 m/s of wind speed were recorded over the monitored period.

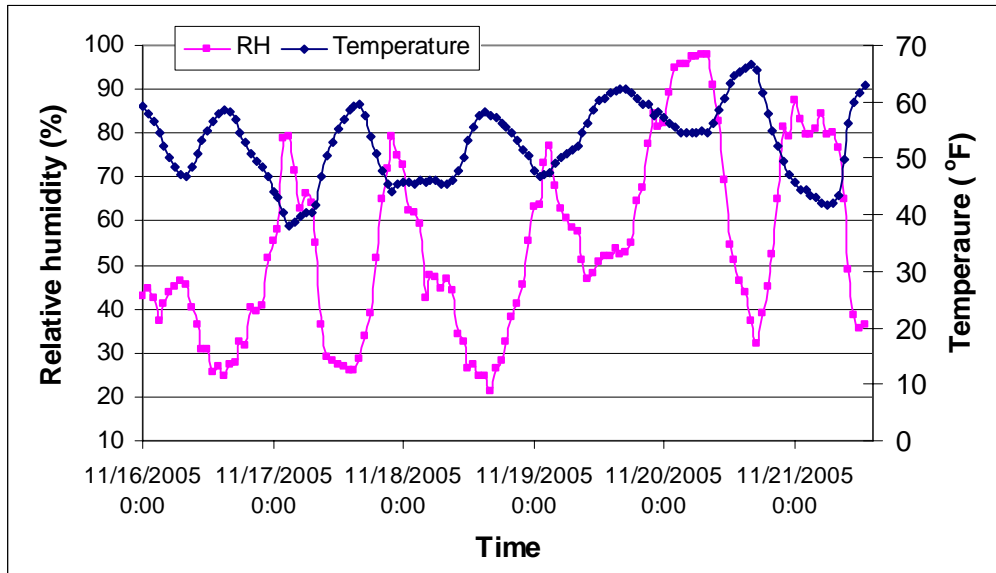


**Figure 6.25 Ambient temperature and relative humidity cycles during field test operation**

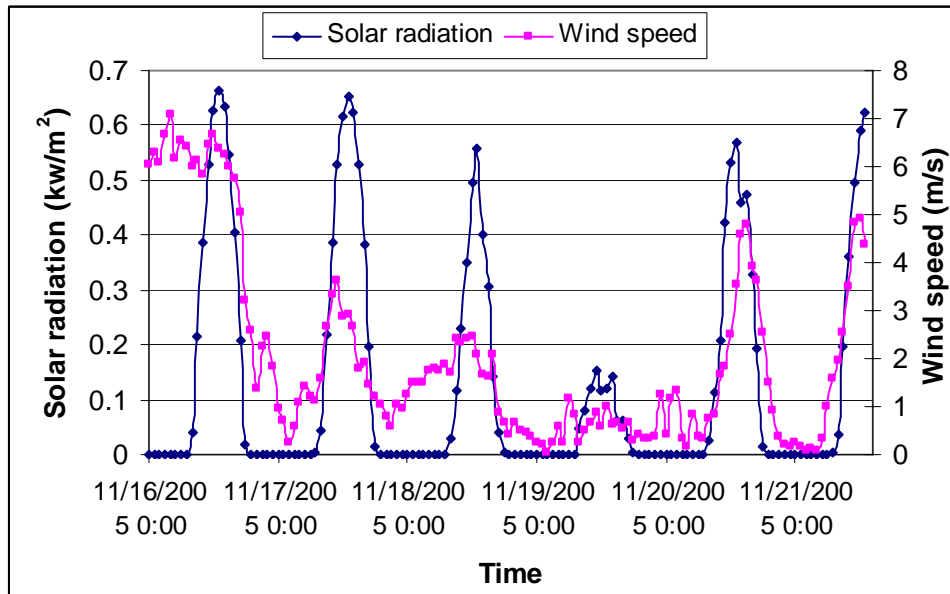


**Figure 6.26 Solar radiation and wind speed cycles during field test operation**

### *Concrete Temperature Profiles*

Vertical temperature profiles through the thickness of the pavement for all the test sections were measured immediately after concrete placement by embedded I-buttons (as shown in Figure 6.27 (a)) at 3 different locations in the concrete (1 inch from the top, mid-depth, and 1 inch from the bottom; and two different transverse locations: 2ft and 6ft from the edge). Figure 6.28 shows the temperature development in the concrete for one of test sections (section 8). Figure 6.29 summarizes the maximum temperature at different locations in the pavement and the associated elapsed time when these temperatures were reached. A complete set of data is provided in Appendix B.

It can be seen that at each location, the development of concrete temperature with time followed a cycling pattern. For almost all test sections, there was an increase in temperature from top to bottom. Different maximum temperature existed for different test sections, which is related to the temperature at the time of placement. Generally, the higher temperature at the time of placement, the higher the maximum temperature which the concrete can reach. Figure 6.30 illustrates the main effects plot for maximum temperature concrete at mid-depth, and Delta statistics (described in Chapter III) was again used to determine the significance of design factors related to the maximum concrete temperature. The higher Delta value represents the higher impact of the design factor on the target value of output (here, maximum concrete temperature). Based on Delta statistics, these factors followed a decreasing rank order with respect to their relative importance to the concrete maximum temperature: curing method, fly ash content, and charging sequencing. Compared with the experimental design in the laboratory, same trend of the relative importance of design factors held, except that the factors of aggregate type and w/cm were not considered in the field design. Maximum temperature of concrete represents the maximum heat evolved during the hydration process. For the factor of curing method, WMC provided higher maximum concrete temperature than the other two curing methods. It is because that the best curing quality provided by WMC enables the least loss of heat energy in the concrete. As for the factor

of fly ash, 25% Class F fly ash provided higher maximum concrete temperature than the combination of 10% ultra-fine fly ash and 15% Class F fly ash. Compared with ultra-fine fly ash, Class F fly ash is coarser. Therefore, the latter has less specific surface areas than the former. Under same condition of w/cm, concrete made with 25% Class F fly ash may have more water to ensure the adequate reaction of hydration products than that made with 10% ultra-fine fly ash and 15% Class F fly ash, which then increases the concrete maximum temperature. In addition, modified charging sequence provided higher concrete maximum temperature than normal one. It may be because that for modified charging sequence, the coarse aggregates are added to the mixer later than other materials, which ensures the sufficient mixing of water with cementitious materials, and then improves the hydration process and increases the concrete maximum temperature.

In general, concrete at the mid-depth and 1 in from the bottom reached their highest temperature at almost the same elapsed time, while the concrete at 1 in from the top reached its highest temperature later than at the other two locations. However, the small difference reflected the effects of different design parameters on the temperature development. Using concrete temperature at mid-depth and comparing section 1 and 2, 10 and 6, and 7 and 8, the associated elapsed time when the maximum temperatures were reached for sections with modified charging sequence (section 1, 10, and 7) was shorter than those with normal charging sequence (section 2, 6, and 8). It also may be due to the improvement of hydration process by modified charging sequence. As for the effect of curing method, in the case of wet mat curing, it took longer time for concrete to reach its maximum temperature than the other two curing methods. However, the effect of fly ash combination is not that significant. It may be because that at very early age of concrete, fly ash mainly plays the role of being the filler. On this basis, there is not big difference between the combination of 10% ultra-fine fly ash and 15% Class F fly ash, and 25% Class F fly ash only.





(a)

(b)

Figure 6.27 I-button and VWG setup

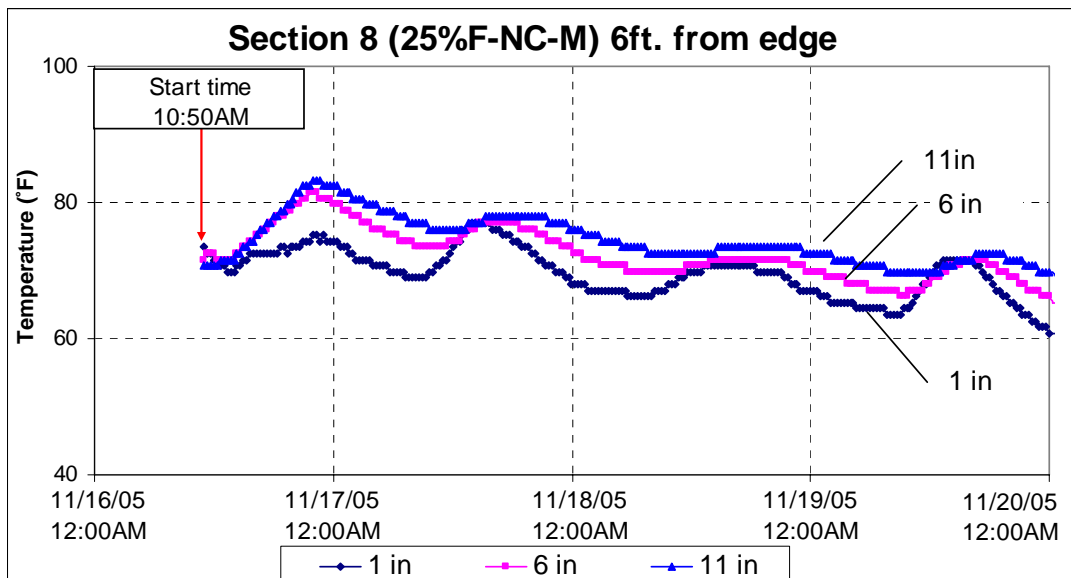


Figure 6.28 Temperature profile of test section 8

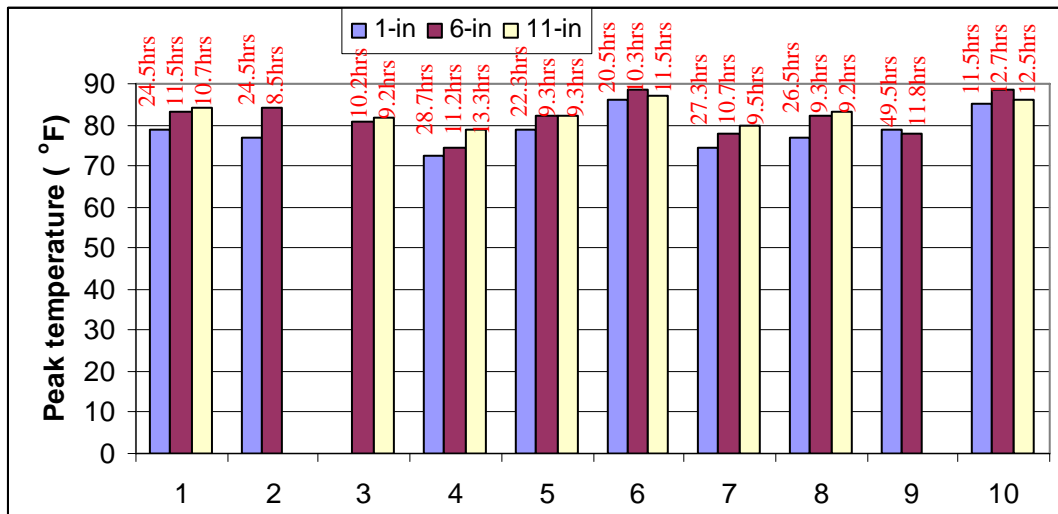


Figure 6.29 Maximum temperature for each test section

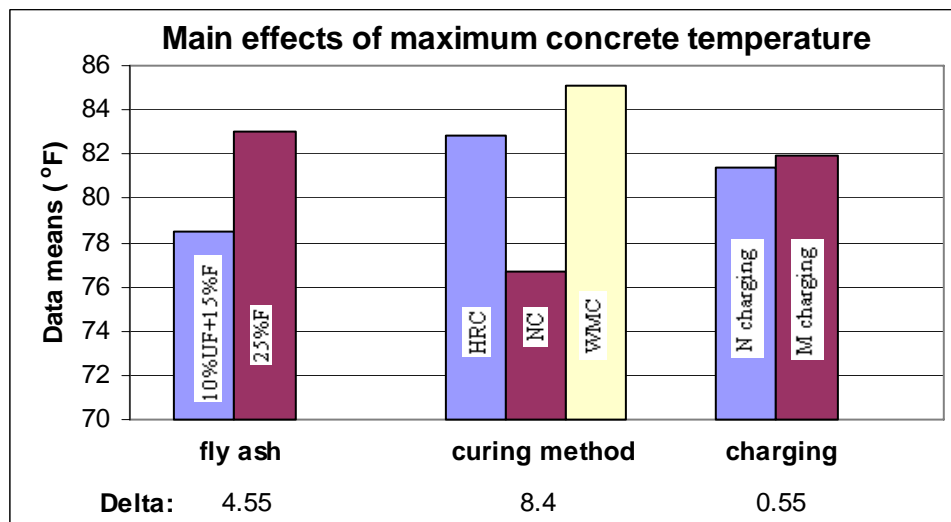
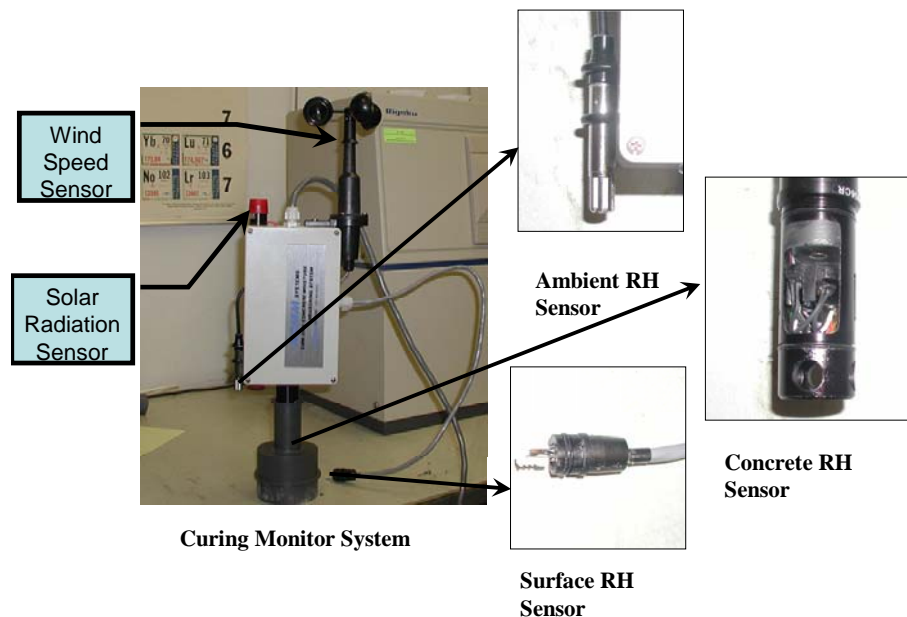


Figure 6.30 Main effects plot for maximum concrete temperature

*Moisture Profiles*

Moisture profiles at different locations (i.e. surface, ambient, and 1 in below the surface) were measured by curing monitor system (CMS) (as shown in Figure 6.31). Figure 6.32

gives an example of time histories of relative humidity for one of test sections (section 2), and complete data can be referred in Appendix B. At any time, the ambient relative humidity was lower than those of concrete. When the concrete is placed initially, the relative humidity values at the surface and 1 in below the surface of concrete were very close to each other, however, with the time, the surface relative humidity becomes lower than the relative humidity at 1 in below the surface. In addition, the development of ambient relative humidity with the time follows a cyclic pattern. However, the moisture profile at the surface and 1 in below the surface varied with the different materials and curing methods. The data of relative humidity at both top and bottom of the concrete slab were used as boundary conditions for stress analysis to assess the possibility of delamination occurrence for each test section, which will be reported later.



**Figure 6.31 CMS setup**

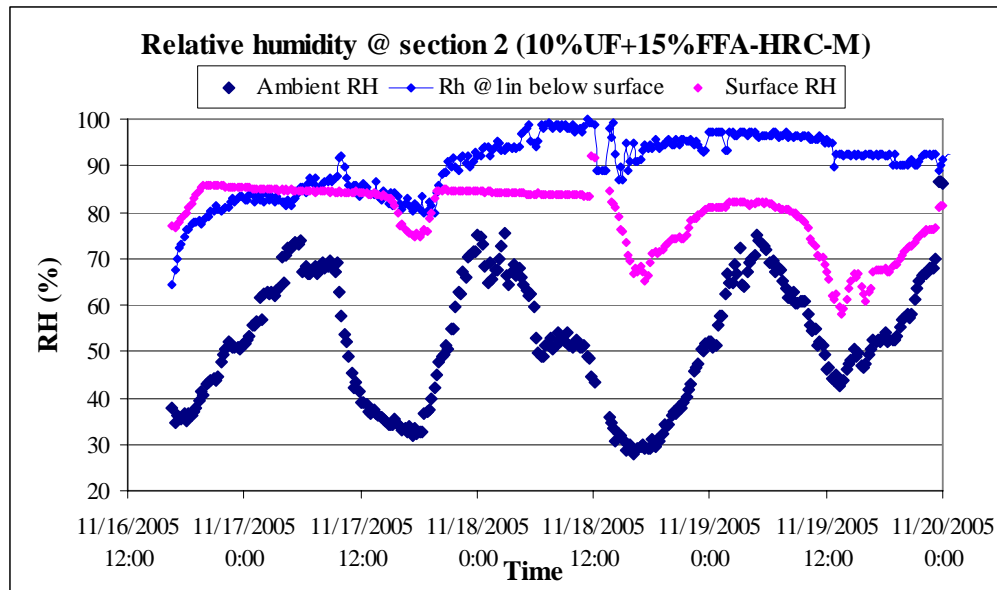


**Figure 6.32 Moisture profiles of test section 2**

Figure 6.33 illustrates total evaporation of concrete sections at 24 hours. The higher total evaporation, the worse curing quality of concrete pavements. As shown in Figure 6.33, the total evaporation of section 2 (HRC + 10% ultra fine fly ash + 15% Class F fly ash + modified charging sequence) at 24 hours was less than half of that of section 4 (NC + 10% ultra fine fly ash + 15% Class F fly ash + modified charging sequence), which indicated much higher curing effectiveness of HRC than NC for concrete at age of one day.

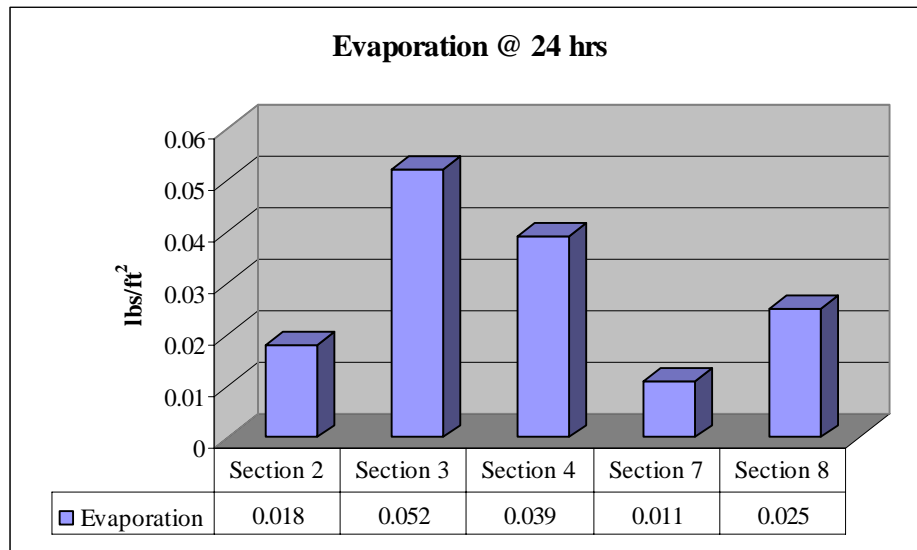


**Figure 6.33 Total evaporation of concrete at 24 hours**

### *Drying Shrinkage*

To measure the strain in the concrete, ten vibrating wire strain gages (VWG, shown in Figure 6.27 (b)) (four from TTI and the other six from CTR) were installed at 1 inch below the surface for all test sections. Ten concrete shrinkage bar specimens were also cast according to ASTM C157 for unrestrained shrinkage strain measurements with VWGs placed within the specimens.

Figure 6.34 illustrates the free shrinkage strain development with time for all test sections. It can be seen that for all most all sections free shrinkage strain increases with time, and maximum free shrinkage strain occurs at the later stage of analysis period. Figure 6.35 illustrates their maximum free shrinkage strain within 7-day analysis period. The comparisons between section 1 and 5, 3 and 7, 4 and 8, and 9 and 10 show that the combination of 10% ultra-fine fly ash and 15% of Class F fly ash presented lower maximum free shrinkage than that of 25% of Class F fly ash. The comparisons between 2 and 4, 6 and 8, and also among 1, 3, and 9, among 5, 7, and 10 show that HRC provided highest maximum free shrinkage strain among these three curing methods,

which implies that HRC appears to be effective at very early age of concrete, and become less effective with the time. These results are also consistent with the result from experimental design analysis shown in Figure 6.36, which illustrates the main effects plot for maximum free shrinkage strain. Again, based on Delta statistics, these factors followed a decreasing rank order with respect to their relative importance to the maximum free shrinkage: curing method, fly ash content, and charging sequencing. Curing method has the most significant effect on the shrinkage development. Compared with the other two design factors, the effect of charging sequence on the maximum free shrinkage strain was not significant.

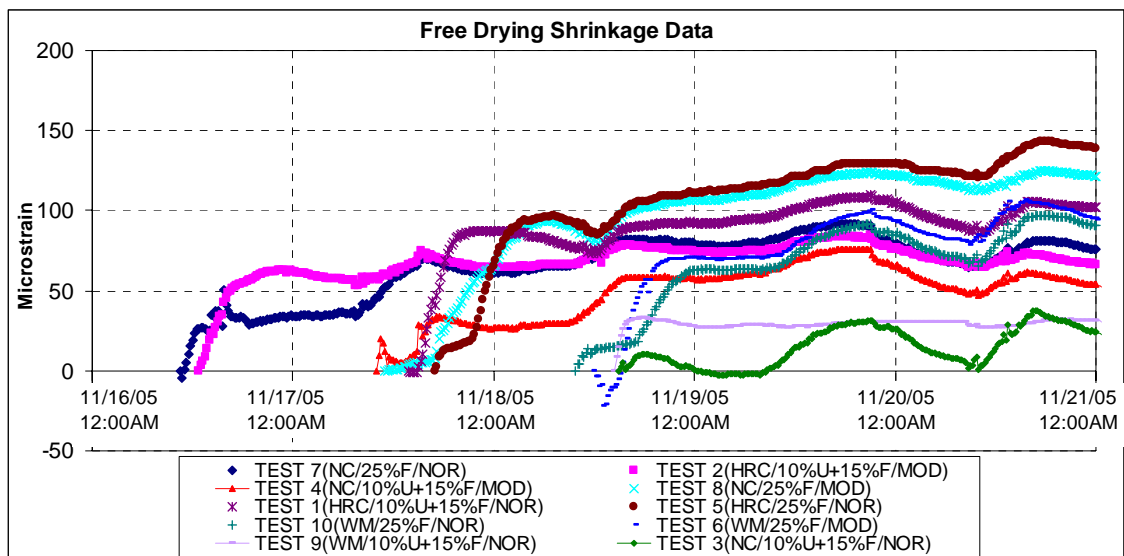


**Figure 6.34 Free shrinkage with time for different sections**

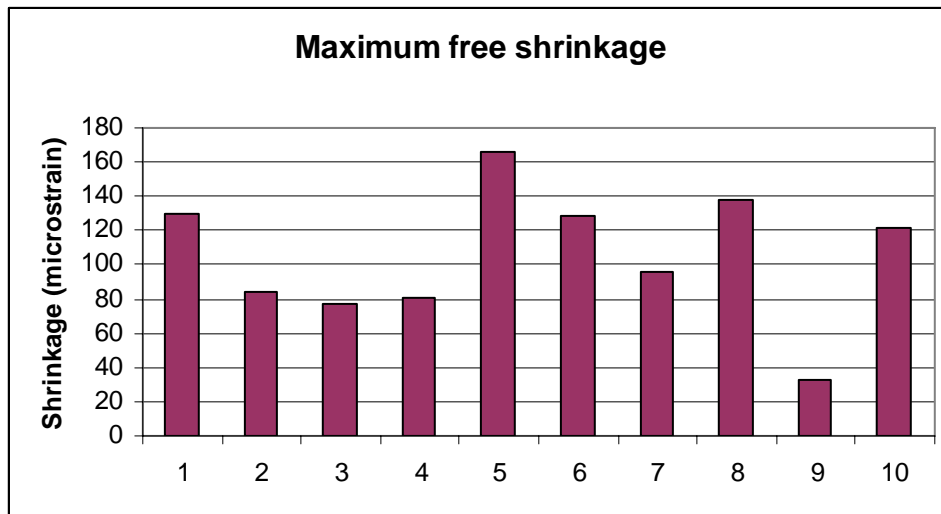


Figure 6.35 Maximum free shrinkage of concrete

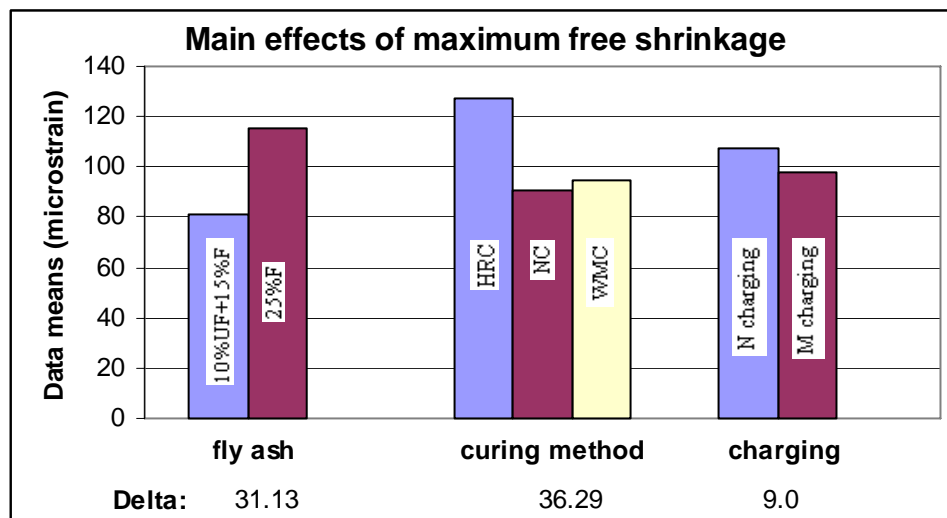
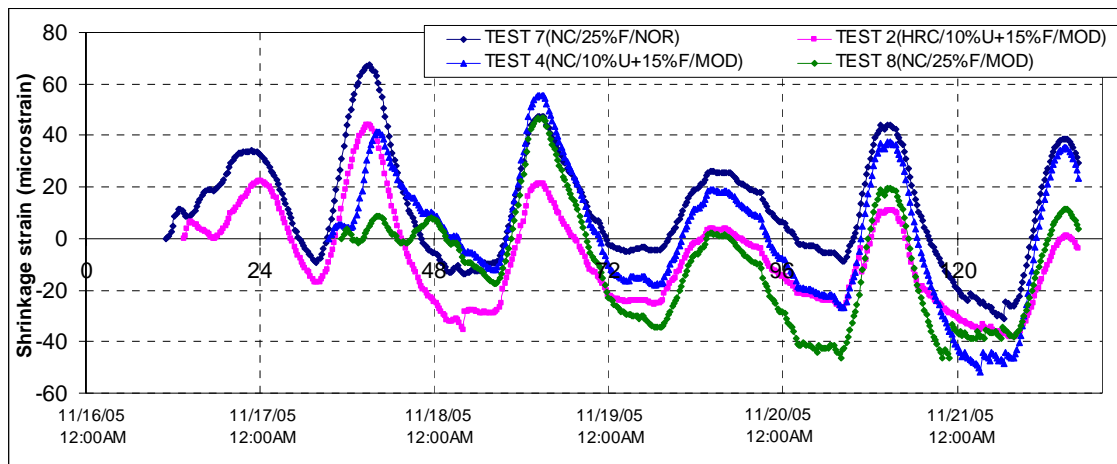


Figure 6.36 Main effects plot for maximum free shrinkage

Figure 6.37 presents the gage shrinkage strain development with time for test section 2, 4, 7, and 8 from VWGs. For all test sections, the development of gage shrinkage in the concrete followed a cyclic pattern, which indicated the gage shrinkage

is a function of not only concrete material properties but also curing methods and environmental effects.



**Figure 6.37 Gage strains with time for different sections**

Figure 6.38 illustrates the maximum creep strains for all test sections after subtracting thermal effect and drying shrinkage from the curves of gage shrinkage strains. Figure 6.39 indicates the significance of each design factor related to the maximum creep of concrete. It is found that these factors showed similar relative importance to the maximum creep strain. With respect to the maximum creep strain, these factors followed a same decreasing rank order as that for the maximum free shrinkage: curing method, fly ash content, and charging sequencing. Again, the combination of 10% ultra-fine fly ash and 15% of Class F fly ash presented lower maximum creep strain than that of 25% of Class F fly ash. HRC provided highest maximum creep strain among these three curing methods, which again implies that HRC appears to be effective at very early age of concrete, and become less effective with the time. Compared with the other two design factors, the effect of charging sequence on the maximum creep strain was not significant because of its very low Delta value.



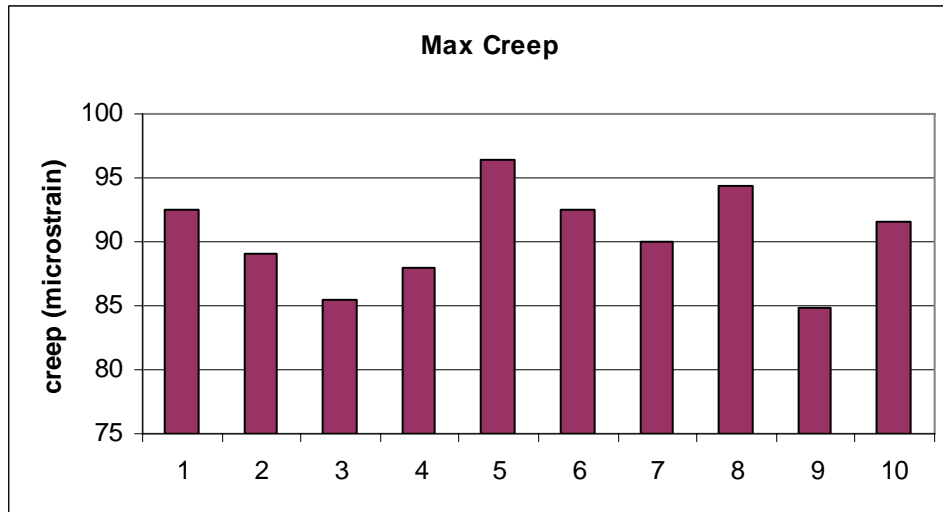


Figure 6.38 Maximum creep for different sections

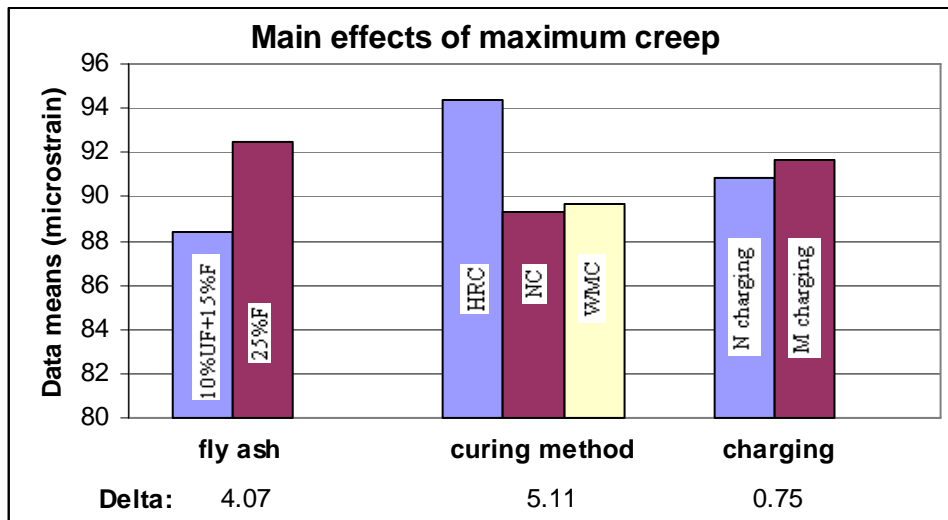
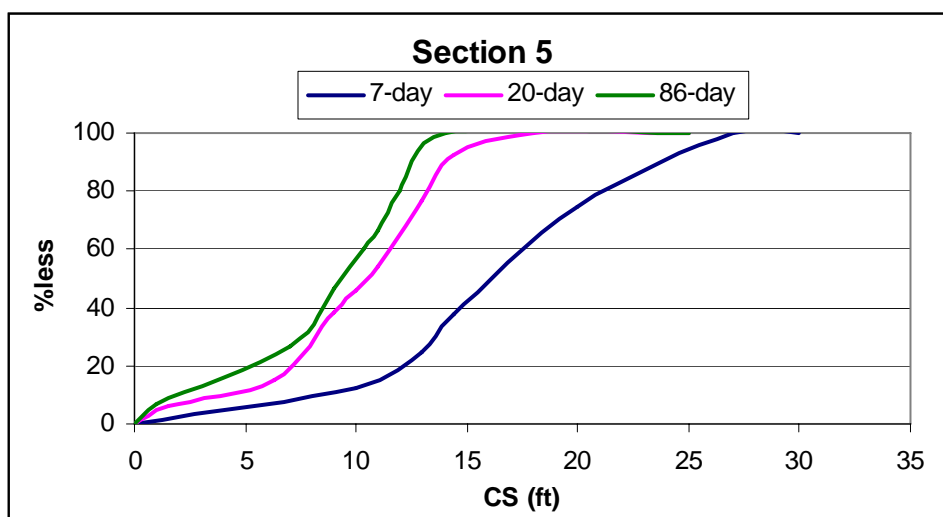


Figure 6.39 Main effects plot for maximum creep

### *Pavement Survey*

Pavement crack survey of ten test sections was conducted on November 19<sup>th</sup>, November 20<sup>th</sup>, November 23<sup>rd</sup>, November 24<sup>th</sup>, November 29<sup>th</sup>, December 7<sup>th</sup>, December 19<sup>th</sup>, February 11<sup>th</sup>, and March 24<sup>th</sup>, which included collecting number of cracks, and crack spacing and crack width of each crack. The first crack was detected on section 7 in the morning of November 19<sup>th</sup> on the 3<sup>rd</sup> day after paving. Figure 6.40 shows the probability of crack spacing at different concrete ages, using data of section 5 as an example. The probability of crack spacing less than a given value presented a sigmoidal shape. With the age, the curve shifted to the left gradually, which indicated that the probability of crack spacing less than a given value increased. Figure 6.41 compares the development of crack spacing for all test sections. At an early age of the concrete the crack spacing for each section was large due to only a few cracks developing. The increase in the numbers of cracks with the time resulted in the decrease of average crack spacing for each section. In addition, the decrease of average crack spacing with time got slower, which can be reflected from close values for crack spacing at 20 days and 126 days of concrete age.



**Figure 6.40 Crack development with time**

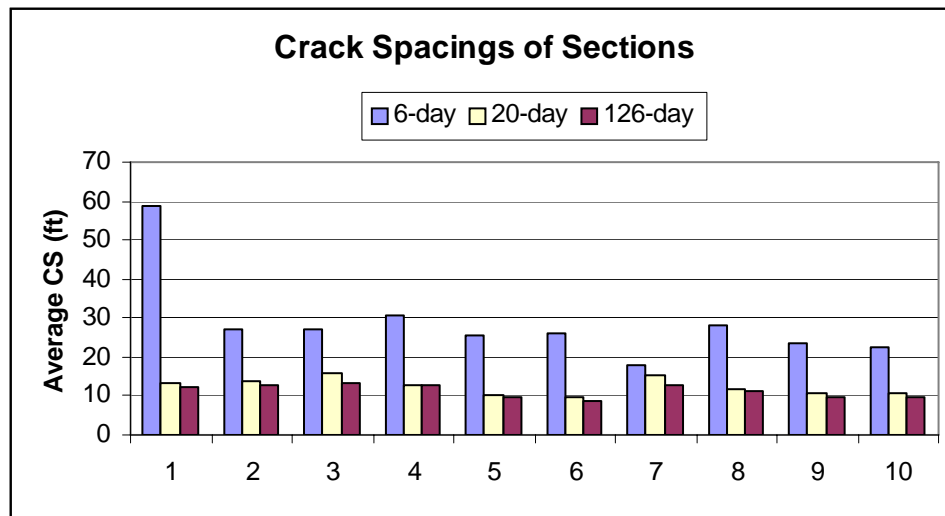


**Figure 6.41 Crack spacing for concrete sections**

### *Concrete Strength*

Figure 6.42 illustrates the 4-day compressive strength of concrete for all sections, and data of other compressive strength, flexural strength, elastic modulus, and coefficient of thermal expansion more strength data is listed in Appendix B. It can be seen that except for section 7, other sections had very similar compressive strength values. This was because that after the concrete specimens for all sections were cast, they were moved to the laboratory and cured in water tank, which then made the design combinations different from the original designs. Instead, the design combinations for section 1, 3, and 9 were same, which was: water curing/10%U+15%F/NOR; those for section 2 and 4 were same, which was water curing/10%U+15%F/MOR; those for section 5, 7, and 10 were same, which was: water curing/25%F/NOR; and those for section 6 and 8 were same, which was: water curing/25%F/MOR. The very close strength data resulted from the exclusion of the effect of curing method in the original designs, which has much more significant effect than the other factors. In addition, section 7 showed the lowest strength data. This is because that the concrete mixture for section 7 was very dry, and it

was difficult to be placed. Additional water was applied to facilitate casting, which at the same time compromised the strength development.

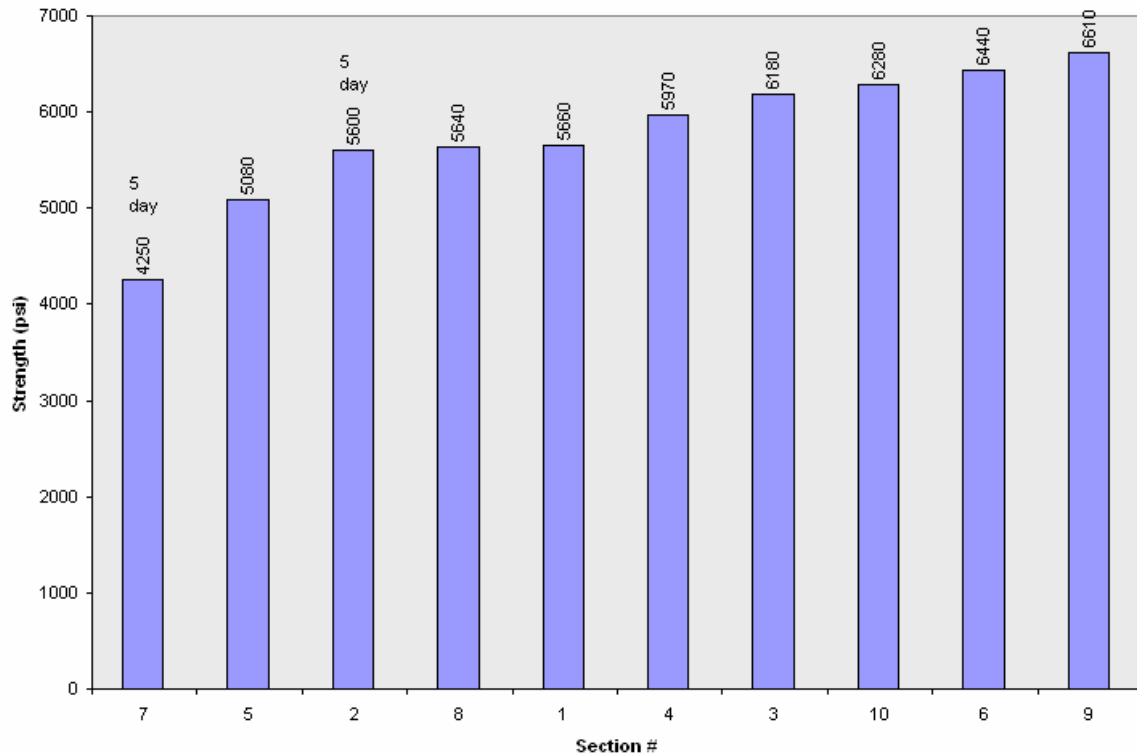


**Figure 6.42 4-day compressive strength of concrete for all test sections**

### *Field Fracture Toughness Testing*

As described in Chapter III, the fracture toughness value at early ages of concrete was used to represent the interfacial bond between aggregate and mortar and the variable-notch one-size split-tensile test method developed at TTI was applied to facilitate measurement of fracture toughness values. During paving, concrete fracture specimens were cast in cylinder molds for the purpose of determining the interfacial bond between aggregate and mortar. Previous field experience has shown that a few days after paving

is the most critical time for delaminations to form in concrete paving. On this basis, test results were obtained for concrete at ages of both 1-day and 3-day. Figure 6.43 (a) and (b) showed the specimens cast in the field and the equipment for split-tensile testing, respectively.

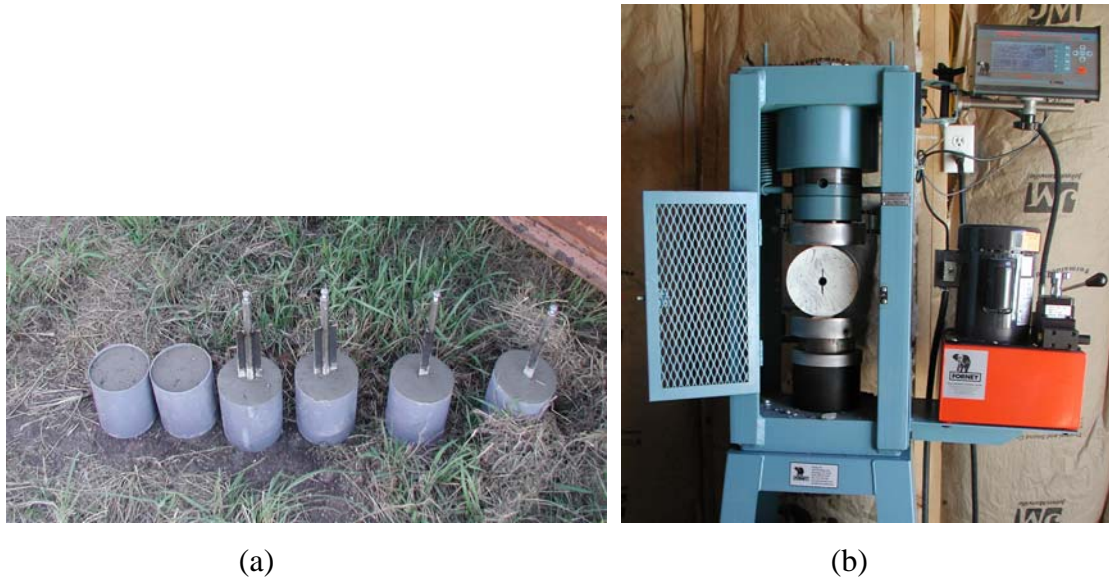


**Figure 6.43 Fracture toughness tests**

Figure 6.44 summarizes fracture toughness results for each test section. It can be seen that the interfacial bond between aggregate and mortar increased at different degrees with the time. Different design combinations produced different improvement of interfacial bond. Section 6 (i.e. 25% Class F fly ash + WMC + modified charging sequence) resulted in highest bonding strength among all test sections. The effectiveness of wet mat curing method can be observed from comparison among section 1, 3, and 9; section 5, 7, and 10; comparison between 2 and 4, and between 6 and 8. However, the effects of other factors on the bonding strength were not clear from results in Figure 6.44 only.

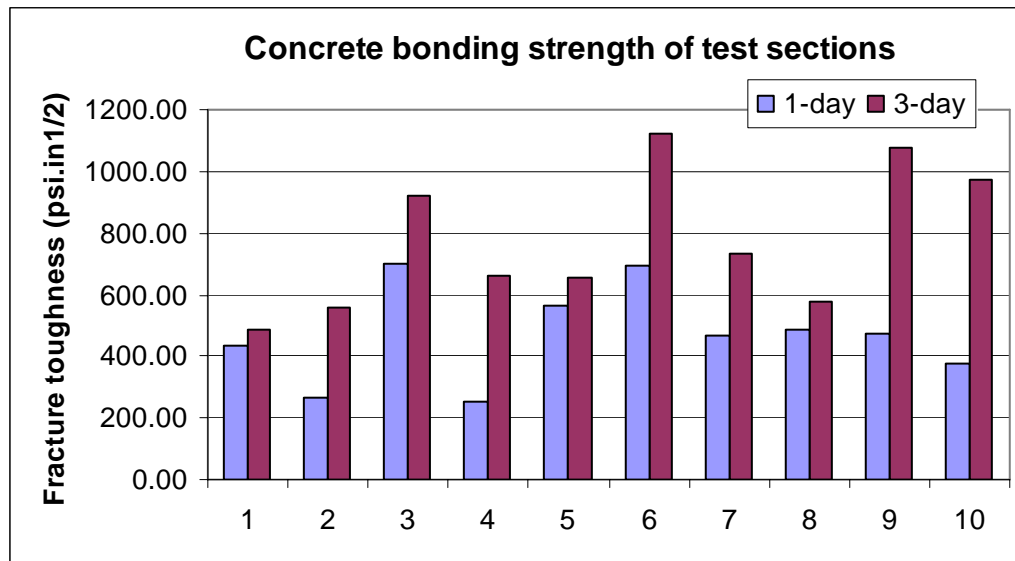


**Figure 6.44 Summary of fracture toughness for each section**

Hence, experimental design analysis was further conducted to check the relative importance of each design factors and the best level for each factor. Figure 6.45 is the main effects plot for means of all design factors at concrete age of 1-day. Based on the Delta values, these factors showed a decreasing order related to their relative importance to the bonding performance: curing method > fly ash > charging sequence. The factor of curing method was identified as the most significant factor relative to the bonding performance. For each factor, higher level average indicates the better level of this factor in terms of the bonding performance. It can be seen that for curing methods, WMC showed the best performance, and HRC was better than NC. With respect to the 1-day bonding performance, the level of 25% of Class F fly ash was better than that of the combination of 10% ultra-fine fly ash and 15% of Class F fly ash. However, the level of normal charging sequence was better than that of modified charging sequence, which was not consistent with the result from the laboratory investigation.

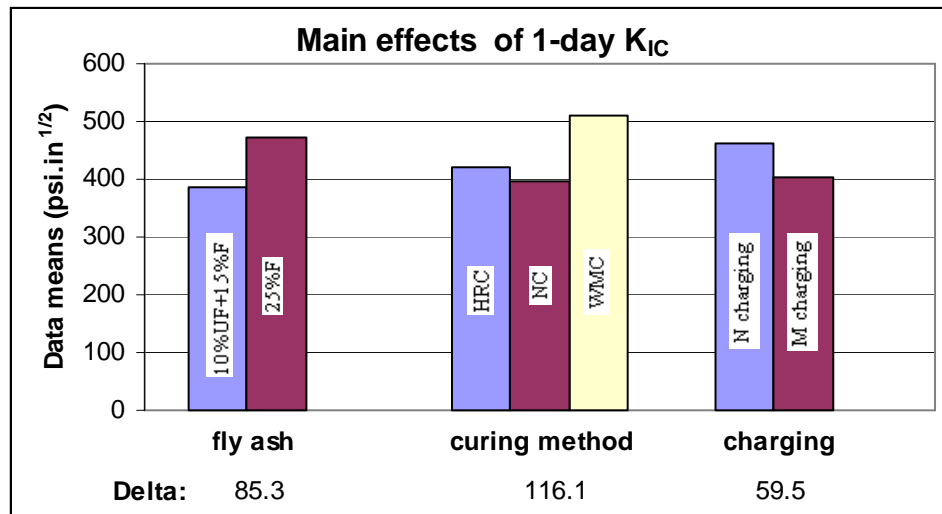
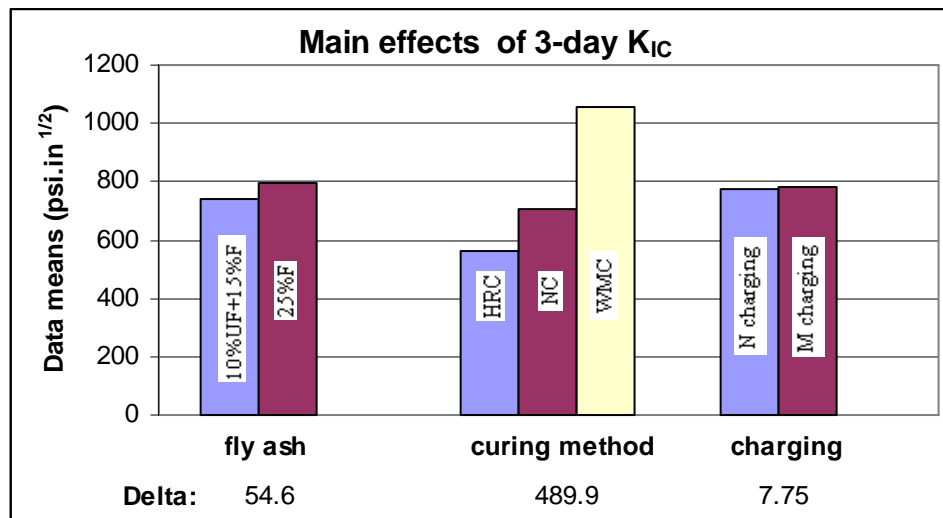


Figure 6.45 Main effects plot for 1-day  $K_{IC}$

Figure 6.46 illustrates the main effects plot for means of all design factors at concrete age of 3-day. Same as the case for 1-day  $K_{IC}$ , these factors followed same trend of their relative importances, and the factor of curing method was identified as the most significant factor relative to the bonding performance. Compared with the levels of each factor for 1-day  $K_{IC}$  case, for curing method, NC showed better 3-day  $K_{IC}$  than HRC. The previous analysis also showed that HRC provided highest shrinkage and creep development at later stage of 7-day period. HRC may be only effective during very short period after paving, which is needed to be testified. About the charging sequence, for output of 3-day  $K_{IC}$ , these two different charging sequences provided very close performance, which means that within the scope of the test sections, this factor was not significantly related to the  $K_{IC}$ . The main reason for this may be that different from the experimental design for the laboratory described in Chapter III, all design combinations for test sections were designed with 0.4 of w/cm and dense-graded aggregates, which already ensured very low probability of delamination and good quality of concrete, as investigated in the laboratory. It will also be addressed in the next section about assessment of delamination probability. As a result, on the basis of low w/cm and dense-

graded aggregates, the improvement of concrete bonding performance provided by charging sequence appear to not as significant as it should be. Furthermore, the actual operation of charging sequences in the field may cause the levels chosen for charging sequence not significantly different.



**Figure 6.46 Main effects plot for 3-day  $K_{IC}$**

#### *Validation of GPR Detection Protocol*

Ground coupled GPR technique was conducted on November 28<sup>th</sup> (within days after placement of the test sections) to track possible delamination development over time. Figures 6.47 and 6.48 give examples of GPR graphic output crossing crack #48 at section 2 and crack #21 at section 4, respectively. The markers in the figures show the locations of the cracks. Complete data of GPR test is included in Appendix A.



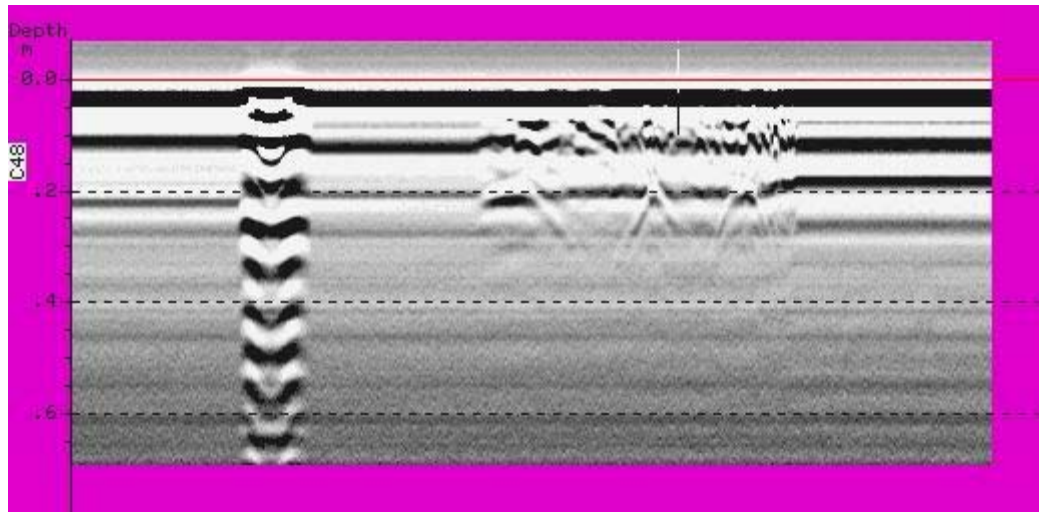


**Figure 6.47 GPR output at crack #48 of section 2**

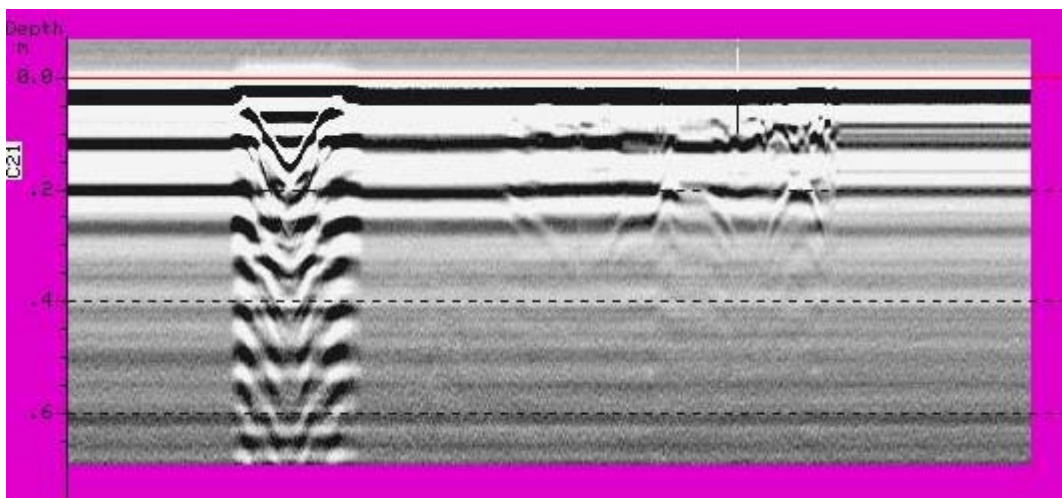


**Figure 6.48 GPR output at crack #21 of section 4**

The delamination detection protocol developed was used to analyze the GPR data collected from test sections. Figure 6.49 illustrates the summary of peak values comparison of GPR data from various locations of test sections, and Figure 6.50 illustrates probability of  $(V_2 - V_1)$  less than a certain value for GPR data. It can be seen

that the probability of  $(V_2 - V_1)$  less than minus 0.3 voltages was zero, which indicated that there was no delamination detected from test sections. This conclusion was also confirmed from visual observation of concrete cores retrieved on November 28<sup>th</sup>, 2005. Eleven cores were taken from tested cracks at all test sections, and there was no any shallow horizontal delamination.

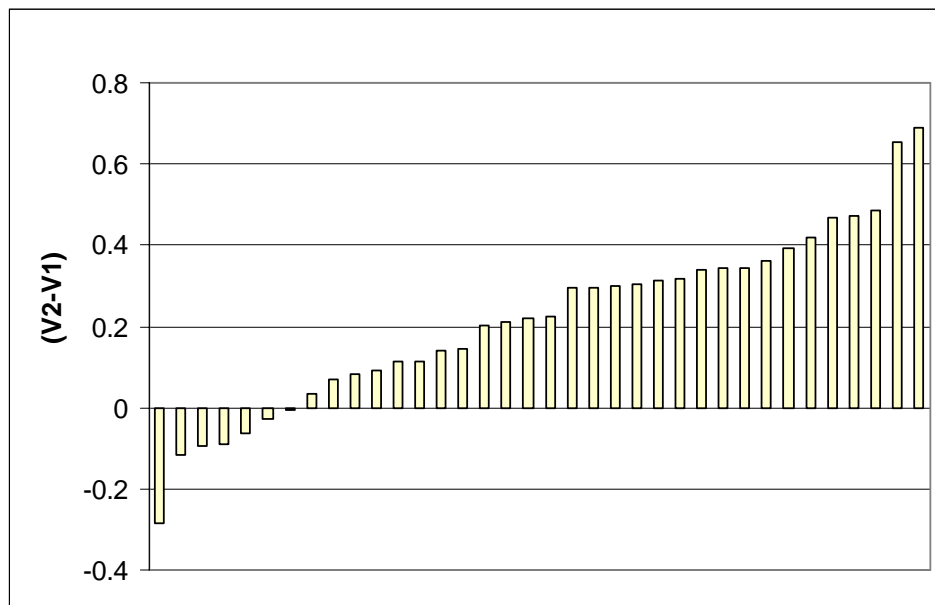


**Figure 6.49 Peak values comparison of GPR data from SH 288**

Figure 6.51 compares the probability of  $(V_2 - V_1)$  less than a specific value for SH 6, US 290 and SH 288. Compared with the curve for SH 6 and US 290, it is obvious that not only the probability of  $(V_2 - V_1)$  less than zero for SH 288 was less, but also that less than minus 0.3 voltages was zero, which indicated that the material design combinations applied in concrete paving on test sections at SH 288 effectively mitigated the early age delamination problem. This result was also correlated to the stress analysis described in previous section.

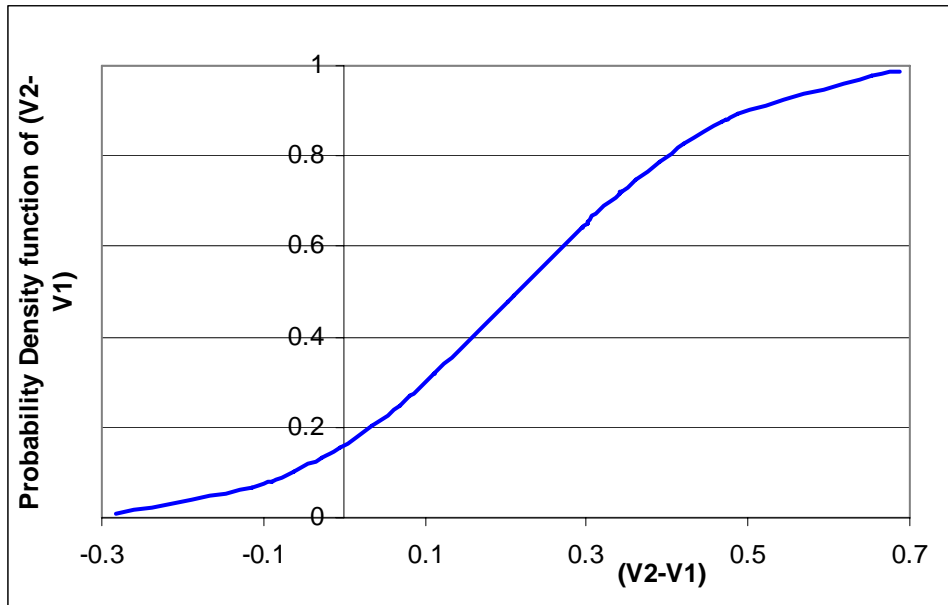


**Figure 6.50 Probability of  $(V_2 - V_1)$  for SH 288**

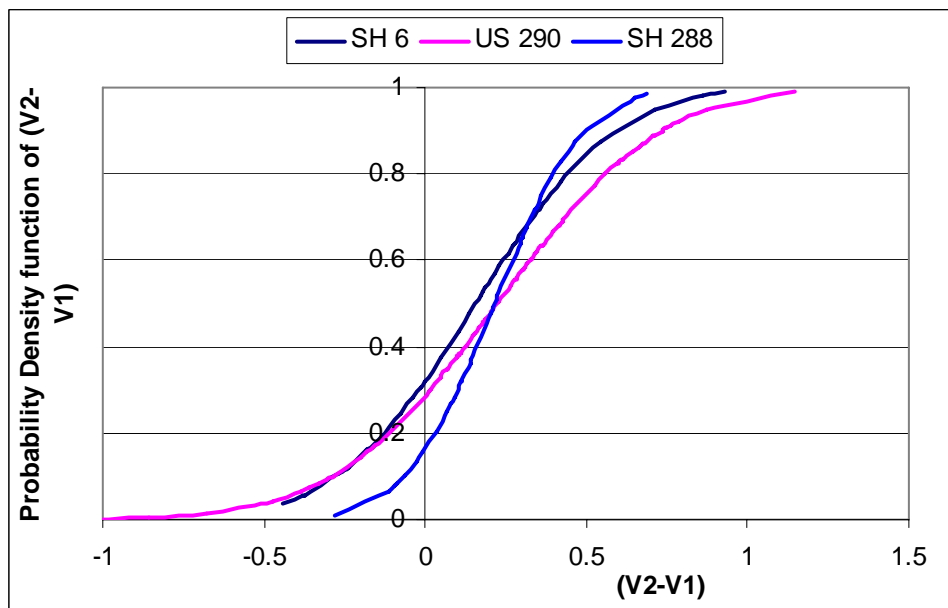


**Figure 6.51 Summary of probability of  $(V_2 - V_1)$**

### *Assessment of Delamination Probability*

In Chapter V, an approach to predict the delamination occurrence by comparing  $K_I$  (stress) and  $K_{IC}$  (strength) was proposed. Therefore, in this section, this approach was applied to assess the delamination occurrence probability. Because delamination results from a combination of material and environment effects, this analysis incorporated the net effect of climatic parameters, mix design parameters, material properties, hydration parameters, curing methods, and concrete properties such as elastic modulus, compressive strength, and shrinkage strains.

The stress analysis for all sections were conducted using the above data as inputs, and the complete results are shown in Appendix B. Here Figures 6.52, 6.53 and 6.54 give some of examples. Figure 6.52 (a) compares the development of stress and strength with the time for section 3. Through the whole analysis period of over 150 hours, the stress didn't surpass the strength at any time, which indicates that there was no delamination. The result was also confirmed from the concrete core taken in section 3, as shown in Figure 6.52 (b). From the core, it can be seen that there was no horizontal delamination at a shallow depth below the surface from both the concrete core and also from the wall of the core hole. Instead, the concrete core broke at the location of the steel bar, where was due to the coring operation. The result was also consistent with analysis from UTEP research team.

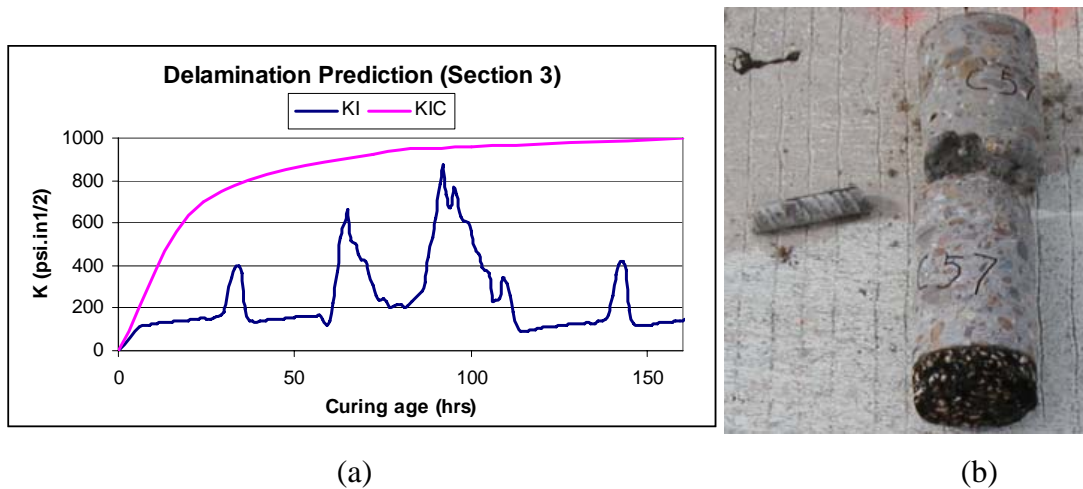


**Figure 6.52 Delamination prediction for section 3**

Figure 6.53 compares the development of stress and strength with the time for section 2. It can be seen that through the whole analysis period of over 150 hours, there were a few occasions where the stress exceeded the strength, which indicates a greater possibility of delamination occurrence. The result was also correlated with the petrography analysis shown in Figure 6.54. At the aggregate-mortar interface, there was a low concentration of  $\text{Ca}(\text{OH})_2$ , which tends to reduce the interfacial bonding, and subsequently, result in an increased probability of horizontal delamination occurrence.

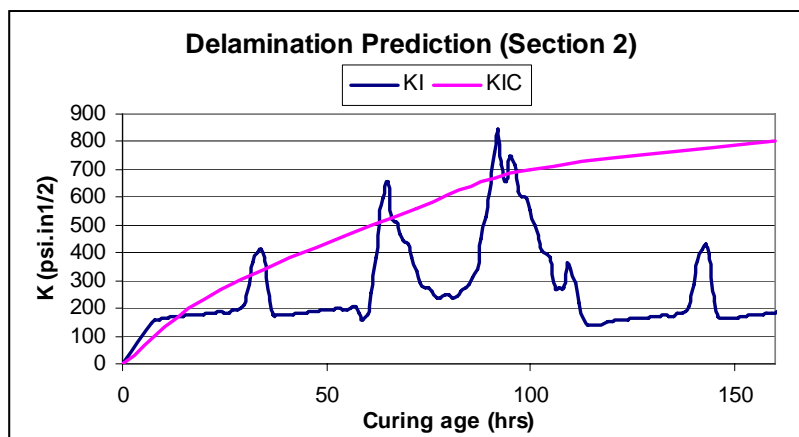


**Figure 6.53 Delamination prediction for section 2**

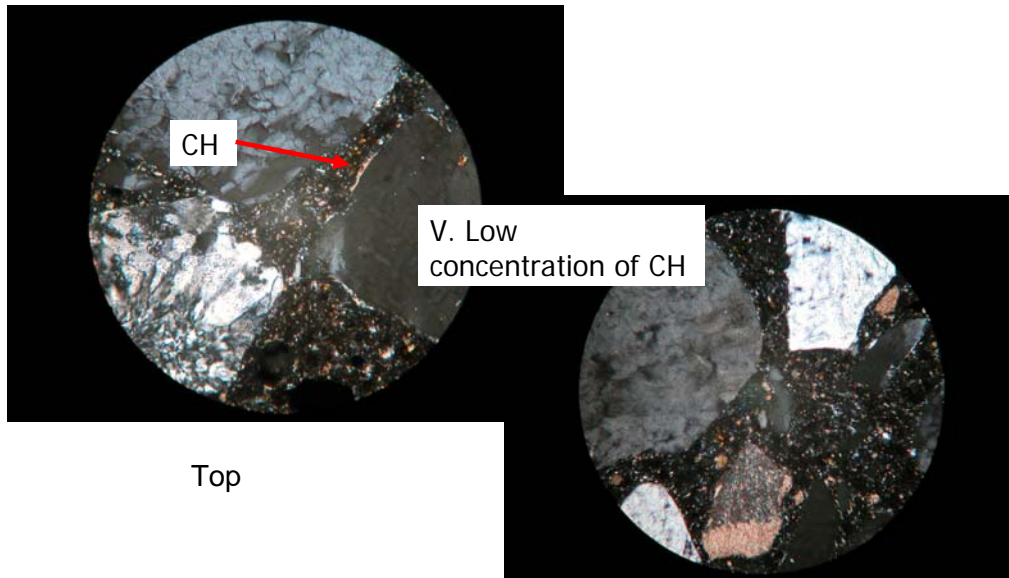


**Figure 6.54 Petrography analysis of section 2**

Figure 6.55 compares the development of stress and strength with the time for section 4. It can be seen that over the analysis period of over 150 hours, there were more occasions where the stress exceeded the strength than section 2, which indicates the higher probability of delamination occurrence. The result was also correlated with the petrography analysis shown in Figure 6.56, where at the aggregate-mortar interface, there was a very fine horizontal crack.

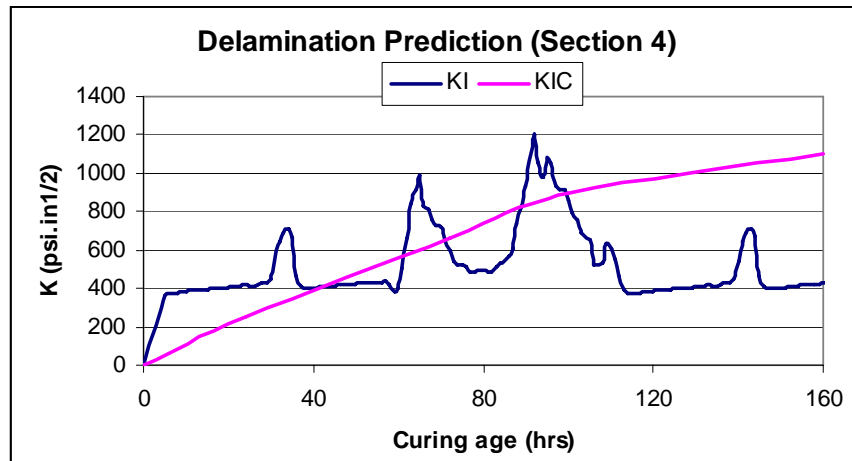
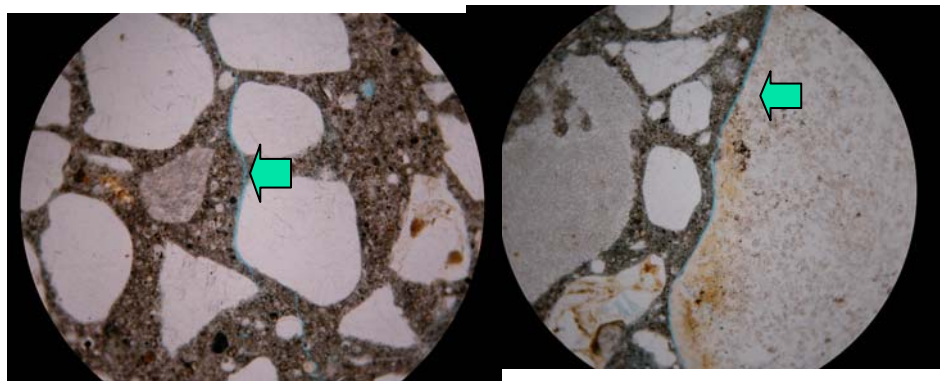


**Figure 6.55 Delamination prediction for section 4**



Fine Horizontal cracking at ~ 0.5 inch)

**Figure 6.56 Petrography analysis of section 4**

### *Establishment of Tentative Guidelines*

For each test section, the probability density function of the difference between strength and stress (i.e.  $x = K_{IC} - K_I$ ) was assumed to follow a normal distribution, as shown in Figure 6.57. Delamination occurs when  $x$  is a negative value. Therefore, the shaded area in Figure 6.57 represents the probability of delamination at a given time, stress and

strength. Table 6.3 summarizes the maximum probability of delamination occurrence for test sections over the analysis period based on the stress analysis. It can be seen that most of test sections showed very low probability of delamination occurrence. The highest probability of delamination occurrence was 28%, which occurred at the curing age of 38 hours in test section 4. The results of the coring tests and NDT analysis indicated that no horizontal delamination at a shallow depth below the pavement surface was detected. Therefore, the probability of delamination occurrence below 25% was tentatively defined as a very low chance of delamination; that ranging from 25% to 50% was defined as low probability; that up to 75% was defined as medium probability; and that above 75% was defined as high probability, as illustrated in Figure 6.58. Figure 6.58 illustrates the relation between the probability of delamination occurrence and effective wind speed, which is the ratio of wind speed to relative humidity, representing the combined environmental effects on delamination occurrence.

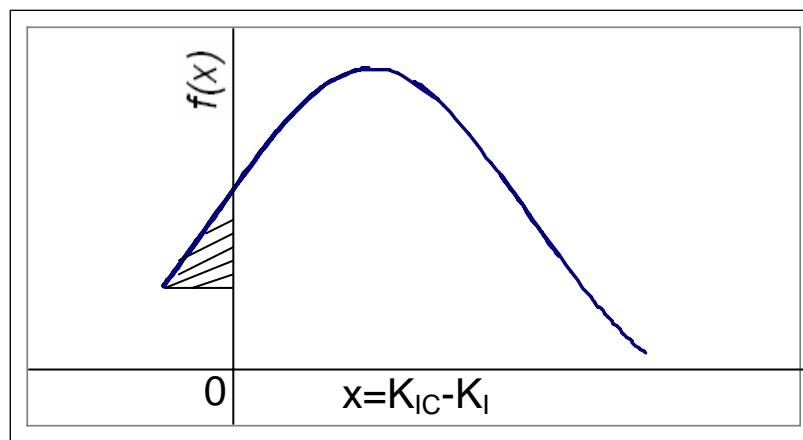


**Figure 6.57 Probability density function of stress difference**



**Table 6.3 Maximum probability of delamination occurrence**

Section	Maximum probability (%)	Curing age (hrs)
1	0.24	100
2	10.44	15
3	0	/
4	28	38
5	3.82	100
6	0	/
7	0	/
8	0	/
9	10.87	64
10	0	/

Evaporation rate (ER) can be used as a parameter to represent the curing quality of concrete pavement, combining its potential of evaporation (which is a function of the environmental factors such as wind speed, ambient temperature, ambient relative humidity, and concrete surface temperature), degree of hydration, surface moisture condition, and effective curing thickness. The higher ER, the worse curing quality of concrete pavements. It is also expected that the probability curve of delamination occurrence will shift to the right by improving the curing quality (decreasing ER), and applying early age sawcutting. The threshold values for different levels of probability of delamination occurrence and the calibration of the curves will be addressed in the future research.

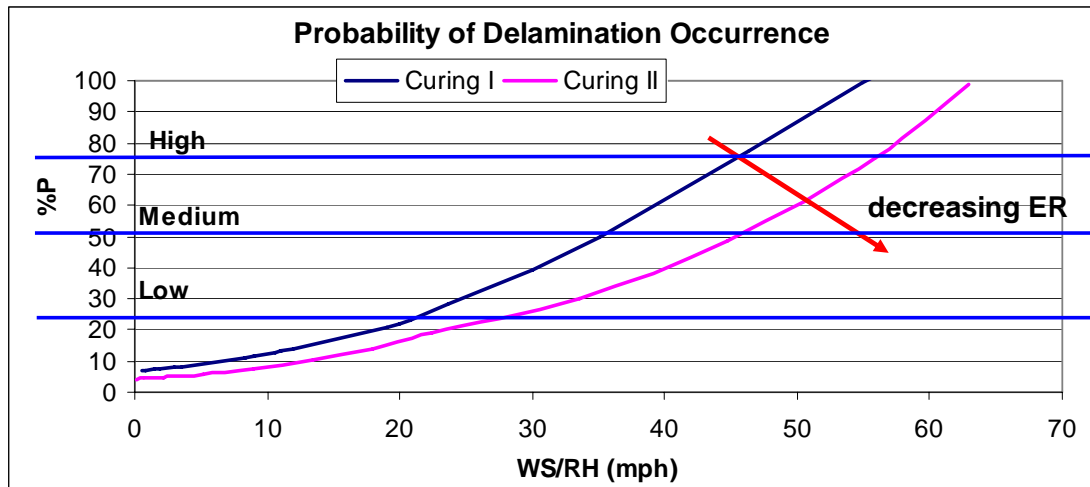


**Figure 6.58 Assessment of probability of delamination occurrence**

The flowchart in Figure 6.59 illustrates the recommendations for using gravel aggregates in concrete paving. Firstly, the overall contribution of aggregates to the concrete bonding performance is evaluated with respect to their physical, geometric and chemical properties (details of this approach can be referred from Appendix A). The rating system ranges from 0 to 10, where 10 indicates the best performance. If the rating value for a given gravel aggregate type is greater than 5, which means the aggregate has beneficial effect on concrete bonding performance, the combination of low w/cm and dense gradation of aggregates is the strategy to ensure the low probability of delamination occurrence. If the rating value for a given gravel aggregate type is less than 5, which means the aggregate type is not desirable, further assessment of probability of delamination occurrence is needed. The probability of delamination occurrence can be evaluated by the approach described above. If the probability is low, the combination of low w/cm and dense gradation of aggregates is the solution; if the probability is at medium level, the design combination will be low w/cm + dense graded aggregates + modified mixing sequence. For the condition of high probability of delamination occurrence, a combination of low w/cm + dense graded aggregates + early-aged saw

cutting or poly burlap curing (which is equivalent to wet mat curing method) is necessary to minimize the delamination problem.

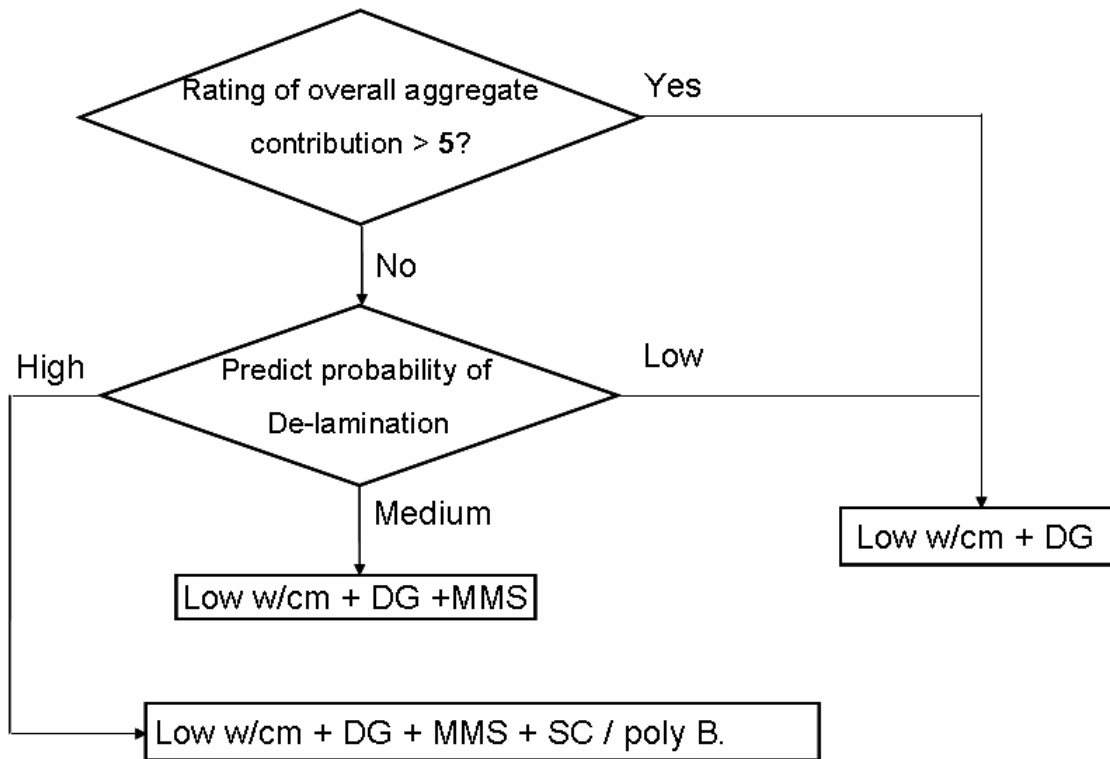


**Figure 6.59** Flowchart structure of guideline

## CHAPTER VII

### CONCLUSIONS AND RECOMMENDATIONS

#### GENERAL

The purpose of this study is to develop a test protocol to measure the bond strength between coarse aggregate and mortar, to gain a better understanding of the construction practices necessary to successfully use gravel aggregates, and to provide guidelines and recommendations to minimize early age delamination in concrete pavements made with gravel aggregates.

#### CONCLUSIONS

The following conclusions could be made from this study:

1. Fracture toughness ( $K_{IC}$ ) value at early ages of concrete was used to represent the interfacial bond between aggregate and mortar of a variety of coarse aggregates types and concrete mixtures. The variable-notch one-size split-tensile test method based on Size Effect law and its generalized theory was applied to facilitate the measurements. This method allows the use of specimens of the same size and shape but with different notch lengths, which provided for a greater amount of convenience in specimen preparation.
2. Various possible corrective measures to improve the interfacial bonding between gravel aggregate and mortar were investigated in the laboratory based on a work plan including different aggregate types, crushed aggregate, dense-gradated aggregate, modified mixing sequence, etc. The crushing treatment of aggregate did not improve the bonding performance, however, dense aggregate gradation and a modified mixing sequence showed a definite improvement in bonding performance.

3. A fractional factorial design (the Taguchi method) was applied to further identify if key material and construction parameters significantly affect the bond strength of concrete at early ages and the relative importance of those parameters in design combinations. Four factors (i.e., aggregate type, w/cm, replacement of ultra-fine fly ash, and curing method) with three levels for each factor based on the orthogonal array were considered. The significances of each factor to achieve better  $K_{IC}$  were determined, and the optimum design combination was subsequently chosen and validated. The experimental design analysis indicated the following decreasing rank order with respect to the relative importance of each factor to  $K_{IC}$ : aggregate type, curing method, w/cm, and ultra-fine fly ash content. Aggregate type was identified as the factor that most strongly affects the bond between aggregate and the mortar. The best levels for these factors included in the test program were Hanson gravel from Garwood, TX, WMC, 0.4 w/cm, and 20% ultra-fine fly ash content, respectively. HG's exhibition of best contribution on bonding performance among the three aggregates types considered in this study is different from previous research findings.
4. The Aggregate Imaging System (AIMS) at TTI was used to investigate the geometric properties (i.e. shape, texture, and angularity) of the aggregate used in the lab program. Based on original statistical parameters from AIMS, three geometric parameters (i.e. STI, SGI, and OS) were proposed to incorporate the overall shape and texture characteristics of aggregates of all sizes. These values all range from 0 to 1. The higher the value of STI, the rougher the aggregate surface. The closer to 1 of SGI, the more angular the aggregate is. In terms of OS, a higher value indicates more flat/elongated aggregates in the concrete. Therefore, these three parameters can represent various effects of aggregate shape (positive or negative effect) on concrete bonding performance.
5. A comprehensive investigation of aggregate properties relative to physical, geometric and chemical characteristics was conducted. The research findings indicated that the aggregate-mortar interfacial bond for a given cement paste was

found not to be a simple function of any one of aggregate properties, but a function of all three properties aggregated together. Different relative importance existed in different aggregate properties and different components within the property as well, which then affected the overall contribution of aggregates to the interfacial bond of concrete. This is also the reason why a specific aggregate type (i.e., HG in our study) had most desirable overall contribution on the bonding performance among the three aggregates studied, which was consistent with analysis by a rating system based on the utility theory.

6. A rating system based on utility theory was applied to evaluate the overall aggregate contribution to the concrete bonding performance and feasibility of design combinations. With appropriate combination of properties, any coarse aggregate type can provide overall positive effects on the bonding performance between the aggregate and the mortar. Based on utility theory, this study also proposed that with appropriate combination of materials and methods, most coarse aggregate deficiencies relative to bonding can be mitigated to provide satisfactory mortar-aggregate interfacial strength. The application of utility theory to the evaluation of overall contribution of aggregate properties to the bonding performance of concrete, and feasibility of design combinations enables agencies to select the best aggregate type, modify aggregates by blending different aggregates, and optimize the design combinations for concrete paving construction, to relieve delamination and further spalling distresses.
7. Reflecting another aspect of the interfacial failure, the interfacial fracture energy between aggregate and mortar which represents the energy necessary to create a crack along the interface was modeled. The model incorporates aggregate failure modes and properties of concrete, mortar and coarse aggregate, considering the concrete as a kind of three-phase composite material with the three phases being hardened cement paste, aggregate and interfacial zone between the hardened cement paste and aggregate. The relation between interfacial surface energy and material and construction factors was investigated. Due to different surface energies and fracture

energies of these two aggregates, there is a big difference of aggregate failure modes. The interfacial fracture energy of concrete made with GL was much higher than that made with VG. For concretes of all material combinations, interfacial fracture energy of concrete increases with the time. In addition, at all age of concrete made with same aggregates, interfacial fracture energy increases with the increase of both the w/cm and the cement factor of concrete. The results indicated that the interfacial fracture energy is related to the tortuosity of its crack path, which depends on the length of crack extension, and the direction of crack propagation. The interfacial fracture energy can be predicted once a design combination is known based on the linear relation with both concrete and mortar fracture energy. This model built the connection between concrete properties at meso-level (represented by the interfacial fracture energy between aggregate and mortar) and at macro-level (represented by fracture toughness of concrete and significant influencing materials and construction factors).

8. A fracture mechanics based approach was proposed with the facilitation of numerical analysis to predict the occurrence of delamination. The criterion for predicting early age delamination occurrence is that delamination occurs when  $K_I > K_{IC}$ . Two finite element software packages — TMAC<sup>2</sup> and ABAQUS were utilized to predict the development of stress intensity factor of concrete pavements at an early age with subroutines. In this numerical study, the effect of shrinkage was investigated by including the effect of the distribution and time history of moisture and time dependant moisture diffusivity. In addition, numerical analysis specifically designed for coupled thermal stress analysis was adopted for the coupled hygro-mechanical stress analysis, which greatly facilitated the calculation. The results showed that the development of  $K_I$  with time followed cycling patterns consistent with the cyclic changes of relative humidity profiles within the analysis period. Through examples of practical design and construction methods, this approach is able to assess the probability of delamination occurrence, which will facilitate selection and evaluation

of the effectiveness of pavement design methods to prevent delamination and spalling problems in concrete paving.

9. The exploration of feasibility and potential of utilizing the GPR technique for detecting delamination in concrete pavements was also performed. Various GPR data were collected from several in-service highways in Houston district, Texas. To further improve the analysis quality and facilitate data interpretation, a site calibration program was developed to obtain data for GPR waveforms (i.e., voltage versus travel time curves) at each trace point. By comparing voltage values of negative intermittent peaks in a typical GPR waveform for various locations of different concrete pavements, a threshold value of negative voltage (minus 0.3) was established to identify delamination occurrence. The results were preliminarily validated through concrete coring tests in the field, and this GPR delamination detection protocol for the field was identified as a potentially promising and useful tool for delamination assessment of concrete pavements.
10. Test sections were established based on the research findings from laboratory investigation, field testing, theoretical modeling, and numerical analysis. It verified the measures and trends relative to the practices and techniques to minimize the development of spall related delamination in CRC paving. It shows that among three design factors, curing method was the most significant factor to the concrete performance in the field. For all levels within each design factor, WMC and 25% Class F fly ash provided the best contribution to the early age concrete bonding performance. It is suggested that curing quality control is the most feasible means for minimizing early age delamination in the field. And it is not necessary to apply ultra-fine fly ash due to the role of mineral admixture being filler for early age concrete instead of pozzolanic reactivity. In addition, both the approaches for predicting delamination occurrence and field delamination detection protocol by GPR technique were further validated through the test sections. A tentative guideline was established for using gravel aggregates in concrete paving.



## RECOMMENDATIONS

The recommendations that result from this study are presented herein:

1. Complete mineralogical and chemical analysis of aggregates by advanced techniques such as XRD and SEM techniques will enhance the evaluation of overall contribution of aggregates to the concrete bonding performance. A systematic study of the ITZ of concretes made with different families of aggregates is also strongly recommended. The  $\text{Ca(OH)}_2$  orientation index can be a quantitative parameter of ITZ, which represents the degree of preferred orientation of  $\text{Ca(OH)}_2$  crystals with their c-axes normal to the aggregate surface. In addition, the investigation of the ITZ structure such as the porosity and pore size distribution with reference to different material combinations of concrete will be also valuable to link the micro-structural features of concrete with resultant engineering properties.
2. The current early age interfacial fracture energy model needs to be further optimized and validated by both numerical and experimental analysis. Multiple-phase model will be applied to simulate the randomly-distributed aggregates in the matrix. Fracture mechanical theories will be applied to simulate the crack process with different crack paths in concrete relative to different materials and construction properties, incorporating various effects of aggregates on the crack propagation such as crack deflecting, bridging, and shielding, etc.
3. In the current rating system for evaluating overall contribution of aggregates and feasibility of design combinations, properly selecting and determining weighting and rating values for each component through further laboratory investigation and engineering experience will be considered in future research to ensure the integrity of the evaluation and analysis.
4. More case studies are needed to calibrate the curve of probability of delamination occurrence vs. effective wind speed, combining improvement of curing quality and construction practice (such as different curing practices and early age sawcutting).

The threshold values for different levels of probability of delamination occurrence and the calibration of the curves need to be addressed in the future research.

5. GPR data collection from in-service concrete pavements with different pavement conditions is highly recommended to further explore application of NDT techniques in evaluating concrete pavement performance. The current filed delamination detection protocol needs to be further validated, and the accuracy of GPR application can be improved by combining its use with other NDT techniques, and facilitating program for GPR data interpretation.

## REFERENCES

- ABAQUS, Inc. (2003). "ABAQUS version 6.4 documentation."
- ACI. (1996). "Building code requirements for structural concrete." *ACI 318-95, ACI manual of concrete practice part 3: use of concrete in buildings – design, specifications, and related topics*, American Concrete Institute, Detroit, MI.
- Ahlich, R. C. (1996). "Influence of aggregate gradation and particle shape/texture on permanent deformation of hot-mix asphalt pavement." *Technical Report GL-96-1*, U. S. Army Corps of Engineers, Vicksburg, MS.
- Ahsan, T. and Taylor, D. A. (1999). "The influence of surface energies of calcium carbonate minerals on mineral-polymer interaction in polyolefin composites." *Fundamentals of adhesion and interfaces*, Gordon and Breach Science Publishers, Amsterdam, The Netherlands, 69-79.
- Akçaoğlu, T., Tokyay, M., and Çelik, T. (2002). "Effect of coarse aggregate size on interfacial cracking under uniaxial compression." *Materials Letters*, 57, 828-833.
- Alexander, K. M., Wardlaw, J., and Gilbert, D. J. (1965). "Aggregate-cement bond, cement paste strength and the strength of concrete." *Proceedings of an International conference, The Structure of Concrete and Its Behavior under Load*, Cement and Concrete Association, London, 59-81.
- Alexander, M. G. (1993). "Two experimental techniques for studying the effects of the interfacial zone between cement paste and rock." *Cement and Concrete Research*, 23, 567-575.
- Al-Rousan, T., Masad, E., Myers, L., and Speigelman, C. (2004). "Aggregate shape classification system using AIMS." *83rd Annual meeting of Transportation Research Board*, Washington, DC (CD-ROM).

Al-Rousan, T. (2004). "Characterization of Aggregate Shape Properties Using a Computer Automated System." Ph.D. dissertation, Texas A&M University, College Station, TX.

Anderson, T. L. (1995). *Fracture mechanics: fundamentals and applications*. 2<sup>nd</sup> edition, CRC Press, Inc., Boca Raton, FL.

Asbridge, A. H., Page, C. L., and Page, M. M. (2002). "Effects of metakaolin, water/binder ratio and interfacial transition zones on the microhardness of cement mortars." *Cement and Concrete Research*, 32, 1365–1369.

ASTM C 192/C. (2000). "Standard practice for making and curing concrete test specimens in the laboratory." Section 4, 04.02, Concrete and Aggregates, *Annual Book of ASTM Standards*, ASTM, West Conshohocken, PA.

Atkinson, B. K. (1987). *Fracture mechanics of rock*. Academic Press Inc., Orlando, FL.

Barrett, P. J. (1980). "The shape of rock particles, a critical review." *Sedimentology*, 27, 291-303.

Basheer, L., Basheer, P., and Long, A. (1999). "Influence of aggregate type, size and grading on interfacial transition zone in concrete." *Proceedings of the International Conference, Utilizing Ready-mixed Concrete and Mortar*, University of Dundee, Scotland, 107-119.

Bazant, Z. P. and Najjar, L. J. (1972). "Nonlinear water diffusion in nonsaturated concrete." *Materials and Structures*, 5 (25), 3-20.

Bazant, Z. P. (1970). "Constitutive equation for concrete creep and shrinkage based on thermodynamics of multiphase systems." *Materials and Structures*, 3(13), 3-36.

Bazant, Z. P. and Panula, L. (1978). "Practical prediction of time-dependent deformations of concrete. part I: shrinkage; part II: basic creep." *Materials and Structures*, 11, 307-328.

Bazant, Z. P. and Pfeifer, P. A. (1987). "Determination of fracture energy from size effect and brittleness number." *ACI Materials Journal*, 84(6), 463-480.

- Beach, E. R., Tormoen, G. W., and Drelich, J. (2002). "Pull-off forces measured between hexadecanethiol self-assembled monolayers in air using an atomic force microscope: analysis of surface free energy." *Journal of Adhesion Science Technology*, 16(7), 845-868.
- Beaudoin, J. J. (1982). "Microhardness-fracture studies: high alumina cement systems." *Cement and Concrete Research*, 12, 289-299.
- Bentur, R. A., and Cohen, M. D. (1987). "Effect of condensed silica fume on the microstructure of the interfacial zone in portland cement mortars." *Journal of the American Ceramic Society*, 70, 738-743.
- Bentz, D. P., Schlangen, E., and Garboczi, E. J. (1987). "Computer simulation of interfacial zone micro structure and its effects on the properties of cement based composites." *Material science of concrete, Vol IV*, J. Skalny and S. Mindess, eds., The American Ceramic Society, Westerville, OH, 155-199.
- Bentz, D. P., and Garboczi, E. J. (1991). "Simulation studies of the effects of mineral admixtures on the cement paste-aggregate interfacial zone." *ACI Materials Journal*, 88, 518-529.
- Bentz, D. P., Garboczi, E. J., and Stutzman, P. E. (1992). "Computer modelling of the interfacial zone in concrete." *International RILEM Conference*, Toulouse, France, E&FN Spon, London, 107- 116.
- Bijen, J., and Selst, I. (1992). "Fly ash as addition to concrete." *CUR report 144*, INTRON, Institute for Material and Environmental Research B.V., A.A. Balkema, Rotterdam.
- Bilby, B. A., and Cardew, G. E. (1975). "The crack with a kinked tip." *International Journal of Fracture*, 11 (4), 708-712.
- Boresi, A., Schmidt, R. J. and Sidebottom, O. M. (1993). *Advanced mechanics of materials*, John Wiley & Sons, Inc., New York.

- Brandt, A. M. (1995). *Cement-based composites: materials, mechanical properties and performance*, E&FN Spon, London.
- Buch, N. and Zollinger, D. G. (1993). "Preliminary investigation on effects of moisture on concrete pavement strength and behavior." *Transportation Research Record 1382*, Transportation Research Board, National Research Council, Washington, DC, 26-31.
- Buch, N. and Early, J. (1999). "The importance of mechanical bond between cement paste and aggregate." *Proceedings of the International Conference on University of Dundee, Scotland, UK, Concrete Durability and Repair Technology*, Thomas Telford Publishing, London, 133-141.
- Büyüköztürk, O., and Lee, K. (1993). "Assessment of interfacial fracture toughness in concrete composites." *Cement & Concrete Composites*, 15, 143-151.
- Carette, G., Bilodeau, A., Chevrier, R. L., and Malhotra, V. M. (1993). "Mechanical properties of concrete incorporating high volumes of fly ash from sources in the U. S." *ACI Materials Journal*, 90, 535-544.
- Chandan, C., Sivakumar, K., Fletcher, T., and Masad, E. (2004). "Geometry analysis of aggregate particles using imaging techniques." *Journal of Computing in Civil Engineering, ASCE*, 18(1), 75-82.
- Charles-Gibergues, A., Grandet, J., and Ollivier, J. P. (1982). "Contact zone between cement paste and aggregate in bond in concrete." *Bond in concrete*, P. Bartos ed., Applied Science Publishers, London, 24-33.
- Cheng, D. (2002). "Surface free energy of asphalt-aggregate system and performance analysis of asphalt concrete based on surface energy." Ph.D. Dissertation, Texas A&M University, College Station, TX.
- Cheng-yi, H., and Feldman, R. F. (1985). "Influence of silica fume on the microstructural development in cement mortars." *Cement Concrete Research*, 15 (2), 285-294.

- Chowdhury, A., and Button, W. J. (2001). "Fine aggregate angularity: conventional and unconventional approach, aggregate contribution to hot-mix asphalt HMA performance." *American Society for Testing and Materials ASTM, Special Technical Publication*, 1412, 144-159.
- Elsharief, A., Cohen, M. D., and Olek, J. (2003). "Influence of aggregate size, water cement ratio and age on the microstructure of the interfacial transition zone." *Cement and Concrete Research*, 33, 1837–1849.
- Erdogan, F. and Sih, G. C. (1963). "On the crack extension in plates under plane loading and transverse shear." *Journal of Basic Engineering*, 85, 519-525.
- Fowkes, F. M. (1962). "Determination of interfacial tensions, contact angles, and dispersion forces in surfaces by assuming additivity of intermolecular interactions in surfaces." *Journal of Physical Chemistry*, 66, 382.
- Fowler, D. W., Zollinger, D. G. Carrasquillo, R.L. and Constantino, C.A. (1996). "Aggregate tests related to performance of portland cement concrete." *Phase I Interim Report. NCHRP Project 4-20*, Transportation Research Board, National Research Council, Washington, DC.
- Goldman, A., and Bentur, A. (1989). "Bond effects in high-strength silica fume concrete." *ACI Materials Journal*, 86, 440–447.
- Goldman, A. and Bentur, A. (1992). "Interface in cementitious composites." *RELEM International Conference*, Toulouse, France, 53-61.
- Good, R. J. (1992). "Contact angle, wetting, and adhesion: a critical review." *Journal of Adhesion Science and Technology*, 6, 1269-1302.
- Grandet, J., and Ollivier, J. P. (1980). "New method for the study of cement-aggregate interfaces." *Seventh International Congress on Chemistry of Cement*, Paris, 3(7), 85- 89.
- Griffith, A. A. (1920). "The phenomena of rupture and flow of solids." *Philosophical Transactions of the Royal Society of London, Series A, Mathematical and Physical Sciences*, 221, 163-198.

Guinea, G. V., El-Sayed, K., Rocco, C. G., Elices, M., and Planas, J. (2002). "The effect of the bond between the matrix and the aggregates on the cracking mechanism and fracture parameters of concrete." *Cement and Concrete Research*, 32, 1961- 1970.

Gutierriz de Velasco, M. and McCullough, B. F. (1981). "Summary report for 1978 CRCP condition survey in Texas." *Research Report 177-20*, Center for Transportation Research, University of Texas at Austin, Austin, TX.

Hayakawa, M. and Itoh, Y. (1982). "A new concrete mixing method for improving bond mechanism." *Bond in concrete*, P. Bartos, ed., Applied Science Publishers, London, 282 – 288.

Hefer, A. W. (2004). "Adhesion in bitumen-aggregate systems and quantification of the effects of water on the adhesive bond." Ph.D. Dissertation, Texas A&M University, College Station, TX.

Hertzberg, R. W. (1976). *Deformation and fracture mechanics of engineering materials*. John Wiley & Sons, New York.

Hsu, T.T.C. and Slate, O. F. (1963). "Tensile bond strength between aggregate and cement paste or mortar." *ACI Journal*, 60(4), 465 -486.

Hu, J. (2004). "Porosity of concrete – morphological study of model concrete." Ph.D. dissertation, Delft University of Technology, The Netherlands.

Huang, C. L. D. (1979). "Multi-phase moisture transfer in porous media subjected to temperature gradient." *International Journal of Heat and Mass Transfer*, 22(9), 1295-1307.

Hutchinson, J. R. (1990). "Mixed mode fracture mechanics of interfaces." *Metal-ceramic interfaces*, M. Rühle et al., eds., Pergamon Press, New York, 295-306.

Irwin, G. R. (1948). "Fracture dynamics." *Fracturing of metals*, American Society for Metals, Cleveland, OH, 147-166.

Irwin, G. R. (1957). "Analysis of stresses and strains near the end of a crack traversing a plate." *Journal of Applied Mechanics*, 79, 361-364.



- Irwin, G. R. (1958). *Fracture encyclopedia of physics*, vol VI, S. Flugge, ed, Springer, Berlin, 551-590.
- Jeong, J. (2003). "Characterization of slab behavior and related material properties due to temperature and moisture effects." Ph.D. Dissertation, Department of Civil Engineering, Texas A&M University, College Station, TX.
- Kasi, S. S. H. and Pihlajavaara, S. E. (1969). "An approximate solution of a quasi-linear diffusion." *Publication No. 153*, The State Institute for Technical Research, Helsinki, Finland.
- Kim, H., Haas, C., Rauch, A. F., and Browne, C. (2002). "Wavelet-based 3D descriptors of aggregate particles." *Transportation Research Record 1787*, Transportation Research Board, Washington, DC.
- Knott, J. F. (1973). *Fundamentals of fracture mechanics*, Butterworths, London.
- Kosmatka, S. H., Kerkhoff, B. and Panarese, W. C. (2002). *Design and control of concrete mixtures*, Portland Cement Association, Skokie, IL.
- Langley, W.S., Carrette, G. G., and Malhotra, V.M. (1989). "Structural concrete incorporating high volumes of ASTM Class F fly ash." *ACI Materials Journal*, 86, 507–514.
- Langton, C. A. and Roy, D. M. (1980). "Morphology and microstructure of cement paste/rock interfacial regions." *7th International Congress on the Chemistry of Cement*, Paris, 127-132.
- Larbi, J.A., and Bijen, J. M. (1990). "Orientation of calcium hydroxide at the portland cement paste – aggregate interface in mortars in the presence of silica fume: A contribution." *Cement Concrete Research*, 20(3), 461–470.
- Ledbetter, W.B. et al. (1977). "Techniques for rehabilitating pavements without overlay – a systems analysis vol.1 – analysis." *Report FHWA-RD-77-132*, Texas Transportation Institute, Texas A&M University, College Station, TX.

- Lim, S. (2002). "Viscoelastic age-dependent analysis of restrained shrinkage stress development in early-age concrete." Ph.D. Dissertation, Department of Civil Engineering, Texas A&M University, College Station, TX.
- Lin, Y. (1998). *Advances in rock mechanics*, World Scientific Publishing Co., New Jersey.
- Liu, J. (2001). "Tool developing of MRR strategy selection." M.S. Thesis, Texas A&M University, College Station, TX.
- Liu, J. and Zollinger, D. G. (2005). "Shrinkage effect on stress intensity factors of concrete pavements at early age." *Workshop on Fracture Mechanics for Concrete Pavements*, International Society for Concrete Pavements, Copper Mountain, CO.
- Liu, J., Mukhopadhyay, A., and Zollinger, D. G. (2006) "Contribution of aggregates to the bonding performance of concrete." *The 85th Transportation Research Board Annual Meeting*, Washington, DC (CD-ROM).
- Liu, R., Li, J., Chen, X., and Xing, H. (2004). "GPR system user guide and troubleshooting guide." *Implementation Report 5-4414-01-1*, Subsurface Sensing Lab, Electrical and Computer Engineering, University of Houston, TX.
- Marez, N. H., and Zhou, W. (2001). "Flat and elongated: advances using digital image analysis." *Proceedings of the 9th Annual Symposium of the International Center for Aggregates Research (ICAR)*, Austin, TX (CD-ROM).
- Masad, E. (2001). "Review of imaging techniques for characterizing the shape of aggregates used in asphalt mixes." *Proceedings of the 9th Annual Symposium of the International Center for Aggregate Research (ICAR)*, Austin, TX (CD-ROM).
- Masad, E. (2003). "The development of a computer controlled image analysis system for measuring aggregate shape properties." *National Cooperative Highway Research Program NCHRP-IDEA Project 77 Final Report*, Transportation Research Board, National Research Council, Washington, DC.
- Maser, K. R. (2000). "Pavement characterization using GPR: state of the art and current practice." *Special Technical Publication 1375*, Nondestructive Testing of Pavements

and Backcalculation of Moduli. American Society for Testing and Materials, West Conshohocken, PA.

Maso, J. C. (1980). "The bond between aggregates and hydrated cement paste." *Proceedings of the 7th International Congress on the Chemistry of Cements*, Paris, 3-15.

Mason, R. L., Gunst, R. F., and Hess, J. L. (1989). *Statistical design and analysis of experiments: with application to engineering and science*, John Wiley & Sons, Inc., New York.

Mathews, P. G. (2004). *Design of experiments with MINITAB*, American Society of Quality, Quality Press, Milwaukee, WI.

Mehta, P. K., and Monteiro, P. J. M. (1988). "Effect of aggregate, cement, and mineral admixtures on the microstructure of the transition zone." *Proceedings of the Symposium, Bonding in Cementitious Composites*, Materials Research Society, Pittsburgh, PA, 114, 65-75.

Meininger, R. C. (1998). "Aggregate test related to performance of portland cement concrete pavement." *National Cooperative Highway Research Program Project 4- 20A Final Report*, Transportation Research Board, National Research Council, Washington, DC.

Mindess, S. (1988). "Bonding in cementitious composites: how important is it?" *Proceedings of the Symposium, Bonding in Cementitious Composites*, December 2-4, 1987, Boston, MA, Materials Research Society, Pittsburgh, PA, 3-20.

Mindess, S., Young, J. F. and Darwin, D. (2002). *Concrete*, Prentice-Hall Inc., Englewood Cliffs, NJ.

Mitsui, K., Li, Z., Lange, D. and Shah, S. P. (1993). "Influence of rock and cement types on the fracture properties of the interfacial zone." *Interfaces in cementitious composition*, J. C. Maso, ed., E&FN Spon, London.

Mitsui, K., Li, Z., Lange, D., and Shah, S.P. (1994). "Relationship between microstructure and mechanical properties of the paste-interface." *ACI Materials Journal*, 91, 30-39.

Mohamed A. R. and Hansen W. (1999). "Micromechanical modeling of crack-aggregate interaction in concrete materials." *Cement & Concrete Composites*, 21, 349-359.

Monteiro, P. J. M., Maso, J.C. and Ollivier, J.P. (1985). "The aggregate mortar interface." *Cement and Concrete Research*, 15, 953-958.

Monteiro, P. J. M. and Mehta, P. K. (1986). "Interaction between carbonate rock and cement paste." *Cement and Concrete Research*, 6, 127-134.

Monteiro, P. J. M. and Ostertag, C. P. (1989). "Analysis of the aggregate-cement paste interface using grazing incidence X-ray scattering." *Cement and Concrete Research*, 19, 987-988.

Morey, R. M. (1998). "Ground penetrating radar for evaluating subsurface conditions for transportation facilities." *NCHRP Synthesis Report of Highway Practice 255*, Transportation Research Board, Washington, DC.

Nehdi, M., and Mindess, S. (1997). "Computer assisted electron microscopy of high-performance concrete made with composite cement." *Proceedings of the 19th International Conference on Cement Microscopy*, Cincinnati, OH, 261-274.

Neville, A. M. (1995). *Properties of concrete*, 4th edition, John Wiley & Sons, Inc., New York.

Nuismer, R. J. (1975). "An energy release rate criterion for mixed mode fracture." *International Journal of Fracture*, 11(2), 245-250.

Orowan, E. (1948). "Fracture and strength of solids." *Report on Progress in Physics*, XII, Cavendish Laboratory, Cambridge, 185-232.

- Ozbolt, J., Reinhardt, H. W., and Xu, S. (1999). "Numerical studies on the double-edge notched mode II geometry." *Proceedings of Fracture Mechanics of Concrete Structures FRAMCOS-3*, Aedificatio Publishers, Freiburg, Germany, 773-782.
- Parrott, L. J. (1988). "Moisture profiles in drying concrete." *Advances in Cement Research*, 1, 164-170.
- Parrott, L. J. (1991). "Factors influencing relative humidity in concrete." *Magazine of Concrete Research*, 43 (154), 45-52.
- Perry, C., and Gillot, J. E. (1977). "The influence of mortar– aggregate bond strength on the behavior of concrete in uniaxial compression." *Cement and Concrete Research*, 7, 553– 564.
- Petersson, P. E. (1980). "Fracture energy of concrete: method of determination." *Cement and Concrete Research*, 10, 78-89.
- Pihlajavaara, S. E. (1964). *Introductory bibliography for research on drying of concrete*, The State Institute for Technical Research, Helsinki, Finland.
- Ping, X., and Beaudoin, J. J. (1992). "Effects of transition zone microstructure on bond strength of aggregate-portland cement paste interfaces." *Cement and Concrete Research*. 22, 23-26.
- Pope, W.A., and Jennings, M.H. (1992). "The influence of mixing on the microstructure of the cement paste/aggregate interfacial zone and on the strength of mortar." *Journal of Materials Society*, 27, 6452 – 6462.
- Popovics, S. (1966). "The use of the fineness modulus for the grading evaluation of aggregates for concrete." *Magazine of Concrete Research*, 18(56), 131-140.
- Prokopski, G. (1991). "Influence of water- cement ratio on micro - cracking of ordinary concrete." *Journal of Materials Society*, 26, 6352- 6356.
- Prokopski, G., Halbiniak, J., and Langier, B. (1997). "The examination of the fracture toughness of concretes with diverse structure." *Journal of Materials Society*, 33, 1819-1825.

- Prokopski, G., and Halbiniak, J. (2000). "Interfacial transition zone in cementitious materials." *Cement and Concrete Research*, 30, 579– 583.
- Prokopski, G., and Langier, B. (2000). "Effect of water/cement ratio and silica fume addition on the fracture toughness and morphology of fractured surfaces of gravel concretes." *Cement and Concrete Research*, 30, 1427- 1433.
- Pye, G. B., and Beaudoin, J. J. (1992). "An energy approach to bond strength determinations in cement systems." *Cement and Concrete Research*, 22, 551-558.
- Ramachandran, V. S. (1995). *Concrete admixture handbook properties, science, and technology*, 2nd edition, Noyes Publications, Norwich, NY.
- Rao, C., Tutumluer, E., and Stefanski, J. A. (2001). "Coarse aggregate shape and size properties using a new image analyzer." *ASTM Journal of Testing and Evaluation*, JTEVA, 29(5), 79-89.
- Rao, G. A. and Prasad, B. K. R. (2002). "Influence of the roughness of aggregate surface on the interface bond strength." *Cement and Concrete Research*, 32, 253-257.
- Rice, J. R. (1988). "Elastic fracture concepts for interfacial cracks." *Journal of Applied Mechanics*, 55, 98-103.
- Richard, H. A., Fulland, M., and Sander, M. (2005). *Fatigue & fracture of engineering materials & structure*, Blackwell Publishing Ltd., Malden, MA.
- Saarenketo, T., and Scullion, T. (1994). "Ground penetrating radar applications on roads and highways." *Research Report 1923-2F*, Texas Transportation Institute, the Texas A&M University System, College Station, TX.
- Saito, M., and Kawamura, M. (1986). "Resistance of the cement–aggregate interfacial zone to propagation of cracks." *Cement and Concrete Research*, 16 (5), 653– 661.
- Saito, M., and Kawamura, M. (1989). "Effect of fly ash and slag on the interfacial zone between cement and aggregate." *Fly Ash, Silica Fume, and Natural Pozzolans in Concrete, SP-114*, v.1, American Concrete Institute, Detroit, MI, 669–688.

Scholer, C. F. (1967). "The role of mortar-aggregate bond strength in the strength of concrete." *Highway Research Record*, 210, National Research Council, 108-117.

Scrivener, K. L. and Pratt, P. L. (1986). "A preliminary study of the microstructure of the cement/sand bond in mortars." *Proceedings, 8th International Congress on the Chemistry of Cement*, Vol III, FINEP, Rio de Janeiro, Brazil, 466-471.

Scrivener, K.L., and Gartner, E. M. (1988). "Micro structural gradients in cement paste around aggregate particles." *Proceedings of a Symposium of Materials Research Society*, 114, 77-85.

Scullion, T., Lau, C., and Chen, Y. (1992). "Implementation of the Texas ground penetrating radar system." *Research Report 1233-1*, Texas Transportation Institute, the Texas A&M University System, College Station, TX.

Scullion, T., Chen, Y., and Lau, C. (1995). "COLORMAP – user's manual with case studies." *Research Report 1341-1*, Texas Transportation Institute, the Texas A&M University System, College Station, TX.

Senadheera, S. and Zollinger, D. G. (1996). "Influence of coarse aggregate in portland cement concrete on spalling of concrete pavements." *Research Report 1244-11*, Texas Transportation Institute, Texas A&M University System, College Station, Texas.

Shelby, M. D. and McCullough, B. F. (1960). "Experience in Texas with continuously reinforced concrete pavement." *Highway Research Board Bulletin* 274, Highway Research Board, National Research Council, Washington, DC, 1-29.

Shilstone, J. M. Sr. (1990). "Concrete mixture optimization." *Concrete International*, 12(6), 33-39.

Sih, G.C. (1974). "Strain-energy-density factor applied to mixed mode crack problems." *International Journal of Fracture*, 10(3), 305-321.

Simeonov, P., and Ahmad, S. (1995). "Effect of transition zone on the elastic behavior of cement-based composites." *Cement and Concrete Research*, 25( 2), 165-175.

- Soares, J. B., and Zollinger, D. G. (1998). "Mechanistic evaluation of spalling distress." *Proc., 8th International Symposium on Concrete Roads; Theme III: Pavement Performance and Evaluation*, Lisbon, Portugal, 91-109.
- Somasundaram, S., Anand, N. K., Suh, Y. B., and Aung, W. (1989). "Analysis of moisture migration in two-dimensional unsaturated porous media with impermeable boundaries." *International Journal of Heat and Mass Transfer*, 32(9), 1733-1739.
- Somayaji, S. (2001). *Civil engineering materials*, 2nd edition, Prentice-Hall, Inc., Englewood Cliffs, NJ.
- Strategic Highway Research Program (SHRP). (1993). "Distress identification manual for the long-term pavement performance project." *Report No. SHRP-P338*, Transportation Research Board, Washington, DC.
- Struble, L., Skalny, J. and Mindess, S. (1980). "A review of the cement-aggregate bond." *Cement and Concrete Research*, 10, 277-286.
- Subramanian, S. (1999). "Interface in concrete- achieving performance." *Proceedings of the International Seminar, Role of Interfaces in Concrete*, University of Dundee, Scotland, UK, 97-109.
- Suh, Y. B., Anand, N. K., Aung, W., and Somasundaram, S. (1988). "Steady-state moisture profile in an unsaturated porous medium with impermeable boundaries." *International Journal of Heat and Mass Transfer*, 11(12), 2587-2589.
- Taguchi, G., Yokoyama, Y., and Wu, Y. (1993). *Taguchi methods: design of experiments*, American Supplier Institute, Inc. in conjunction with the Japanese Standards Association, Livonia, MI.
- Tamimi, A.K. (1994). "The effect of a new mixing technique on the properties of the cement paste-aggregate interface." *Cement and Concrete Research*, 24(7), 1299-1304.
- Tan, D. M., Tschegg, E. K., Rotter, H., and Kirchner, H. O. K. (1995). "Cracks at mortar-stone interfaces." *Acta Metal. Mater.*, 43(10), 3701-3707.



- Tang, T., Zollinger, D. G. and Senadheera, S. P. (1993). "Analysis of concave curling in concrete slabs." *ASCE Journal of Transportation Engineering*, 119(4), 618-633.
- Tang, T., Zollinger, D. G., and McCullough, B. F. (1994). "Field tests and analyses of concrete pavement in Texarkana and La Porte, Texas." *Research Report 1244-7*, Texas Transportation Institute, Texas A&M University System, College Station, TX.
- Tang, T., Bazant, Z. P., Yang, S., and Zollinger, D. G. (1996). "Variable-notch one-size test method for fracture energy and process zone length." *Engineering Fracture Mechanics*, 55 (3), 383-404.
- Tang, T., Yang, S. and Zollinger, D. G. (1999). "Determination of fracture energy and process zone length using variable-notch one-size specimens." *ACI Materials Journal*, 96 (1), 3-10.
- Tasong, W. A., Cripps, J. C. and Lynsdale, C. J. (1998). "Aggregate-cement chemical interaction." *Cement and Concrete Research*, 28, 1037-1048.
- Tasong, W.A., Lynsdale, C.J. and Cripps, J.C. (1999). "Aggregate– cement paste interface: part I. influence of aggregate geochemistry." *Cement and Concrete Research*, 29, 1019-1025.
- Taylor M. A., and Brooms, B. B. (1964). "Shear bond strength between coarse aggregate and cement paste or mortar." *Journal of the American Concrete Institute*, 939-957.
- Timoshenko, S. P. and Goodier, J. N. (1970). *Theory of elasticity*, 3rd edition, McGraw-hill Book Company, New York.
- Toutanji, H. A., Liu, L., El-Korchi, T. (1999). "The role of silica fume in the direct tensile strength of cement-based materials." *Materials and Structure*, 32, 203–209.
- Trende, U., and Buyukozturk, O. (1998). "Size effect and influence of aggregate roughness in interface fracture of concrete composites." *ACI Materials Journal*, 95(4), 331– 338.

- Tschegg, E.K., Rotter, H. M., Roelfstra, P. E., Bourgund, U., and Jussel, P. (1995). "Fracture mechanical behavior of aggregate-cement matrix interfaces." *Journal of Materials in Civil Engineering*, ASCE, 7, 199–203.
- Tutumluer, E., Rao, C., and Stefanski, J. (2000). "Video image analysis of aggregates." *Final Project Report, FHWA-IL-UI-278*, Civil Engineering Studies UILU-ENG-2000-2015, University of Illinois Urbana-Champaign, Urbana, IL.
- Tyler, W. S. (2001). *Particle size and shape analyzers (CPA)*, Product Brochure, Mentor, OH.
- Underwood, E. (1968). *Quantitative stereology*, Addison-Wesley Publishing Company, Reading, MA.
- Wainwright, P J, and Cabrera, J. G. (1990). "Assessment of the efficiency of chemical membranes to cure concrete." *Proceedings of an International Conference on the Protection of Concrete*, Dundee, Scotland, 907-920.
- Wang, L. and Zollinger, D. G. (2000). "A mechanistic design framework for spalling distress." *Transportation Research Record 1730*, Transportation Research Board, Washington, DC, 18-24.
- Weingart, R. L., and Prowell, B. D. (1999). "Specification development using the VDG-40 videograder for shape classification of aggregates." *Proceedings of the 7th Annual Symposium*, International Center for Aggregate Research (ICAR), University of Texas, Austin, TX, B1-2-1-B1-2-12.
- Westergaard, H. M. (1927). "Analysis of stresses in concrete pavements due to variation of temperature." *Proceedings of Highway Research Board*, Highway Research Board, Washington, DC, 6, 201-215.
- Will, J. J. (2000). "High-performance concrete using Nevada aggregates." Ph.D. dissertation, University of Nevada, Reno.

- Winslow, D. N., Cohen, M. D., Bentz, D. P., Snyder, K. A. and Garboczi, E. J. (1994). "Percolation of interfacial zone pores in cement mortar and concrete." *Cement and Concrete Research*, 24, 25-37.
- Wittmann, F. H. (1983). *Fracture mechanics of concrete*, Elsevier, Amsterdam.
- Wong, Y.L., Lam, L., Poon, C.S., and Zhou, F. P. (1999). "Properties of fly ash-modified cement mortar-aggregate interfaces." *Cement and Concrete Research*, 29, 1905-1913.
- Wu, K., Liu, J., Zhang, D. and Yan, A. (1999). "Rupture probability of coarse aggregate on fracture surface of concrete." *Cement and Concrete Research*, 29, 1983-1987.
- Wu, K., Yan, A., Yao, W., and Zhang, D. and (2002). "The influence of RPCA on the strength and fracture toughness of HPC." *Cement and Concrete Research*, 32, 351-355.
- Xin, D., Zollinger, D. G., and Allen, G. D. (1995). "An approach to determine diffusivity in hardening concrete based on measured humidity profiles." *Advanced Cement Based Materials*, 2, 138-144.
- Xu, G., Beaudoin, J. J., Jolicoeur, C. and Pagé, M. (2000). "The effect of a polynaphthalene sulfonate superplasticizer on the contribution of the interfacial transition zone to the electrical resistivity of mortars containing silica and limestone fine aggregate." *Cement and Concrete Research*, 30, 683-691.
- Yildirim, I. (2001). "Surface free energy characterization of powders". Ph.D. Dissertation, Virginia Polytechnic Institute and State University, Blacksburg, VA.
- Yuan, C., and Gud, W. J. (1998). "Effect of bond between aggregate and cement paste on the mechanical behavior of concrete." *MRS Symposium Proceedings 114*, 41-47.
- Zhang, M. H., and Gjørsv, O. E. (1990). "Microstructure of the interfacial zone between lightweight aggregate and cement paste." *Cement and Concrete Research*, 20(4), 610-618.

Zhang, M. H., Lastra, R., and Malhotra, V.M. (1996). "Rice-husk ash paste and concrete: some aspects of hydration and the microstructure of the interfacial zone between the aggregate and paste." *Cement and Concrete Research*, 26(6), 963-977.

Zhang, X. (2004). "Consolidation theories for saturated-unsaturated soils and numerical simulations of residential buildings on expansive soils." Ph.D. Dissertation, Department of Civil Engineering, Texas A&M University, College Station, TX.

Zimbelmann, R. (1985). "A contribution to the problem of cement aggregate bond." *Cement and Concrete Research*, 15, 801-808.

Zimbelmann, R. (1987). "A method for strengthening the bond between cement stone and aggregates." *Cement and Concrete Research*, 17(4), 651-660.

Zollinger, D. G., Tang, T., and Yoo, R. H. (1993). "Fracture toughness of concrete at early ages." *ACI Materials Journal*, 90(5), 463-471.

Zollinger, D. G., Senadheera, S. P., and Tang, T. (1994) "Spalling of continuously reinforced concrete pavements." *ASCE Journal of Transportation Engineering*, 120(3), 394-411.

Zollinger, D. G., Murphy, J., Shrestha, P., and McCullough, B. F. (1998). "Assessment of field tests to ensure structural design criteria for rigid pavements." *Research Report 1783-1*, Texas Transportation Institute, Texas A&M University System, College Station, TX.

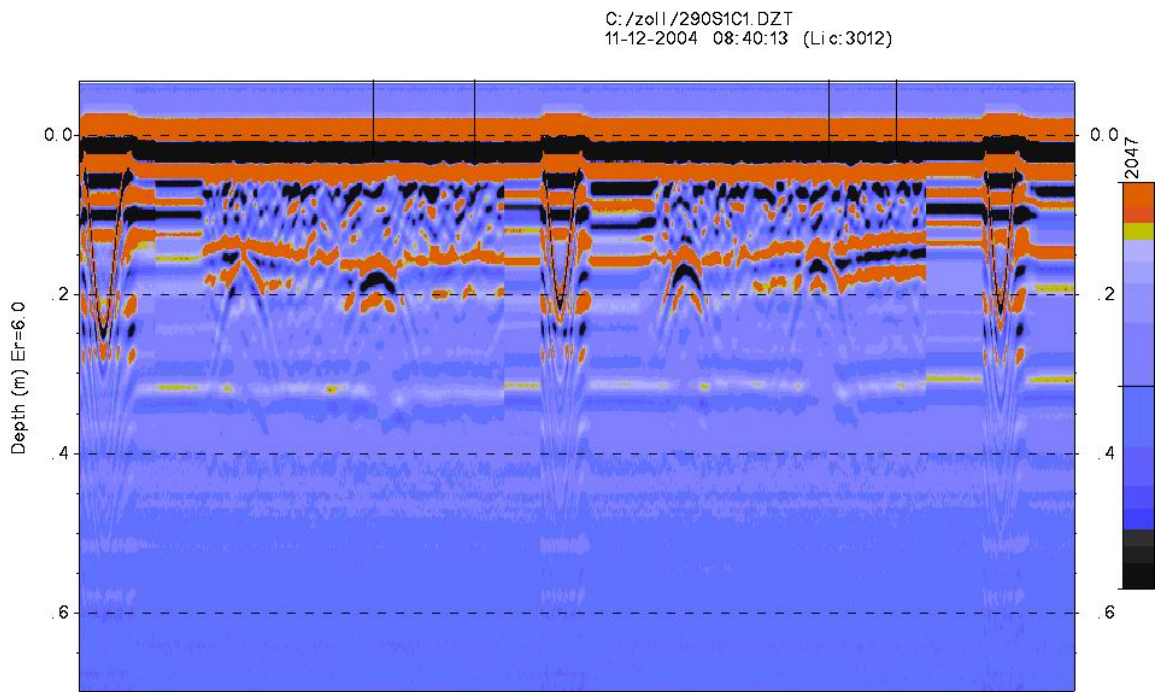
Zollinger, D. G., Tayabji, S., and Smith, K. (2004). "Repair and rehabilitation of concrete pavement: volume I." *Report FHWA-01-00080*, Texas Transportation Institute, Texas A&M University System, College Station, TX.

**APPENDIX A**

**GPR TESTS**



(a)



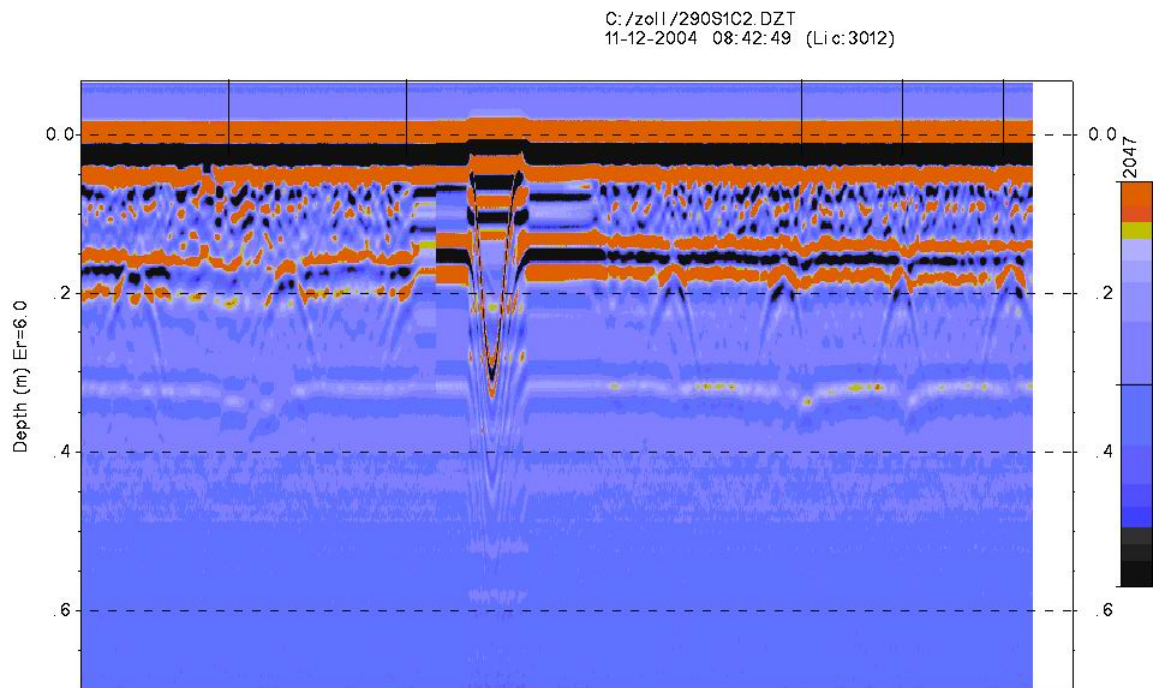
Texas Transportation Institute

(b)

**Figure A-1 US 290 crack #1 and associated GPR waveform**



(a)



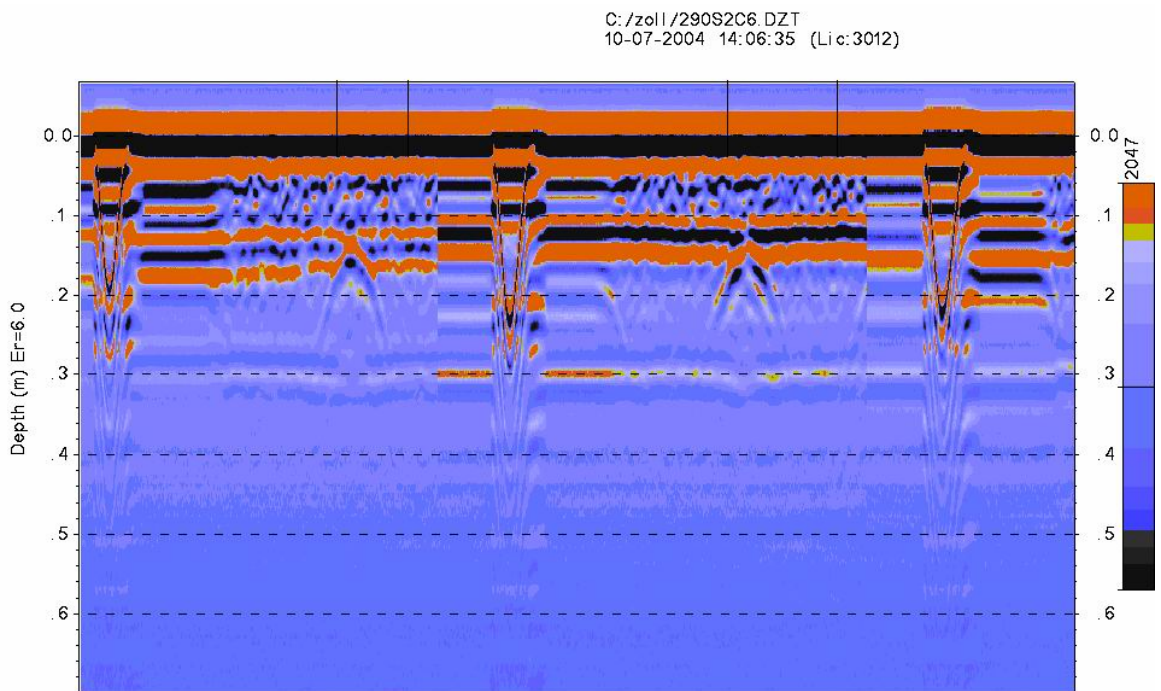
Texas Transportation Institute

(b)

**Figure A-2 US 290 crack #2 and associated GPR waveform**



(a)



Texas Transportation Institute

(b)

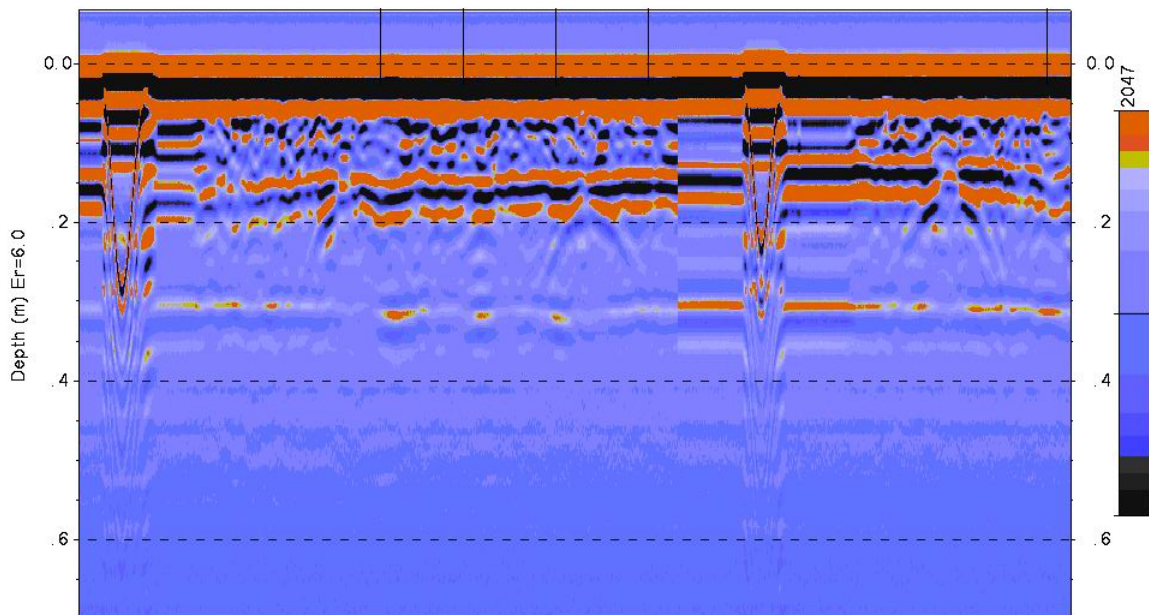
**Figure A-3 US 290 crack #6 and associated GPR waveform**





(a)

C:/zoll/290S3C7.DZT  
11-12-2004 08:35:36 (Lic:3012)



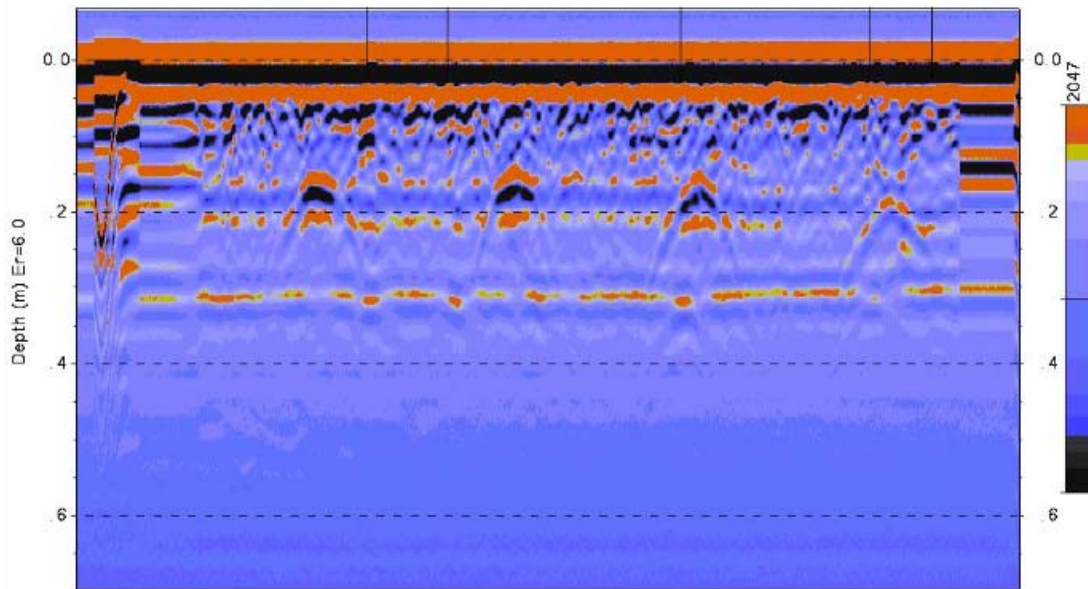
Texas Transportation Institute

(b)

**Figure A-4 US 290 crack #7 and associated GPR waveform**



(a)

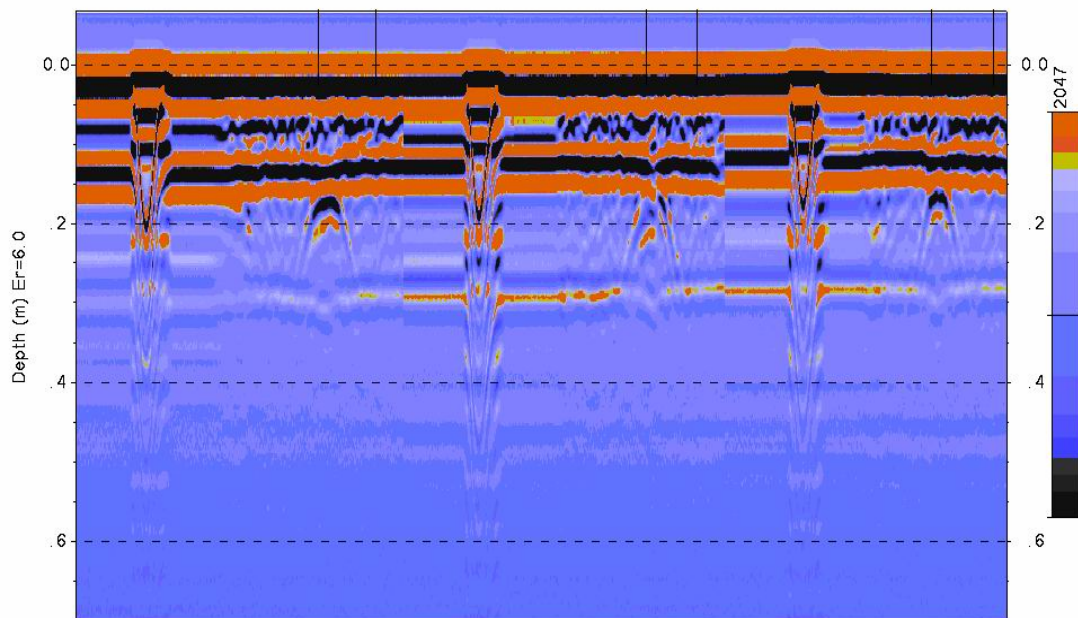


(b)

**Figure A-5 US 290 crack #8 and associated GPR waveform**



(a)

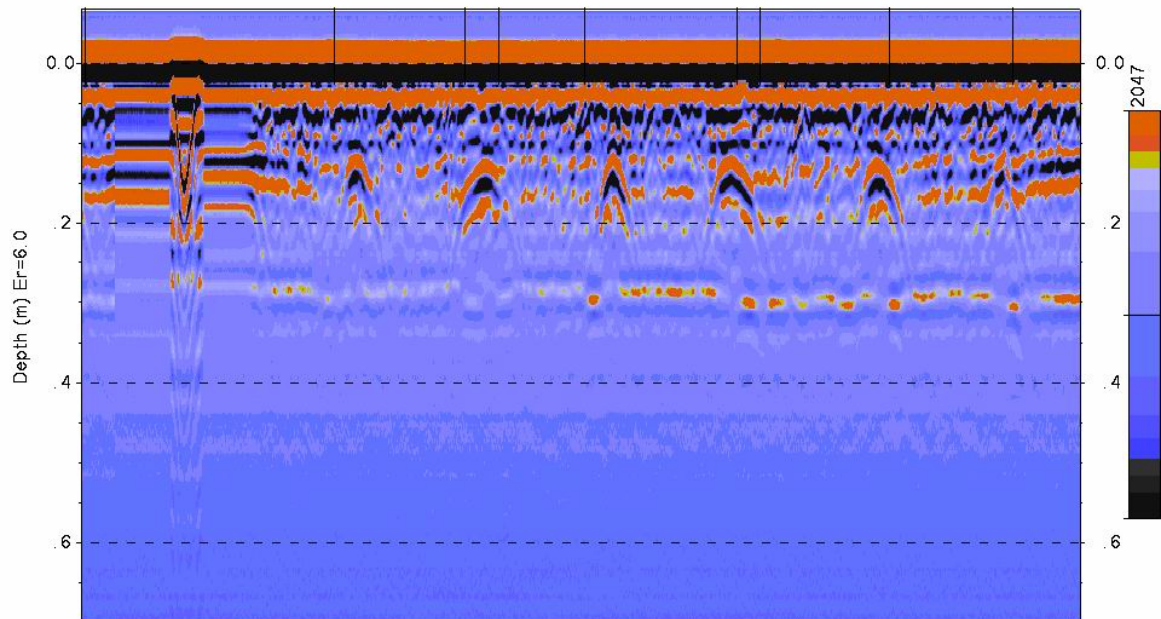


(b)

**Figure A-6 US 290 crack #11 and associated GPR waveform**



(a)

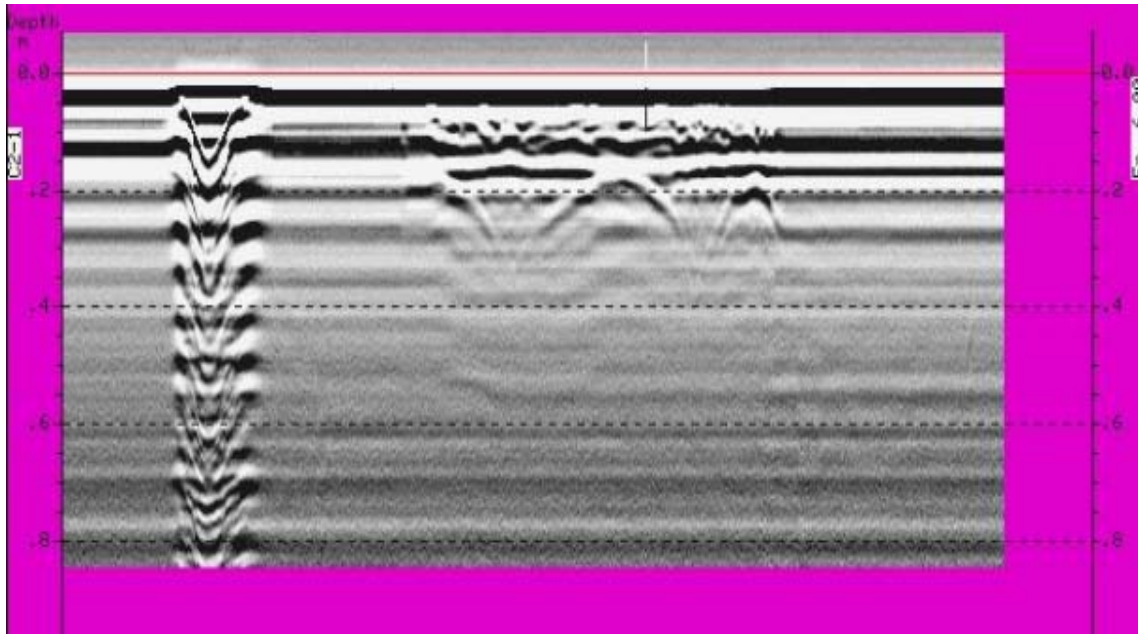


(b)

**Figure A-7 US 290 crack #12 and associated GPR waveform**



(a)

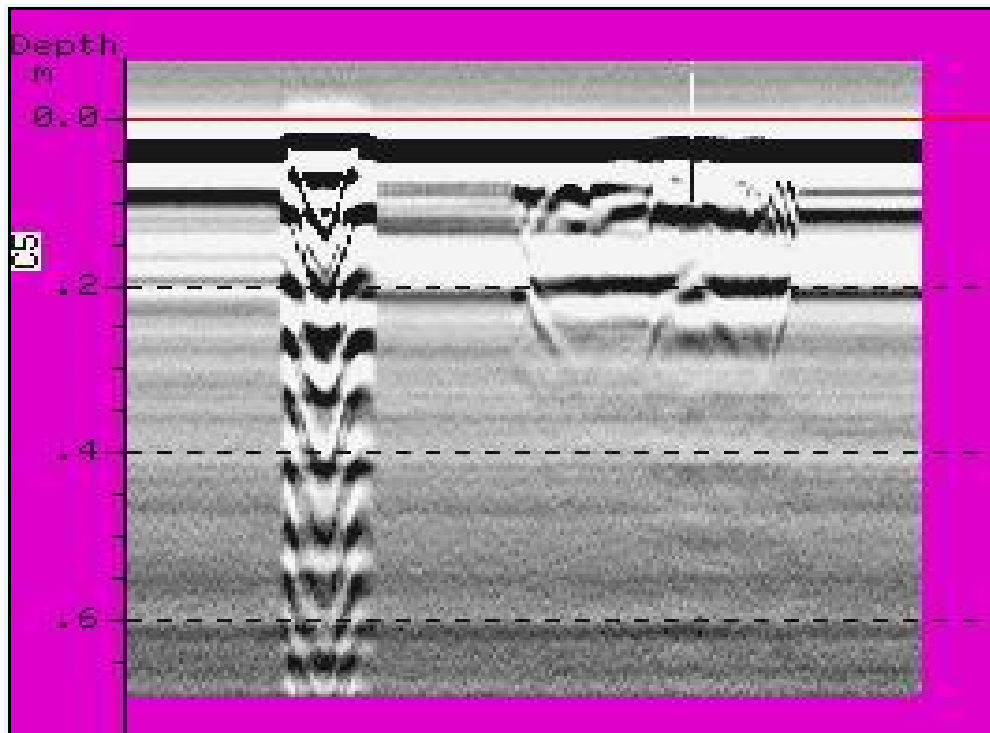


(b)

**Figure A-8 SH 288 crack #2 and associated GPR waveform**



(a)

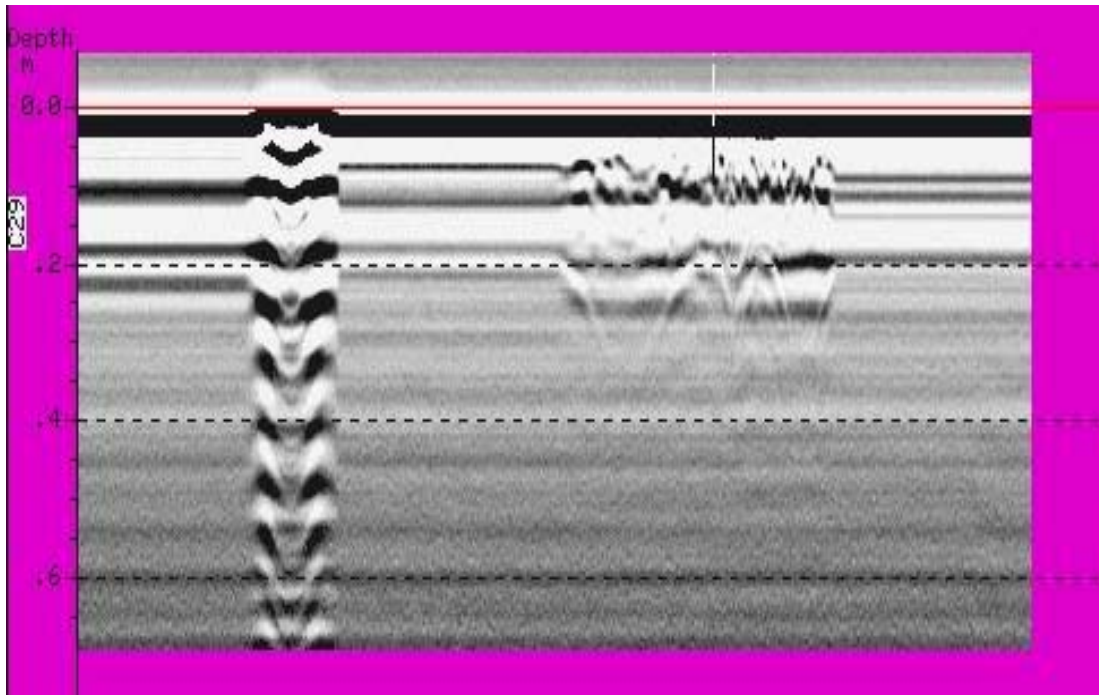


(b)

**Figure A-9 SH 288 crack #5 and associated GPR waveform**



(a)



(b)

**Figure A-10 SH 288 crack #29 and associated GPR waveform**

**Table A-1 Intermittent negative peaks for GPR waveforms**

Cracks	Location No.	Intermittent negative peak (voltage)		
		good ( $V_1$ )	bad ( $V_2$ )	( $V_2-V_1$ )
SH6stn2	1	-0.691	-0.693	-0.002
	2	-0.757	-0.215	0.542
	3	-0.293	-0.103	0.19
	4	-0.884	-0.669	0.215
	5	-0.454	-0.693	-0.239
	6	-0.557	-0.112	0.445
	7	-0.986	-0.85	0.136
	8	-1.162	-0.889	0.273
	9	-0.684	-0.698	-0.014
	10	-0.991	-0.063	0.928
	11	-0.557	-0.933	-0.376
	12	-0.85	-1.289	-0.439
	13	-1.221	-0.361	0.86
	14	-0.679	-1.06	-0.381
SH6st1p1	1	-0.5565	-0.376	0.1805
	2	-0.313	-0.142	0.171
	3	-0.757	-0.835	-0.078
	4	-0.43	-0.01	0.42
	5	-0.70167	-0.352	0.34967
SH6st1p4	1	-0.425	-0.239	0.186
	2	-0.41	-0.361	0.049
	3	-0.854	-0.503	0.351
	4	-0.166	-0.313	-0.147
	5	-0.327	-0.049	0.278
SH6st1p8	1	-0.879	-0.649	0.23
	2	-0.64	0.073	0.713
	3	-0.2395	-0.137	0.1025
	4	-0.2905	-0.542	-0.2515
	5	-0.5105	-0.146	0.3645
SH6st2p1	1	-0.1245	-0.303	-0.1785
SH6st3cr1	1	-0.4735	-0.742	-0.2685
	2	-0.647	-0.684	-0.037
	3	-0.569	-0.093	0.476
	4	-0.4665	-0.21	0.2565



Table A-1 Continued

Cracks	Location No.	Intermittent negative peak (voltage)		
		good ( $V_1$ )	bad ( $V_2$ )	( $V_2-V_1$ )
US290s2c4	1	-0.886	-1.27	-0.384
	2	-0.886	-0.869	0.017
	3	-0.9715	-0.669	0.3025
	4	-0.9715	-0.786	0.1855
	5	-0.708	-0.601	0.107
	6	-0.708	-0.527	0.181
US290s2c5	1	-0.745	-0.405	0.34
	2	-0.745	-0.244	0.501
	3	-0.745	-0.146	0.599
	4	-1.15	-0.537	0.613
	5	-1.15	-0.439	0.711
	6	-1.15	-0.41	0.74
	7	-0.618	-1.113	-0.495
	8	-0.618	-0.752	-0.134
	9	-0.618	-0.439	0.179
US290s2c6	1	-0.7275	-0.625	0.1025
	2	-0.7275	-0.459	0.2685
	3	-0.586	-0.767	-0.181
	4	-0.586	-0.596	-0.01
	5	-0.8545	-1.353	-0.4985
	6	-0.8545	-0.537	0.3175
US290s3c7	1	-0.613	-0.41	0.203
	2	-0.613	-0.903	-0.29
	3	-0.613	-0.444	0.169
	4	-0.613	-1.084	-0.471
	5	-0.999	-0.327	0.672
	6	-0.999	-0.601	0.398
	7	-0.999	-0.249	0.75
	8	-0.999	-0.669	0.33
	9	-0.637	-0.41	0.227
	10	-0.637	-0.332	0.305
	11	-0.637	-0.532	0.105
	12	-0.637	-0.942	-0.305

Table A-1 Continued

Cracks	Location No.	Intermittent negative peak (voltage)		
		good ( $V_1$ )	bad ( $V_2$ )	( $V_2-V_1$ )
US290s3c8	1	-0.735	-1.592	-0.857
	2	-0.735	-1.094	-0.359
	3	-0.735	-0.122	0.613
	4	-0.735	-0.557	0.178
	5	-0.735	-0.132	0.603
	6	-1.2695	-0.991	0.2785
	7	-1.2695	-0.483	0.7865
	8	-1.2695	-0.845	0.4245
	9	-1.2695	-1.226	0.0435
	10	-1.2695	-0.562	0.7075
	11	-0.9305	-0.371	0.5595
	12	-0.9305	-0.649	0.2815
	13	-0.9305	-0.605	0.3255
	14	-0.9305	-0.776	0.1545
US290s3c9	1	-0.6055	-0.117	0.4885
	2	-0.6055	-0.176	0.4295
	3	-0.6055	-0.537	0.0685
	4	-0.6055	-0.01	0.5955
	5	-0.6055	-0.176	0.4295
	6	-0.6055	-0.396	0.2095
	7	-0.593	-0.41	0.183
	8	-0.593	-0.493	0.1
	9	-0.593	-0.488	0.105
US290c10	1	-0.9475	-1.104	-0.1565
	2	-0.9475	-1.108	-0.1605
	3	-0.8665	-0.947	-0.0805
	4	-0.8665	-0.454	0.4125
	5	-1.311	-0.83	0.481
	6	-1.311	-0.962	0.349
US290s4c11	1	-1.1645	-1.494	-0.3295
	2	-1.1645	-0.879	0.2855
	3	-1.057	-0.962	0.095
	4	-1.057	-1.338	-0.281
	5	-0.7155	-1.836	-1.1205
	6	-0.7155	-1.396	-0.6805

Table A-1 Continued

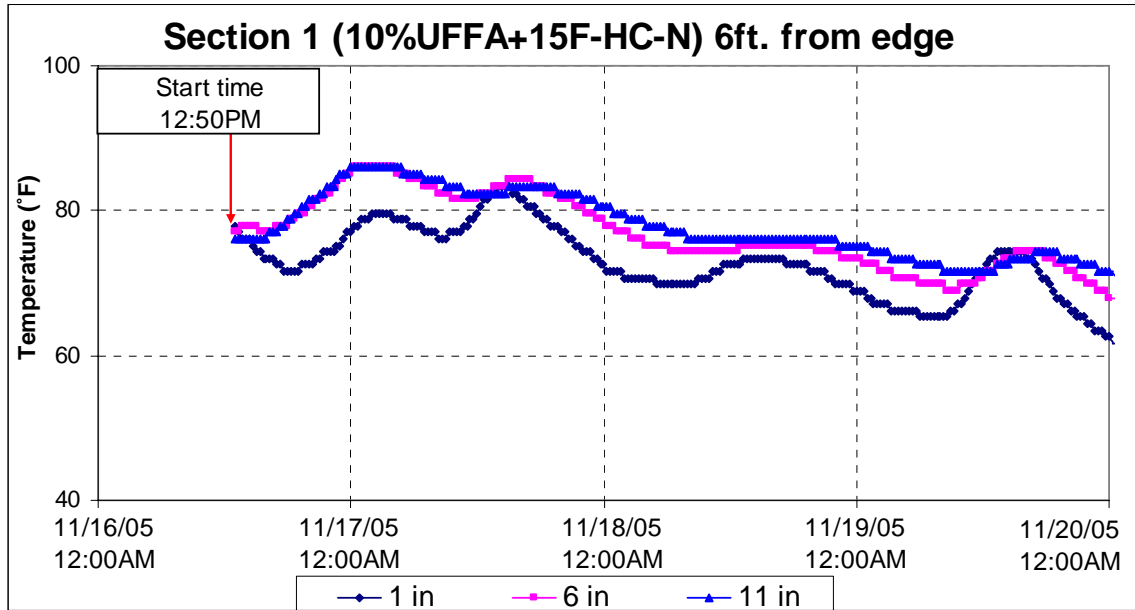
Cracks	Location No.	Intermittent negative peak (voltage)		
		good (V <sub>1</sub> )	bad (V <sub>2</sub> )	(V <sub>2</sub> -V <sub>1</sub> )
US290s4c12	1	-1.135	-0.449	0.686
	2	-1.135	-0.4	0.735
	3	-1.135	-1.084	0.051
	4	-1.135	-0.986	0.149
	5	-1.135	-1.123	0.012
	6	-1.135	-1.25	-0.115
	7	-1.135	-1.182	-0.047
	8	-1.135	-0.723	0.412
	9	-1.135	-0.771	0.364
	10	-1.299	-1.499	-0.2
	11	-1.299	-1.172	0.127
	12	-1.299	-0.63	0.669
	13	-1.299	-1.191	0.108
	14	-1.299	-0.938	0.361
	15	-1.299	-0.776	0.523
	16	-1.299	-0.654	0.645
	17	-1.299	-0.537	0.762
	18	-1.299	-0.625	0.674
	19	-1.57	-0.957	0.613
	20	-1.57	-0.425	1.145
	21	-1.57	-0.698	0.872
	22	-1.57	-1.504	0.066
	23	-1.57	-0.82	0.75
	24	-1.57	-1.523	0.047
	25	-1.57	-0.908	0.662
	26	-1.57	-1.26	0.31
SH288c51	1	-0.5905	-0.288	0.3025
	2	-0.4835	-0.264	0.2195
SH288c50	1	-0.7325	-0.259	0.4735
	2	-0.642	-0.347	0.295
SH288c5	1	-0.52	-0.635	-0.115
	2	-0.747	-0.405	0.342
SH288c49	1	-0.9375	-0.547	0.3905
	2	-0.8225	-0.479	0.3435

Table A-1 Continued

Cracks	Location No.	Intermittent negative peak (voltage)		
		good (V <sub>1</sub> )	bad (V <sub>2</sub> )	(V <sub>2</sub> -V <sub>1</sub> )
SH288c48	1	-0.8915	-0.425	0.4665
	2	-0.5665	-0.342	0.2245
SH288c47	1	-0.5465	-0.513	0.0335
	2	-0.288	-0.571	-0.283
SH288c4	1	-0.691	-0.547	0.144
	2	-0.574	-0.493	0.081
SH288c30	1	-0.5735	-0.273	0.3005
	2	-0.8445	-0.156	0.6885
SH288c29	1	-0.635	-0.215	0.42
	2	-0.73	-0.244	0.486
SH288c27	1	-0.4395	-0.122	0.3175
	2	-0.857	-0.205	0.652
SH288c24	1	-0.493	-0.381	0.112
	2	-0.581	-0.586	-0.005
SH288c23	1	-0.659	-0.752	-0.093
	2	-0.7205	-0.63	0.0905
SH288c22	1	-0.6445	-0.283	0.3615
	2	-0.5955	-0.527	0.0685
SH288c21	1	-0.615	-0.503	0.112
	2	0.2345	0.146	-0.0885
SH288c2	1	-0.359	-0.156	0.203
	2	-0.8205	-0.61	0.2105
SH288c19	1	-0.398	-0.259	0.139
	2	-0.5395	-0.225	0.3145
SH288c17	1	0.115	0.088	-0.027
	2	-0.3665	-0.073	0.2935
SH288c1	1	-0.542	-0.605	-0.063
	2	-0.6345	-0.293	0.3415

**APPENDIX B**

**DATA DETAILS FOR WINTER TEST SECTIONS**



**Figure B-1 Temperature profile of test section 1**

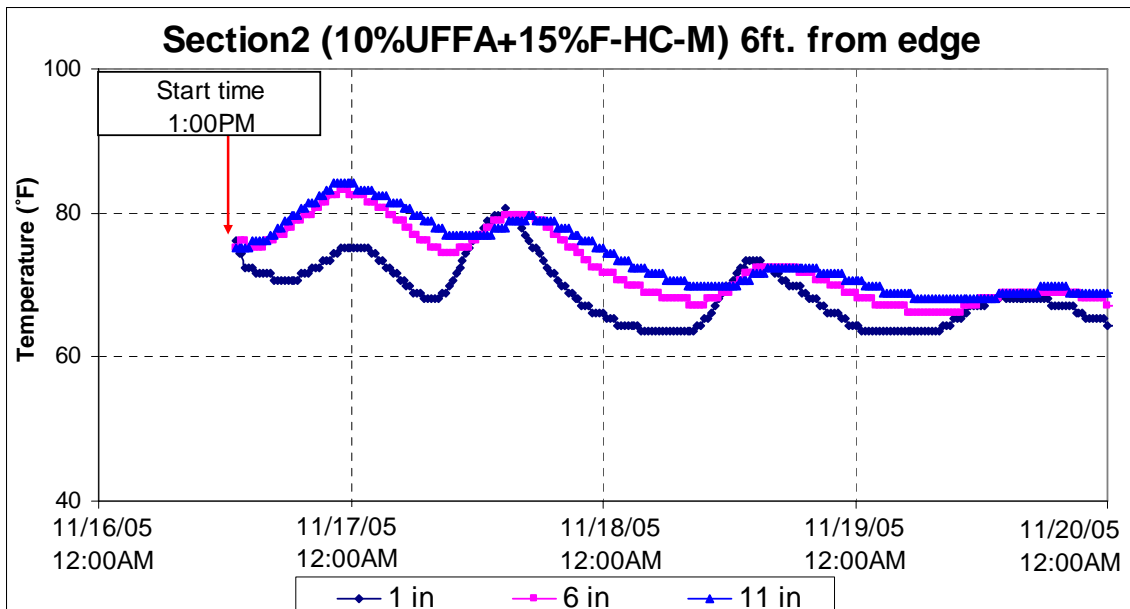


**Figure B-2 Temperature profile of test section 2**

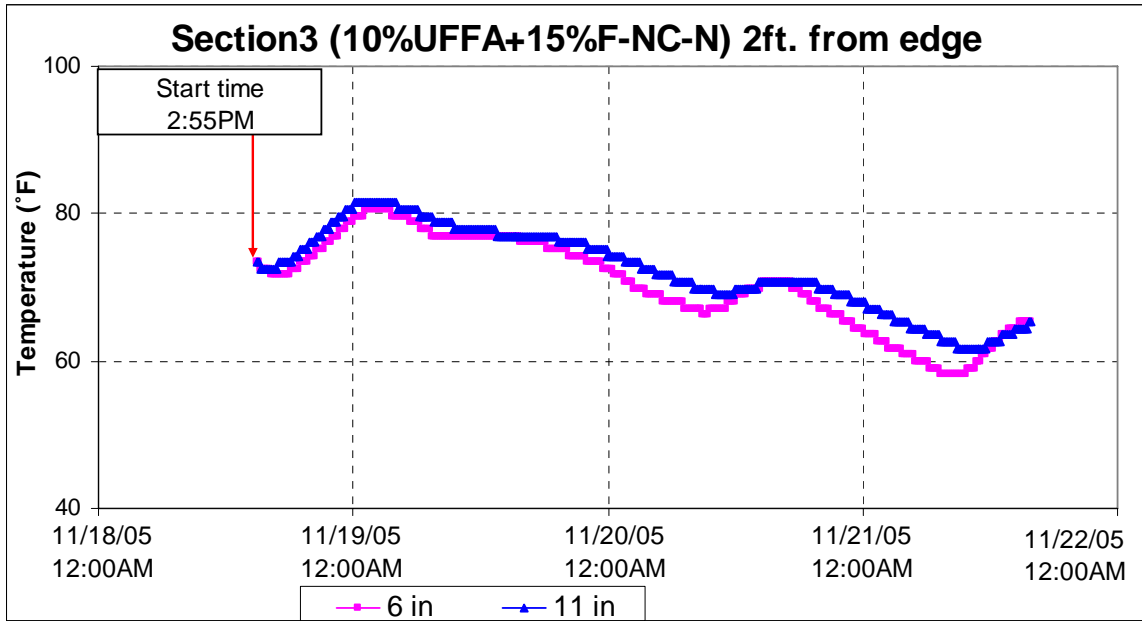


**Figure B-3 Temperature profile of test section 3**

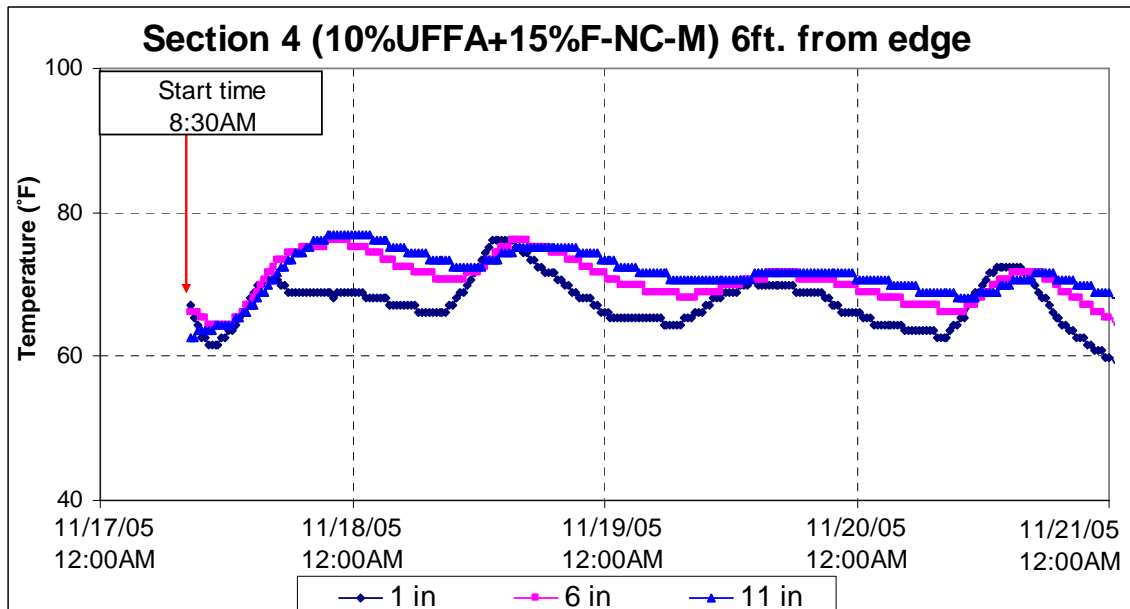


**Figure B-4 Temperature profile of test section 4**

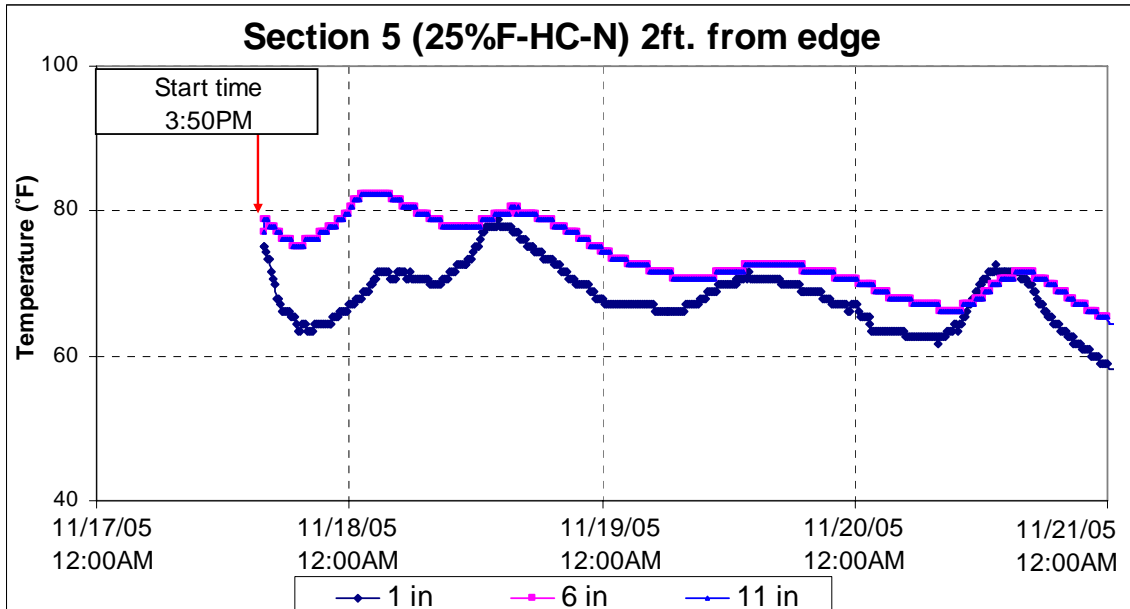


**Figure B-5 Temperature profile of test section 5**

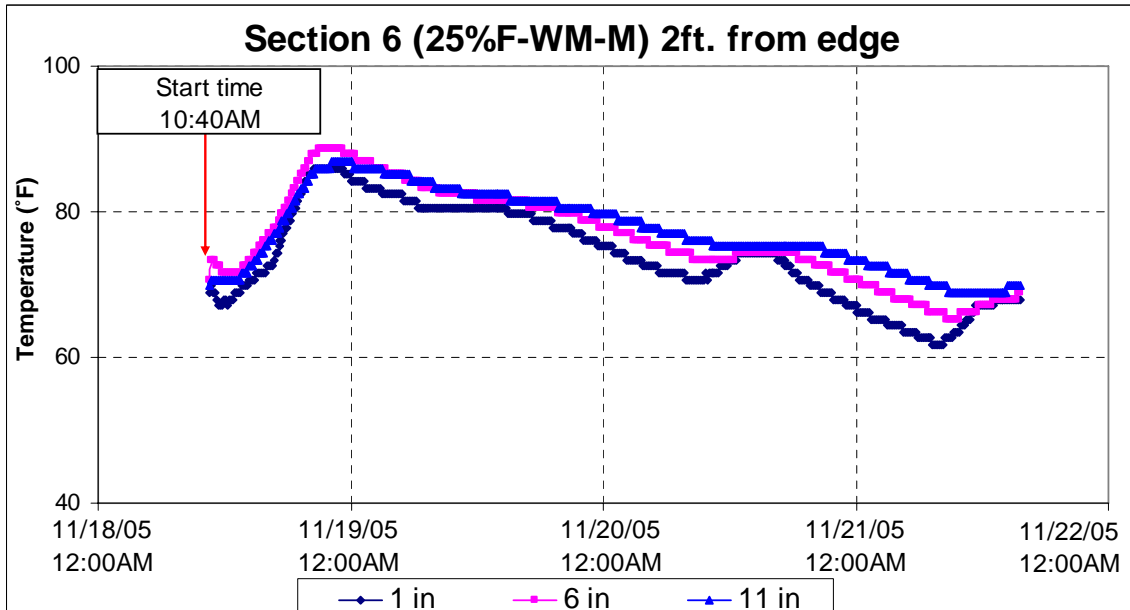


**Figure B-6 Temperature profile of test section 6**



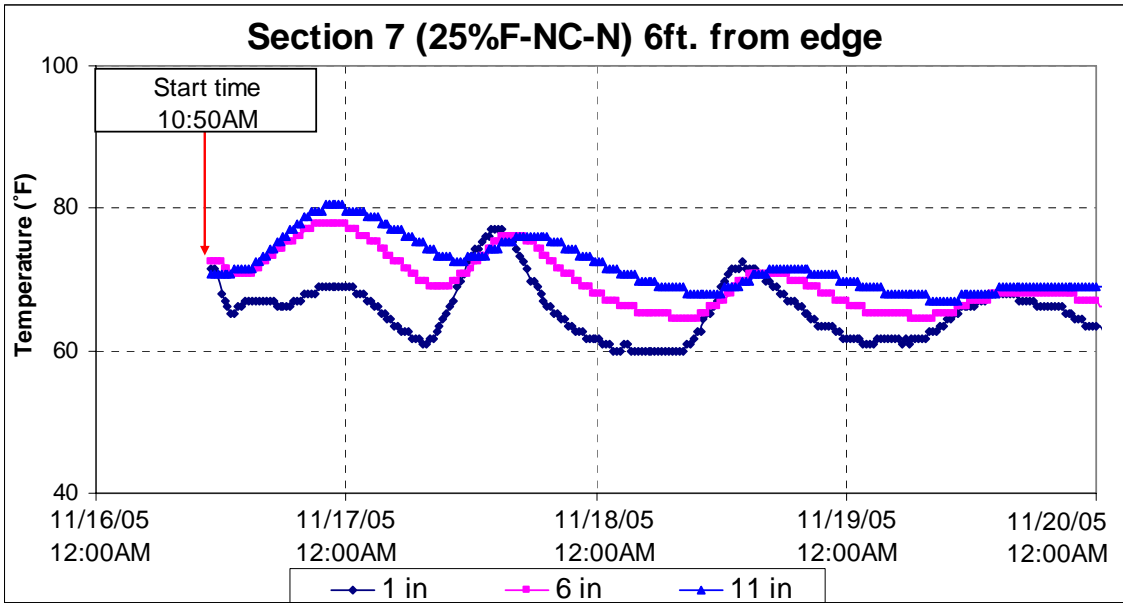


**Figure B-7 Temperature profile of test section 7**

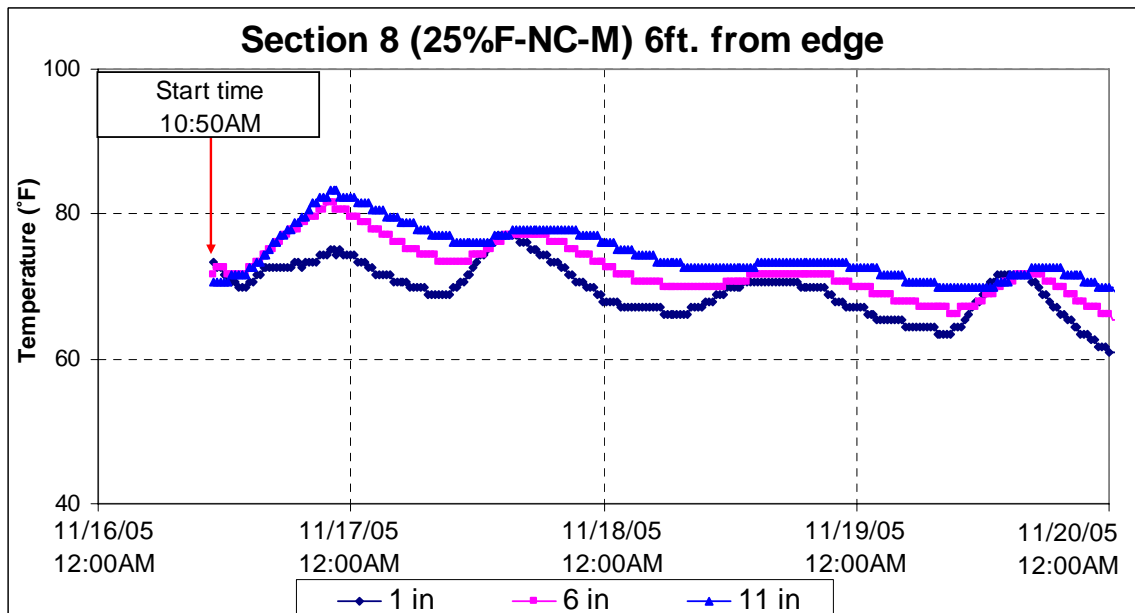


**Figure B-8 Temperature profile of test section 8**

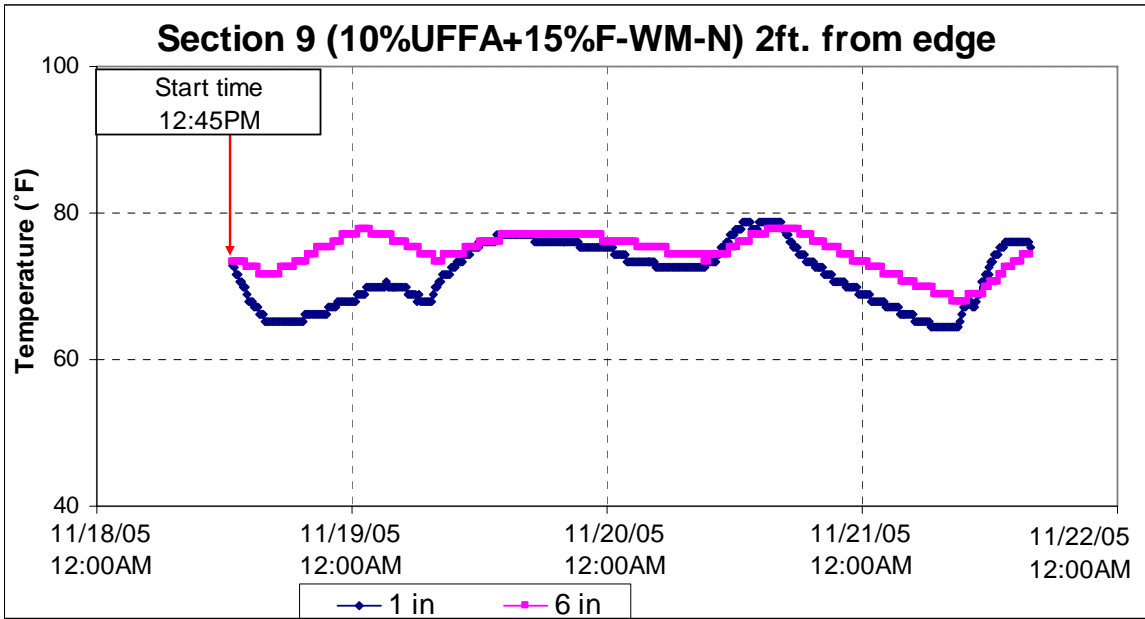


**Figure B-9 Temperature profile of test section 9**

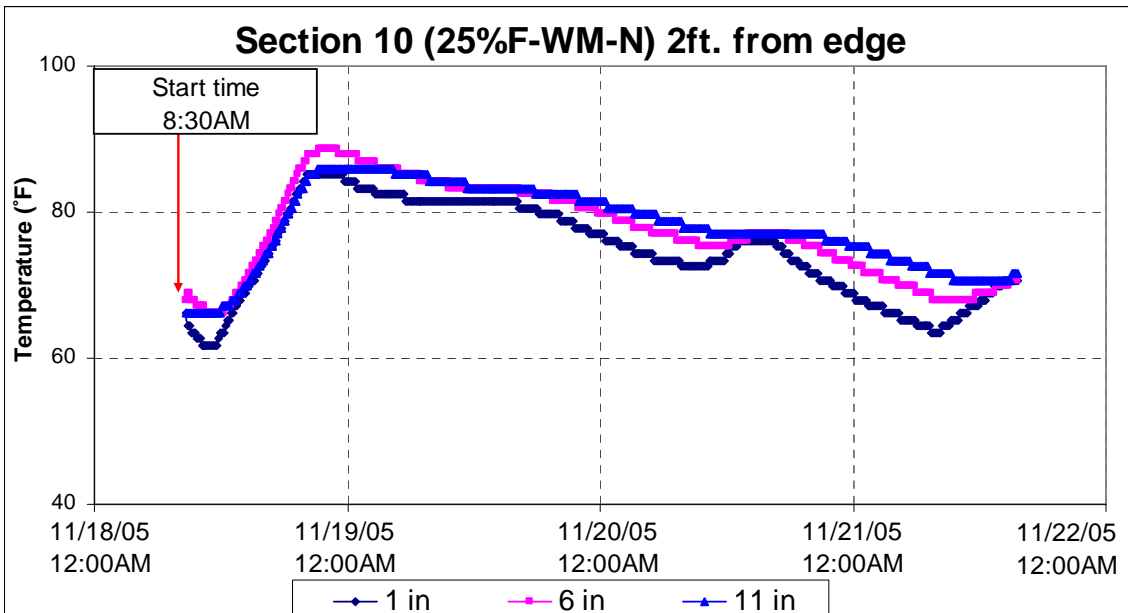


**Figure B-10 Temperature profile of test section 10**

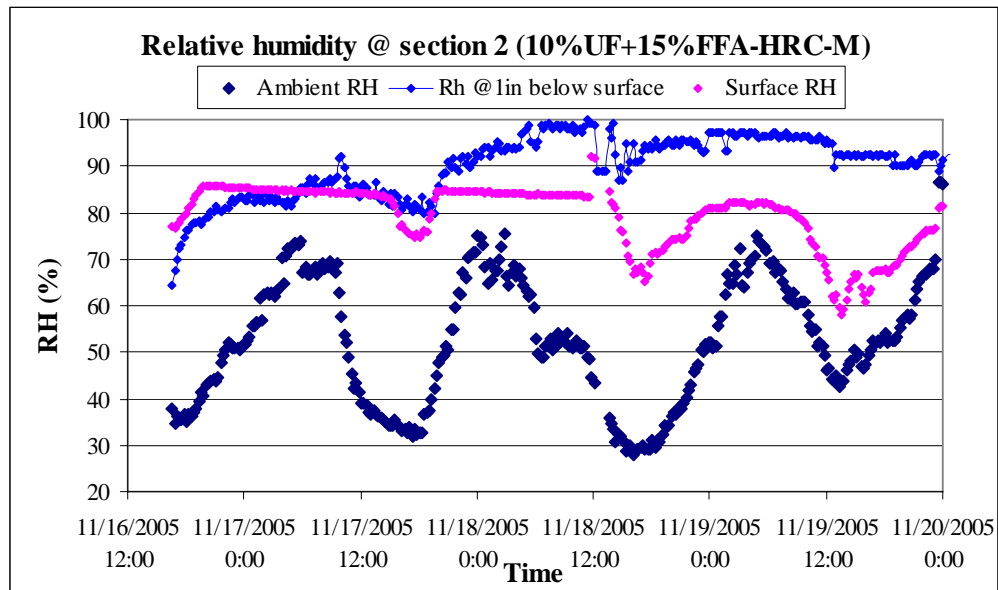


**Figure B-11 Moisture profiles of test section 2**

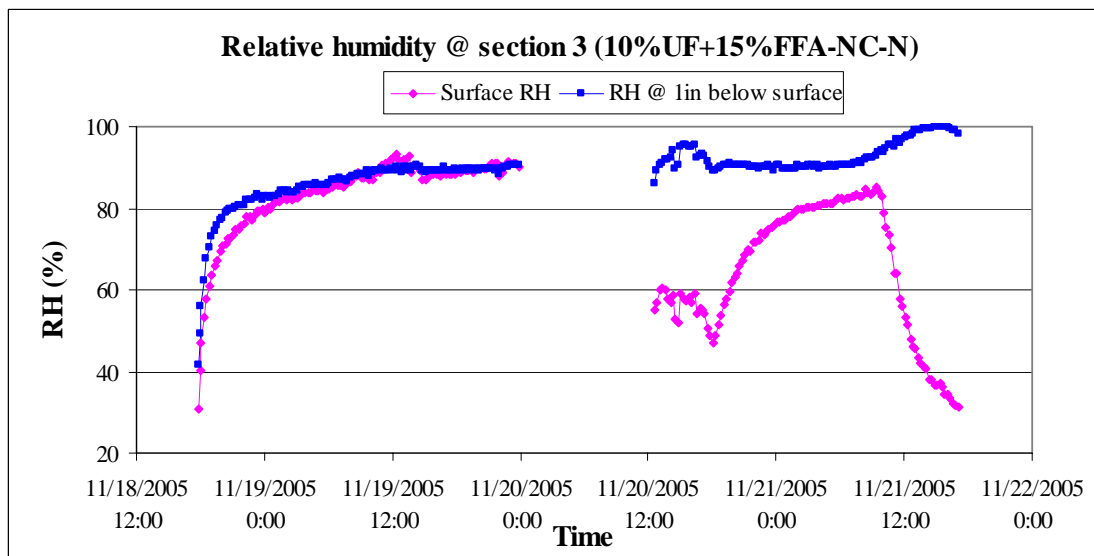


**Figure B-12 Moisture profiles of test section 3**

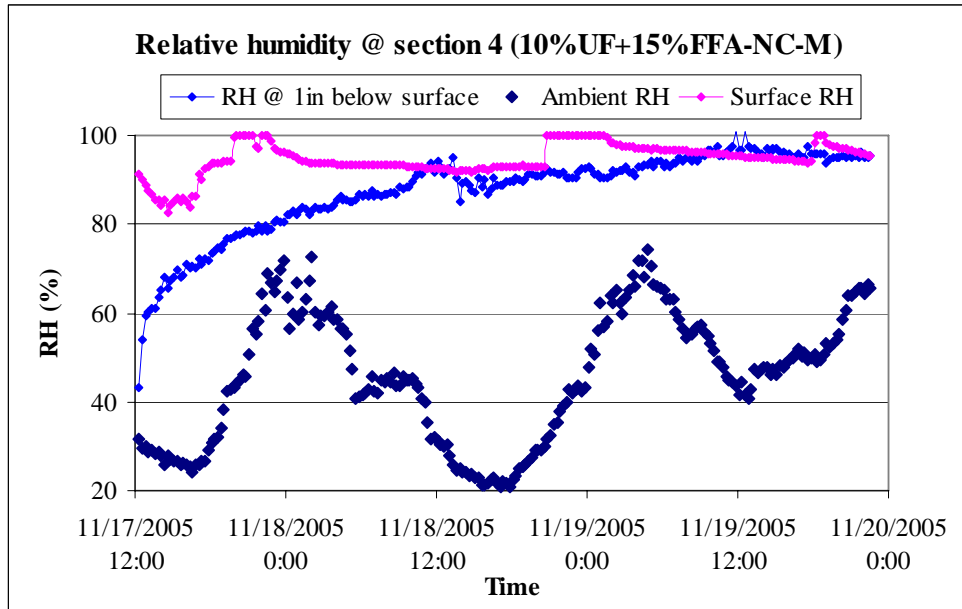


**Figure B-13 Moisture profiles of test section 4**

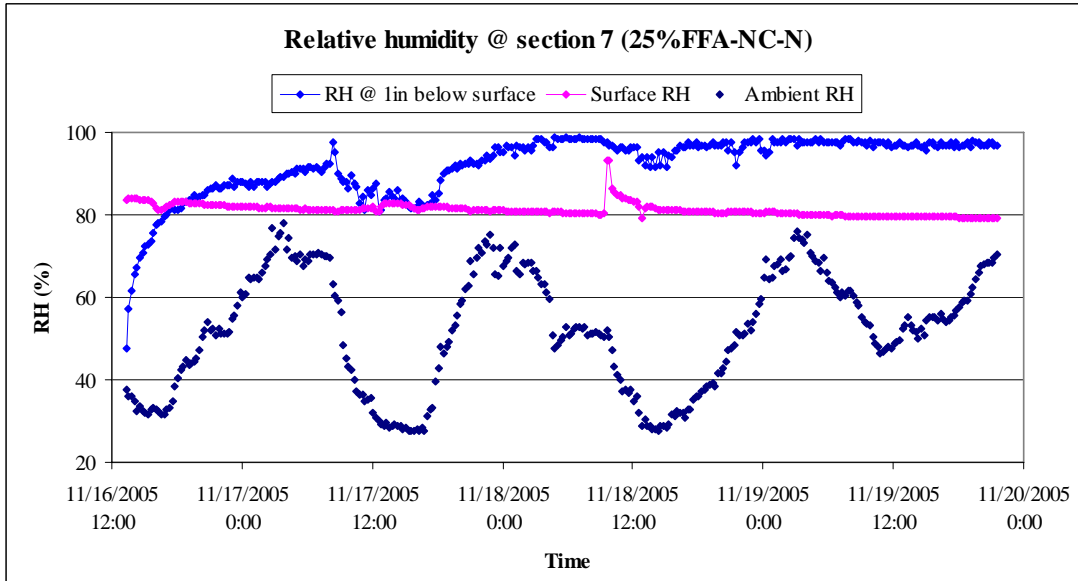


**Figure B-14 Moisture profiles of test section 7**

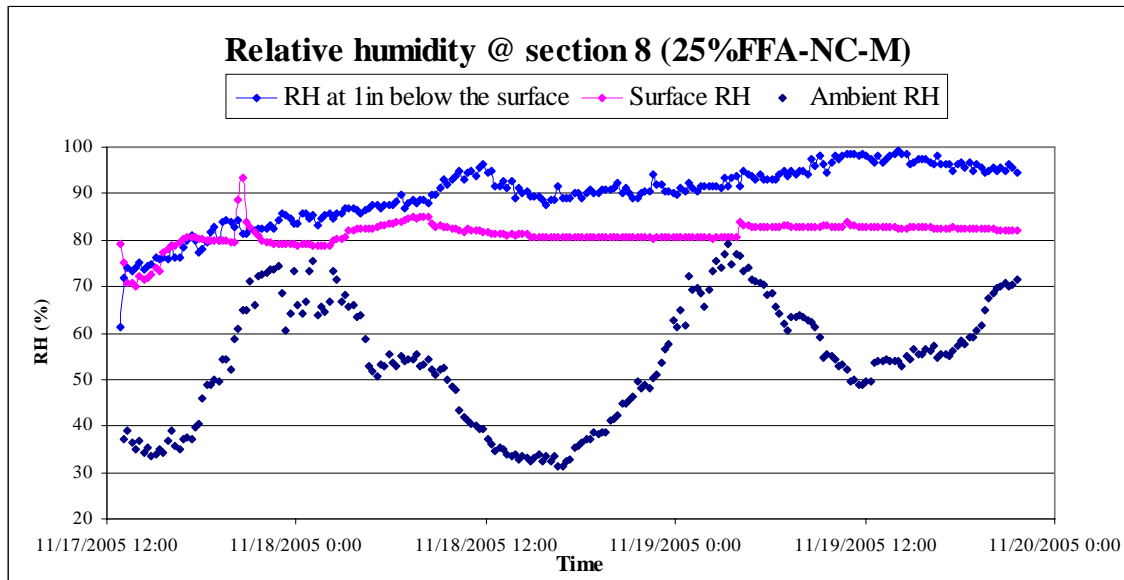


**Figure B-15 Moisture profiles of test section 8**

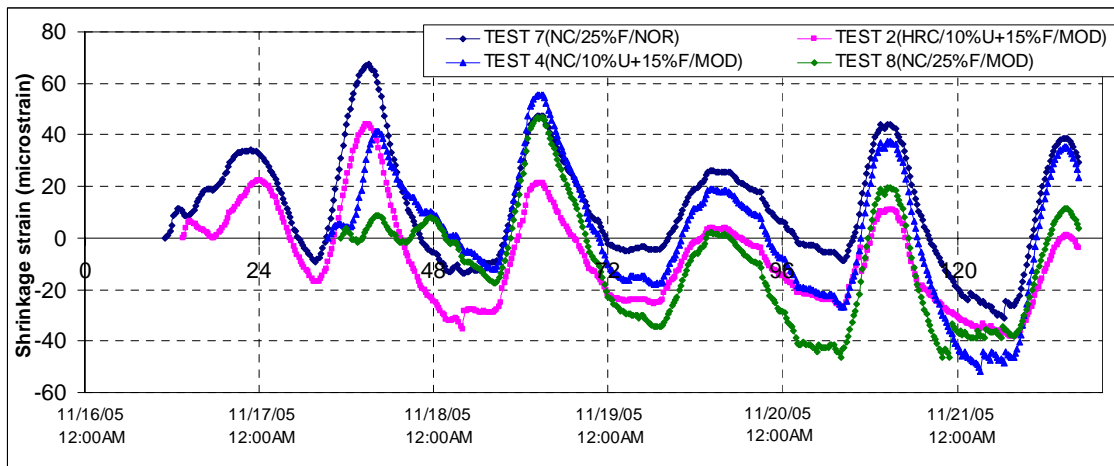


**Figure B-16 Drying shrinkage with time for different sections**

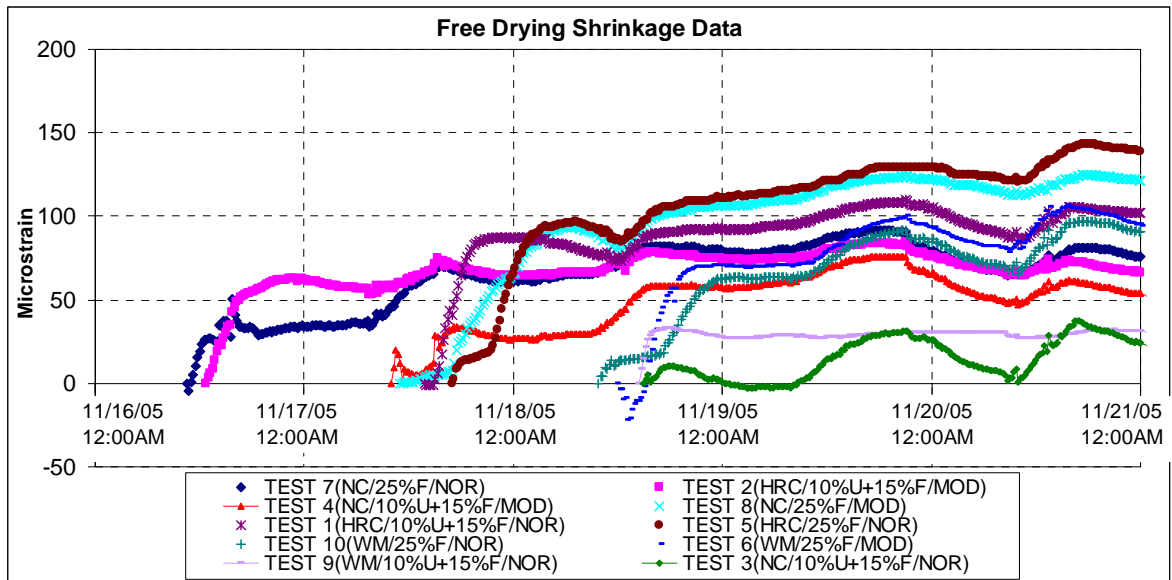


**Figure B-17 Free shrinkage with time for different sections**

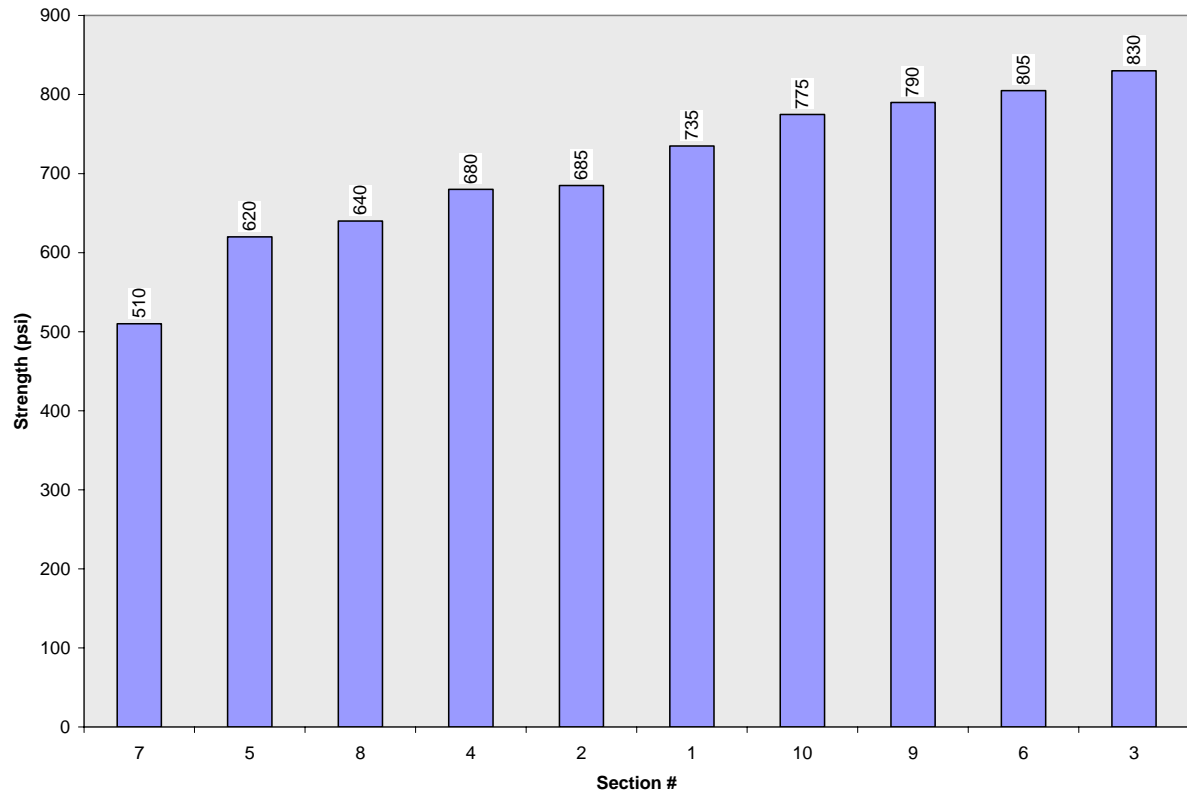


**Figure B-18 7-day flexural strength of concrete for all test sections**

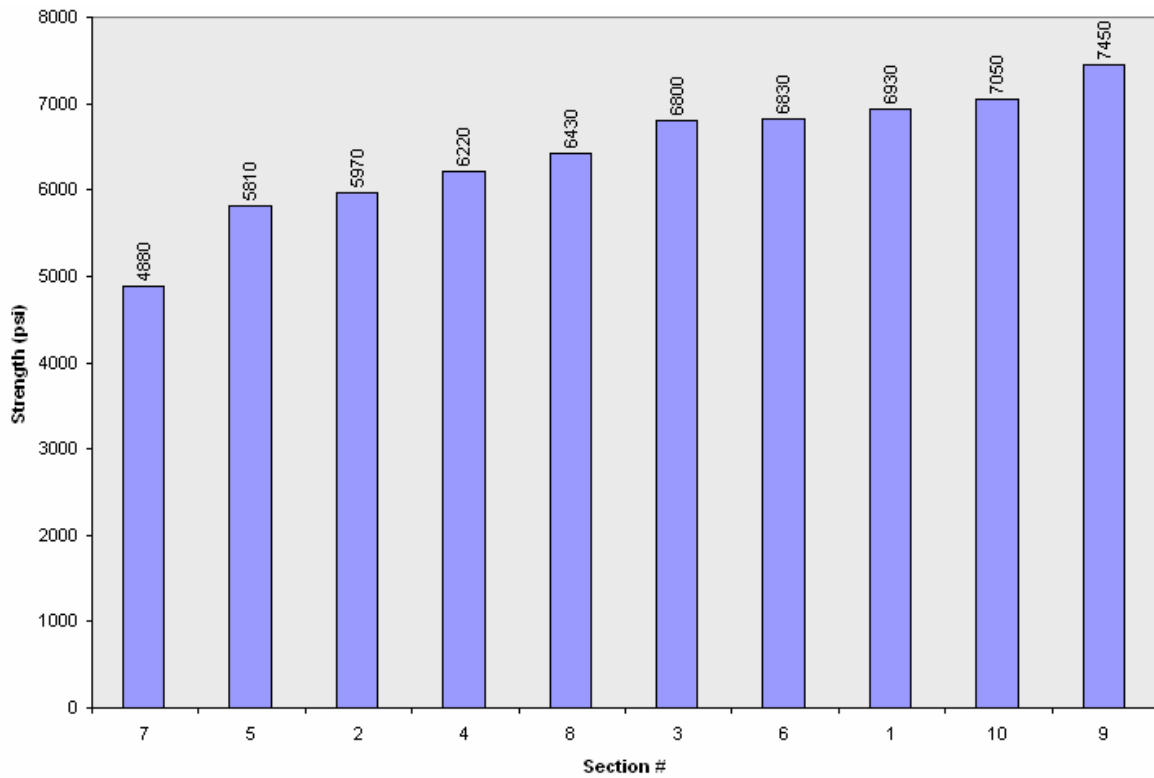


**Figure B-19 7-day compressive strength of concrete for all test sections**



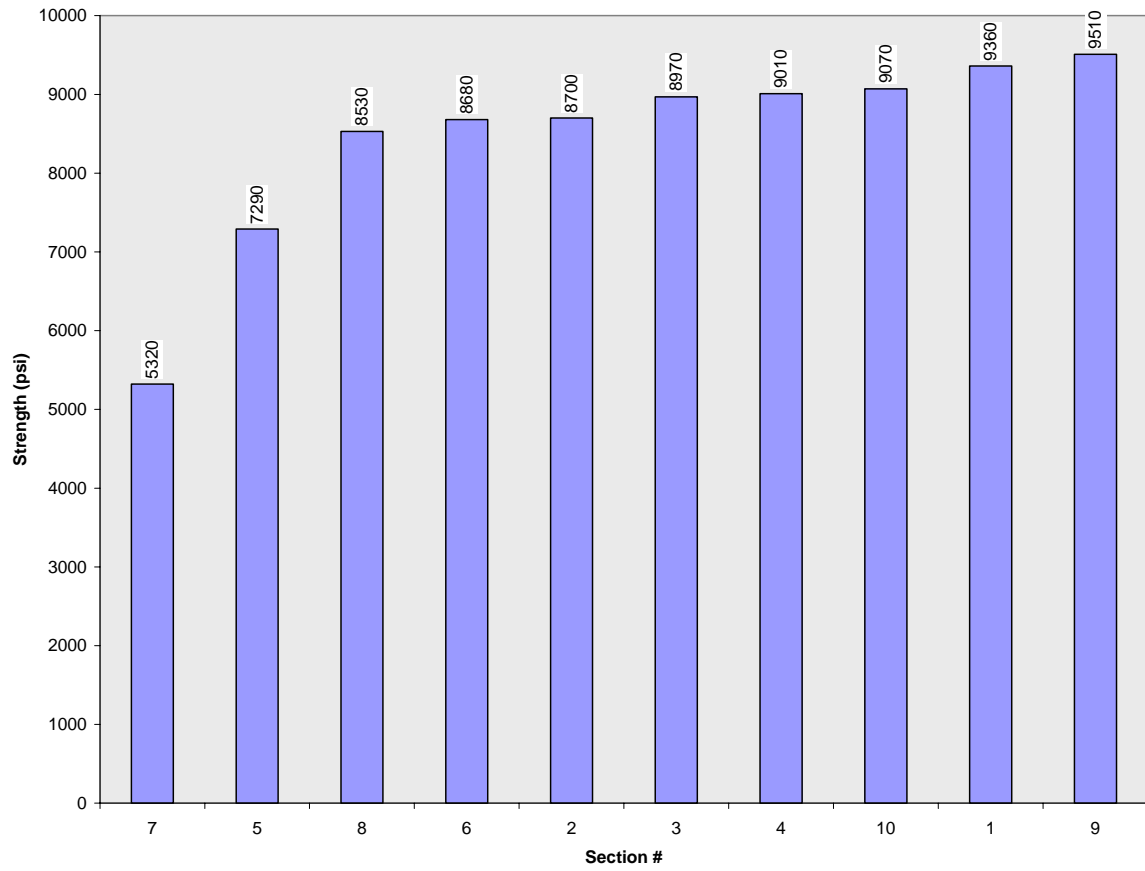


**Figure B-20 28-day compressive strength of concrete for all test sections**

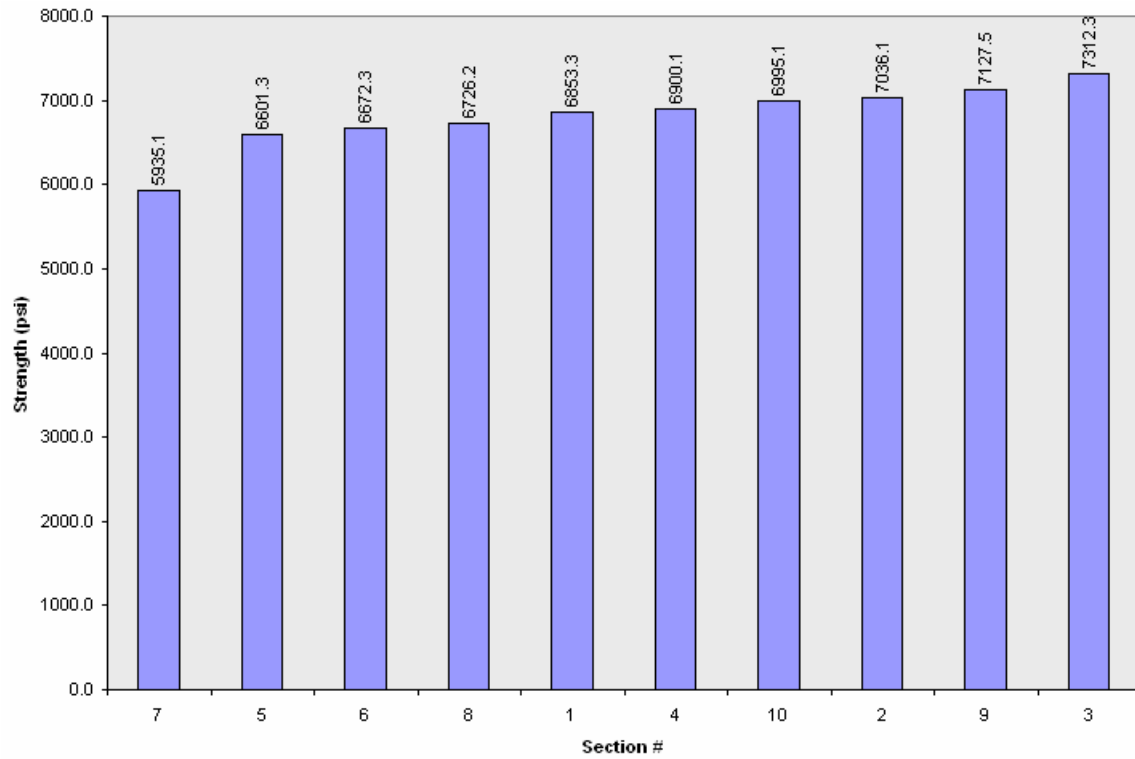


**Figure B-21 7-day elastic modulus of concrete for all test sections by free-free test**

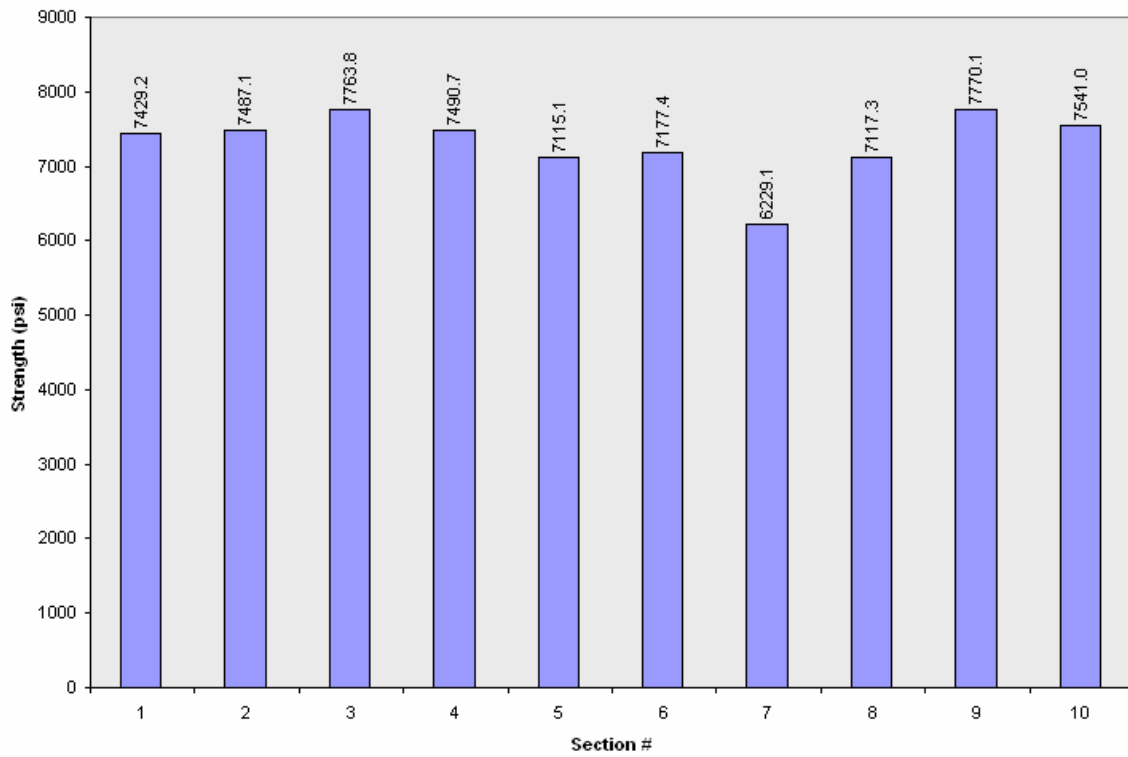


**Figure B-22 28-day elastic modulus of concrete for all test sections by free-free test**

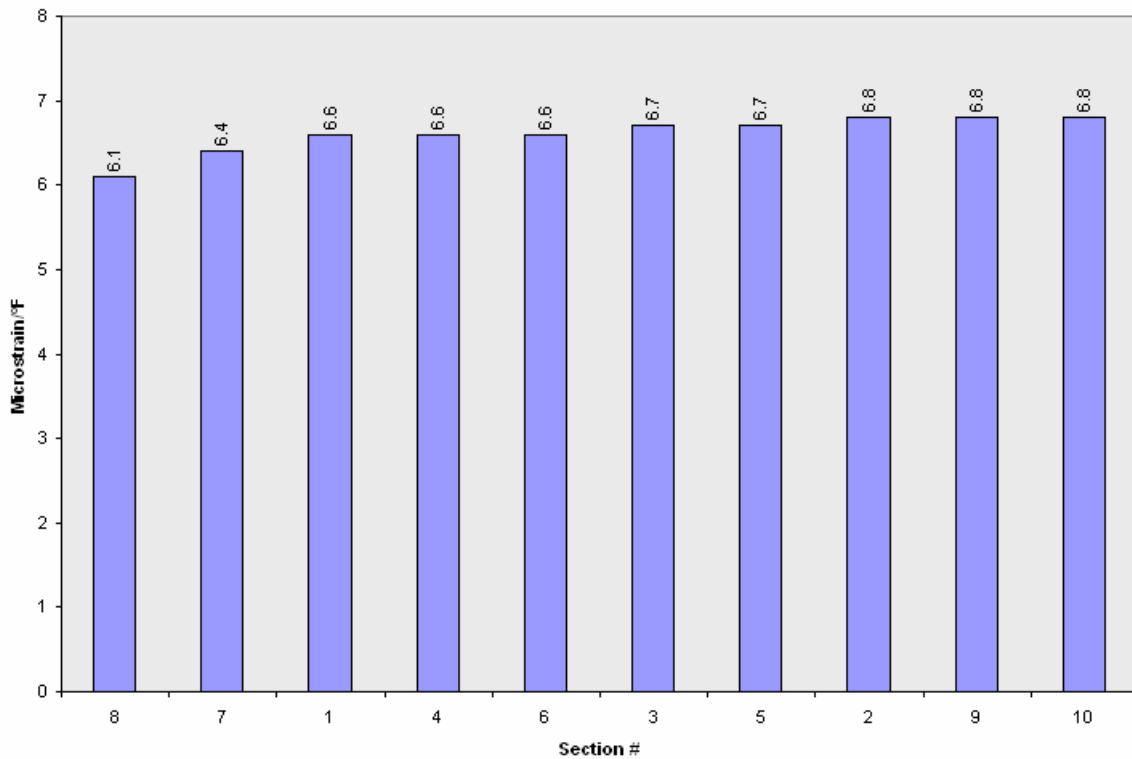
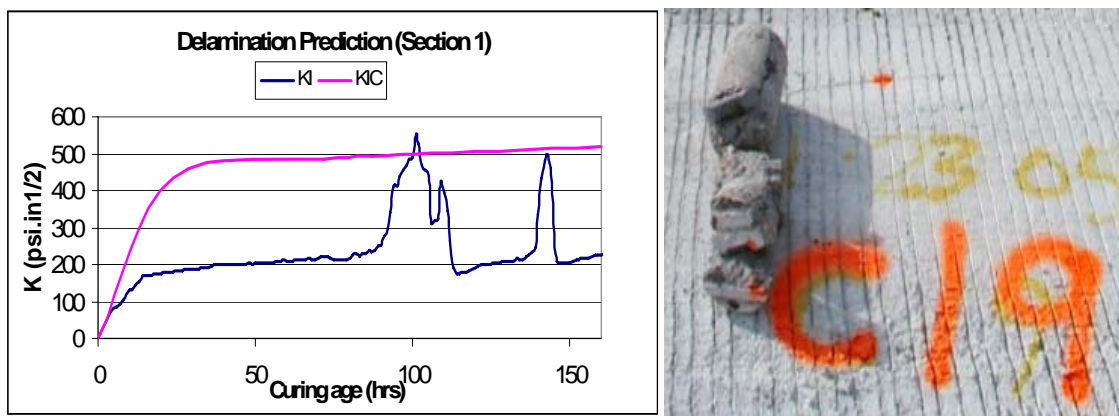


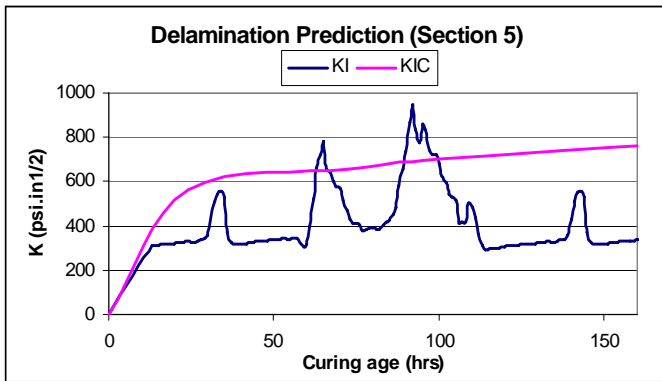
Figure B-23 19~26-day coefficient of thermal expansion of concrete for all test sections



(a)

(b)

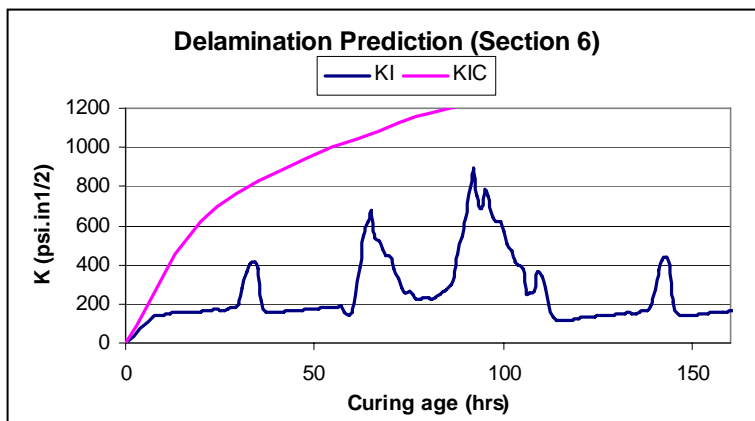
Figure B-24 Delamination prediction for section 1



(a)

(b)

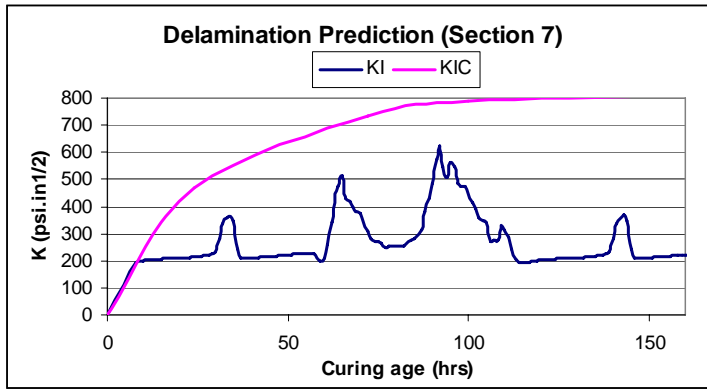
**Figure B-25 Delamination prediction for section 5**



(a)

(b)

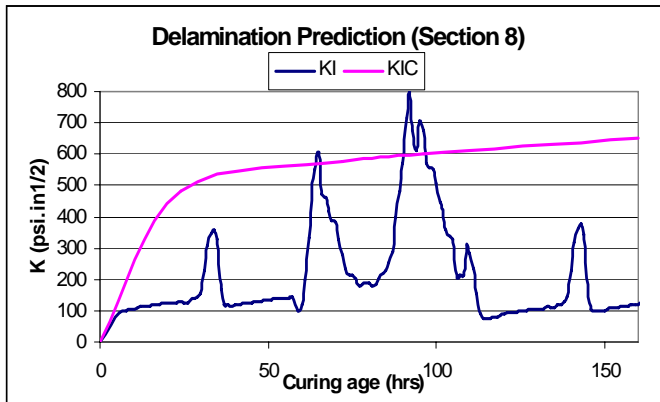
**Figure B-26 Delamination prediction for section 6**



(a)

(b)

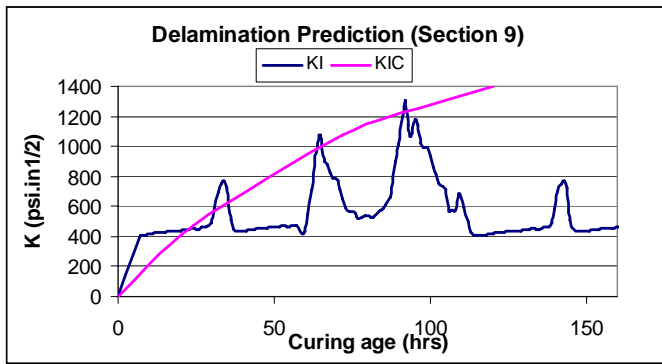
**Figure B-27 Delamination prediction for section 7**



(a)

(b)

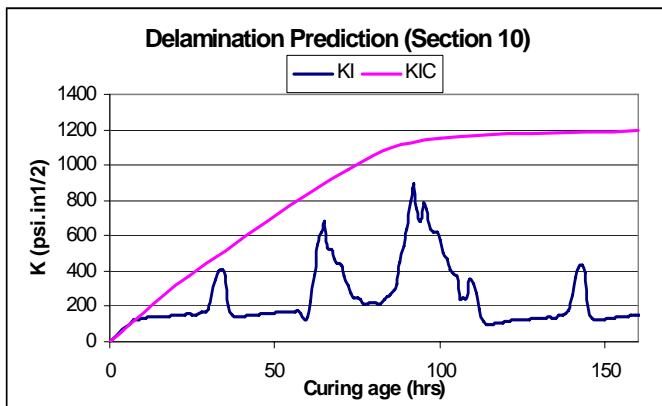
**Figure B-28 Delamination prediction for section 8**



(a)

(b)

**Figure B-29 Delamination prediction for section 9**



(a)

(b)

**Figure B-30 Delamination prediction for section 10**

## VITA

Name: JUANYU LIU

Permanent Address: Room 501H, CE/TTI Building, Texas A&M University System,  
College Station, TX 77843-3135

### EDUCATION

B.E. in Material Science and Engineering, Tongji University, Shanghai, P. R. China,  
July 1995.

M.S. in Civil Engineering, Texas A&M University, College Station, TX, December  
2001.

### PROFESSIONAL EXPERIENCE

- Since June 2001: Graduate Research Assistant, Texas Transportation Institute
- August 2005 to December 2005: Graduate Teaching Assistant, Department of Civil Engineering, Texas A&M University
- September 2000 to May 2001: Graduate Assistant Non-Teaching, Department of Civil Engineering, Texas A&M University
- August 1995 to Spring 2000: Assistant Researcher, State Key Laboratory of Concrete Materials Research, Tongji University, P. R. China